Universidade de Aveiro
2012/2013

Secção Autónoma de Ciências da Saúde

Ana Rita Freitas Colaço

Transporte transmembranar de cloreto por *Squaramides*: estudo *in silico*

Transmembrane transport of chloride by Squaramides: *in silico* study

Universidade de Aveiro
2012/2013

Secção Autónoma de Ciências da Saúde

Ana Rita Freitas Colaço

Transporte transmembranar de cloreto por *Squaramides*: estudo *in silico*

Transmembrane transport of chloride by Squaramides: *in silico* study

Dissertação apresentada à Universidade de Aveiro para cumprimento dos requisitos necessários à obtenção do grau de Mestre em Biomedicina Molecular, realizada sob a orientação científica do Doutor Vítor Manuel Sousa Félix, Professor Associado com Agregação do Departamento de Química da Universidade de Aveiro.

Os estudos apresentados nesta dissertação foram realizados com recursos computacionais adquiridos ao abrigo do Programa Operacional Factores de Competitividade (COMPETE) e a Fundos Nacionais da Fundação para a Ciência e a Tecnologia (FCT) sob o projeto PTDC/QUI-QUI/101022/2008.

Dedico este trabalho aos meus pais,

sem eles não teria conseguido.

o júri

presidente

Professora Doutora Odete Abreu Beirão da Cruz e Silva

Professora auxiliar com agregação da Universidade de Aveiro

Professor Doutor Vítor Manuel Sousa Félix

Professor associado com agregação da Universidade de Aveiro

Doutor Paulo Jorge Ferreira de Matos Costa

Equiparado a investigador auxiliar da Unidade de Investigação de Química Orgânica, Produtos Naturais e Agroalimentares da Universidade de Aveiro

agradecimentos

Ao Professor Vítor Félix, pelo apoio, orientação e disponibilidade que sempre demonstrou durante este período. Por me ter proporcionado esta experiência enriquecedora e ter partilhado os seus conhecimentos.

À Professora Odeteda Cruz e Silva, directora do Mestrado em Biomedicina Molecular, pelo apoio à minha formação académica.

Aos colegas do Grupo de Moledação Molecular, Igor, Paulo e Sílvia, pelos momentos de descontração e pelo companheirismo. Por me acolherem tão bem e fazerem sentir parte do grupo. Um obrigado especial ao Igor, sem os seus conselhos e paciência não teria "sobrevivido".

Aos meus pais e a toda a minha família, sem o seu apoio e sacrifício não teria chegado aqui. Tudo o que sou devo-lhes a eles.

Às amigas de "viagem", Rita Ribeiro, Cindy, Sónia e Inês. Obrigada por todos os momentos bons e menos bons, por me conhecerem tão bem e estarem sempre lá para o que der e vier.

Às amigas que, apesar da distância, nunca me deixaram e sempre me apoiaram, Li e Sandra.

palavras-chave Fibrose quística, simulações de dinâmica molecular, transporte transmembranar de cloreto, *squaramides*, GAFF, parametrização, POPC

resumo

O transporte de aniões através de membranas celulares é essencial para o funcionamento da célula e a sua regulação depende de canais transmembranares. O mau funcionamento destes canais leva a canalopatias, designadamente o dano dos canais de cloreto associado à fibrose quística. Estas doenças têm motivado os químicos supramoleculares para o desenvolvimento de novos transportadores sintéticos de cloreto visando uma potencial aplicação em terapias de substituição de canais. Neste contexto, esta dissertação reporta um estudo *in silico* em que se avalia a capacidade de cinco *squaramides* (amidas quadrangular planas) assistirem o transporte de cloreto através de uma bicamada de POPC. De facto, estudos experimentais anteriores demonstraram que estas pequenas moléculas são capazes de mediar o efluxo de cloreto de vesículas de POPC com maior eficiência do que os seus análogos tioureias e ureias, actuando como transportadores móveis através de um mecanismo de permuta de aniões.

Esta investigação teórica foi realizada com base em cálculos quânticos e simulações de dinâmica molecular num modelo de membrana POPC. As simulações foram precedidas pelo desenvolvimento de parâmetros específicos para as ligações e ângulos da unidade central da *squaramide*, sendo que o resto das moléculas descritas com parâmetros de defeito do GAFF. Os fosfolipídos foram descritos com parâmetros do campo de forças LIPID11. A difusão passiva dos complexos de cloreto foi investigada colocando cada um dos receptores em diferentes posições de partida: na fase aquosa e no meio da bicamada de POPC. Em ambos os casos, os receptores moveram-se em direcção à interface da membrana tendo-se posicionado abaixo das cabeças dos lípidos. No primeiro caso, o cloreto foi libertado ainda na fase aquosa antes do receptor chegar à interface. Enquanto que no segundo caso a libertação do cloreto ocorreu concomitantemente com a aproximação do receptor à interface. Durante o tempo de simulação os receptores interactuaram principalmente com as cabeças dos lípidos *via* ligações de hidrogénio N-H···O.

keywords Cystic fibrosis, molecular dynamics simulations, chloride transmembrane transport, squaramides, GAFF, parameterization, POPC

abstract The anion transport across cellular membranes is essential to the cell functioning and its regulation depends on transmembrane channels. The malfunction of ion channels leads to channelopathies. In particularly, the impairment of chloride ion channels is associated with cystic fibrosis. These diseases have motivated the supramolecular chemists for the development of new chloride synthetic transporters with potential use in channel replacement therapies. In this context, this thesis reports an *in silico* study performed to evaluate the ability of five squaramides to assist the chloride transport across a POPC bilayer. Indeed, earlier experimental studies have shown that these small molecules were able to mediate the chloride efflux across POPC vesicles more efficiently than their analogous thioureas and ureas, as mobile-carriers using an anion-exchange mechanism.

This theoretical investigation was carried out by a combination of quantum calculations and Molecular Dynamics simulations in a POPC membrane model. The MD simulations were preceded by the development of specific bond term parameters for the squaramide moiety using the crystal data from an extensive series of squaramides. The remaining parts of these molecules were described with GAFF default parameters. The phospholipids were described with parameters taken from LIPID11. The passive diffusion of chloride complexes was investigated by placing each receptor in two different starting positions: in the water slab and in the bilayer core of the POPC membrane model. In both cases the receptor moved towards the water/lipid interface and accommodated themselves below the lipid head groups. In the first case, the chloride release occurred in the water slab before the receptor reaches the water/lipid interface. By contrast, in the second case the chloride is released concomitantly with the receptor approach to the interface. The squaramides interact with phospholipid head groups mainly *via* N-H···O hydrogen bonds as analyzed along the thesis.

publicações e comunicações científicas

durante a realização desta dissertação, foram elaborados os seguintes trabalhos científicos:

Artigos científicos

- Marques, I., Colaço, A. R., Costa, P. J., Busschaert, N., Gale, P. A. and Félix, V. *Tris-Thiourea Tripodal-based Molecules as Chloride Transmembrane Transporters: Insights from Molecular Dynamics Simulations*, 2013, (submitted).

Pósteres científicos

- Colaço, A. R., Marques, I. and Félix, V., *Transmembrane transport of chloride by Squaramides: an in silico study,* Encontro de Jovens Investigadores de Biologia Computacional Estrutural (EJIBCE 2013), Porto, 2013.
- I. Marques, Costa, P.J., Colaço, A.R., Félix V., *Tris-Thiourea Tripodal-based Molecules as Chloride Transmembrane Transporters: Insights from Molecular Dynamics Simulation*s, Encontro de Jovens Investigadores de Biologia Computacional Estrutural (EJIBCE 2013), Porto, 2013.

Index

Figures Index ... iii
Tables Index ... xiii
Abbreviations ... xvii
1. Introduction ... 1
1.1. Biological membranes and channelopathies ... 1
1.1.1. Biological membranes: overview ... 1
1.1.2. Membrane proteins ... 3
1.1.3. Transport of small molecules across the lipid membrane ... 5
1.1.4. Channelopathies ... 8
1.2. Synthetic anion transporters ... 10
1.2.1. General considerations ... 10
1.2.2. Development of synthetic anionophores ... 10
1.3. Squaramides as anion receptors ... 16
1.3.1. Applications ... 19
1.4. Molecular dynamics simulations of biomembrane systems ... 21
1.4.1. Molecular modelling studies ... 21
1.4.2. MD simulations of membrane models ... 24
1.5. Objectives ... 30
2. Force filed parameterization of the squaramide receptors ... 31
2.1. Parameterization of the squaramide moiety ... 31
2.2. Conformational analyses ... 52
2.2.1. Conformational analysis of the free receptors ... 52
2.2.2. Conformational analysis of chloride associations ... 57
3. Chloride transport across a phospholipid bilayer with squaramide receptors ... 59
3.1. Pure membranes ... 60
3.2. Membranes and squaramide receptors ... 68
3.2.1. MD Simulations of the receptors starting from the water phase ... 69
3.2.2. MD Simulations of the receptors starting from within the membrane ... 87
4. Conclusions ... 105
5. Future work ... 107
6. References ... 109
7. Appendix 1 ... 119

Figures Index

Figure 1 – Schematic representation of an animal cell with the cellular membrane enclosing the intracellular organelles, also surrounded by biomembranes, responsible for maintaining the specific composition of cytosol and organelles' mediums. 1

Figure 2 – Phospholipid distribution across the membrane bilayer. The two leaflets do not have the same composition. Image adapted from reference (4). 3

Figure 3 – Schematic representation of the membrane proteins. In blue integral protein (transmembrane protein), in green lipid-anchored proteins, in red cytosolic peripheral protein, in pink and orange exoplasmic peripheral. proteins. In the cytosolic face, peripheral proteins interact with cytoskeleton filaments (green filaments). 4

Figure 4 – Schematic representation of the glycosylphosphatidylinositol (GPI) anchor. 4

Figure 5 – Schematic representation of the mechanisms by which synthetic ionophores operate. 11

Figure 6 – Schematic representation of HCl co-transport by prodigiosin molecule as a mobile carrier.(18) 11

Figure 7 – Terabutylamide calix[4]arene showing chloride transmembrane transport activity in *1,3-alternate* (left) and *cone* (right) conformations. 12

Figure 8 – Examples of dipyrrole (*a* and *b*) and polypyrrole (*c*) molecules from Sessler´s et al studies. (30-33) 13

Figure 9 – Amidopyrroles derivatives with chloride transmembrane transport activity incorporating and imizadole (a) and pyridine groups (b).(34) 13

Figure 10 – Bis-indolylurea (a) (36) and bisurea (b) (37) transporters developed by Gale and co-workers. 13

Figure 11 – Functionalization of the cholic acid (left) with different binding and transport groups (right).(42, 43) 14

Figure 12 – Schematic representation of the relay mechanism. 15

Figure 13 – Phospholipid derivative with an ionophore with a relatively high affinity for Cl^- (4-nitrophenylurea group) appended. 15

Figure 14 – Schematic representation of a squaric acid molecule. 16

Figure 15 – Squaramides can form up to four hydrogen bonds (two acceptor and two donor). 16

Figure 16 – Schematic representation of *anti/anti* (a), *syn/syn* (b) and *syn/anti (c)* conformations of a squaramide. 17

Figure 17 – Crystal structure of squaramide S01 (EWOCAV) organized in a chain, according to their *anti/anti* conformation, showing a head-to-tail packing (left) and π-stacking interactions between phenyl groups (right). Image adapted from CSD with *Pymol* software. 17

Figure 18 – Crystal structure of the chloride complex with *p*-dinitrophenyl squaramide (CSD Refcode MUYYOV). Oxygen, carbon, nitrogen and hydrogen atoms are in red, wheat, blue and white, respectively. Chloride anion is in green and hydrogen bonds are drawn as black dashes 18

Figure 19 – MP2 optimized squaramides, bond lengths (Å) in the ring tend to equalization as more hydrogen bonds are established, up to the four possible ones. I – none hydrogen bond; II – two acceptor hydrogen bonds; III – two donor hydrogen bonds; IV – four hydrogen bonds. Image adapted from Quiñonero et al.(56) 19

Figure 20 – Schematic representation of the valve-like mechanism from Muthyala *et al*.(71) 20

Figure 21 – Lennard-Jones potential curve. 23

Figure 22 –The four types of phospholipids commonly used in MD simulations as membrane models: 1, 2-dioleoyl-*sn*-glycero-3-phosphocholine (DOPC), 1-palmitoyl-2-oleoyl-*sn*-glycero-3-phosphocholine (POPC), 1, 2-dimyristoyl-*sn*-glycero-3-phosphocholine (DMPC), and 1, 2-dipalmitoyl-*sn*-3-phosphocholine (DPPC). 25

Figure 23 – Snapshots taken from the MD simulation illustrating the passive diffusion of a bisurea transporter along the lipid bilayer.(37) 28

Figure 24 – Snapshots taken from the MD simulation illustrating the internalization process of bis-indolylurea transporter, into the POPC phospholipid bilayer.(36) 29

Figure 25 – Schematic representation of the squaramide motif used in the CSD search (left) and of the squaramide moiety with the GAFF default atom-types (right) 31

Figure 26 – Squaramides compounds whose single crystal X-ray diffraction structures were deposited with CSD 34

Figure 27 – Squaramides compounds whose single crystal X-ray diffraction structures were deposited with CSD (continuation). 35

Figure 28 – Schematic representation of squaramide moiety with the atom types: in black the default GAFF atom types; in red the new atom types created for the specific parameterization. 39

Figure 29 – Squaramide series from the collaboration project with Prof. Phil A. Gale's group. 41

Figure 30 – Squaramide series from the collaboration project with Prof. Phil A. Gale's group (continuation). 42

Figure 31 – Diagram for the receptor preparation before conformational analyses and MD simulations. 43

Figure 32 – DFT optimized structures (B3LYP/6-311+G** level) of S30 organized in dimer (a and b) or trimmer (c, d and e) structures. Carbon, oxygen, nitrogen and hydrogen atoms are represented in wheat, red, blue and white, respectively. Black dashes represent hydrogen bonds between monomers. 48

Figure 33 – Diagram for conformational analysis of the free squaramides. 53

Figure 34 –Atomic numbering adopted for S01-S20 53

Figure 35 – Molecular mechanics structures a- *anti/anti* (a), *syn/syn* (b) and *syn/anti* (c) conformations of S01. 56

Figure 36 – Lowest energy conformations found in conformational analysis of chloride associations with S01, S09, S10, S19 and S20. Carbon, oxygen, nitrogen, hydrogen, chloride and fluorine atoms are represented in wheat, red, blue, white, green and cyan, respectively. Chloride anion is represented as a green sphere and the hydrogen bonds are represented as black dashed lines. 58

Figure 37 – Evolution of the area per lipid in the MD simulation of membrane model II (red line) in comparison with reference values from Kučerka (117) (green line) and Félix (118) (blue line). 63

Figure 38 – Evolution of bilayer thickness in the 50ns of MD simulation time (red line) in in comparison with experimental values from Kučerka (117) (green line) and Félix (118) (blue line). 63

Figure 39 – Computed order parameters, $|S_{CD}|$, for the palmitoyl and oleyl chains for the last 20 ns of imulation time of model II. The $|S_{CD}|$ calculated values are in red and in green for the *sn*-1 and *sn*-2 chains, respectively. The error bars shown correspond to the standard

deviation. In plot *a* the experimental values for the *sn*-1 chain were obtained from reference (132) (brown) and (133) (orange), while the values for *sn*-2 chain were taken from reference (134) (magenta) and (133) (blue). In plot *b,* the reference values for $|S_{CD}|$ were obtained from LIPID11 paper (84) (*sn*-1 chain in orange and *sn*-2 chain in brown) and from Félix *et al*. paper (118) (*sn*-1 chain in blue and *sn*-2 chain in magenta). 64

Figure 40 – Electron density profiles of the pure membrane model II for the last 20 ns of MD simulation with full system profile plotted in black, water in blue, phospholipids in green and phosphorus in dark yellow. The z=0 Å corresponds to the core of the POPC bilayer. In plot *a*, the X-ray scattering of the POPC bilayer profile at 303 K is shown as a magenta line (117). In plot *b*, the full system density profile for the pure membrane simulated by Félix *et al* is shown as a red line.(118)..... 66

Figure 41 - Snapshots of system A, taken at different simulation times (0, 50 and 100 ns), showing the diffusion of S01. Images show the different positions of the receptor in the membrane. The receptor is drawn in a space filling model with carbon atoms in wheat, oxygen atoms in red, nitrogen atoms in blue and hydrogen atoms in white. The chloride ion and the phosphorus atoms are represented as green and orange spheres, scaled to 0.7 vdW radius, respectively. In POPC lipids, carbon, nitrogen and oxygen atoms are drawn as grey, blue and red lines, respectively, while C-H hydrogen atoms have been omitted for clarity. 70

Figure 42 – Snapshots of system B showing S09 diffusion towards the membrane. Fluorine atoms and sodium ion are drawn as cyan and magenta spheres, respectively. Remaining details as given in Figure 41. 70

Figure 43 - Snapshots of system C showing S10 diffusion towards the membrane. Fluorine atoms and sodium ion are drawn as cyan and magenta spheres, respectively. Remaining details as given in Figure 41. 71

Figure 44 - Snapshots of system D showing S19 diffusion towards the membrane. Fluorine and chloride atoms are drawn as cyan and green spheres, respectively. Remaining details as given in Figure 41. 71

Figure 45 - Snapshots of system E showing S20 diffusion towards the membrane. The sodium ion is drawn as a magenta sphere. Remaining details as given in Figure 41. 71

Figure 46 - Evolution of the receptor and chloride relative positions to the water/lipid interface (*z*=0 Å). In green is represented the chloride ion, in red the centre of mass of the oxygen atoms from the receptor, in blue the centre of mass of the nitrogen atoms, in magenta

and cyan are represented the phenyl groups (A, B and C); a phenyl group and an aliphatic chain (D) or an aliphatic chain and a butyl group (E), respectively. Data was smoothed using Bézier curves. 73

Figure 47 – Variation of the number of water molecules within the solvation shell defined by a cut-off of 3.5Å from receptors S01 (A), S09 (B), S10 (C), S19 (D) and S20 (E). Data was smoothed using Bézier curves. 75

Figure 48 – Average number of hydrogen bonds *vs* the relative position of the centre of mass of each receptor. The following colour scheme was used for the hydrogen bonds established between the receptor and water molecules (red), chloride ion (green), POPC head groups (blue), ester groups from POPC *sn*-1 chains (magenta) and *sn*-2 chains (cyan). 76

Figure 49 – Schematic representation of the sqauaramide's core. The atoms involved in the dihedral angles analysis are identified in red. 77

Figure 50 – Frequency histograms showing the distribution of the two C=C-N-C torsion angles values of S01, S09 and S10 in systems A, B and C, before the interaction with the water/lipid interface (*pre interaction*) and after (*post interaction*). 78

Figure 51 – Frequency histograms showing the distribution of the two C=C-N-C torsion angles values of S19 and S20 in systems D and E, before the interaction with the water/lipid interface (*pre interaction*) and after (*post interaction*). 79

Figure 52 – Evolution of area per lipid through the course of the MD simulation time is represented in red. The reference value from Félix *et al* (118) is plotted as a blue line. 81

Figure 53 – Evolution of the bilayer thickness (red line) through the MD simulation of systems A-E. Comparison with theoretical values from membrane model I simulation (64.9 Å in blue). 82

Figure 54 – Electron density profiles of the membrane systems A-E, estimated for the last 40 ns of MD simulation. The receptor is plotted as a red line and scaled 5 times. The full system is plotted in black, the water in blue, the phospholipids in green and the phosphorus in dark yellow. *z*= 0 Å corresponds to the core of the POPC bilayer. Reference profile from membrane model is represented in magenta. 84

Figure 55 – Computed $|S_{CD}|$ for palmitoyl and oleyl chains for 40 ns of sampling of simulations A, B and D; for the last 15 ns of sampling of system C and for the last 10ns of system E. The $|S_{CD}|$ values calculated for the *sn*-1 chain are shown in red, while the values for the *sn*-2 chain are shown in green. The error bars associated with these results correspond to the standard

deviation. The computed $|S_{CD}|$ values from reference model I are presented in blue (*sn*-1 chain), and magenta (*sn*-2 chain). 85

Figure 56 – Snapshots of system F, taken at different simulation times (0, 50 and 100 ns), showing the diffusion of S01. Images show the different positions of the receptor in the membrane. The receptor is drawn in a space filling model with carbon atoms in wheat, oxygen atoms in red, nitrogen atoms in blue and hydrogen atoms in white. The chloride and sodium ions, as well as the phosphorus atoms from the bilayer are represented as green, magenta and orange spheres, scaled to 0.7 vdW radius, respectively. In POPC lipids, carbon, nitrogen and oxygen atoms are drawn as grey, blue and red lines, respectively, while C-H hydrogen atoms have been omitted for clarity. 88

Figure 57 - Snapshots of system G, illustrating the diffusion process of S09. Fluorine atoms are drawn as cyan spheres. Remaining details as given in Figure 56. 88

Figure 58 - Snapshots of system H, illustrating the diffusion process of S10. Fluorine atoms are drawn as cyan spheres. Remaining details as given in Figure 56. 89

Figure 59 - Snapshots of system I, illustrating the diffusion process of S19. Fluorine atoms are drawn as cyan spheres. Remaining details as given in Figure 56. 89

Figure 60 - Snapshots of system J, illustrating the diffusion process of S20. Remaining details as given in Figure 56. 89

Figure 61 - Evolution of the receptor and chloride relative positions to the water/lipid interface (z = 0 Å). In green is represented the chloride ion, in red the centre of mass of the oxygen atoms from the receptor, in blue the centre of mass of the nitrogen atoms, in magenta and cyan are represented the phenyl groups (F, G and H); a phenyl group and an aliphatic chain (I) or an aliphatic chain and a butyl group (J), respectively. Data was smoothed using Bézier curves. 90

Figure 62 - Variation of the number of water molecules within the solvation shell defined by a cut-off of 3.5Å from receptors S01 (F), S09 (G), S10 (H), S19 (I) and S20 (J). Data was smoothed using Bèzier curves. 92

Figure 63 - Average number of hydrogen bonds *vs* the relative position of the centre of mass of each receptor. The following colour scheme was used for the hydrogen bonds established between the receptor and water molecules (red), chloride ion (green), POPC head groups (blue), ester groups from POPC *sn*-1 chains (magenta) and *sn*-2 chains (cyan). 94

Figure 64 - Frequency histograms showing the distribution of the two C=C-N-C torsion angles values of S01-S20 in simulations F-J, in the last 40ns of simulation time..... 96

Figure 65 - Evolution of area per lipid through the course of the MD simulation time is represented in red. The reference value from the simulation of membrane model II is plotted as a blue line. 98

Figure 66 - Evolution of the bilayer thickness (red line) through the MD simulation of systems A-E. The reference value from the simulation of membrane model II is plotted as a blue line. 99

Figure 67 - Electron density profiles of the membrane systems F-J, estimated for the last 40 ns of MD simulation. The receptor is plotted as a red line and scaled 5 times. The full system is plotted in black, the water in blue, the phospholipids in green and the phosphorus in dark yellow. z =0 Å corresponds to the core of the POPC bilayer. System profile from membrane model II simulation is represented in magenta..... 101

Figure 68 – Computed $|S_{CD}|$ for palmitoyl and oleyl chains for 40 ns of sampling of simulations F-J. The $|S_{CD}|$ values calculated for the *sn*-1 chain are shown in red, while the values for the *sn*-2 chain are shown in green. The error bars associated with these results correspond to the standard deviation. The computed $|S_{CD}|$ values from membrane model II simulation are presented in blue (*sn*-1 chain), and brown (*sn*-2 chain)..... 103

Figure 69 – Snapshots of system A, taken at different simulation times (0ns, 50ns and 100ns), showing the diffusion of S01. Images show the initial and final positions of the receptor in the membrane. The receptor is drawn as a space filing model with carbon atoms in wheat, oxygen atoms in red, nitrogen atoms in blue and hydrogen atoms in white. The chloride and sodium ions, as well as the phosphorus atoms from the bilayer are represented as green, magenta and orange spheres, respectively, and scaled to 0.7 vdW radius. In POPC lipids, carbon atoms are drawn as grey lines and C-H hydrogen atoms have been omitted..... 119

Figure 70 – Snapshots of system B showing S09 diffusion towards the membrane. Fluorine atoms are drawn as cyan spheres. Remaining details as given in Figure 69. 119

Figure 71 – Snapshots of system C showing S10 diffusion towards the membrane. Fluorine atoms are drawn as cyan spheres. Remaining details as given in Figure 69. 120

Figure 72 – Snapshots of system D showing S19 diffusion towards the membrane. Fluorine atoms are drawn as cyan spheres. Remaining details as given in Figure 69. 120

Figure 73 – Snapshots of system E showing S20 diffusion towards the membrane. Remaining details as given in Figure 69. 120

Figure 74 – Evolution of the receptor and chloride relative positions to the water/lipid interface (z = 0 Å). In green is represented the chloride ion, in red the centre of mass of the oxygen atoms from the receptor, in blue the centre of mass of the nitrogen atoms, in magenta and cyan are represented the phenyl groups (A, B and C); a phenyl group and an aliphatic chain (D) or an aliphatic chain and a butyl group (E), respectively. Data was smoothed using Bézier curves. 121

Figure 75 – Variation of the number of water molecules within the solvation shell defined by a cut-off of 3.5 Å from receptors S01 (A), S09 (B), S10 (C), S19 (D) and S20 (E). Data was smoothed using Bèzier curves. 122

Figure 76 – Average number of hydrogen bonds *vs* the relative position of the centre of mass of each receptor. The following colour scheme was used for the hydrogen bonds established between the receptor and water molecules (red), chloride ion (green), POPC head groups (blue), ester groups from POPC *sn*-1 chains (magenta) and *sn*-2 chains (cyan). 123

Figure 77 – Frequency histograms showing the distribution of the two C=C-N-C torsion angles values of S01, S09 and S10 in systems A, B and C, before the interaction with the water/lipid interface (*pre interaction*) and after (*post interaction*). 124

Figure 78 – Frequency histograms showing the distribution of the two C=C-N-C torsion angles values of S19 and S20 in systems D and E, before the interaction with the water/lipid interface (*pre interaction*) and after (*post interaction*). 125

Figure 79 – Evolution of area per lipid through the course of the MD simulation time is represented in red. The reference value from Félix *et al* (118) is plotted as a blue line. 126

Figure 80 – Evolution of the bilayer thickness (red line) through the MD simulation of systems A-E. Comparison with theoretical values from membrane model I simulation (64.9 Å in blue). 127

Figure 81 – Electron density profiles of the membrane systems A-E, estimated for the last 40 ns of simulations A, B and D; for the last 15 ns of sampling of system C and for the last 10ns of system E. The receptor is plotted as a red line and scaled 5 times. The full system is plotted in black, the water in blue, the phospholipids in green and the phosphorus in dark yellow. z= 0 Å corresponds to the core of the POPC bilayer. Reference profile from membrane model is represented in magenta. 128

Figure 82 – Computed $|S_{CD}|$ for palmitoyl and oleyl chains for 40 ns of sampling of simulations A, B and D; for 15 ns of sampling of system C and for 10ns of system E. The $|S_{CD}|$ values calculated for the *sn*-1 chain are shown in red, while the values for the *sn*-2 chain are shown in green. The error bars associated with these results correspond to the standard deviation. The computed $|S_{CD}|$ values from reference model I are presented in blue (*sn*-1 chain), and magenta (*sn*-2 chain). 129

Figure 83 – Snapshots of system F, taken at different simulation times (0, 50 and 100 ns), showing the diffusion of S01. Images show the different positions of the receptor in the membrane. The receptor is drawn in a space filling model with carbon atoms in wheat, oxygen atoms in red, nitrogen atoms in blue and hydrogen atoms in white. The chloride and sodium ions, as well as the phosphorus atoms from the bilayer are represented as green, magenta and orange spheres, scaled to 0.7 vdW radius, respectively. In POPC lipids, carbon, nitrogen and oxygen atoms are drawn as grey, blue and red lines, respectively, while C-H hydrogen atoms have been omitted for clarity. 130

Figure 84 – Snapshots of system G, illustrating the diffusion process of S09. Fluorine atoms are drawn as cyan spheres. Remaining details as given in Figure 83. 130

Figure 85 – Snapshots of system H, illustrating the diffusion process of S10. Fluorine atoms are drawn as cyan spheres. Remaining details as given in Figure 83. 131

Figure 86 – Snapshots of system I, illustrating the diffusion process of S19. Fluorine and chloride atoms are drawn as cyan and green spheres. Remaining details as given in Figure 83. 131

Figure 87 – Snapshots of system J, illustrating the diffusion process of S20. Remaining details as given in Figure 83. 131

Figure 88 – Evolution of the receptor and chloride relative positions to the water/lipid interface (z = 0 Å). In green is represented the chloride ion, in red the centre of mass of the oxygen atoms from the receptor, in blue the centre of mass of the nitrogen atoms, in magenta and cyan are represented the phenyl groups (F, G and H); a phenyl group and an aliphatic chain (I) or an aliphatic chain and a butyl group (J), respectively. Data was smoothed using Bézier curves. 132

Figure 89 – Variation of the number of water molecules within the solvation shell defined by a cut-off of 3.5Å from receptors S01 (F), S09 (G), S10 (H), S19 (I) and S20 (J). Data was smoothed using Bèzier curves. 133

Figure 90 – Average number of hydrogen bonds *vs* the relative position of the centre of mass of each receptor. The following colour scheme was used for the hydrogen bonds established between the receptor and water molecules (red), chloride ion (green), POPC head groups (blue), ester groups from POPC *sn*-1 chains (magenta) and *sn*-2 chains (cyan). 134

Figure 91 – Frequency histograms showing the distribution of the two C=C-N-C torsion angles values of S01-S20 in simulations F-J, in the last 40ns of simulation time..... 135

Figure 92 – Evolution of area per lipid through the course of the MD simulation time is represented in red. The reference value from the simulation of membrane model II is plotted as a blue line. 136

Figure 93 – Evolution of the bilayer thickness (red line) through the MD simulation of systems A-E. The reference value from the simulation of membrane model II is plotted as a blue line. 137

Figure 94 – Electron density profiles of the membrane systems F-J, estimated for the last 40 ns of MD simulation. The receptor is plotted as a red line and scaled 5 times. The full system is plotted in black, the water in blue, the phospholipids in green and the phosphorus in dark yellow. *z* =0 Å corresponds to the core of the POPC bilayer. System profile from membrane model II simulation is represented in magenta. 138

Figure 95 – Computed $|S_{CD}|$ for palmitoyl and oleyl chains for 40 ns of sampling of simulations F-J. The $|S_{CD}|$ values calculated for the *sn*-1 chain are shown in red, while the values for the *sn*-2 chain are shown in green. The error bars associated with these results correspond to the standard deviation. The computed $|S_{CD}|$ values from membrane model II simulation are presented in blue (*sn*-1 chain), and brown (*sn*-2 chain). 139

Tables Index

Table 1 – Differences between the two classes of natural ion transporters, carrier proteins and ion channels. 5

Table 2 – Summary of the transport mechanisms of small molecules and ions across the lipid membrane. 6

Table 3 – Functional units that compose an ion channel 7

Table 4 – Ion channel functions. 7

Table 5 – Classes of CF gene mutations associated with cystic fibrosis. 9

Table 6 – Force Field types currently used and phospholipids tested. 26

Table 7 – Crystal structures deposited with Cambridge Structural Data Base with their CSD Refcodes and references. 32

Table 8 – Bond lengths (Å) in the squaramide moiety in the crystal structures deposited with CSD. 32

Table 9 – Bond angles (°) in the squaramide moiety in the crystal structures deposited with CSD. 33

Table 10 – Bond lengths (Å) of MM optimized squaramides using AM1-BCC charges and GAFF default parameters 37

Table 11 – Bond lengths (Å) of MM optimized squaramides using RESP charges and GAFF default parameters 38

Table 12 – Parameters to estimate the bond stretching force constants in GAFF for bonds involving C/C, C/N and C/O atom pairs. (109) 39

Table 13 – Parameters to estimate the bond angle bending force constants in GAFF.(109) 40

Table 14 – Force field parameters for the bond lengths of the squaramide moiety. 40

Table 15 – Force field parameters for the bond angles of the squaramide moiety. 40

Table 16 – Comparison between the average bond lengths (Å) from X-ray structures and MM optimized structures with GAFF default parameters and AM1-BCC and RESP charges. 44

Table 17 – Bond lengths (Å) of the selected squaramides optimized at the B3LYP/6-31G* level. 45

Table 18 – Bond lengths (Å) of the selected squaramides optimized at the B3LYP/6-311+G**. 46

Table 19 – Bond lengths (Å) of the selected squaramides optimized at the MP2/6-31G* level. 47

Table 20 – Comparison between the bond lengths (Å) from MM optimizations with GAFF default parameters and quantum optimizations at B3LYP/6-31G*, B3LYP/6-311+G** and MP2/6-31G* 48

Table 21 – – Bond lengths (Å) for S30 arranged in dimer or trimmer assembles optimized at B3LYP/6-311+G**. 49

Table 22 – Bond lengths (Å) of the MM optimized squaramides using AM1-BCC charges and x-ray parameters. 50

Table 23 – Bond lengths (Å) of the MM optimized squaramides using RESP charges and x-ray parameters 50

Table 24 – RMSD calculated for structures optimized with AM1-BCC charges. 51

Table 25 – RMSD calculated for structures optimized with RESP charges. 51

Table 26 – Atom types and RESP charges for S01. 54

Table 27 – Atom types and RESP charges for S09. 54

Table 28 – Atom types and RESP charges for S10. 54

Table 29 – Atom types and RESP charges for S19. 55

Table 30 – Atom types and RESP charges for S20. 55

Table 31 – Relative molecular mechanics energies (kcal/mol) for *syn/syn*, *syn/anti* and *anti/anti* conformations of S01-S20 56

Table 32 – RMSD values calculated between *anti/anti* conformations of S01-S20. 57

Table 33 – Number and dimensions of N-H···Cl^- hydrogen bonds found in lowest energy conformations of receptor chloride associations. 58

Table 34 – Summary of simulation conditions used to simulate pure membrane models. 60

Table 35 – Comparison between the structural parameters for the MD simulations of pure membrane model II and of reference data. 67

Table 36 – Summary of the simulation conditions of the membrane systems with receptors S01, S09, S10, S19 and S20. 68

Table 37 – Relative distance (Å) between the receptors and the closest water/lipid interface for systems A-E for the last 40ns of simulation time. 72

Table 38 – Summarized information of receptor hydration of systems A-E, in the last 40ns of simulation time. 74

Table 39 – Summarized results of area per lipid ($Å^2$) parameter for systems A-E, over 40ns of sampling time..... 80

Table 40 – Summarized results of bilayer thickness parameter for systems A-E, over 40ns of sampling time..... 83

Table 41 –Comparison between the parameters for the MD simulations of systems A to E. ... 86

Table 42 – Relative distance (Å) of the receptors to the water/lipid interface for systems F-J, for the last 40ns of simulation time. 91

Table 43 – Summarized information of receptor's hydration of systems F-J, in the last 40ns of simulation time. 93

Table 44 – Summarized results of area per lipid ($Å^2$) parameter for systems F-J, over 40ns of sampling time..... 97

Table 45 – Summarized results of bilayer thickness parameter for systems A-E, over 40ns of sampling time..... 100

Table 46 - Comparison between biophysical parameters for the phospholipid bilayer systems F-J. 104

Abbreviations

Item	Definition
AIDS	**A**cquired **I**mmuno**D**eficiency **S**yndrome
AM1-BCC	semi-empirical **A**ustin **M**odel **1** **B**ond **C**harge **C**orrections
AMBER	**A**ssisted **M**odel **B**uilding and **E**nergy **R**efinement
AMP	**A**denosine **M**ono**P**hosphate
AQP	**AQ**ua**P**orine
ATP	**A**denosine **T**ri**P**hosphate
cAMP	**c**yclic **A**denosine **M**ono**P**hosphate
CF	**C**ystic **F**ibrosis
CFTR	**C**ystic **F**ibrosis **T**ransmembrane conductance **R**egulator
CHARMM	**C**hemistry at **HAR**vard **M**olecular **M**echanics
CSD	**C**ambridge **S**tructural **D**atabase
CUDA	**C**ompute **U**nified **D**evice **A**rchitecture
CyPLOS	**Cy**clic **P**hosphate-**L**inked **O**ligosaccharide**S**
DFT	**D**ensity **F**unctional **T**heory
DLPC	1,2-didodecanoyl-sn-glycero-3-phosphocholine
DMPC	1,2-dimyristoyl-sn-glycero-3-phosphocholine
DNA	**D**eoxyribo**N**ucleic **A**cid
DOPC	1,2-dioleoyl-sn-glycero-3-phosphocholine
DPPC	1,2-dihexadecanoyl-*sn*-glycero-3-phosphocholine
EC_{50}	Half maximal effective concentration
ENaC	**E**pithelial sodium (**Na**$^+$) **C**hannel
ER	**E**ndoplasmic **R**eticulum
ESP	**E**lectro**S**tatic **P**otential
frcmod file	AMBER force field modification file
GABA	**G**amma-**A**mino **B**utyric **A**cid
GAFF	**G**eneral **A**MBER **F**orce **F**ield
GlyR	**Gly**cine **R**eceptor
GPI	**G**lycosyl**P**hosphatidyl**I**nositol
GROMACS	**GRO**ningen **MA**chine for **C**hemical **S**imulations
GROMOS	**GRO**ningen **MO**lecular **S**imulation

Item	Definition
LMOD	**L**ow-**MOD**e
MARTINI	**MAR**rink **T**oolkit **INI**tiative
MD	**M**olecular **D**ynamics
MM	**M**olecular **M**echanics
MOL2 file	Tripos mol2 molecule model file
NPT	Isothermal–isobaric ensemble
NVT	Canonical ensemble
OPLS	**O**ptimized **P**otentials for **L**iquid **S**imulations
ORCC	**O**utwardly-**R**ectifying **C**hloride **C**hannel
PAA	**P**hosphono**A**cetic **A**cid
PC	**P**hosphatildyl**C**holine
PDB file	**P**rotein **D**ata **B**ank file
PE	**P**hosphatidyl**E**thanolamine
PES	**P**otential **E**nergy **S**urface
PFA	**P**hosphono**F**ormic **A**cid
PKA	**P**rotein **K**inase **A**
PKC	**P**rotein **K**inase **C**
PME	**P**article **M**esh **E**wald
PMF	**P**otential **M**ean **F**orce
POPC	1-palmitoyl-2-oleoyl-sn-glycero-3-phosphocholine
POPE	1-palmitoyl-2-oleoyl-sn-glycero-3-phosphoethanolamine
POPG	1-palmitoyl-2-oleoyl-sn-glycero-3-phospho-rac-(1-glycerol)
PS	**P**hosphatidyl**S**erine
PyMOL	**Py**thon-enhanced **MOL**ecular graphics tool
REMD	**R**eplica-**E**xchange **M**olecular **D**ynamics
RESP	**R**estrained **E**lectro**S**tatic **P**otential
RMSD	**R**oot-**M**ean-**S**quare **D**eviation
RNA	**R**ibo**N**ucleic **A**cid
$\lvert S_{CD} \rvert$	Deuterium order parameter
SCMTR	**S**ynthetic **C**hloride **M**embrane **TR**ansporter
SM	**S**phingo**M**yelin
sn-1	**S**tereospecific **n**umber **1**
sn-2	**S**tereospecific **n**umber **2**

Item	**Definition**
sn-3	**S**tereospecific **n**umber **3**
SPC	**S**ingle **P**oint **C**harge
TIP3P	**T**ransferable **I**ntermolecular **P**otential **3** **P**oint

1. Introduction

1.1. Biological membranes and channelopathies

1.1.1. *Biological membranes: overview*

Cell membranes are essential to cell's life and its proper functioning.(1) The plasma membrane encloses the cell, defines its boundaries and maintains the differences between the cytosol and the extracellular environment providing a relatively impermeable barrier to the passage of most of water-soluble molecules (*see* Figure 1).(1-3)

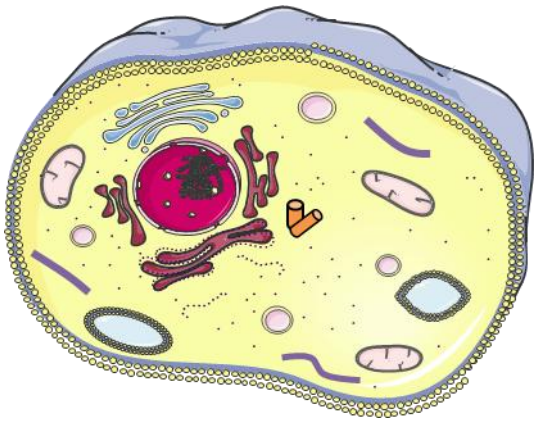

Figure 1 – Schematic representation of an animal cell with the cellular membrane enclosing the intracellular organelles, also surrounded by biomembranes, responsible for maintaining the specific composition of cytosol and organelles' mediums.

The composition and organization of biological membranes may vary slightly according to their specific functions. However, there is a general structure common to all of them: two thin films of lipids assembled together in a bilayer through non-covalent interactions.(1) This supramolecular assembly also contains embedded proteins, cholesterol and glycolipids. The structure is not rigid, in fact, cell membranes are dynamic and fluid biological structures and most of lipids can switch between layers (1), which means that the extracellular (outside) and cytosolic (inside) membrane interfaces have different lipid composition (1-2), affecting the cellular shape and function as well as the proteins anchored to the membrane.(2)

The basic structural units of cell membranes, phospholipids, are amphipathic molecules and small animal cells are estimated to have 10^9 lipid molecules.(1-2) These molecules are composed of a hydrophilic (polar) head and two hydrophobic (nonpolar) tails, which explains their ability to spontaneously aggregate in water environment (1-2). Indeed, they can form spherical micelles with the heads turned outward and the tails protected inside the micelle,

or they can form "sheet-like" phospholipid bilayers with the tails between the hydrophilic head groups (1). In eukaryotic cell membranes there are four major phospholipids, phosphatildylcholine (PC), sphingomyelin (SM), phosphatidylserine (PS) and phosphatidylethanolamine (PE) as sketched in Figure 2.(1-2) PS is the only one with a negative charge while the other three are electrically neutral at physiological pH. Inositol phospholipids are present in small quantities in spite of their important functional role in cell signalling.(1)

One of the most important characteristics of a lipid bilayer is its fluidity, for example, some enzymatic activities can stop when the bilayer viscosity increases beyond a threshold level.(1) The fluidity of the membrane depends on its composition and temperature.(2) Shorter hydrocarbon tails reduce the phase transition temperature from liquid to crystalline state[1], the tendency of tails to interact with each other and the formation of C-C double bonds, avoiding the kinks that make them more difficult to pack together.(1-2)

Eucaryotic cell membranes contain large amounts of cholesterol to enhance their permeable properties. The cholesterol is a rigid steroid molecule with a rigid skeleton and hydroxyl group which interacts with polar phospholipids head groups by hydrogen (1-2), leading to a decrease of the mobility of the phospholipids. The lipid bilayer becomes less deformable and the permeability of the membrane to small water-soluble molecules decreases. However, at high concentrations, as in eukaryotic cells, cholesterol prevents the aggregation and crystallization of the hydrocarbon chains, inhibiting phase transitions.(1)

The phospholipid composition differs between sheets of the plasma membrane (1-2), as can be seen in Figure 2. This difference occurs due to the phospholipid translocators in the endoplasmic reticulum (ER) when the membrane is synthesized. For instance, in the cytoplasmic face there is a high concentration of PS molecules (1-2), required for the protein kinase C (PKC) membrane binding and subsequent signaling transduction; similarly, the inositol phospholipids are also concentrated in the cytoplasmic half of the membrane allowing specific enzymes to cleave them into two smaller fragments, which will be further used as mediators in the signaling transduction. (1)

[1] Change of state from liquid to rigid crystalline, at a characteristic freezing point.

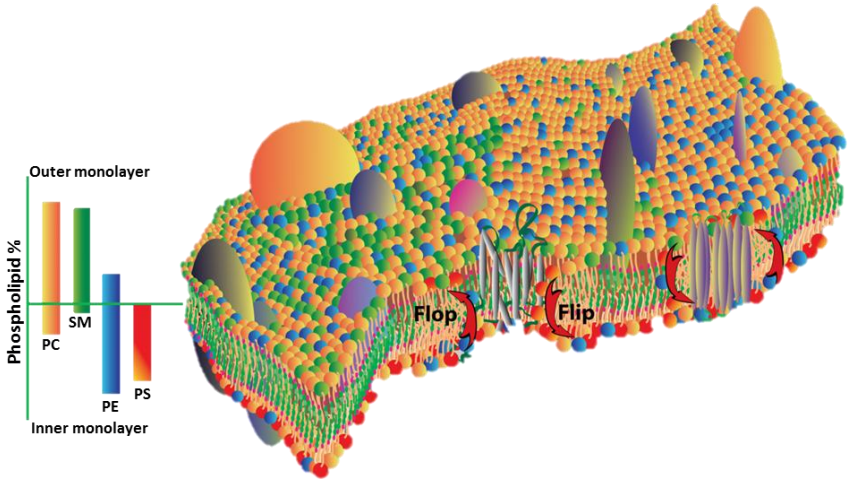

Figure 2 – Phospholipid distribution across the membrane bilayer. The two leaflets do not have the same composition. Image adapted from reference (4).

Glycolipids are located only in the extracellular face of the plasma membrane mediating the interactions of the cell with the surrounding environment. These molecules are generated by the addition of sugars to lipid molecules in the Golgi apparatus, showing also an asymmetrical distribution across the membrane.(1)

1.1.2. *Membrane proteins*

As mentioned above, the proteins are essential components of biological lipid bilayers being responsible for most of the membrane's specific functions. They are spread across the membrane and their functions and locations within the plasma membrane are highly variable.(1-2) These proteins can operate alone or associated with other relevant biological molecules such as other proteins and intracellular messengers. Furthermore, it is also common to find membrane proteins associated with oligosaccharides in the plasma membrane. These complexes create an exterior surface with the carbohydrates forming a cell coat (or glycocalyx).(1)

According to their interactions and location within or at the surface of the lipid bilayer, membrane proteins can be classified into integral, lipid-anchored and peripheral proteins (2), as shown in Figure 3.

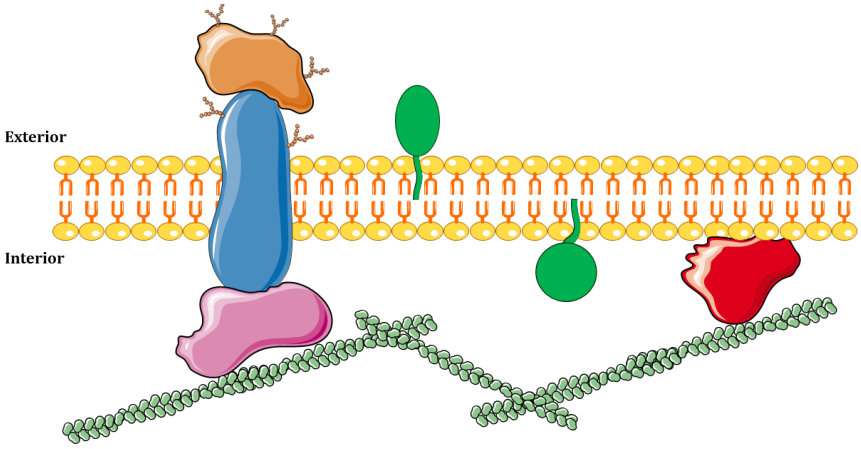

Figure 3 – Schematic representation of the membrane proteins. In blue integral protein (transmembrane protein), in green lipid-anchored proteins, in red cytosolic peripheral protein, in pink and orange exoplasmic peripheral. proteins. In the cytosolic face, peripheral proteins interact with cytoskeleton filaments (green filaments).

Integral membrane proteins (transmembrane proteins) cross the lipid bilayer and their membrane-spanning domain interact with the hydrocarbon core of phospholipids (2, 5), while the lipid-anchored membrane proteins are in the membrane surface covalently bonded to one or more phospholipids (1-2) by a glycosylphosphatidylinositol (GPI) anchor (1) (see Figure 4). By contrast, the peripheral membrane proteins are usually bonded indirectly to the plasma membrane by non-covalent interactions with transmembrane proteins or with lipid head groups (1-2). Membrane proteins are essential to several survival processes, one of the most important is the transmembrane transport of small molecules that do not need to be internalized or secreted by the cell.(1, 5)

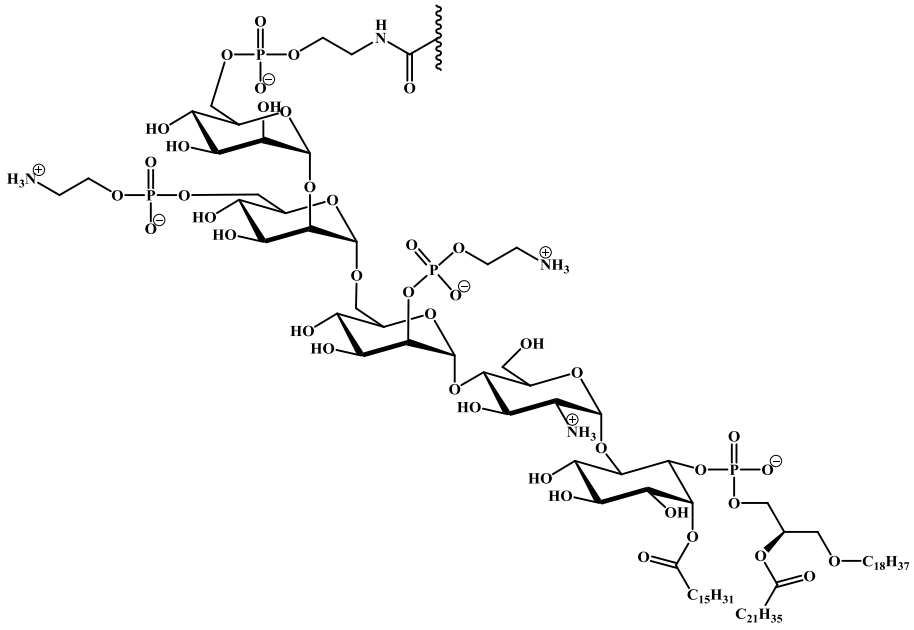

Figure 4 – Schematic representation of the glycosylphosphatidylinositol (GPI) anchor.

1.1.3. *Transport of small molecules across the lipid membrane*

Unlike large biological molecules, small molecules are transported through the membrane by passive transport[2] or active transport[3].(5)

The passive transport of molecules across the membrane can occur *via* simple diffusion or facilitated diffusion without the energy spending, while the active movement has necessarily an energy cost. Indeed, some molecules move spontaneously and according to the concentration and the electrochemical gradients (Simple Diffusion), while the transmembrane transport of other molecules and ions may require the assistance of proteins, which is the case of facilitated diffusion and active transport.(5)

In facilitated diffusion, small neutral or ionic species bind to integral proteins on one side of the membrane and are released on the other side (carrier proteins) or they may move through channel-like structures that expand across the entire phospholipid bilayer (ion channels). This is a uniport system in which only a single type of species is transported accordingly to its concentration gradient.(5)

A comparison between the two classes of natural ion transporters is presented in Table 1 and the corresponding mechanisms are discussed in more detail in the following section.

Table 1 – Differences between the two classes of natural ion transporters, carrier proteins and ion channels.

Carrier Proteins	**Ion Channels**
Transport ions with high selectivity	Lower selectivity in ion transport
Transport rate below the limit of diffusion	Transport rate approaches limit of diffusion
Usually monomeric	Usually oligomers of identical subunits
Transport activity not gated	Transport activity often gated responsive to cellular events

This table was adapted from reference (6)

In contrast, the active transport systems are energy activated and are used to transport species against their concentration gradients or electrical potentials, using metabolic energy from the hydrolysis of adenosine-5'-triphosphate (ATP) molecule. Primary active transport requires specific types of ion channels called ion pumps (ATPases), one of the most important

[2] Does not require directly spending metabolic energy.
[3] Requires the use of metabolic energy to transport the solute.

of them is the sodium-potassium pump (Na^+/K^+ -ATPases) that yields potential energy further used in secondary active transport. The secondary active transport requires the assistance of co-transporters, being energy dependent of Na^+/K^+ -ATPases and only carrying certain types of molecules (glucose and aminoacids). Secondary transport systems are also liable to saturation and competitive inhibition and can operate using a symport (solute moves in the same direction of the sodium ion) or antiport (solute and sodium ion move in opposite directions) mechanism.

A summary and characterization of the different small molecule transmembrane transport mechanisms is presented in Table 2.

Table 2 – Summary of the transport mechanisms of small molecules and ions across the lipid membrane.

	Transport Mechanism			
Property	Passive Diffusion	Facilitated Diffusion	Primary Active Transport	Secondary Active Transport
Require specific protein	**-**	**+**	**+**	**+**
Solute transported against its gradient	**-**	**-**	**+**	**+**
Coupled to ATP hydrolysis	**-**	**-**	**+**	**-**
Driven by movement of a co-transported ion down its gradient	**-**	**-**	**-**	**+**

This table was adapted from reference (2)

In order to fully understand the transport mechanisms and the channelopathies described later, it is essential to comprehend the ion channels normal functioning.

As aforementioned, ion channels are integral protein complexes composed of one or several polypeptide subunits spawning the membrane with basic functional components gathered in Table 3.

Table 3 – Functional units that compose an ion channel.

Component	Function
Gate	Determines if the channel is open or closed (change in the conformation of the membrane protein).
Sensors	One or more. Respond to one of several different types of signals: changes in membrane potential, second messengers or ligands (neurohumoral agonists).
Selectivity Filter	Determines the classes of ions or the particular ions able to cross through the channel pore.
Open-channel pore	The actual channel that allows a continuous flow of ions through the membrane while the channel is open.

This table was adapted from reference (7)

The ion channels operate through a gating mechanism as response to membrane potential changes beyond a certain reference value (voltage-gated ion channels) or when stimulated by the binding of a specific intra or extracellular ligand (ligand-gated ion channels).(8) By contrast, the non-gated channels are permanently open independent of internal or external stimuli.(8) The main biological functions of the ion channels are summarized in Table 4.

Table 4 – Ion channel functions.

	Function
Cellular Level	• Regulation of membrane potential • Regulation of the osmotic balance • Regulation of the pH through proton flux • Regulation of Ca^{2+} concentrations • Sensory transduction • Nerve and muscle excitation
Organism Level	• Hormonal Secretion • Learn and Memory • Regulation of blood pressure • Transepithelial transport • Bone metabolism

This table summarizes information from references (8-9).

The malfunction of ion channels is the cause of many human diseases, commonly called as channelopathies, which have motivated, along the last decade, an increasing interest in the research and development of drugs to treat specific mutations in ion channels (10), as well as drug-like molecules for channel replacement therapies.(11-12)

1.1.4. *Channelopathies*

Channelopathies can arise through mutations in the promoter or in the coding region of an ion channel gene or through mutations in the genes encoding regulatory molecules of the channel activity or defects in the pathways responsible for their production.(9) These disorders were initially reported as skeletal muscle excitability disorders and then as disorders of the brain and peripheral nervous system.(8-9) There are three common features between channelopathies of the brain and channelopathies of skeletal muscle: symptoms are intercalated with normal function, most of these diseases are inherited as autosomal dominant traits and there is just one organ involved.(8) Autoantibodies and toxins or venoms to ion channels and their proteins are also responsible for some channelopathies.(9)

Overall, channelopathies have been identified with malfunction of voltage-gated ion channels (Na^+, K^+, Ca^{2+} and Cl^-), fast ligand-gated channels (nicotinic acetylcholine receptor, glycine receptor and GABA receptor), intracellular channels and intercellular channels (conexins).(8)

Channelopathies Associated with Chloride Transport

The chloride anion is one of the most abundant and common ions in the human body and is a critical chemical entity for the metabolism, digestion and maintenance of acid-base balance. Thus, the chloride channels are important for the control of membrane excitability, transepithelial transport and regulation of cell volume and intracellular pH.(9) These chloride channels can be gathered into three families, voltage-gated chloride channels, cystic fibrosis transmembrane conductance regulator (CFTR) and ligand-gated Cl^- channels opened by GABA and glycine.(9)

Mutations in different families of chloride channels produce different channelopathies. For instance, mutations in the gene encoding the skeletal muscle voltage-gated chloride channels cause two forms of myotonia, congenital and generalized (9), while mutations in genes encoding $GABA_A$ receptors (a type of ligand-gated chloride channels) have been associated

with inherited epilepsy.(13) Furthermore, CFTR mutations alter the selectivity and conductance of the channel causing cystic fibrosis (CF), one of the most common severe human diseases, with an incidence ratio of one in 3268 births in Brittany (France), between 2005 and 2009.(14) This disease is characterized by a thick mucus secretion that blocks the smaller airways and secretory ducts and promotes infection, inflammation and destruction of the tissues.(9) There have been identified more than 400 mutations in the CF gene but only a small amount of them have been characterized until now and those can be grouped into different classes as summarized in Table 5.

Table 5 – Classes of CF gene mutations associated with cystic fibrosis.

Class	Consequence
I	Premature truncation of the protein because of splice-site abnormalities (deletions, insertions, non-sense mutations).
II	Alteration of the correct trafficking of the protein leads to dramatic loss of CFTR expression at the cell surface.
III	Regulation of the channel is defective.
IV	Channels with altered conduction properties.

This table summarizes the information on pages 218-222 from reference (9)

The CFTR channel is chloride selective and its activation depends on protein kinase A (PKA) and existence of intracellular complex MgATP.(9) Besides chloride channel activity, CFTR regulates an outwardly-rectifying chloride channel (ORCC) and an epithelial sodium channel (ENaC) (9). In cystic fibrosis, neither ORCC nor ENaC are regulated which lead to a reduction in epithelial Cl^- permeability and an enhanced Na^+ permeability.(9)

A clever approach to cystic fibrosis treatment would be to replace the mutated chloride channels for synthetic ion transporters that could mimic the natural chloride efflux mechanisms. In the subsequent section, a brief overview of the assisted anion transmembrane transport is presented using selected synthetic transporters reported in the literature along the last decade.

1.2. Synthetic anion transporters

1.2.1. *General considerations*

Nowadays, dozens of diverse and effective ionophores have been developed to facilitate ion transport across the lipid bilayer when there is a malfunction of the natural transporters.

Indeed, the synthetic transporters have necessarily ionophore properties, considering that these particular molecules are "*chemical agents that increase the permeability of biological or artificial lipid membranes to specific ions. Most ionophores are relatively small organic molecules that act as mobile carriers within membranes or coalesce to form ion permeable channels across membranes*."(15). Moreover, the ionophores must satisfy several requirements including: partition in the membrane, interact selectively with ions, shield ions from the hydrocarbon core of the phospholipid bilayer and at the same time transport them from one side of the membrane to the other. Therefore, ionophores must be amphipathic molecules with a polar binding site for ion recognition, which are covalentely attached to a lipophilic scaffold.(16) They can be naturally occurring compounds such as peptides, cyclic depsipeptides, macrotetrolides, polyether ionophores or synthetic molecules.(17)

In contrast with cation ionophores, there are only a few natural occurring products that act as anion transporters reported (6), being the most prominent examples the prodigiosins (18).

1.2.2. *Development of synthetic anionophores*

Chloride, bicarbonate and phosphate are the most abundant anions in the human body fluids, with distinct distribution in tissues, cells and different intracellular organelles.(19) As mentioned above, the abnormal transmembrane transport of these anions has a dramatic impact in the human health, which has motivated the molecular designers, along the last two decades, for the development of synthetic anion receptors (3) with potential to be used in channel replacement therapies, opening a new avenue in the supramolecular chemistry field.

The synthetic ion transporters, mimicking the action of natural ion transporters, can be classified as mobile carriers or ion channels, (19-20) as illustrated in Figure 5.

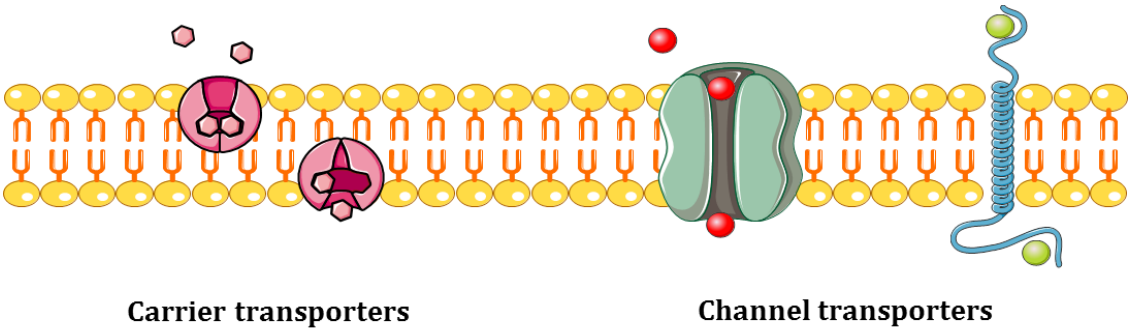

Figure 5 – Schematic representation of the mechanisms by which synthetic ionophores operate.

As depicted in Figure 5, synthetic anion carriers are small organic molecules that shuttle ions from one side of the bilayer to the other.(19) They are often highly selective transporters and reversibly bind the anions to form lipophilic ion-carrier complexes.(3) In contrast, synthetic ion channels are static structures that provide an ion-conductance pathway (19), they can be constituted by a single molecule that spawns the entire phospholipid bilayer (monomeric channel) or by several self-assembled molecular entities (self-assembled pores) exemplified as follows.(3)

Prodigiosins are small low-molecular-weight molecules and extremely efficient chloride transporters with antibiotic, antitumor and immunosuppressive activities.(3, 19, 21) These natural molecules promote the chloride transport across the membrane, as mobile carriers, using H^+/Cl^- symport mechanism.(3, 19) Indeed, the protonated prodigiosins uptake chloride from inside the cell and diffuse across the membrane releasing HCl in the other side (18), as illustrated in Figure 6. On the other hand, Davis *et al* showed that they can also mediate chloride transport as anion exchangers through NO_3^-/Cl^- antiport.(18)

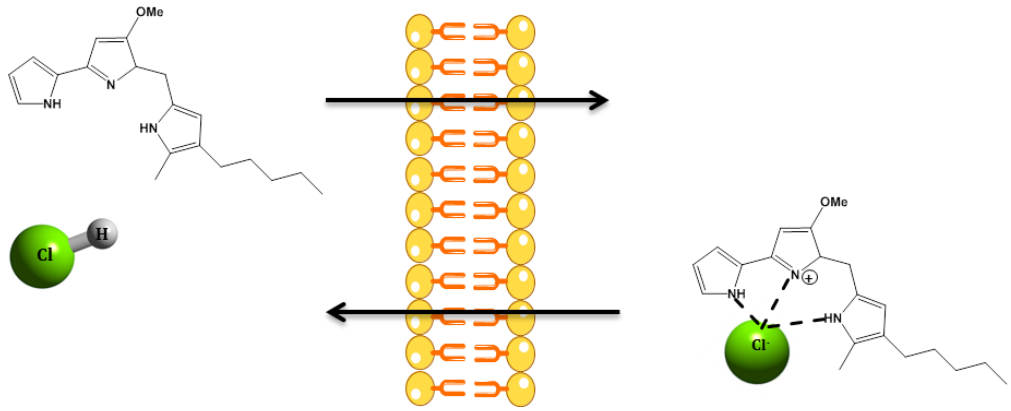

Figure 6 – Schematic representation of HCl co-transport by prodigiosin molecule as a mobile carrier.(18)

Along the last decade, synthetic transporters inspired in the prodigiosins binding unit have been reported. The Quesada group has investigated the anion transport properties of isophthalamides and tambjamine alkaloids. Similarly to the prodigiosins, both series of synthetic receptors promote the release of chloride from POPC liposomes through a Cl^-/HCO_3^- exchange system.(22-24)

In contrast, Davis *et al* reported the first synthetic calix[4]arene[4] architectures able to promote the anion transport across phospholipid vesicles (see Figure 7). The calix[4]arene skeleton displays an apparent rigid structure capable of binding neutral and ionic species when functionalized with appropriate recognition units. Moreover, these artificial receptors with ionophore properties adopt different chemical conformations, *cone*, *partial-cone*, *1,3-alternate* and *1,2-alternate* (26-29), which determines the anion transport mechanism. For instance, tetrabutylamide calix[4]arene derivative (2) in 1,3-alternat conformation (see Figure 7), is able to carry out selective chloride transmembrane transport through Cl^-/OH^- antiport or H^+/Cl^- symport mechanisms, using a static channel formed by the assembly of two calix[4]arene units by two water bridges.(26) On the other hand, the same molecule in cone conformation also shows chloride transport activity across the phospholipid bilayer, but as a mobile carrier.(26)

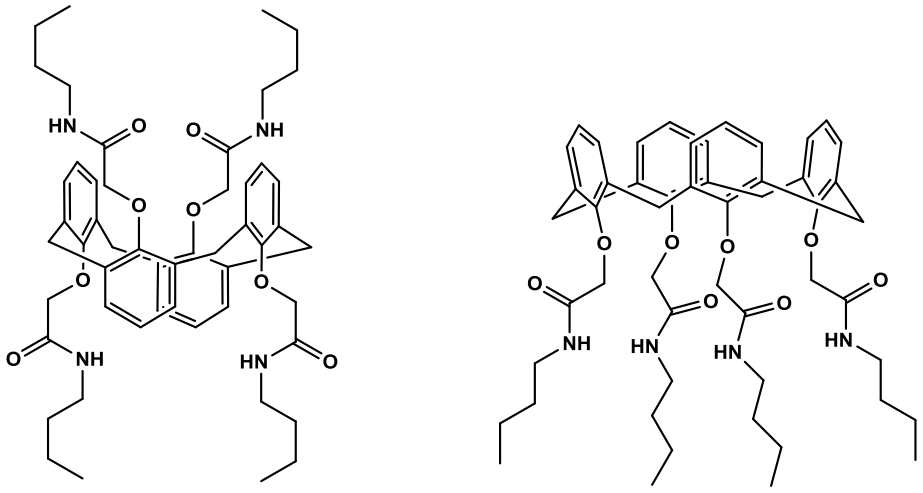

Figure 7 – Terabutylamide calix[4]arene showing chloride transmembrane transport activity in *1,3-alternate* (left) and *cone* (right) conformations.

[4] Calixarenes are versatile building block that have been used in the design of cation receptors.(25)

Sessler's investigations of the anion transport ability of dipyrrole and polypyrrole derivatives have shown that the protonated forms promote the release of chloride from the interior of the vesicles in a short period of time.(30-33) Examples of these molecules are depicted in Figure 8. Gale and co-workers have also performed similar studies on two amidopyrrole receptors containing imidazole and pyridine appendages, sketched in Figure 9. It is noteworthy that only the imidazole derivative (2) with a structure similar to prodigiosin is able to operate the transmembrane H^+/Cl^- co-transport.(6, 34-35) Other urea-based anion transporters such as bis-indolylureas and bis-ureas (see Figure 10) have also been investigated by the same group and were shown to facilitate the transmembrane transport of chloride through POPC bilayers.(36-37)

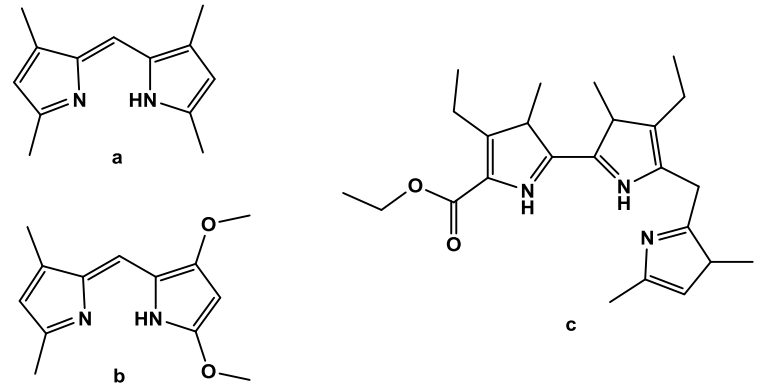

Figure 8 – Examples of dipyrrole (*a* and *b*) and polypyrrole (*c*) molecules from Sessler´s *et al* studies. (30-33)

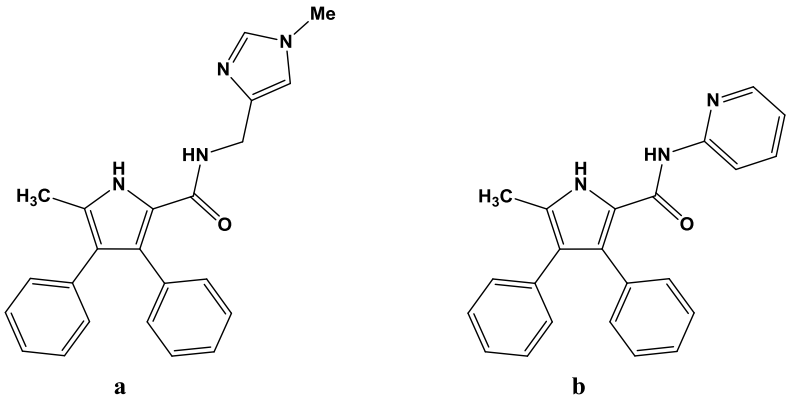

Figure 9 – Amidopyrroles derivatives with chloride transmembrane transport activity incorporating and imizadole (a) and pyridine groups (b).(34)

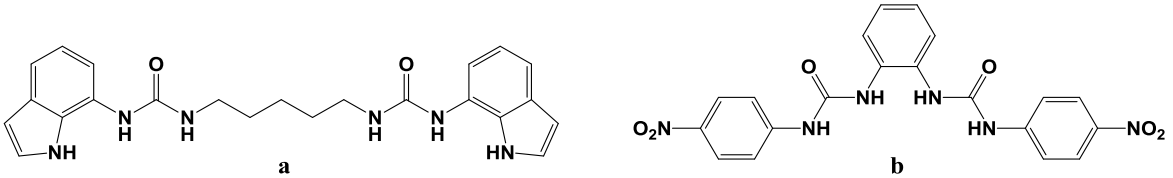

Figure 10 – Bis-indolylurea (a) (36) and bis-urea (b) (37) transporters developed by Gale and co-workers.

Gin and co-workers developed a highly active synthetic trasnporter, namely a monomeric cyclodextrin-based ion channel (38). The channel comprises a β-cyclodextrin head group and oligoether chains sufficiently hydrophobic to insert the channel into the phospholipid bilayer and long enough to span the membrane. In spite of the large number of the oxygen atoms present in the β-cyclodextrin macrocycle skeleton, the studies revealed that anions were transported faster than cations. (38)

Di Fabio *et al*. developed a new family of cyclic glycomimetic named CyPLOS (cyclic phosphate-linked oligosaccharides). These transporters are characterized by an anionic macrocycle skeleton with high stability to acidic and enzymatic hydrolysis and that can be easily modified and functionalized.(39) The addition of linear chains to these molecules led to a jellyfish-like derivative capable of anchor to the polar surface of the membrane while the linear chains permeate the membrane, altering and locally destabilizing it. This alteration in the membrane properties allows the ion permeation through unselective processes.(16)

Another family of anion transporters based on natural compounds was developed from cholic acid (see Figure 11), by Davis' group. The cholic acid is a rigid steroid platform with lipophilic properties and several hydroxyl groups that can be functionalized with suitable anion binding units leading to a series of anion transporters called cholapods (see Figure 11).(40-42) Electroneutral cholapod molecules promote the anion transport as mobile carriers by an exchange mechanism.(3, 43) The chloride transport efficiency is remarkable, namely when incorporated into the phospholipid bilayer.(40) Bis-carbamide and the tris-sulfonamide were the first synthetized cholapods and it was demonstrated that the addition of electron-withdrawing substituents, such as trifluoromethyl (CF_3) and nitro (-NO_2) groups, increased their H-bond donor properties (41, 44) as well as the anion encapsulation ability, which improves their transporter activity.(44)

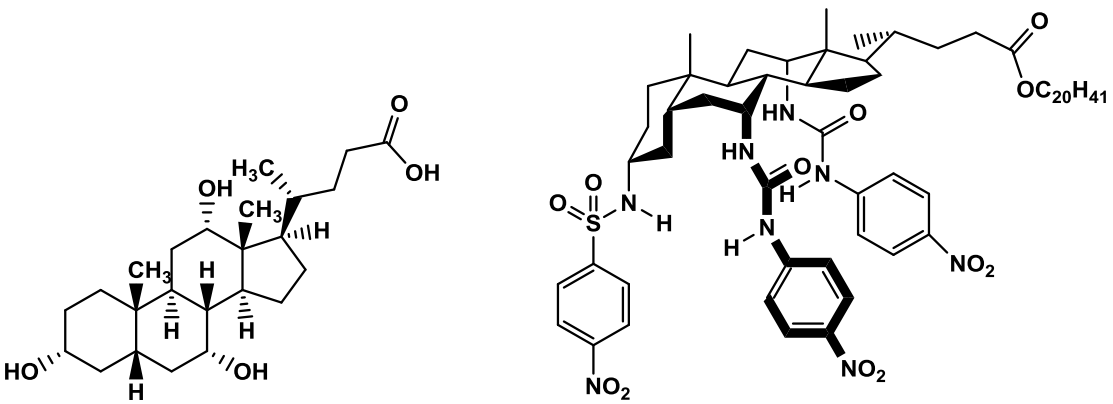

Figure 11 – Functionalization of the cholic acid (left) with different binding and transport groups (right).(42-43)

Several other synthetic anionophores were developed over the last three decades, including the peptide-based channels developed by Tomich and co-workers (GlyR) (45), Gokel and co-workers (SCMTR) (46-49) and Matile and co-workers (*p*-octiphenyl β-barrels) (19, 50-52), as well as the steroid-based channels by Regen and co-workers (molecular umbrellas).(53-54)

Next generation synthetic transporters must follow requirements for pharmaceutical success, acceptable solubility in physiological solution, appropriate cell targeting and subsequent membrane partitioning and lengthy residence time in the apical plasma membrane target cells (20). This way, a new type of membrane transporters was created, operating by a relay mechanism (20), shown on Figure 12. The transporter is a phospholipid derivative with an anionophore appended, an urea group to bind Cl^- (see Figure 13), however, it may be possible to use other substituents selective for other anions, cations or neutral species (20).

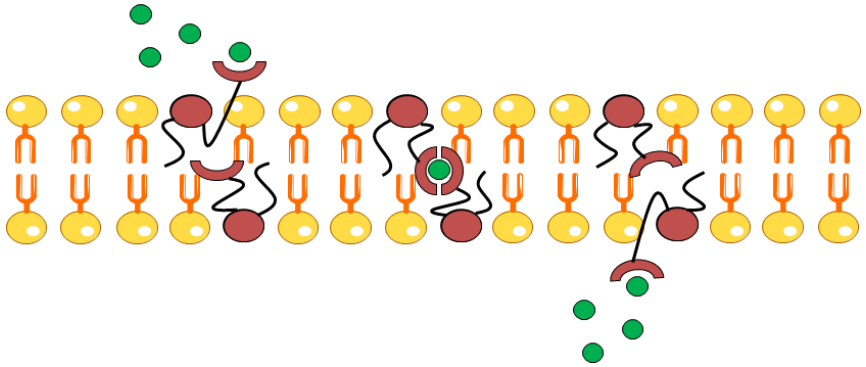

Figure 12 – Schematic representation of the relay mechanism.

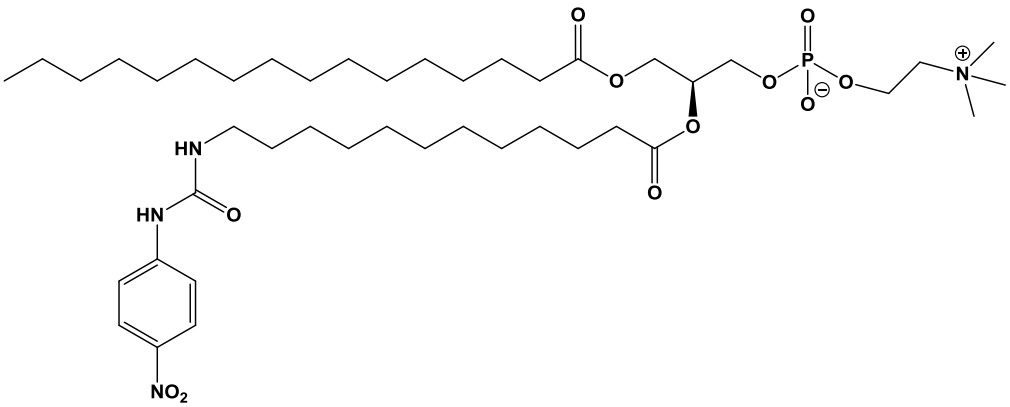

Figure 13 – Phospholipid derivative with an ionophore with a relatively high affinity for Cl^- (4-nitrophenylurea group) appended.

1.3. Squaramides as anion receptors

Squaramides are amide derivatives of the squaric acid, an organic compound with a four-membered ring system and two carbonyl groups conjugated through a C-C double bond (see Figure 14). Moreover, the squaramide motif displays two hydrogen bond acceptor (the carbonyl groups) and two hydrogen bond donor (amide groups) binding sites as depicted in Figure 15.

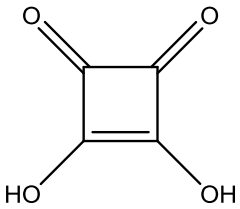

Figure 14 – Schematic representation of a squaric acid molecule.

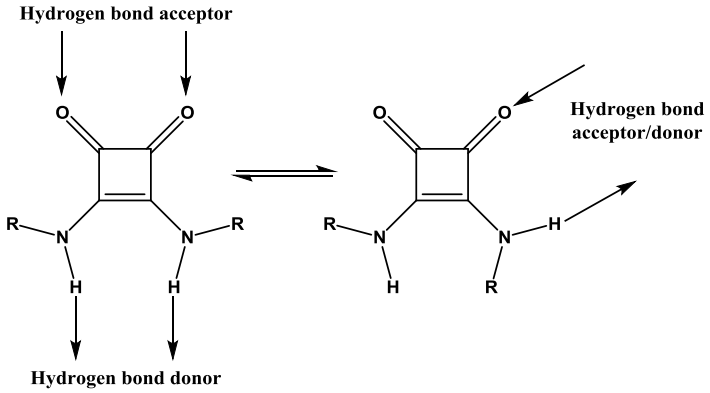

Figure 15 – Squaramides can form up to four hydrogen bonds (two acceptor and two donor).

According to several studies (55-58), it was demonstrated that the acceptor/donor character of squaramides is related to the gain in aromaticity of the quadratic ring when hydrogen bonds are established with carbonyl oxygen groups and N-H groups.(59-60)

In the squaramide core, the rotation of the two N-H groups around the corresponding C-N bonds is partially restricted by the electron delocalization through the apparently rigid squaramide motif.(59-60) In spite of this limited conformational freedom, the squaramides can exhibit three different conformations with the N-H groups adopting the spatial dispositions *anti/anti*, *syn/anti* and *syn/syn* as depicted in Figure 16 for squaramide S01.(59-60)

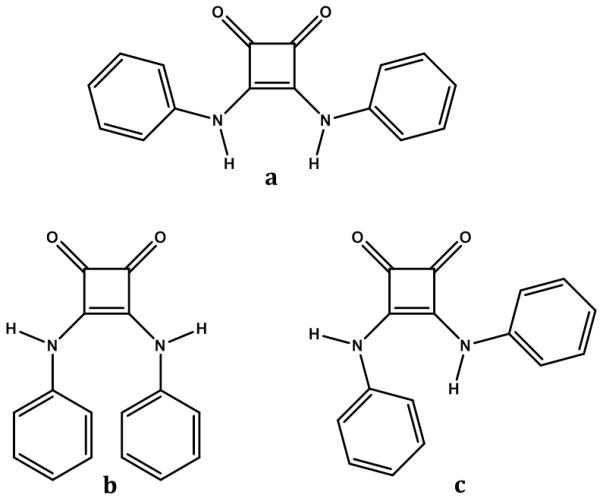

Figure 16 – Schematic representation of *anti/anti* (a), *syn/syn* (b) and *syn/anti (c)* conformations of a squaramide.

The hydrogen donor and acceptor ability of the aforementioned squaramide motif leads to the self-assembling of *anti/anti* conformations , in solid state, in a head-to-tail arrangement, very difficult to perturb by other competing functional groups (see Figure 17) (60), as supported by a search in the Cambridge Structural Database (CSD). Moreover, in squaramides with phenyl substituents directly bonded to the squaramide core (see *infra*), the *anti/anti* conformation has the possibility to be stabilized by intramolecular C-H···O hydrogen bonds, as well as by π-stacking interactions between aromatic rings. (59, 61) 1-D head-to-tail arrangement between squaramide monomers is illustrated in Figure 17. The *syn/syn* conformation is most unlikely to be observed due to the steric hindrance caused by the bulky substituents.

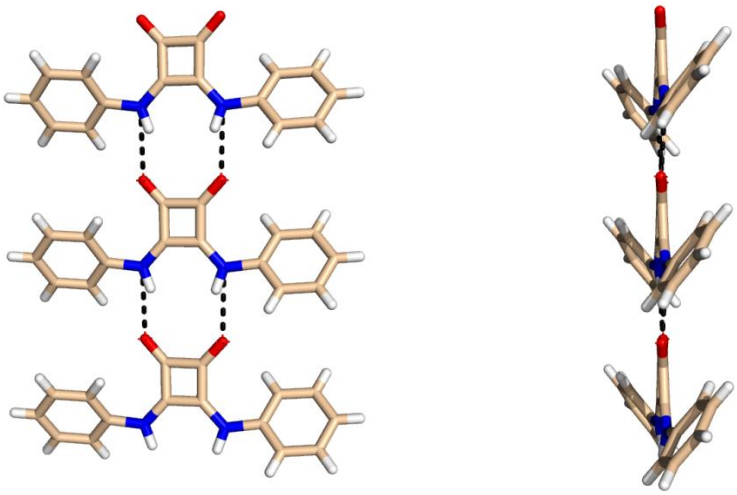

Figure 17 – Crystal structure of squaramide S01 (EWOCAV) organized in a chain, according to their *anti/anti* conformation, showing a head-to-tail packing (left) and *π*-stacking interactions between phenyl groups (right). Image adapted from CSD with *Pymol* software.

In the *anti/anti* conformation, once the first intermolecular N-H···O interaction is established, the second one becomes less favourable, but this effect is compensated with the addition of more monomers.(60) This can be explained through the cooperative induction effect, where an electronic polarization occurs as a consequence of monomer linkage to an *anti/anti* aggregate and the interaction with subsequent monomers is reinforced.(60) In the *syn/syn* aggregate the polarization effect does not take place.(60)

The squaramides have a high affinity for cations and anions, much higher than other compounds like ureas.(62-63), in agreement with electrostatic potential calculations that showed the ability of squaramides to form stronger acceptor/donor interactions than ureas.(59) The squaramide moiety has been incorporated in synthetic transporters as binding unit of cations (polyalkylammonium cations) (64) and anions (halides, dihydrogen phosphate, sulphate and bicarbonate) (56) Recently, other groups used squaramide-based receptors for the uptake of chloride, sulphate and carboxylates. (62, 65-68) The stoichiometry receptor:anion in chloride complex is 1:1 as depicted in Figure 18.

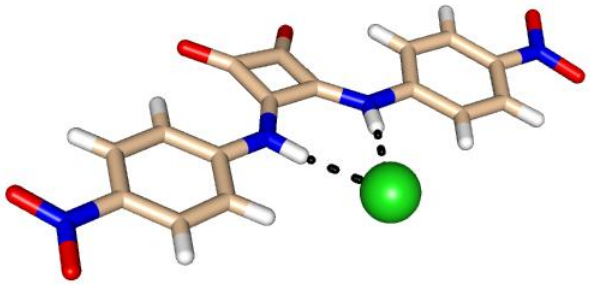

Figure 18 – Crystal structure of the chloride complex with *p*-dinitrophenyl squaramide (CSD Refcode MUYYOV). Oxygen, carbon, nitrogen and hydrogen atoms are in red, wheat, blue and white, respectively. Chloride anion is in green and hydrogen bonds are drawn as black dashes.

Quantum calculations on free squaramide moiety (I), as well as in ammonium (II), sulphate (III) and ammonium and sulphate (IV) complexes (see Figure 19), at the MP2/6-311+G** level of theory.(55-56, 58-59, 64, 69), showed a progressive equalization of the bond lengths in the four-membered ring upon cation and/or anion binding.(55-56)

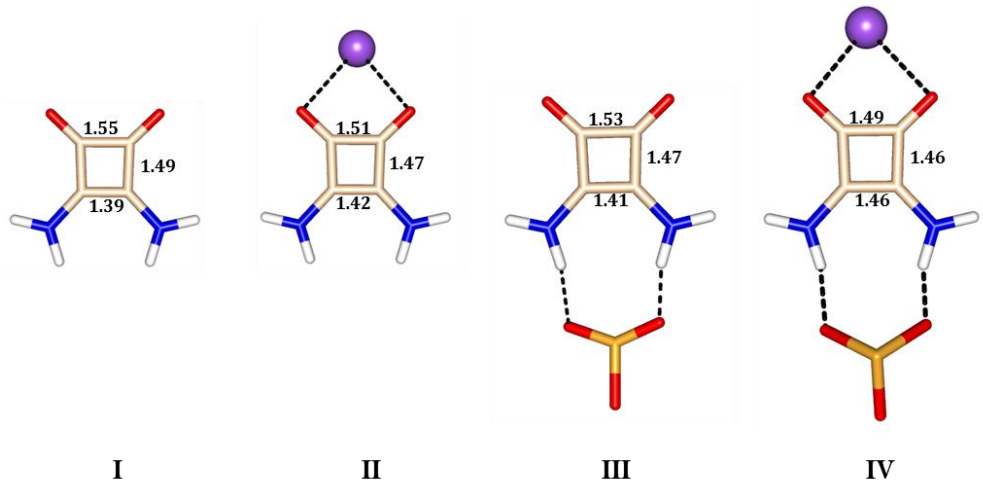

Figure 19 – Schematic representation of the MP2 optimized geometries of a squaramide example showing relevant bond lengths (Å), tending to equalization as more hydrogen bonds are established, up to the four possible ones. I – none hydrogen bond; II – two acceptor hydrogen bonds; III – two donor hydrogen bonds; IV – four hydrogen bonds. Image adapted from Quiñonero et al.(56)

1.3.1. *Applications*

Various applications for squaramides have been reported. In medicinal chemistry, the interest has increased due to advances in squaramide synthesis and commercial availability of precursors.(59) Every progress entails concerns such as the reactivity of these compounds or the risk of *in vitro* toxicity.(59) However, squaramides proved to be quite stable to nucleophilic attack, requiring extreme conditions to displace the amine groups, increasing the confidence of drug designers on them.(59)

Currently, the pharmaceutical companies are incorporating the squaramide motif in molecular design as H-bonding unit to replace more toxic functionalities including ureas, guanidine, and others. Squaramides are investigated and developed for therapeutic targets as kinases, metalloproteases, receptors and ion channels.(59)

The main application for squaramides is as replacements for amino acids (59) or carboxylic acids in phosphonoformic acid (PFA) and phosphonoacetic acid (PAA).(70) Recently, PFA was approved as a viral RNA/DNA polymerase inhibitor for the treatment of cytomegalovirus in AIDS patients. Moreover, when tested as inhibitor of influenza DNA polymerase, the new compound with the squaramide motif revealed activity comparable to PAA.(59)

Another example of the application of squaramides in the field of the anion binding was the interesting research developed by Muthyala and co-workers (71), with the synthesis of an

environment-sensitive chloride squaramide. The anion recognition occurs through a "valve-like mechanism", being the valve closed in apolar solvents by intramolecular N-H···O hydrogen bonds, as depicted in Figure 20, and consequently preventing the chloride binding.

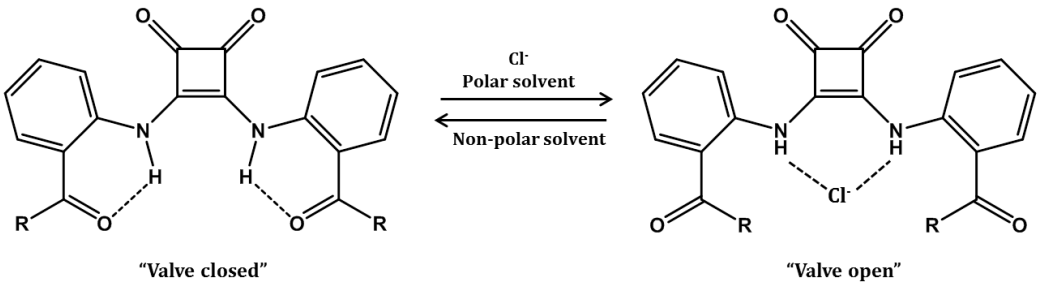

Figure 20 – Schematic representation of the valve-like mechanism from Muthyala *et al.*(71)

Recent experimental efflux studies with simple squaramides have shown that these low-weight molecules are able to transport chloride out of POPC vesicles much efficiently than their analogous thioureas and ureas, using either mobile-carrier or anion-exchange mechanisms.(72) This seminal study opened new perspectives in the use of these drug-like molecules in the treatment of channelopathies as cystic fibrosis and it was the driving force for the theoretical investigation reported in the next Chapters.

1.4. Molecular dynamics simulations of biomembrane systems

The Molecular Dynamics (MD) simulation is powerful tool to study the diffusion and interaction of artificial receptors with phospholipid bilayers as reported along this thesis.(73) Thus, in the subsequent subsections a brief description of the fundamentals of molecular mechanics and molecular dynamics simulations is presented.

1.4.1. *Molecular modelling studies*

The total energy of a chemical system is given as the sum of the potential and kinetic energies (see Eq. 1).

$$E_{Total} = E_{potential} + E_{kinetic} \quad \text{Eq. 1}$$

The kinetic energy derives from the motion of the body and represents the work needed to accelerate it (see Eq. 2)

$$E_{kinetic} = \frac{1}{2} mv^2 \quad \text{Eq. 2}$$

where *m* is the object's mass and *v* its velocity.

The potential energy, on the other hand, is determined by the position and arrangement of the particles. When the chemical behavior is manly determined by the nucleus positions the potential energy is the molecular mechanics energy. In other words, the system can be described using the formulism of classical mechanics or Newtonian mechanics.(74)

Molecular Mechanics (MM) energy can be decomposed into several components called force potentials as given by the Eq. 3 and Eq. 4

$$E_{MM} = E_{bonded} + E_{non-bonded} \quad \text{Eq. 3}$$

$$E_{MM} = E_{bond} + E_{angle} + E_{torsion} + E_{electrostatic} + E_{van\ der\ Waals} \quad \text{Eq. 4}$$

The bond stretching, angle bending and torsional angles terms of Eq. 4 correspond to the bonded terms, while the electrostatic and van der Waals interactions terms represent the non-bonded terms.(75)

Potential energy for bond stretching increases when bonds are compressed or stretched and it can be described by Hooke´s law for a spring as given in Eq. 5.

$$v(l) = \frac{\mathrm{k}}{2}\,(l - l_0)^2 \qquad \text{Eq. 5}$$

where k is the force constant for the spring, l is the actual bond length and l_0 is the equilibrium bond length.(74)

Angle bending energies are modeled by polynomial expansions and increase as the angles are bent from their normal position as given by Eq. 6.

$$v(\theta) = \frac{\mathrm{k}}{2}\,(\theta - \theta_0)^2[1 - k'(\theta - \theta_0) - k''(\theta - \theta_0)^2 - k'''(\theta - \theta_0)^3 \ldots] \qquad \text{Eq. 6}$$

where θ is the actual valence angle and θ_0 is the natural valence angle.(74)

Torsion energies result from intramolecular rotations and these energies increase as the distance between 1-4 atoms decreases. The torsion potential is an expansion of a periodic cosine function given by Eq. 7 and takes into account all 1-4 bond relationships.(76)

$$v(\omega) = \sum_{n=0}^{N} \frac{V_n}{2}\,[1 + cos(n\omega - \gamma)] \qquad \text{Eq. 7}$$

where ω is the torsion angle and V_n is the 'barrier' height that gives a qualitative indication of the relative barriers to rotation. n is the multiplicity and γ is the phase factor.(76)

Whereas the force constants for the bond and angles terms are usually obtained through an empirical equation as exemplified for general Amber force field (GAFF) in Chapter 2 (see Eq. 10 and Eq. 11), the force constants for torsion angles are determined *via* quantum calculations.

Electrostatic interactions are accounted by atomic point charges and bond dipole moments. The energy is calculated according to Coulomb's law and considering all the dipole-dipole moments in the molecule. For a pair of atoms the electrostatic energy is given by the Eq. 8.(76)

$$U_{AB} = \frac{q_A\, q_B}{\varepsilon_{AB}\, r_{AB}} \qquad \text{Eq. 8}$$

where q is the atomic charge of each atom, ε is the dielectric constant and r is the distance between the atoms involved.

Van der Waals interactions are easily understood considering the approach of two noble gas atoms and the Eq. 9. As the two become closer the attraction energy increases until its maximum when the distance between them equals the sum of their van der Waals radius. If the atoms continue to approach one another, a repulsive force starts to increase as depicted in Figure 21.(74, 76)

$$v(r) = 4\varepsilon\left[\left(\frac{\sigma}{r}\right)^{12} - \left(\frac{\sigma}{r}\right)^{6}\right] \qquad \text{Eq. 9}$$

where σ is the separation for which the energy is zero and ε is the well depth.

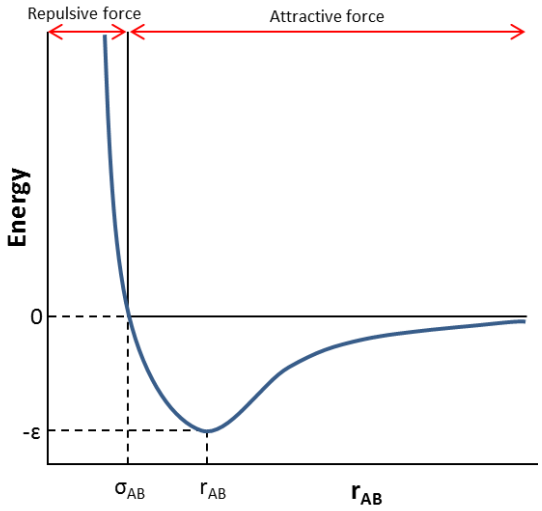

Figure 21 – Lennard-Jones potential curve.

The assembly of all parameters defined by the equations aforementioned is a force field. Indeed, following the definition given by Leach, a *force field is a set of form and parameters of mathematical functions used to describe the potential energy of atoms or molecules in a system*.(74)

Different force fields are available with equivalent functional equations. but each one of them has their own strengths and weaknesses depending on their parameters set.(77) There are three types of force fields: all-atoms, united-atoms and coarse-grained. In all-atoms force fields there is an explicit representation of all the species present in a molecule,(74) contrasting with the united-atoms force fields that reduce the interaction sites by considering non-polar hydrogen atoms with a carbon atom as a single atom.(74, 77) Coarse-grained models, represent an entire fragment, for instance an amino acid, as a single interaction site (78), speeding the simulation but losing information and precision.

Molecular Mechanics can be applied to predict the local minima on molecular potential energy surface (PES), however MM does not account of zero-point vibrations and the calculations refer to molecules at 0 K (75). Therefore, computational chemists seek for techniques capable of accurately reproduce molecular behaviour while allowing to "watch" the time development of collections of atoms and molecules. (75) Molecular Dynamics (MD) is one of the methods that can be used for this purpose (76). MD is a deterministic method, associated with Newton's second law, meaning that the state of the system at any future time can be predicted from its current state, (74, 76), resulting in a phase space trajectory. (76) It is important to refer that phase space trajectories cannot cross one another but they can be periodic, assembling repeatedly in space, these are called periodic boundary conditions (PBC). (76)

Periodic boundary conditions (PBC) are a set of boundary conditions used to simulate a large system by modeling only a small part, a unit cell or simulation box, *i.e.,* when an object passes through one face of the unit cell it reappears on the opposite face with the same velocity and properties.(74) PBC requires unit cells with certain characteristics, the shape is extremely important. It must tile perfectly as a three-dimensional crystal so it cannot be spherical; the most common box shapes used in MD simulations are the cubical and rectangular prism or the truncated octahedron. Each system can have infinite tiled copies of its unit cell (images), however, during the simulation time only the properties of a single unit cell need to be recorded and are then applied to the images.(74)

The first MD simulations were performed by Alder et al. in 1957 (79) using hard-sphere potential, a very simple model in which the particles move in straight lines at constant velocity between collisions and there is no force between particles until they collide (74). In contrast, in Lennard-Jones model the force between two atoms or molecules changes continuously with their separation.(74)

In summary, the equations introduced along this sub section are the basis of MM and MD simulations of molecular systems, such as proteins, lipids, and the phospholipid bilayers studied in this work.

1.4.2. *MD simulations of membrane models*

Currently, MD simulations of phospholipid bilayers are used to investigate pure species or mixed composition bilayers, lipid rafts and cellular processes.(74) Four types of phospholipids are commonly used in simulated membrane models, DOPC, POPC, DMPC and

DPPC, which are depicted in Figure 22. These lipids share a zwitterioninc phosphatidylcholine head group (*sn*-3) and two acyl chains (*sn*-1 and *sn*-2). In the case of POPC, the phospholipid used in this work, the *sn-1* chain is saturated and the *sn-2* chain is monounsaturated.

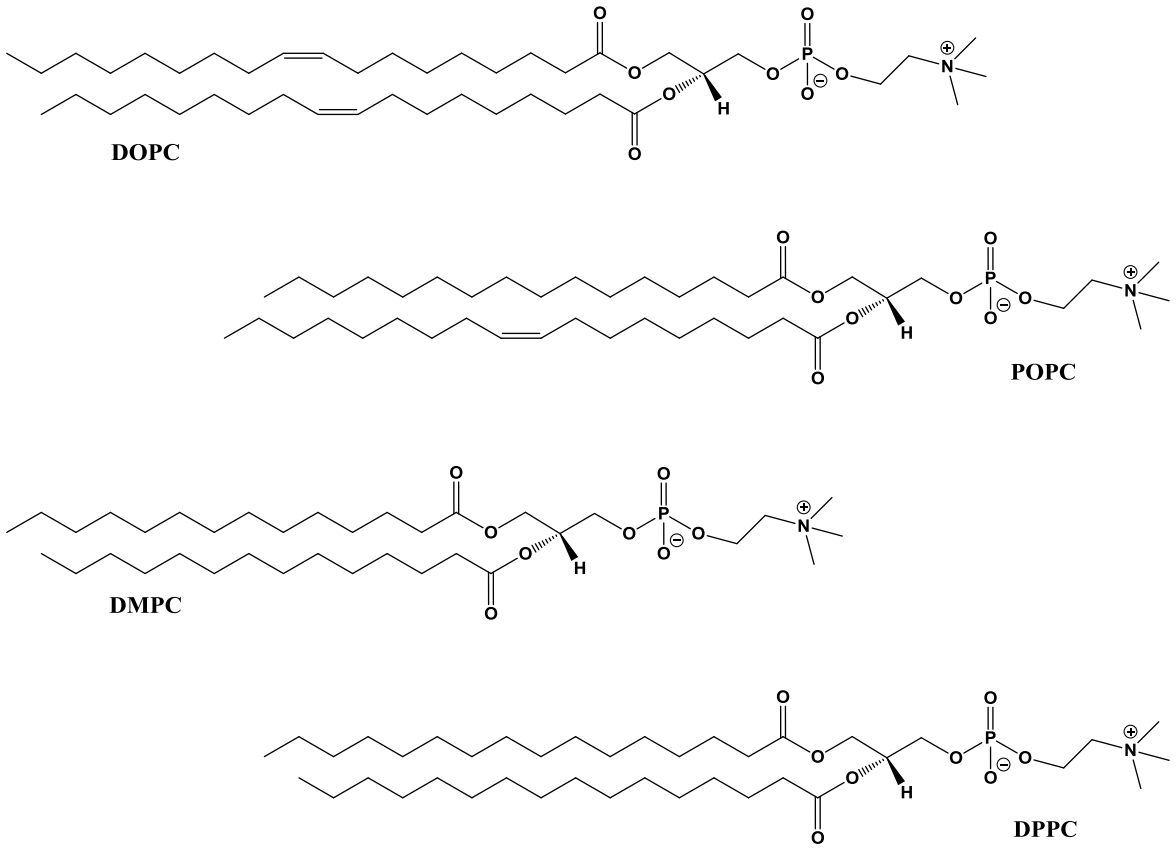

Figure 22 –The four types of phospholipids commonly used in MD simulations as membrane models: 1, 2-dioleoyl-*sn*-glycero-3-phosphocholine (DOPC), 1-palmitoyl-2-oleoyl-*sn*-glycero-3-phosphocholine (POPC), 1, 2-dimyristoyl-*sn*-glycero-3-phosphocholine (DMPC), and 1, 2-dipalmitoyl-*sn*-3-phosphocholine (DPPC).

The major concern in any MD simulations is the force field used. A force field has to be transferable from one molecule to other strictly related molecules, in order to predict the geometry of a new one using derived data to the first one. Thus, a large molecule is no more than the sum of features known for small molecules, combined in different ways.(75) In the Table 6 are summarized the force fields available in the most popular software packages for molecular dynamics simulations.

Table 6 – Force Field types currently used and phospholipids tested.

Type of Force Field	Force field	Tested phospholipids	Ref.
All-atoms	CHARMM36 (C36)	POPC, POPG	(80)
		DPPC, DMPC, POPC, DLPC, DOPC, POPE	(81)
	GAFF	DOPC	(73)
		DOPC, DMPC	(82-83)
		POPC	(83)
	LIPID11	DOPC, POPC, POPE	(84)
	GAFFLipid	DLPC, DMPC, DPPC, DOPC, POPC, POPE	(85)
United-atoms	GROMOS 43A1-S3	DLPC, DMPC, DPPC, DOPC	(86-87)
		POPC	(87)
	GROMOS $G53A6_L$	DLPC, DMPC, POPC, DOPC	(86)
Coarse-grained	MARTINI	DPPC, DOPC, DOPE, DPPE	(78)

Although united-atoms GROMOS force fields have shown considerable success in molecular dynamics of membrane systems, all-atoms force fields allow the complete description at the atomic level the interactions between the phospholipids and a given molecule, introduce in the phospholipid bilayer.(82) The CHARMM36 is an all-atoms force field created from the precedent CHARMM27 in order to simulate heterogeneous biomolecular systems using a NPT ensemble.(80-82)

By contrast with CHARMM, GAFF was designed to allow extension to arbitrary organic molecules without compromise the parameters and forms of the other existing force field (73) within the AMBER universe. Concerning the phospholipid simulations, GAFF accuracy was compared with other force fields such as CHARMM27 and united-atom force field of Berger.(73) GAFF reproduced most of the structural and dynamical bilayer properties of common lipids, including order asymmetry at the beginning of the phospholipids' chains.(73, 82) Besides, GAFF, as a general force field, is compatible with other force fields, within the

AMBER software package, such as for nucleic acids and proteins (ff12SB) (10) and carbohydrates (GLYCAM).(88)

In 2007, Jójárt and Martinek tested the original GAFF in a fully hydrated POPC membrane bilayer composed of 128 POPC molecules and 2985 TIP3P water molecules (83). The simulations were performed in a tensionless NPT ensemble and in an NPγT ensemble with surface tension of 60 mNm^{-1} per bilayer. In the first case the results obtained showed a high compression of the membrane resulting in low areas per lipid and high order parameters, comparing to experimental values. However when a surface tension was applied together with an NPT ensemble, an excellent agreement between the values of these parameters and the experimental ones was obtained.(83) Thus, GAFF/TIP3P combination proved to be a good model to use for aqueous membrane bilayer simulations with an acceptable accuracy for biomolecular modelling.(83)

New AMBER compatible force fields for lipids were recently published (2012): Lipid11 (84) and GAFFLipid (85).The second force field was created by Gould and co-workers from the GAFF development of specific parameterization for DLPC, DMPC, DPPC, DOPC, POPC and POPE, which includes different atomic charges for the common fragments between these lipids. This force filed has as the main advantage of performing simulations of a lipid bilayer with no superficial tension (tensionless force field).(85) However, the use of GAFFLipid force field is limited to the six neutral phospholipids. By contrast the LIPID11 force field was developed to be a flexible and modular framework, in order to be used with other AMBER force fields.(84) This force field is different from GAFFLipid because it uses a “plug and play” approach; charge model and atom typing and naming were developed to head groups and tails separately, allowing phospholipids to be built out of simple residue-like building blocks heads and tails. This approach can be applied to an extensive range of fatty acid tails and head groups combinations. The great disadvantage is the need for artificial surface tension term, an artifact that cannot be circumvented.

Application of GAFF inspired force fields in the simulation of synthetic receptors in a POPC membrane model

Over the last decade, our group has been developing a pioneer theoretical investigation on the anion transmembrane transport mediated by small artificial receptors. These studies were performed by the extensive use of MD simulations with GAFF parameters for receptors and GAFF-based force fields for POPC molecules. MD simulations have also been applied to a series of anionophores including bis-indolylureas (36) and bis-ureas (37) (see Figure 10). In the case of bis-ureas, the MD simulations showed that these compounds permeate the POPC bilayer and that the more lipophilic compounds are internalized more deeply. By contrast, less lipophilic compounds can also permeate the membrane but prefer staying near the phospholipid head groups establishing a higher number of N-H···O=P hydrogen bonds with amide binding sites (see Figure 23). These series had a low impact on the structural properties of the membrane.(37)

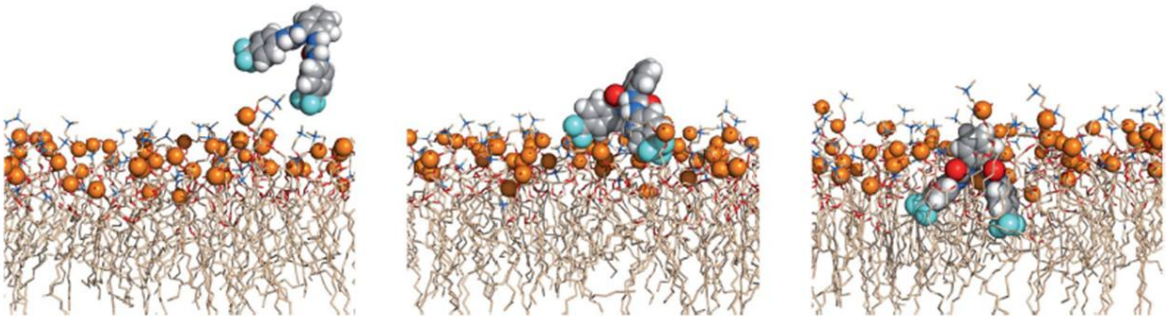

Figure 23 – Snapshots taken from the MD simulation illustrating the passive diffusion of a bisurea transporter along the lipid bilayer.(37)

Experimental efflux studies showed that bis-indolylureas are able to mediate the chloride transport across POPC vesicle bilayers (see Figure 24). The passive diffusion of these was investigated using MD simulations.(36) The distances from the receptor to the water/lipid interface were monitored throughout the course of the simulations, demonstrating the permeation of the POPC bilayer. It was also concluded that the variation of the alkyl spacer length allows the modulation of the transport activity and that bis-alkyl urea-based receptors were more effective than the equivalent mono-ureas. The combination of the experimental and theoretical investigations demonstrated that an increase of the receptor flexibility leads to an increased carrier efficiency. Furthermore, the interaction between the transporter and the lipid bilayer showed to be crucial to anion transport properties. (36)

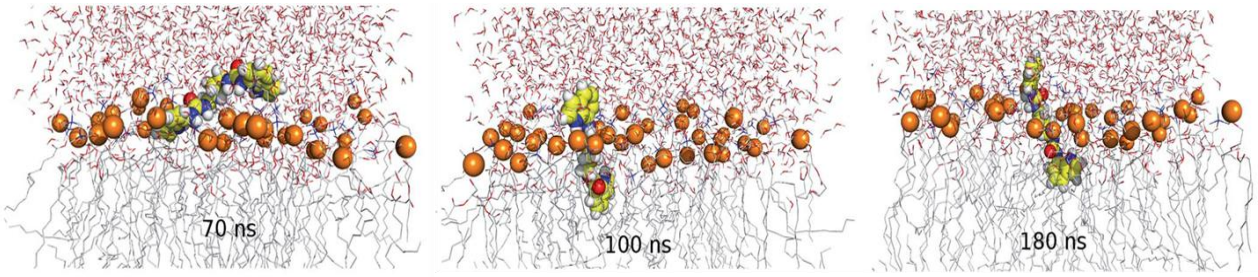

Figure 24 – Snapshots taken from the MD simulation illustrating the internalization process of bis-indolylurea transporter, into the POPC phospholipid bilayer.(36)

Similar methodology will be followed to study the interaction and diffusion of squaramides as chloride transmembrane transporters along this thesis.

1.5. Objectives

The study and development of new synthetic anion transporters is a matter of great importance for the treatment of channelopathies such as cystic fibrosis, which is commonly associated with a deficient chloride transmembrane transport. Thus, this thesis aims to investigate the diffusion and the interaction of squaramides with a POPC bilayer membrane model by the extensive use of molecular dynamics simulations. The structural findings obtained will give the first valuable insights to understand the transmembrane transport of chloride by the squaramides. This main objective will be accomplished through the following sub-objectives:

- Evaluate the recognition of squaramides for chloride anion, using gas-phase molecular simulation methods.

- Evaluate the structural properties of two different POPC pure membrane models using the Molecular Dynamics simulation methodology, in comparison with the published experimental and computational data.

- Carry out MD simulations with the chloride complexes positioned in water slabs or within the phospholipid bilayer core

- Evaluate the impact of squaramide receptors in the structural properties of the POPC phospholipid bilayer.

2. Force filed parameterization of the squaramide receptors

This chapter describes the force field parameterization developed for the squaramide receptors. Preliminary gas-phase molecular mechanics (MM) optimizations were performed on squaramide molecules using default GAFF parameters. This analysis revealed that GAFF is unsuitable to reproduce accurately the bond lengths and angles of the squaramide core, determined by single crystal X-ray diffraction for a large series of squaramides (see below). Furthermore, Quiñonero, *et al.* developed specific force field parameters for squaramides from OPLS force field.(89) However, likewise in GAFF, the C-C bonds between the carbonyl groups were systematically lengthier than the observed in the crystal structures, namely when the squaramide molecules are involved in network of hydrogen bonds. Therefore, the squaramide moiety was parameterized as follows.

2.1. Parameterization of the squaramide moiety

Methodology

A search in the Cambridge Structural Database (CSD) (90) was performed using the squaramide structural motif drawn in Figure 25. In addition squaramides coordinated to metal centres or/and structures with an *R*-factor higher than 10% were rejected. This search yielded 21 entries, which are listed in Table 7 together with corresponding CSD Refcodes. The bond lengths and angles in the squaramides moiety, based on Figure 25, are listed in Table 8 and Table 9, respectively.

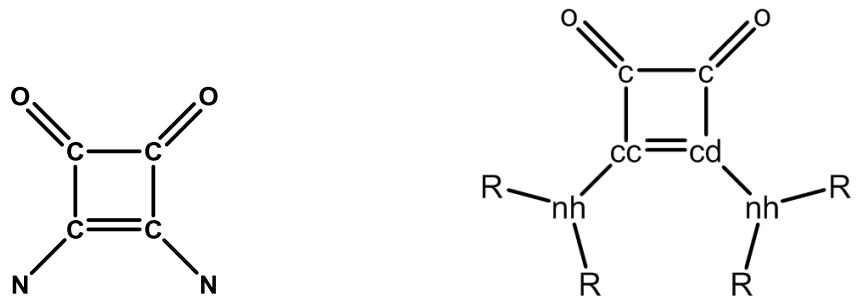

Figure 25 – Schematic representation of the squaramide motif used in the CSD search (left) and of the squaramide moiety with the GAFF default atom-types (right).

Table 7 – Crystal structures deposited with Cambridge Structural Data Base with their CSD Refcodes and references.

Entry	CSD Refcode	Ref	Entry	CSD Refcode	Ref	Entry	CSD Refcode	Ref
1	AKOGAJ	(91)	8	MUYYOV	(62)	15	QORQIY	(92)
2	AKOGEN	(91)	9	NANQUO	(93)	16	RAKZAG	(94)
3	EWOCAV	(95)	10	NIZXIE	(57)	17	REPGIE	(96)
4	FATSUP	(97)	11	NIZXOK	(57)	18	XOPWEF	(98)
5	GAHMEH	(99)	12	NOLRIQ	(100)	19	XUFMER	(101)
6	LANVOM	(69)	13	OMUKAJ	(66)	20	WECCAK	(60)
7	MUYYIP	(62)	14	OMUKEN	(66)	21	WECCIS	(60)

Table 8 – Bond lengths (Å) in the squaramide moiety in the crystal structures deposited with CSD.

Query	CSD Refcode	Squaramide	Bond							
			c-c	cc-cd	c-cc	c-cd	c-o	c-o	cc-nh	cd-nh
1	AKOGAJ	S31	1.517	1.384	1.472	1.463	1.218	1.224	1.322	1.321
2	AKOGEN[a]	S32	1.519	1.384	1.473	1.473	1.214	1.214	1.336	1.336
3			1.528	1.383	1.467	1.467	1.211	1.211	1.330	1.330
4	EWOCAV	S01	1.488	1.421	1.473	1.473	1.226	1.226	1.332	1.332
5	EWOCAV01	S01	1.479	1.417	1.472	1.472	1.226	1.226	1.330	1.330
6	FATSUP	S33	1.505	1.412	1.472	1.465	1.216	1.216	1.339	1.337
7	GAHMEH	S34	1.489	1.425	1.471	1.471	1.222	1.222	1.324	1.324
8	LANVOM	S25	1.499	1.396	1.451	1.475	1.230	1.210	1.318	1.328
9	MUYYIP	S02	1.511	1.382	1.487	1.480	1.208	1.212	1.350	1.356
10	MUYYOV[a]	S02	1.499	1.396	1.476	1.476	1.218	1.217	1.337	1.343
11			1.507	1.390	1.471	1.465	1.215	1.218	1.349	1.350
12	NANQUO	S35	1.476	1.429	1.470	1.470	1.220	1.222	1.330	1.327
13	NANQUO02[a]	S35	1.489	1.442	1.479	1.479	1.229	1.230	1.331	1.332
14			1.490	1.441	1.481	1.479	1.230	1.229	1.332	1.331
15	NIZXIE	-	1.490	1.425	1.458	1.476	1.246	1.227	1.321	1.327
16	NIZXOK	S03	1.492	1.426	1.474	1.480	1.231	1.226	1.316	1.321
17	NOLRIQ	S04	1.482	1.425	1.454	1.469	1.234	1.233	1.312	1.321
18	OMUKAJ	S05	1.504	1.392	1.473	1.482	1.216	1.217	1.349	1.354
19	OMUKEN	S06	1.502	1.406	1.480	1.468	1.216	1.222	1.345	1.337
20	QORQIY	S08	1.493	1.432	1.468	1.470	1.230	1.231	1.326	1.329
26	RAKZAG	S27	1.509	1.400	1.458	1.453	1.220	1.227	1.322	1.320
27	REPGIE	S26	1.530	1.408	1.493	1.493	1.215	1.214	1.354	1.354
21	XOPWEF	S07	1.467	1.414	1.471	1.473	1.241	1.245	1.311	1.312
22	XOPWEF01	S07	1.471	1.401	1.462	1.462	1.230	1.230	1.319	1.319
23	XUFMER[b]	S28	1.480	1.411	1.443	1.469	1.225	1.240	1.320	1.321
24			1.493	1.400	1.463	1.460	1.230	1.235	1.313	1.317
25			1.492	1.394	1.458	1.448	1.230	1.224	1.329	1.328
28	WECCAK	S30	1.488	1.428	1.469	1.461	1.232	1.239	1.314	1.315
29	WECCIS	S29	1.486	1.422	1.459	1.459	1.228	1.228	1.320	1.320
Average			1.496	1.410	1.469		1.225		1.329	
Standard Deviation			0.015	0.018	0.010		0.009		0.012	

[a)/b)] The asymmetric unit is composed by two and three independent molecules, respectively.

Table 9 – Bond angles (°) in the squaramide moiety in the crystal structures deposited with CSD.

Entry	CSD Refcode	Squaramide	Angle											
			cc-c-c	c-c-cd	c-cd-cc	cd-cc-c	nh-cc-c	nh-cd-c	cc-c-o	cd-c-o	nh-cc-cd	nh-cd-cc	o-c-c	c-c-o
1	AKOGAJ	S31	87.2	87.6	92.7	92.5	142.5	142.9	136.6	136.4	125.0	124.4	135.9	136.2
2	AKOGEN[a]	S32	87.4	87.3	92.6	92.6	142.8	142.8	135.8	135.8	124.6	124.6	136.8	136.8
3			87.2	87.1	92.8	92.8	142.7	142.7	136.3	136.3	124.4	124.4	136.6	136.6
4	EWOCAV	S01	88.6	88.6	91.2	91.2	135.7	135.7	137.1	137.2	133.0	133.0	134.1	134.2
5	EWOCAV01	S01	88.7	88.7	91.1	91.1	135.7	135.7	137.0	137.0	133.1	133.1	134.2	134.2
6	FATSUP	S33	87.9	88.2	91.8	91.6	133.0	133.3	135.7	136.1	135.4	134.9	135.6	136.3
7	GAHMEH	S34	88.7	88.7	91.2	91.2	130.0	130.0	134.8	134.8	138.7	138.7	136.4	136.4
8	LANVOM	S25	88.4	87.5	91.5	92.5	135.7	134.9	134.9	134.6	131.7	133.5	137.8	136.6
9	MUYYIP	S02	87.2	87.7	92.5	92.5	137.7	138.8	137.7	137.6	129.7	128.7	134.6	135.0
10	MUYYOV[a]	S02	87.5	87.9	92.2	92.3	139.3	139.2	138.1	137.8	128.3	128.6	134.3	134.4
11			87.6	88.2	91.6	92.2	139.0	139.8	138.1	137.4	128.7	128.6	134.3	134.3
12	NANQUO	S35	89.1	89.0	90.8	90.8	129.8	129.6	135.6	135.5	139.4	139.4	135.4	135.3
13	NANQUO02[a]	S35	89.1	89.0	90.9	90.9	129.7	129.7	135.8	135.6	139.4	139.4	135.3	135.1
14			88.9	89.1	90.9	90.9	129.9	129.6	135.7	135.7	139.1	139.4	135.2	135.3
15	NIZXIE	-	89.4	88.0	91.3	91.3	134.5	135.6	135.8	136.8	134.1	133.1	135.1	134.8
16	NIZXOK	S03	88.9	88.5	91.3	91.2	134.4	133.9	135.1	136.2	134.3	134.7	135.4	135.9
17	NOLRIQ	S04	89.1	88.6	90.8	91.5	133.3	134.4	134.8	135.3	135.2	134.8	136.0	136.1
18	OMUKAJ	S05	87.8	87.8	91.8	92.5	138.6	138.6	137.9	138.3	128.9	129.5	133.9	134.3
19	OMUKEN	S06	88.2	88.0	92.5	91.3	136.8	137.4	137.3	137.1	131.8	129.9	134.8	134.5
20	QORQIY	S08	88.9	88.8	91.1	91.2	130.9	130.2	135.4	135.3	137.8	138.7	135.9	135.7
21	REPGIE	S27	87.7	87.7	92.3	92.3	138.7	138.7	137.3	137.3	128.9	129.0	135.0	134.0
22	RAKZAG	S26	87.7	88.1	92.1	92.1	135.8	135.8	136.0	135.1	132.0	132.0	136.3	136.8
23	XOPWEF	S07	89.2	88.7	91.2	90.8	134.6	134.5	135.1	135.7	134.6	134.2	135.6	135.6
24	XOPWEF01	S07	88.6	88.6	91.4	91.4	133.6	133.6	135.3	135.3	135.0	135.0	136.1	136.1
25	XUFMER[b]	S28	88.8	88.5	90.5	92.3	135.1	135.8	134.6	134.7	132.7	133.7	136.9	136.6
26			88.2	88.1	92.0	91.6	135.3	134.1	136.1	135.7	133.1	133.9	136.1	135.6
27			88.1	88.0	92.3	91.5	134.8	134.3	135.9	135.0	133.6	133.3	136.9	135.9
28	WECCIS	S30	88.7	88.7	91.3	91.2	131.0	131.0	134.0	134.0	138.0	138.0	137.3	137.3
29	WECCAK	S29	88.7	88.7	91.2	91.2	131.0	131.0	134.0	134.0	138.0	138.0	137.3	137.3
Average			88.304		91.661		135.267		135.984		133.042		135.669	
Standard Deviation			0.609		0.631		3.848		1.150		4.356		1.007	

[a)/b)] The asymmetric unit is composed by two and three independent molecules, respectively.

The structures of the molecules in this series of squaramides are sketched in Figure 26 and Figure 27 with their CSD Refcodes and corresponding numbering scheme adopted.

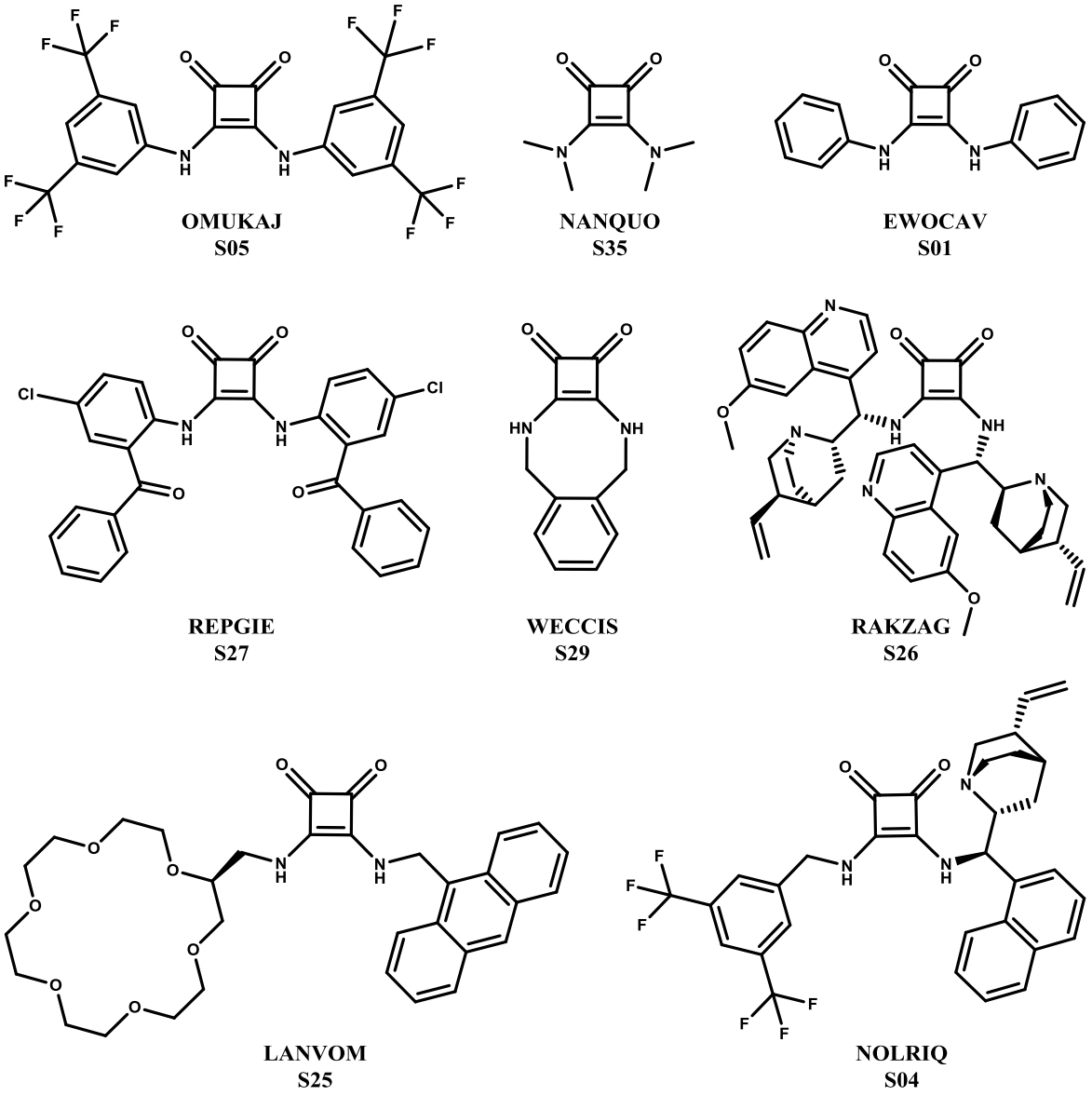

Figure 26 – Squaramides compounds whose single crystal X-ray diffraction structures were deposited with CSD

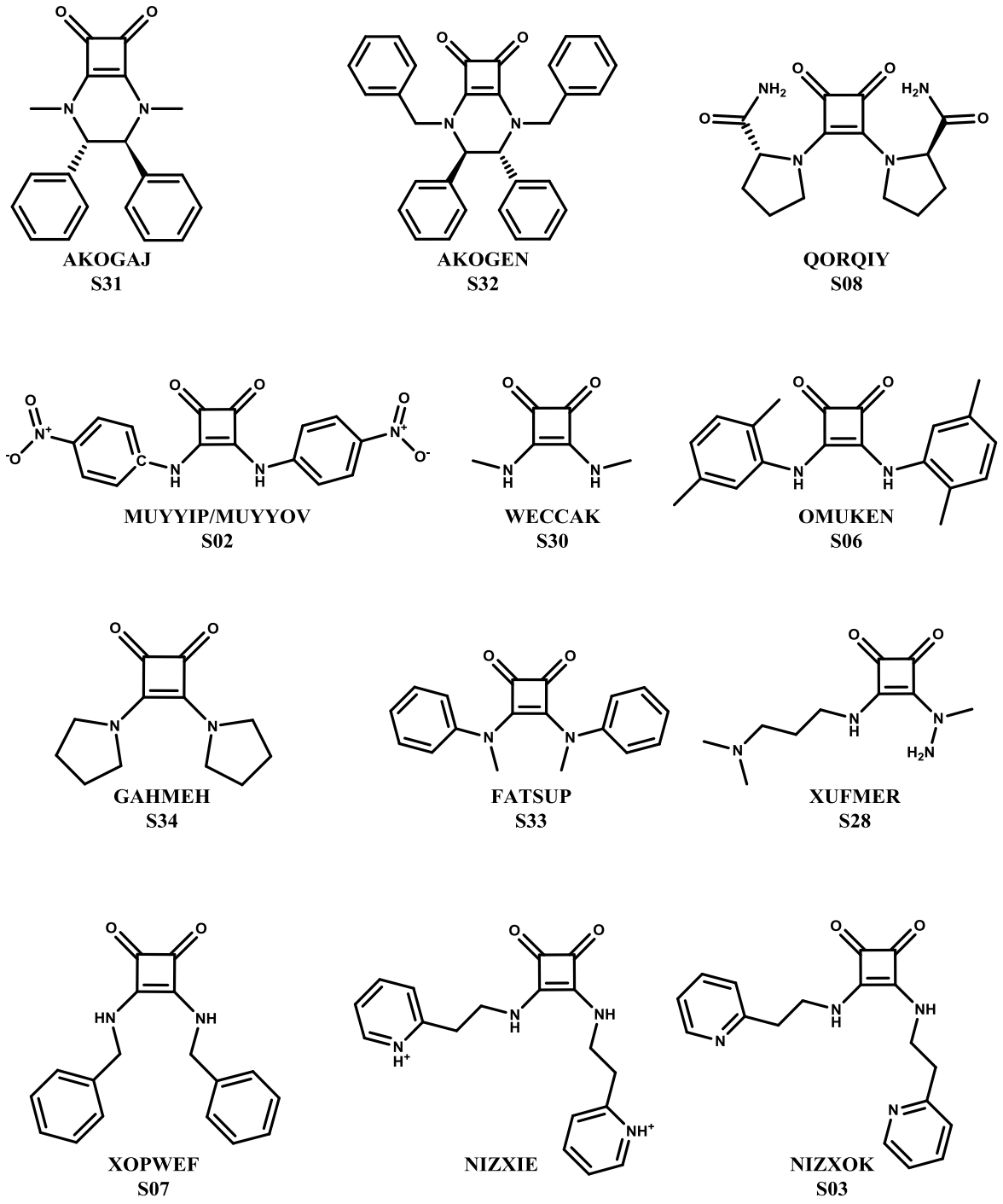

Figure 27 – Squaramides compounds whose single crystal X-ray diffraction structures were deposited with CSD (continuation).

In the theoretical study reported in this thesis, the GAFF was used to describe the squaramide receptors. This force field is compatible with both the restrained electrostatic potential (RESP) charge model (102) and the semi-empirical Austin model 1 bond charge corrections

(AM1-BCC) atomic charges.(103-104) Therefore, both charge models were used in the development of the specific force field parameters for the squaramide moiety.

To obtain the AM1-BCC atomic charges, the Protein Database (pdb) file of each selected receptor was directly used as input file in the *antechamber* package, as implemented in Ambertools13 (105) to generate a Tripos MOL2 molecule model (mol2) file with the atomic coordinates, AM1-BCC atomic charges and GAFF atom types, assigned according to intramolecular connectivities. The AM1-BCC charges were calculated from structures optimized with the *SQM* package.(106)

The RESP charges, in agreement with the GAFF paper methodology, were calculated with the squaramide molecule previously optimized at the HF/6-31G* level using *Gaussian 09*.(107) Subsequently, the electrostatic potential was obtained through a single point calculation at the same theory level using four concentric layers for each atom and six density points in each layer (*Gaussian 09* internal options: Pop=MK IOp(6/33=2, 6/41=4, 6/42=6)). The atomic charges were then calculated for a single molecular conformation by two successive RESP fittings, leading to a mol2 file containing the atomic coordinates, RESP charges and atom types.

Afterwards, a force field modification (frcmod) file was created for each molecule, with the missing force field parameters, using the *parmchk* program within Ambertools13.(105) The GAFF and frcmod parameter files (read in this order), and the mol2 file (with AM1-BCC or RESP atomic charges) were loaded into t*LEaP* and a topology and coordinate files were generated for each squaramide molecule. The structures of 18 squaramides were energy minimized by MM with the default parameters from GAFF and with the two charge models. The bond lengths are listed in Table 10 and Table 11.

Table 10 – Bond lengths (Å) of MM optimized squaramides using AM1-BCC charges and GAFF default parameters

Query	Squaramide	CSD Refcode	Bond							
			c-c	cc-cd	c-cc	c-cd	c-o	c-o	cc-nh	cd-nh
1	S01	EWOCAV	1.563	1.367	1.475	1.476	1.219	1.220	1.377	1.376
2	S02	MUYYIP	1.561	1.369	1.475	1.476	1.219	1.219	1.379	1.379
3	S03	NIZXOK	1.565	1.367	1.476	1.475	1.222	1.221	1.375	1.376
4	S04	NOLRIQ	1.564	1.365	1.475	1.474	1.220	1.220	1.370	1.375
5	S05	OMUKAJ	1.561	1.370	1.476	1.477	1.218	1.218	1.378	1.378
6	S06	OMUKEN	1.562	1.369	1.477	1.476	1.219	1.220	1.377	1.378
7	S07	XOPWEF	1.565	1.367	1.471	1.475	1.220	1.221	1.376	1.375
8	S08	QORQIY	1.563	1.372	1.472	1.471	1.222	1.222	1.378	1.379
9	S25	LANVOM	1.568	1.363	1.473	1.474	1.220	1.221	1.370	1.371
10	S31	AKOGAJ	1.585	1.339	1.470	1.470	1.220	1.220	1.364	1.362
11	S32	AKOGEN	1.579	1.345	1.470	1.469	1.220	1.220	1.364	1.366
12	S33	FATSUP	1.558	1.377	1.472	1.473	1.221	1.221	1.383	1.382
13	S34	GAHMEH	1.562	1.374	1.473	1.472	1.221	1.222	1.377	1.378
14	S35	NANQUO	1.561	1.375	1.473	1.474	1.221	1.220	1.379	1.379
15	S26	REPGIE	1.562	1.367	1.475	1.475	1.219	1.220	1.377	1.377
16	S27	RAKZAG	1.566	1.365	1.476	1.476	1.223	1.222	1.373	1.374
17	S29	WECCIS	1.564	1.372	1.470	1.472	1.220	1.220	1.376	1.376
18	S30	WECCAK	1.564	1.372	1.470	1.472	1.220	1.220	1.376	1.376
Average			**1.565**	**1.366**	**1.474**		**1.220**		**1.375**	
Standard Deviation			**0.006**	**0.009**	**0.002**		**0.001**		**0.005**	

Table 11 – Bond lengths (Å) of MM optimized squaramides using RESP charges and GAFF default parameters.

Query	Squaramide	CSD Refcode	Bond							
			c-c	cc-cd	c-cc	c-cd	c-o	c-o	cc-nh	cd-nh
1	S01	EWOCAV	1.560	1.372	1.472	1.471	1.219	1.217	1.378	1.378
2	S02	MUYYIP	1.560	1.371	1.471	1.471	1.217	1.217	1.378	1.378
3	S03	NIZXOK	1.565	1.370	1.473	1.473	1.221	1.220	1.378	1.378
4	S04	NOLRIQ	1.565	1.368	1.469	1.472	1.220	1.221	1.373	1.375
5	S05	OMUKAJ	1.559	1.372	1.470	1.471	1.217	1.218	1.379	1.378
6	S06	OMUKEN	1.563	1.369	1.472	1.473	1.219	1.219	1.376	1.376
7	S07	XOPWEF	1.564	1.369	1.471	1.471	1.221	1.221	1.376	1.376
8	S08	QORQIY	1.568	1.372	1.467	1.467	1.222	1.221	1.374	1.373
9	S25	LANVOM	1.572	1.366	1.463	1.469	1.218	1.219	1.366	1.367
10	S31	AKOGAJ	1.576	1.347	1.465	1.463	1.218	1.218	1.362	1.360
11	S32	AKOGEN	1.577	1.346	1.462	1.462	1.218	1.217	1.360	1.360
12	S33	FATSUP	1.563	1.375	1.470	1.468	1.219	1.220	1.378	1.378
13	S34	GAHMEH	1.567	1.374	1.467	1.466	1.219	1.219	1.372	1.373
14	S35	NANQUO	1.564	1.375	1.467	1.467	1.220	1.219	1.375	1.375
15	S26	REPGIE	1.564	1.368	1.471	1.471	1.219	1.218	1.376	1.375
16	S27	RAKZAG	1.568	1.368	1.472	1.471	1.223	1.224	1.374	1.374
17	S29	WECCIS	1.566	1.371	1.466	1.465	1.218	1.219	1.373	1.373
18	S30	WECCAK	1.566	1.369	1.471	1.472	1.221	1.221	1.375	1.374
Average			**1.566**	**1.368**	**1.469**		**1.219**		**1.373**	
Standard Deviation			**0.005**	**0.008**	**0.003**		**0.002**		**0.005**	

As further discussed, it was necessary to develop specific bond lengths and bond angles parameters to accurately describe the geometry of the squaramide moiety found in the crystal structures. The new parameterization was accomplished through the creation of new atom types (***dc*** and ***db***) for some atoms. The van der Walls parameters of these atom types was the same that *antechamber* assigned by default. These new atom types were necessary because the original atom types (**c** and **cc/cd**) are also assigned to other atoms in the same molecule, with similar atomic intramolecular connectivities. In these circumstances, the absence of the new atoms types would preclude the correct description of the entire molecule. The newly assigned ***db*** and ***dc*** atom types and are depicted in Figure 28, together with the default GAFF atom types for the squaramide moiety.

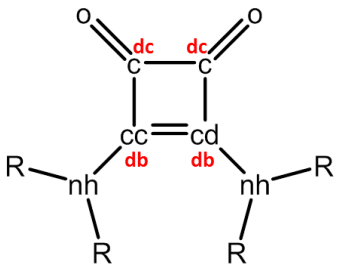

Figure 28 – Schematic representation of squaramide moiety with the atom types: in black the default GAFF atom types; in red the new atom types created for the specific parameterization.

The force constants for the ideal bond lengths and ideal bond angles were calculated in agreement with the equations in the GAFF paper. (108-109) Similarly to the previous MMFF94 force field (110), GAFF applies an empirical rule to estimate the missing parameters of bond length force constants using the following equation:

$$K_r = K_{ij} \left(\frac{1}{r_{ij}}\right)^m \qquad \text{Eq. 10}$$

where K_r is the calculated force constant; r_{ij} is the actual bond length; K_{ij} is the empirical parameter of element *i* and *j*; and *m* is the power order of GAFF. GAFF developers tested Eq. 10 with different *m* values and based on their results a mean value of 4.5 for *m* was chosen. The K_{ij} values are directly obtained from the *ln* K_{ij} values reported in the original GAFF reference and are listed in Table 9 for C/C, C/N and C/O bonds.(108)

Table 12 – Parameters to estimate the bond stretching force constants in GAFF for bonds involving C/C, C/N and C/O atom pairs. (108)

i	j	r_{ij}^{ref}	ln K_{ij}
C	C	1.526	7.643
C	N	1.470	7.504
C	O	1.440	7.347

GAFF also applies empirical formulas to estimate the bond angle force constants by means of the following equations:

$$K_{ijk}^{\theta} = 143.9\, Z_i C_j Z_k \left(r_{ij}^{eq} + r_{jk}^{eq}\right)^{-1} \left(\theta_{ijk}^{eq}\right)^{-\frac{1}{2}} \exp(-2D) \qquad \text{Eq. 11}$$

$$D = \frac{\left(r_{ij}^{eq} - r_{jk}^{eq}\right)^2}{\left(r_{ij}^{eq} + r_{jk}^{eq}\right)^2} \qquad \text{Eq. 12}$$

where, Z_i, C_j and Z_k are empirical parameters for the first, second and third atoms in an angle, in this order. The r_{ij}^{eq} and r_{jk}^{eq} are the equilibrium bond lengths and θ_{ijk}^{eq} is the equilibrium bond angle. Z and C parameters for C, N, O are listed in Table 13.(108)

Table 13 – Parameters to estimate the bond angle bending force constants in GAFF.(108)

Element	C	Z
C	1.339	1.183
N	1.300	1.212
O	1.249	1.219

In the original GAFF force field parameterization, the equilibrium bond lengths and angles were obtained mainly from crystal data complemented with gas phase structures optimized at the MP2/6-31G* level of theory. Herein, the r_{ij} and θ_{ijk}^{eq} are the mean values calculated with all single crystal X-ray diffraction data listed in Table 8 and Table 9. The newly developed r_{ij} and θ_{ijk}^{eq} parameters with corresponding force constants are gathered in Table 14 and Table 15.

Table 14 – New force field parameters for the bond lengths of the squaramide moiety.

Parameters	Bond							
	db-db	dc-dc	db-dc	dc-o	dc-n	ca-nh[a]	nh-hn[a]	c3-nh[a]
r_{ij} (Å)	1.410	1.496	1.469	1.225	1.329	1.364	1.014	1.458
K_r (kcal/mol Å²)	444.454	340.503	368.455	627.108	504.758	449.000	401.200	332.700

[a] Parameters taken directly from GAFF.

Table 15 – New force field parameters for the bond angles of the squaramide moiety.

Parameter	Angle								
	dc-dc-db	dc-db-db	db-db-nh	dc-db-nh	o-dc-dc	o-dc-db	db-nh-ca	db-nh-c3	db-nh-hn
θ_{ijk}^{eq} (°)	88.30	91.67	133.04	135.27	135.67	135.98	129.91	121.18	117.16
K_r (kcal/mol rad²)	73.25	73.99	66.08	63.94	65.06	65.86	64.54	64.32	49.95

[a] Parameters taken directly from GAFF.

New topology files with modified GAFF parameters were generated for all X-ray structures of squaramides, and their structures were re–optimized in gas-phase until convergence was achieved. The entire parameterization process was performed with standard and modified parameters, as is depicted in the flow chart present in Figure 31.

In order to ascertain if the electronic structure of squaramides moiety is determined by packing effects including hydrogen bonds (see Figure 15), the crystal structures listed in Table 10, except **S08** and **S25**, were optimized in the gas-phase at the B3LYP/6-31G*, B3LYP/6-311G** and MP2/6-31G* level of theory. These density functional theory (DFT) and MP2 calculations were also extended to a new series of squaramides, sketched in Figure 29 and Figure 30, as part of our collaboration with the Prof. Gale's group and in line with the *in silico* studies reported in this thesis. These molecules were designated from S09 to S24 (72) and their starting geometries were generated from the crystal structure of **S01** by means of appropriate chemical manipulation. All energy optimizations were carried out with *Gaussian 09* and the computed distances are summarized below.

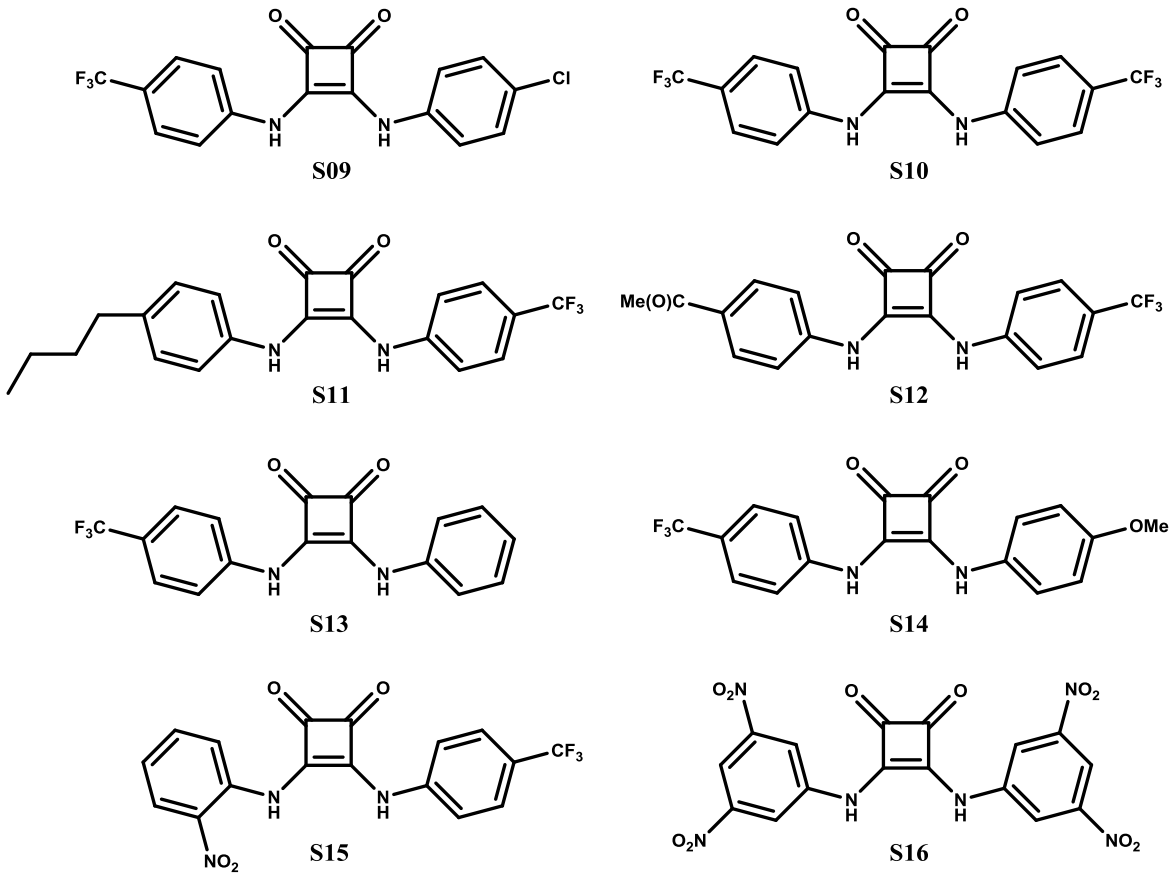

Figure 29 – Squaramide series from the collaboration project with Prof. Phil A. Gale's group.

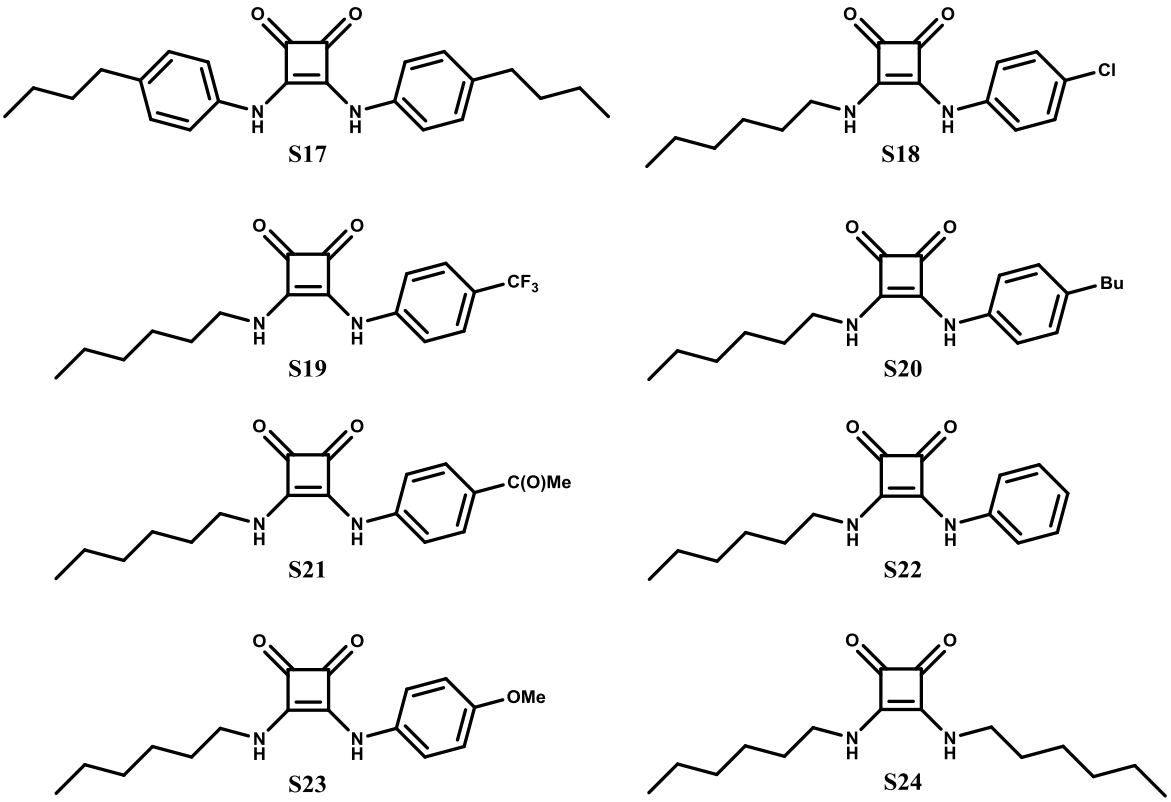

Figure 30 – Squaramide series from the collaboration project with Prof. Phil A. Gale's group (continuation).

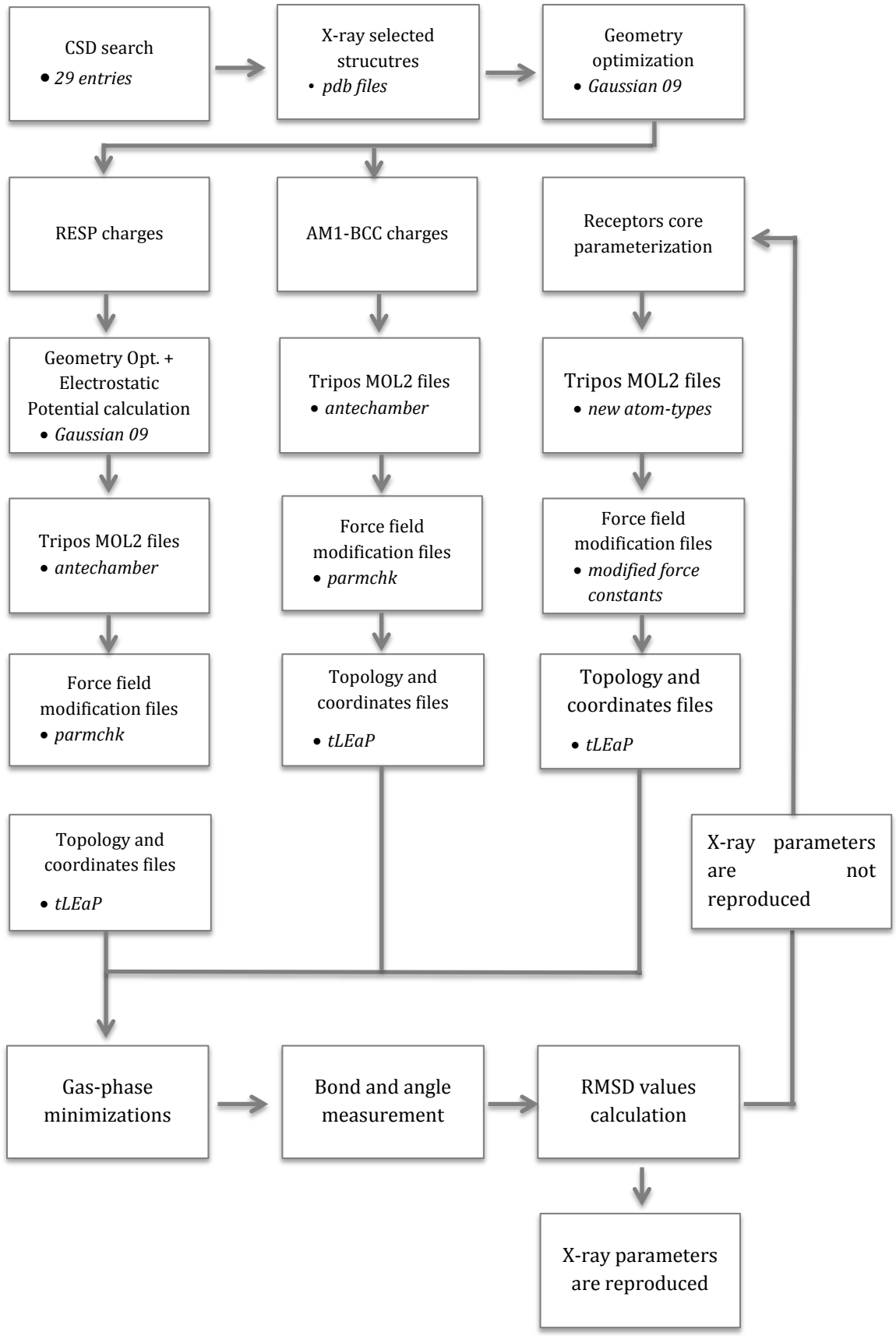

Figure 31 – Diagram for the receptor preparation before conformational analyses and MD simulations.

Results and Discussion

A comparison between the average bond lengths in the crystal structures and those obtained by molecular mechanics optimization, using RESP and AM1-BCC atomic charges and GAFF default parameters for the squaramides unit, is presented in Table 16. Inside of the core, the *cc-cd* bond length is slightly shorter than the crystal ones by 0.04 Å, while the *c-c* distances increase by 0.07 Å for both atomic charge schemes. Therefore, we decided to develop specific bond terms for this structural motif.

Table 16 – Comparison between the average bond lengths (Å) from X-ray structures and MM optimized structures with GAFF default parameters and AM1-BCC and RESP charges.

		Bond				
		c-c	*cc-cd*	*c-cc/c-cd*	*c-o*	*cc-nh/cd-nh*
X-ray	Average	1.496	1.410	1.469	1.225	1.329
	Std. Dev.	0.015	0.018	0.010	0.009	0.012
MM (AM1-BCC)	Average	1.565	1.366	1.474	1.220	1.375
	Std. Dev.	0.006	0.009	0.002	0.001	0.005
MM (RESP)	Average	1.566	1.368	1.469	1.219	1.373
	Std. Dev.	0.005	0.008	0.003	0.002	0.005

A large series of molecules composed of 34 squaramides including the crystal structures were optimized by DFT, using the functional B3LYP and the basis sets 6-31G* and 6-311+G**, and at the MP2/6-31G* theory level. The corresponding bond lengths are listed in Table 17, Table 18 and Table 19, respectively. The MP2/6-31G* optimizations were performed taking into account that the GAFF force field parameters were originally derived from the structures calculated at this theory level. The average bond lengths calculated by the three quantum approaches for the squaramide moiety follows an equivalent trend as the observed for MM optimized structures with GAFF default parameters (see Table 20). Indeed, the bond lengths within the squaramide core seem to be almost independent from the theory level used and the basis set size.

Table 17 – Bond lengths (Å) of the selected squaramides optimized at the B3LYP/6-31G* level.

Query	Squaramide	CSD Refcode	Bond							
			c-c	cc-cd	c-cc	c-cd	c-o	c-o	cc-nh	cd-nh
1	S01	EWOCAV	1.532	1.406	1.493	1.493	1.213	1.213	1.355	1.355
2	S02	MUYYIP	1.536	1.402	1.497	1.497	1.209	1.209	1.358	1.359
3	S03	NIZXOK	1.539	1.400	1.488	1.488	1.217	1.217	1.351	1.351
4	S04	NOLRIQ	1.535	1.399	1.486	1.484	1.219	1.216	1.346	1.353
5	S05	OMUKAJ	1.536	1.400	1.496	1.496	1.210	1.210	1.358	1.358
6	S06	OMUKEN	1.534	1.406	1.493	1.493	1.212	1.212	1.356	1.356
7	S07	XOPWEF	1.538	1.400	1.486	1.487	1.218	1.216	1.350	1.349
8	S08	QORQIY	1.516	1.424	1.483	1.483	1.226	1.226	1.340	1.340
9	S25	LANVOM	1.533	1.407	1.484	1.481	1.220	1.224	1.341	1.343
10	S31	AKOGAJ	1.565	1.380	1.487	1.487	1.213	1.212	1.351	1.351
11	S32	AKOGEN	1.558	1.385	1.485	1.485	1.215	1.215	1.348	1.348
12	S33	FATSUP	1.535	1.412	1.493	1.493	1.214	1.214	1.357	1.357
13	S34	GAHMEH	1.528	1.417	1.491	1.491	1.216	1.216	1.346	1.346
14	S35	NANQUO	1.525	1.416	1.491	1.491	1.217	1.217	1.351	1.351
15	S09	-	1.533	1.403	1.495	1.492	1.212	1.212	1.355	1.358
16	S10	-	1.534	1.402	1.495	1.495	1.211	1.211	1.357	1.357
17	S11	-	1.534	1.404	1.490	1.496	1.213	1.211	1.360	1.353
18	S12	-	1.535	1.403	1.494	1.496	1.211	1.210	1.357	1.357
19	S13	-	1.534	1.403	1.497	1.491	1.211	1.212	1.353	1.359
20	S14	-	1.533	1.405	1.496	1.488	1.212	1.213	1.351	1.360
21	S15	-	1.536	1.404	1.489	1.499	1.212	1.211	1.360	1.352
22	S16	-	1.538	1.398	1.497	1.497	1.208	1.208	1.360	1.360
23	S17	-	1.533	1.405	1.492	1.493	1.213	1.213	1.354	1.355
24	S18	-	1.537	1.401	1.485	1.497	1.214	1.214	1.344	1.361
25	S19	-	1.537	1.401	1.486	1.496	1.213	1.214	1.343	1.363
26	S20	-	1.535	1.403	1.482	1.498	1.216	1.214	1.345	1.359
27	S21	-	1.537	1.402	1.496	1.487	1.213	1.213	1.363	1.341
28	S22	-	1.535	1.402	1.498	1.484	1.214	1.214	1.359	1.345
29	S23	-	1.536	1.403	1.482	1.498	1.215	1.214	1.348	1.356
30	S24	-	1.539	1.399	1.488	1.488	1.216	1.216	1.351	1.350
31	S26	REPGIE	1.530	1.408	1.493	1.493	1.215	1.214	1.354	1.354
32	S27	RAKZAG	1.522	1.410	1.478	1.478	1.224	1.224	1.338	1.339
33	S29	WECCIS	1.530	1.408	1.493	1.493	1.215	1.214	1.354	1.354
34	S30	WECCAK	1.538	1.400	1.487	1.487	1.216	1.217	1.348	1.348
Average			**1.535**	**1.403**	**1.491**		**1.214**		**1.353**	
Standard Deviation			**0.008**	**0.008**	**0.005**		**0.004**		**0.006**	

Table 18 – Bond lengths (Å) of the selected squaramides optimized at the B3LYP/6-311+G**.

Query	Designation	CSD Refcode	Bond							
			c-c	cc-cd	c-cc	c-cd	c-o	c-o	cc-n	cd-n
1	S01	EWOCAV	1.532	1.402	1.491	1.491	1.206	1.206	1.353	1.353
2	S02	MUYYIP	1.534	1.399	1.495	1.495	1.203	1.203	1.357	1.358
3	S03	NIZXOK	1.535	1.399	1.485	1.486	1.212	1.210	1.346	1.345
4	S04	NOLRIQ	1.530	1.399	1.484	1.481	1.213	1.211	1.341	1.347
5	S05	OMUKAJ	1.535	1.399	1.495	1.495	1.203	1.202	1.356	1.357
6	S06	OMUKEN	1.531	1.403	1.492	1.491	1.206	1.206	1.355	1.354
7	S07	XOPWEF	1.532	1.399	1.485	1.484	1.211	1.211	1.346	1.346
8	S08	QORQIY	1.513	1.421	1.481	1.481	1.219	1.219	1.339	1.339
9	S25	LANVOM	1.527	1.407	1.484	1.480	1.214	1.218	1.339	1.340
10	S31	AKOGAJ	1.559	1.382	1.485	1.486	1.207	1.207	1.347	1.348
11	S32	AKOGEN	1.551	1.385	1.483	1.483	1.210	1.210	1.345	1.345
12	S33	FATSUP	1.534	1.412	1.491	1.491	1.208	1.208	1.354	1.354
13	S34	GAHMEH	1.522	1.418	1.489	1.489	1.211	1.211	1.343	1.343
14	S35	NANQUO	1.521	1.416	1.490	1.489	1.212	1.212	1.347	1.348
15	S09	-	1.532	1.401	1.494	1.491	1.205	1.206	1.353	1.357
16	S10	-	1.534	1.400	1.494	1.494	1.204	1.204	1.356	1.356
17	S11	-	1.532	1.403	1.488	1.496	1.206	1.205	1.358	1.349
18	S12	-	1.534	1.401	1.492	1.495	1.204	1.204	1.357	1.355
19	S13	-	1.532	1.401	1.496	1.489	1.204	1.206	1.351	1.358
20	S14	-	1.532	1.402	1.496	1.487	1.205	1.207	1.348	1.359
21	S15	-	1.534	1.401	1.489	1.498	1.206	1.203	1.358	1.350
22	S16	-	1.536	1.396	1.496	1.496	1.201	1.201	1.359	1.359
23	S17	-	1.533	1.403	1.490	1.491	1.206	1.207	1.353	1.353
24	S18	-	1.534	1.401	1.484	1.494	1.208	1.207	1.341	1.359
25	S19	-	1.534	1.400	1.486	1.493	1.207	1.207	1.339	1.361
26	S20	-	1.533	1.400	1.482	1.495	1.209	1.208	1.343	1.356
27	S21	-	1.533	1.400	1.493	1.486	1.208	1.207	1.361	1.339
28	S22	-	1.533	1.400	1.496	1.482	1.208	1.208	1.357	1.342
29	S23	-	1.532	1.401	1.480	1.496	1.210	1.208	1.343	1.354
30	S24	-	1.535	1.400	1.486	1.486	1.211	1.211	1.345	1.345
31	S26	REPGIE	1.530	1.404	1.492	1.492	1.207	1.207	1.352	1.352
32	S27	RAKZAG	1.519	1.407	1.477	1.477	1.219	1.218	1.336	1.337
33	S29	WECCIS	1.540	1.396	1.484	1.484	1.208	1.208	1.344	1.344
34	S30	WECCAK	1.535	1.390	1.485	1.486	1.211	1.210	1.346	1.345
Average			**1.533**	**1.401**	**1.489**		**1.208**		**1.350**	
Standard Deviation			**0.008**	**0.008**	**0.005**		**0.004**		**0.007**	

Table 19 – Bond lengths (Å) of the selected squaramides optimized at the MP2/6-31G* level.

Query	Designation	CSD Refcode	Bond							
			c-c	cc-cd	c-cc	c-cd	c-o	c-o	cc-n	cd-n
1	S01	EWOCAV	1.533	1.409	1.491	1.491	1.223	1.223	1.354	1.354
2	S02	MUYYIP	1.535	1.406	1.494	1.494	1.221	1.221	1.356	1.356
3	S03	NIZXOK	1.534	1.404	1.484	1.485	1.228	1.228	1.351	1.350
4	S04	NOLRIQ	-	-	-	-	-	-	-	-
5	S05	OMUKAJ	1.535	1.405	1.493	1.493	1.221	1.221	1.357	1.357
6	S06	OMUKEN	1.534	1.410	1.491	1.491	1.224	1.223	1.354	1.354
7	S07	XOPWEF	1.534	1.405	1.485	1.485	1.227	1.227	1.352	1.351
8	S08	QORQIY	1.516	1.426	1.482	1.481	1.235	1.235	1.336	1.336
9	S25	LANVOM	-	-	-	-	-	-	-	-
10	S31	AKOGAJ	1.567	1.387	1.485	1.485	1.222	1.222	1.354	1.352
11	S32	AKOGEN	-	-	-	-	-	-	-	-
12	S33	FATSUP	1.546	1.414	1.486	1.486	1.225	1.225	1.349	1.348
13	S34	GAHMEH	1.527	1.420	1.487	1.487	1.227	1.227	1.344	1.344
14	S35	NANQUO	1.539	1.409	1.488	1.488	1.224	1.225	1.356	1.356
15	S09	-	1.533	1.408	1.493	1.491	1.222	1.223	1.354	1.356
16	S10	-	1.535	1.408	1.493	1.493	1.222	1.222	1.355	1.355
17	S11	-	1.533	1.408	1.489	1.494	1.224	1.221	1.358	1.352
18	S12	-	1.534	1.407	1.492	1.494	1.222	1.221	1.356	1.355
19	S13	-	1.533	1.408	1.494	1.490	1.221	1.223	1.352	1.358
20	S14	-	1.533	1.408	1.495	1.488	1.222	1.224	1.350	1.358
21	S15	-	1.533	1.409	1.490	1.495	1.223	1.221	1.356	1.351
22	S16	-	1.540	1.403	1.497	1.497	1.218	1.218	1.359	1.359
23	S17	-	1.533	1.410	1.491	1.491	1.223	1.222	1.354	1.354
24	S18	-	1.531	1.408	1.481	1.496	1.226	1.224	1.341	1.359
25	S19	-	1.535	1.405	1.480	1.499	1.224	1.223	1.348	1.359
26	S20	-	1.532	1.406	1.479	1.498	1.226	1.224	1.345	1.357
27	S21	-	1.535	1.405	1.500	1.480	1.222	1.226	1.358	1.349
28	S22	-	1.533	1.408	1.480	1.498	1.225	1.224	1.344	1.357
29	S23	-	1.535	1.406	1.501	1.476	1.223	1.226	1.354	1.353
30	S24	-	1.535	1.403	1.485	1.485	1.226	1.226	1.350	1.350
31	S26	REPGIE	-	-	-	-	-	-	-	-
32	S27	RAKZAG	-	-	-	-	-	-	-	-
33	S29	WECCIS	-	-	-	-	-	-	-	-
34	S30	WECCAK	-	-	-	-	-	-	-	-
Average			**1.535**	**1.408**	**1.490**		**1.224**		**1.353**	
Standard Deviation			**0.008**	**0.006**	**0.006**		**0.003**		**0.005**	

Table 20 – Comparison between the bond lengths (Å) from MM optimizations with GAFF default parameters and quantum optimizations at B3LYP/6-31G*, B3LYP/6-311+G** and MP2/6-31G*.

		Bond				
		c-c	*cc-cd*	*c-cc/c-cd*	*c-o*	*cc-nh/cd-nh*
MM (AM1-BCC)	Average	1.565	1.366	1.474	1.220	1.375
	Std. Dev.	0.006	0.009	0.002	0.001	0.005
MM (RESP)	Average	1.566	1.368	1.469	1.219	1.373
	Std. Dev.	0.005	0.008	0.003	0.002	0.005
B3LYP/ 6-31G*	Average	1.535	1.403	1.491	1.214	1.353
	Std. Dev.	0.008	0.008	0.005	0.004	0.006
B3LYP/ 6-311+G**	Average	1.533	1.401	1.489	1.208	1.350
	Std. Dev.	0.008	0.008	0.005	0.004	0.007
MP2/ 6-31G*	Average	1.535	1.408	1.490	1.224	1.302
	Std. Dev.	0.008	0.006	0.006	0.003	0.365

Furthermore the quantum calculations also suggest that the bond lengths observed in the crystal structures are affected by packing effects including hydrogen bonding interactions. Indeed the analysis of the crystal packing of several single crystal X-ray structures shows that, in solid state, the squaramides compounds are self-assembled by cooperative N-H···O hydrogen bonds as illustrated for S01 in Figure 17. Further insights into this structural feature were obtained by the optimization, at B3LYP/6-311+G**, of a dimer and trimer composed of S30 molecules and organized in a head-to-tail arrangement. The optimized structures are shown in Figure 32 while the corresponding bond lengths are listed in Table 21.

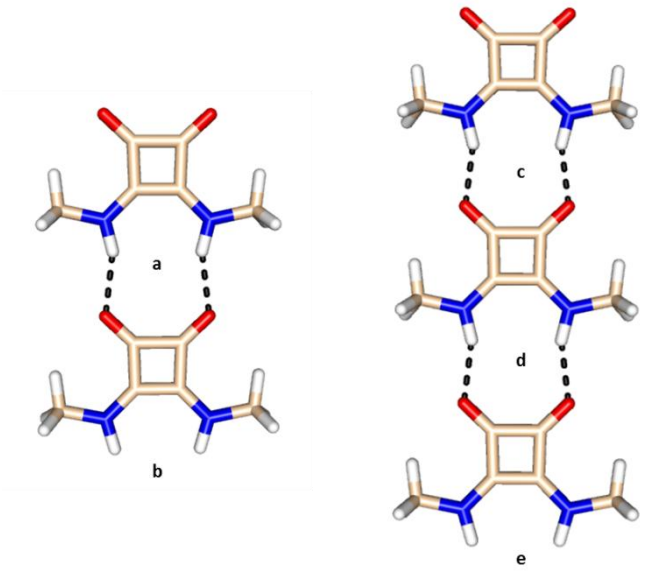

Figure 32 – DFT optimized structures (B3LYP/6-311+G** level) of S30 organized in dimer (a and b) or trimmer (c, d and e) structures. Carbon, oxygen, nitrogen and hydrogen atoms are represented in wheat, red, blue and white, respectively. Black dashes represent hydrogen bonds between monomers.

Table 21 – – Bond lengths (Å) for S30 arranged in dimer or trimmer assembles optimized at B3LYP/6-311+G**.

Monomer		Bond							
		c-c	**cc-cd**	**c-cc**	**c-cd**	**c-o**	**c-o**	**cc-nh**	**cd-nh**
Dimer	a	1.525	1.407	1.482	1.482	1.217	1.219	1.339	1.339
	b	1.515	1.409	1.477	1.477	1.217	1.217	1.338	1.338
Trimmer	c	1.524	1.410	1.481	1.481	1.217	1.217	1.338	1.338
	d	1.504	1.418	1.474	1.474	1.224	1.224	1.332	1.332
	e	1.512	1.412	1.476	1.476	1.219	1.219	1.336	1.336
X-ray		1.496	1.410	1.469		1.225		1.329	
		0.015	0.018	0.010		0.009		0.012	

In the dimer the optimized *c-c* bond length in molecule *b* (1.515 Å), with carbonyl groups directly involved in two N-H···O hydrogen bonds, becomes closer to the average X-ray bond length. On the other hand, in molecule *a*, this distance (1.525 Å) is similar to the calculated value for the single optimized monomer at the same theory level (1.533 Å). The optimized *cc-cd* distances in the isolated molecule, as well as in molecules *a* and *b,* exhibit identical values. In the trimer, the bond lengths dimensions in molecules *c* and *e* are identical to *a* and *b* molecules in the dimer, as would be expected. By contrast, the central molecule *d*, with carbonyl and amide groups forming hydrogen bonds, displays *c-c* and *cc-cd* bond lengths similar to the ones observed in the X-ray structures. In other words, all these calculations show that the dimensions of the squaramide moiety are affected by the hydrogen bonds established. Considering these findings and that in the membrane simulations the squaramides may interact with water molecules and phospholipids through the hydrogen bonds, we decided to parameterize the squaramides entity using single crystal X-ray diffraction data. The computed distances for MM optimized structures with bond terms parameters based on crystal data are listed in Table 22, for AM1-BCC charges, and in Table 23, for RESP charges. As would be expected, the new MM optimized structures reproduce more accurately the X-ray data, as corroborated by the Root-Mean-Square-Deviations[5] (RMSD) calculations, between the MM structures against the corresponding single crystal X-ray structures, given in Table 24 and Table 25 for both charge models. The bond lengths from the AM1-BCC and RESP optimizations are identical, as the AM1-BCC charge model was created to mirror the RESP charge model. However, the RMSD values for RESP charges are lower than the ones observed for AM1-BCC charges. Therefore, RESP charge model will be used on the following studies.(103)

[5] The RMSD is the measure of the average distance between the atoms of homologue structures. It is frequently used to measure the differences between values predicted and the values actually observed.

Table 22 – Bond lengths (Å) of the MM optimized squaramides using AM1-BCC charges and new force field parameters (this work).

Query	Squaramide	CSD Refcode	Bond							
			c-c	cc-cd	c-cc	c-cd	c-o	c-o	cc-nh	cd-nh
1	S01	EWOCAV	1.502	1.411	1.483	1.483	1.231	1.230	1.341	1.341
2	S02	MUYYIP	1.501	1.412	1.484	1.484	1.230	1.230	1.341	1.341
3	S03	NIZXOK	1.504	1.410	1.483	1.482	1.232	1.233	1.337	1.338
4	S04	NOLRIQ	1.505	1.407	1.482	1.480	1.231	1.231	1.335	1.338
5	S05	OMUKAJ	1.500	1.411	1.483	1.483	1.230	1.230	1.341	1.341
6	S06	OMUKEN	1.502	1.411	1.483	1.483	1.231	1.231	1.340	1.340
7	S07	XOPWEF	1.504	1.410	1.481	1.481	1.231	1.231	1.337	1.336
8	S08	QORQIY	1.501	1.419	1.478	1.478	1.234	1.233	1.342	1.342
9	S25	LANVOM	1.504	1.407	1.480	1.480	1.233	1.232	1.335	1.336
10	S31	AKOGAJ	1.515	1.391	1.478	1.478	1.231	1.232	1.332	1.332
11	S32	AKOGEN	1.515	1.389	1.477	1.477	1.231	1.231	1.331	1.332
12	S33	FATSUP	1.499	1.422	1.477	1.478	1.232	1.231	1.344	1.345
13	S34	GAHMEH	1.501	1.420	1.479	1.479	1.232	1.232	1.341	1.341
14	S35	NANQUO	1.501	1.420	1.480	1.480	1.231	1.232	1.343	1.343
15	S26	REPGIE	1.502	1.411	1.482	1.482	1.231	1.231	1.341	1.342
16	S27	RAKZAG	1.505	1.407	1.482	1.482	1.233	1.234	1.338	1.337
17	S29	WECCIS	1.499	1.424	1.479	1.479	1.231	1.231	1.342	1.343
18	S30	WECCAK	1.498	1.424	1.479	1.479	1.232	1.232	1.342	1.342
Average			**1.503**	**1.411**	**1.481**		**1.232**		**1.339**	
Standard Deviation			**0.005**	**0.009**	**0.002**		**0.001**		**0.004**	

Table 23 – Bond lengths (Å) of the MM optimized squaramides using RESP charges and new force field parameters (this work).

Entry	Designation	CSD Refcode	Bond							
			c-c	cc-cd	c-cc	c-cd	c-o	c-o	cc-nh	cd-nh
1	S01	EWOCAV	1.500	1.416	1.479	1.479	1.229	1.229	1.342	1.342
2	S02	MUYYIP	1.498	1.416	1.478	1.478	1.228	1.228	1.341	1.341
3	S03	NIZXOK	1.504	1.413	1.480	1.480	1.232	1.232	1.341	1.340
4	S04	NOLRIQ	1.504	1.410	1.475	1.480	1.231	1.232	1.337	1.338
5	S05	OMUKAJ	1.499	1.416	1.478	1.478	1.228	1.228	1.341	1.341
6	S06	OMUKEN	1.502	1.412	1.480	1.480	1.230	1.230	1.341	1.341
7	S07	XOPWEF	1.504	1.412	1.478	1.478	1.232	1.231	1.339	1.338
8	S08	QORQIY	1.506	1.418	1.473	1.473	1.232	1.232	1.338	1.338
9	S25	LANVOM	1.508	1.412	1.471	1.474	1.230	1.231	1.330	1.332
10	S31	AKOGAJ	1.517	1.386	1.469	1.469	1.230	1.229	1.327	1.327
11	S32	AKOGEN	1.519	1.384	1.469	1.469	1.229	1.228	1.325	1.325
12	S33	FATSUP	1.502	1.419	1.475	1.475	1.231	1.230	1.342	1.341
13	S34	GAHMEH	1.506	1.420	1.474	1.474	1.230	1.230	1.336	1.336
14	S35	NANQUO	1.503	1.420	1.473	1.473	1.231	1.231	1.338	1.338
15	S26	REPGIE	1.503	1.413	1.479	1.478	1.229	1.230	1.340	1.340
16	S27	RAKZAG	1.505	1.411	1.478	1.478	1.234	1.234	1.337	1.336
17	S29	WECCIS	1.500	1.422	1.473	1.473	1.231	1.231	1.340	1.340
18	S30	WECCAK	1.505	1.413	1.479	1.479	1.231	1.231	1.338	1.338
Average			**1.505**	**1.412**	**1.476**		**1.230**		**1.337**	
Standard Deviation			**0.005**	**0.010**	**0.004**		**0.002**		**0.005**	

Table 24 – RMSD calculated for structures optimized with AM1-BCC charges.

Entry	Designation	CSD Refcode	RMSD1[6]		RMSD2[7]	
			Specific atoms[9]	*Core*[9]	*Specific atoms*[9]	*Core*[9]
1	S01	EWOCAV	0.163	0.074	0.299	0.069
2	S02	MUYYIP	0.542	0.079	0.415	0.047
3	S03	NIZXOK	0.094	0.051	0.201	0.046
4	S04	NOLRIQ	2.515	0.095	0.984	0.059
5	S05	OMUKAJ	0.896	0.086	1.195	0.051
6	S06	OMUKEN	1.031	0.064	0.386	0.025
7	S07	XOPWEF	0.363	0.042	1.921	0.035
8	S08	QORQIY	0.719	0.045	0.768	0.072
9	S25	LANVOM	0.797	0.052	0.815	0.031
10	S31	AKOGAJ	0.300	0.046	0.273	0.039
11	S32	AKOGEN	0.978	0.130	0.632	0.020
12	S33	FATSUP	0.461	0.093	0.254	0.056
13	S34	GAHMEH	0.164	0.059	0.295	0.054
14	S35	NANQUO	0.234	0.044	0.313	0.063
15	S26	REPGIE	1.226	0.065	0.962	0.032
16	S27	RAKZAG	1.700	0.050	1.591	0.035
17	S29	WECCIS	0.047	0.038	0.039	0.038
18	S30	WECCAK	0.047	0.038	0.060	0.038
Average			**0.682**	**0.064**	**0.633**	**0.045**
Standard Deviation			**0.631**	**0.024**	**0.514**	**0.015**

Table 25 – RMSD calculated for structures optimized with RESP charges.

Entry	Designation	CSD Refcode	RMSD1[7]		RMSD2[8]	
			Specific atoms[9]	*Core*[9]	*Specific atoms*[9]	*Core*[9]
1	S01	EWOCAV	0.176	0.072	0.314	0.061
2	S02	MUYYIP	0.509	0.082	0.385	0.041
3	S03	NIZXOK	0.129	0.052	0.200	0.041
4	S04	NOLRIQ	1.930	0.077	1.941	0.064
5	S05	OMUKAJ	1.329	0.089	1.144	0.062
6	S06	OMUKEN	0.252	0.054	0.436	0.034
7	S07	XOPWEF	0.253	0.043	0.263	0.031
8	S08	QORQIY	0.674	0.042	0.703	0.058
9	S25	LANVOM	0.744	0.061	0.700	0.032
10	S31	AKOGAJ	0.346	0.176	0.256	0.033
11	S32	AKOGEN	0.987	0.173	1.185	0.044
12	S33	FATSUP	0.375	0.093	0.183	0.060
13	S34	GAHMEH	0.114	0.059	0.213	0.047
14	S35	NANQUO	0.212	0.041	0.286	0.054
15	S26	REPGIE	1.240	0.070	0.931	0.037
16	S27	RAKZAG	0.640	0.054	0.596	0.028
17	S29	WECCIS	0.529	0.038	0.063	0.033
18	S30	WECCAK	0.053	0.038	0.063	0.033
Average			**0.583**	**0.073**	**0.548**	**0.044**
Standard Deviation			**0.491**	**0.040**	**0.475**	**0.012**

[6] RMSD values of the X-ray structures against the MM minimized structures using GAFF default parameters.
[7] RMSD values of the X-ray structures against the MM minimized structures using x-ray parameters.
[8] Structures without hydrogen atoms.

2.2. Conformational analyses

2.2.1. *Conformational analysis of the free receptors*

The theoretical studies performed in a POPC bilayer with squaramides S01, S09, S10, S19 and S20 reported in Chapter 3 were preceded by conformational analyses of the free squaramides as well as of their chloride complexes, as follows.

Methodology

RESP charges were initially calculated for the five squaramides with single conformation as previously mentioned. Subsequently, in order to obtain RESP charges less dependent on molecular conformation or orientation, S01, S09, S10 S19 and S20 were subjected to a conformational analysis using Low-MODe (*LMOD*) optimization method with exception of S10. The *LMOD* conformational search procedure is based on small perturbations of the systems in order to explore its conformational space and directly calculates the modes, using them to improve Monte Carlo sampling. The *LMOD* procedure employs the *XMIN* algorithm for energy relaxation and minimization: the initial molecular structure energy is minimized, the system is continuously perturbed and the new minimum-energy conformations are saved in a conflib file.(111-114)

The conformational analysis of S10 was carried out *via* MD quenched run, in the gas phase, at 1000 K for 1 ns and using a 1 fs time step. This high temperature allowed a stochastic search of the conformational space and surmount of the energetic barriers. Frames were saved every 0.1 ps leading to a trajectory file composed of 10000 structures, which were further full MM minimized until the convergence criteria of 0.0001 kcal/mol was attained.

Subsequently, the 10000 frames were sorted by energy and four *anti/anti* conformations with different torsion angles were selected for S09, S10, S19 and S20. For S01 just three conformations with substantially different torsion angles centred at C-N bonds were found. Only *anti/anti* conformations were selected taking into account that this is the conformation required for the anion recognition as evident from the crystal structures of anion squaramide complexes deposited with CSD (see Figure 15).(90) These conformations were then selected for HF/6-31G* optimizations followed by Electrostatic Potential calculations. Using the *espgen* tool (105), the individual electrostatic potential (ESP) for the individual conformations of each squaramide was extracted from the corresponding *Gaussian 09* output

file, and were concatenated and further used to generate the input files for the subsequent two-stage Restrained Electrostatic Potential fittings. This procedure was performed with the *resp* program from Ambertools13 (105) and illustrated in Figure 33. The multi-RESP charges for S01-S20, together with the corresponding atom types are given in Table 26, Table 27, Table 28, Table 29 and Table 30, while the corresponding atomic numbering scheme adopted is shown in Figure 34.

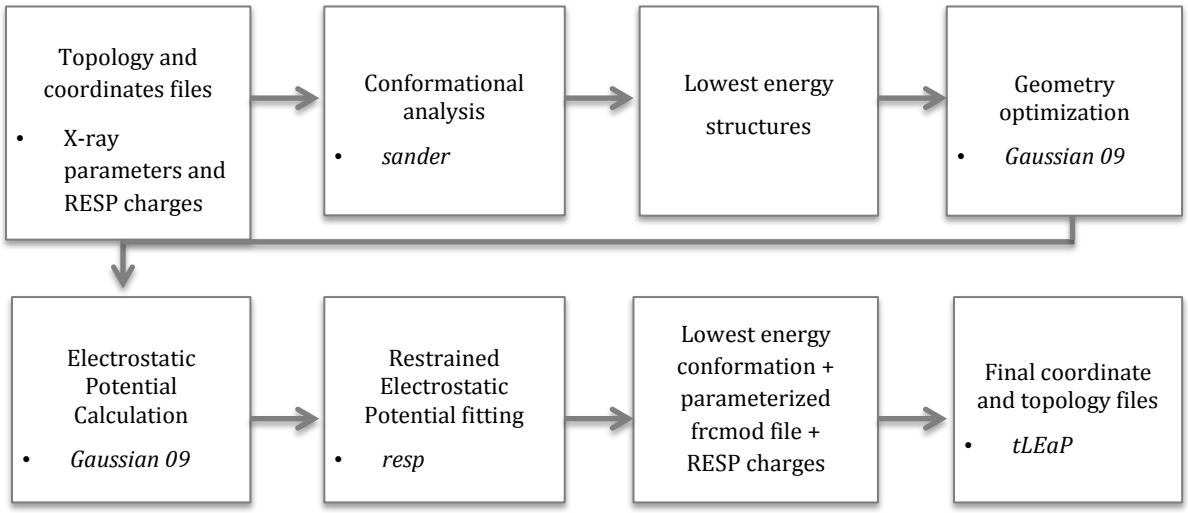

Figure 33 – Diagram for conformational analysis of the free squaramides.

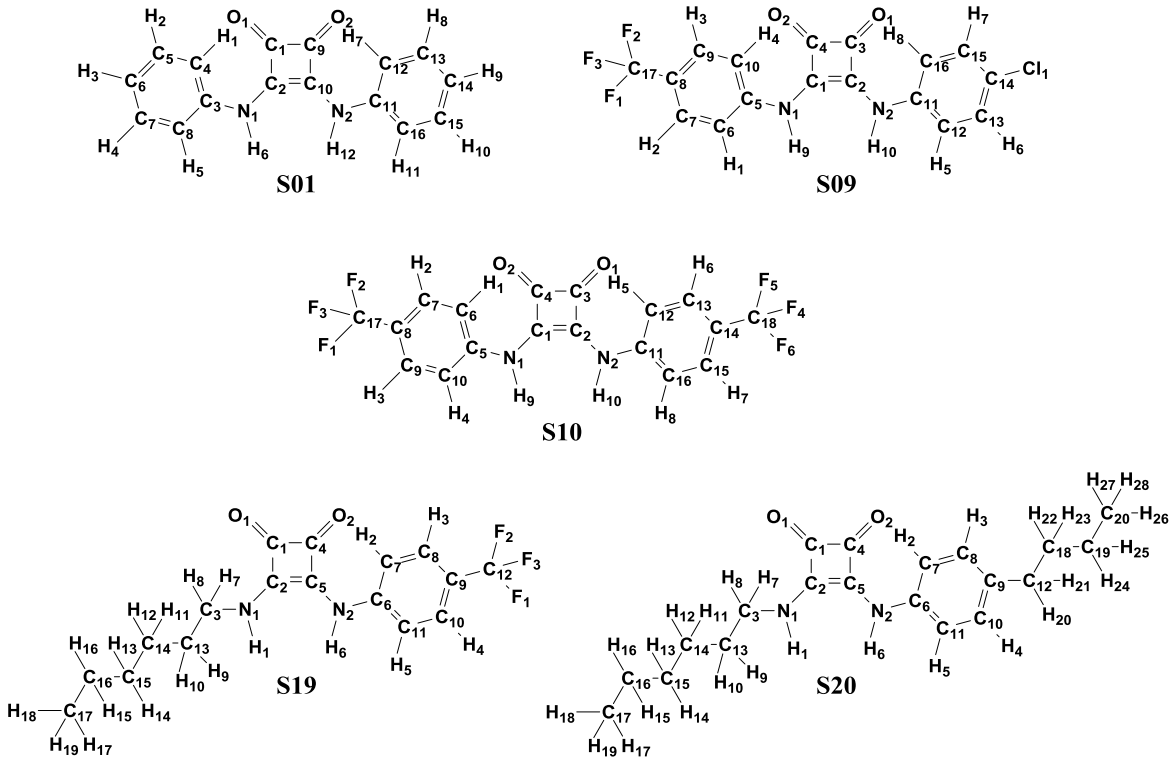

Figure 34 –Atomic numbering adopted for S01-S20.

Table 26 – Atom types and RESP charges for S01.

ID[a]	AT[b]	Charge	ID[a]	AT[b]	Charge	ID[a]	AT[b]	Charge	ID[a]	AT[b]	Charge
N1	nh	-0.646448	H2	ha	0.143795	N2	nh	-0.646448	H8	ha	0.143795
O1	o	-0.438862	C6	ca	-0.211927	O2	o	-0.438862	C14	ca	-0.211927
C1	dc	0.322969	H3	ha	0.146739	C9	dc	0.322969	H9	ha	0.146739
C2	db	0.190422	C7	ca	-0.070356	C10	db	0.190422	C15	ca	-0.070356
C3	ca	0.484707	H4	ha	0.143795	C11	ca	0.484707	H10	ha	0.143795
C4	ca	-0.343583	C8	ca	-0.343583	C12	ca	-0.343583	C16	ca	-0.343583
H1	ha	0.178288	H5	ha	0.178288	H7	ha	0.178288	H11	ha	0.178288
C5	ca	-0.070356	H6	hn	0.336111	C13	ca	-0.070356	H12	hn	0.336111

[a]ID corresponds to the atom number shown in Figure 34.

[b]AT is the correspondent atom type.

Table 27 – Atom types and RESP charges for S09.

ID[a]	AT[b]	Charge	ID[a]	AT[b]	Charge	ID[a]	AT[b]	Charge	ID[a]	AT[b]	Charge
C1	db	0.204691	C8	ca	-0.138947	H6	ha	0.139893	H10	hn	0.330570
C2	db	0.165150	C9	ca	-0.095933	C14	ca	-0.070027	C17	c3	0.715682
C3	dc	0.333579	H3	ha	0.167760	C15	ca	0.014942	Cl1	cl	-0.116565
C4	dc	0.315798	C10	ca	-0.322757	H7	ha	0.139893	O1	o	-0.430915
C5	ca	0.474451	H4	ha	0.179995	C16	ca	-0.395016	O2	o	-0.428462
C6	ca	-0.322757	C11	ca	0.489892	H8	ha	0.199380	F1	f	-0.235118
H1	ha	0.179995	C12	ca	-0.395016	N1	nh	-0.642161	F2	f	-0.235118
C7	ca	-0.095933	H5	ha	0.199380	H9	hn	0.337810	F3	f	-0.235118
H2	ha	0.167760	C13	ca	0.014942	N2	nh	-0.611720			

[a]ID corresponds to the atom number shown in Figure 34.

[b]AT is the correspondent atom type.

Table 28 – Atom types and RESP charges for S10.

ID[a]	AT[b]	Charge	ID[a]	AT[b]	Charge	ID[a]	AT[b]	Charge	ID[a]	AT[b]	Charge
C1	db	0.183046	C9	ca	-0.099485	C15	ca	-0.099485	O2	o	-0.426306
C2	db	0.183046	H3	ha	0.168671	H7	ha	0.168671	F1	f	-0.233134
C3	dc	0.325400	C10	ca	-0.316885	C16	ca	-0.316885	F2	f	-0.233134
C4	dc	0.325400	H4	ha	0.180637	H8	ha	0.180637	F3	f	-0.233134
C5	ca	0.455579	C11	ca	0.455579	N1	nh	-0.613325	C18	c3	0.708262
C6	ca	-0.316885	C12	ca	-0.316885	H9	hn	0.330579	F4	f	-0.233134
H1	ha	0.180637	H5	ha	0.180637	N2	nh	-0.613325	F5	f	-0.233134
C7	ca	-0.099485	C13	ca	-0.099485	H10	hn	0.330579	F6	f	-0.233134
H2	ha	0.168671	H6	ha	0.168671	C17	c3	0.708262			
C8	ca	-0.129709	C14	ca	-0.129709	O1	o	-0.426306			

[a]ID corresponds to the atom number shown in Figure 34.

[b]AT is the correspondent atom type.

Table 29 – Atom types and RESP charges for S19.

ID[a]	AT[b]	Charge	ID[a]	AT[b]	Charge	ID[a]	AT[b]	Charge	ID[a]	AT[b]	Charge
N1	nh	-0.555870	C7	ca	-0.285480	H7	h1	0.039643	H14	hc	0.00891
O1	o	-0.473740	H2	ha	0.170659	C13	c3	-0.043630	H15	hc	-0.01698
C1	dc	0.435742	C8	ca	-0.133690	H8	h1	0.039643	H16	hc	-0.01698
C2	db	0.000983	H3	ha	0.173261	H9	hc	0.015063	C17	c3	-0.17591
C3	c3	0.169739	C9	ca	-0.114610	H10	hc	0.015063	H17	hc	0.03973
H1	hn	0.349167	C10	ca	-0.133690	C14	c3	0.011576	H18	hc	0.03973
N2	nh	-0.723090	H4	ha	0.173261	H11	hc	0.006865	H19	hc	0.03973
O2	o	-0.432310	C11	ca	-0.285480	H12	hc	0.006865	F1	f	-0.23516
C4	dc	0.246584	H5	ha	0.170659	C15	c3	-0.035730	F2	f	-0.23516
C5	db	0.333397	H6	hn	0.344436	H13	hc	0.008910	F3	f	-0.23516
C6	ca	0.466299	C12	c3	0.708920	C16	c3	0.117834			

[a]ID corresponds to the atom number shown in Figure 34.

[b]AT is the correspondent atom type.

Table 30 – Atom types and RESP charges for S20.

ID[a]	AT[b]	Charge	ID[a]	AT[b]	Charge	ID[a]	AT[b]	Charge	ID[a]	AT[b]	Charge
N1	nh	-0.554760	C8	ca	-0.188860	H10	hc	-0.018350	H19	hc	0.043020
O1	o	-0.482980	H3	ha	0.172156	C14	c3	0.057915	H20	hc	0.041808
C1	dc	0.407554	C9	ca	0.092588	H11	hc	-0.019130	C18	c3	0.067123
C2	db	0.031693	C10	ca	-0.188860	H12	hc	-0.019130	H21	hc	0.041808
C3	c3	0.153669	H4	ha	0.172156	C15	c3	0.003846	C19	c3	0.147321
H1	hn	0.342572	C11	ca	-0.328420	H13	hc	-0.005430	H22	hc	-0.015110
N2	nh	-0.664540	H5	ha	0.179703	C16	c3	0.121596	H23	hc	-0.015110
O2	o	-0.447430	H6	hn	0.323506	H14	hc	-0.005430	H24	hc	-0.030910
C4	dc	0.292483	C12	c3	-0.133330	H15	hc	-0.023770	C20	c3	-0.177240
C5	db	0.262158	H7	h1	0.033799	H16	hc	-0.023770	H25	hc	-0.030910
C6	ca	0.468897	C13	c3	0.043447	C17	c3	-0.189050	H26	hc	0.036306
C7	ca	-0.328420	H8	h1	0.033799	H17	hc	0.043020	H27	hc	0.036306
H2	ha	0.179703	H9	hc	-0.018350	H18	hc	0.043020	H28	hc	0.036306

[a]ID corresponds to the atom number shown in Figure 34.

[b]AT is the correspondent atom type.

Results and Discussion

The conformational analysis of each receptor yielded conformations within a narrow energy range, in agreement steric bulk and requirements of the substituents attached to the squaramide moiety. Indeed, the energies, listed in Table 31, indicate that for S01, S09, S10 and S20, the *syn/anti* configuration is the favoured one, with an energy variation of less than 2 kcal/mol from the *anti/anti* conformation. For S19 this conformation is disfavoured relatively to the *anti/anti* by 1.82 kcal/mol. The three conformational arrangements are illustrated in Figure 35 for S01.

Table 31 – Energy variation (kcal/mol) between conformations optimized in gas-phase with B3LYP/6-31G*.

		Lowest energy conformation	**Conformation**		
			syn/syn	*syn/anti*	*anti/anti*
	S01	syn/anti	2.69	-	1.77
	S09	syn/anti	2.63	-	1.40
△E	**S10**	syn/anti	2.47	-	1.17
	S19	anti/anti	0.58	1.82	-
	S20	syn/anti	3.46	-	1.74

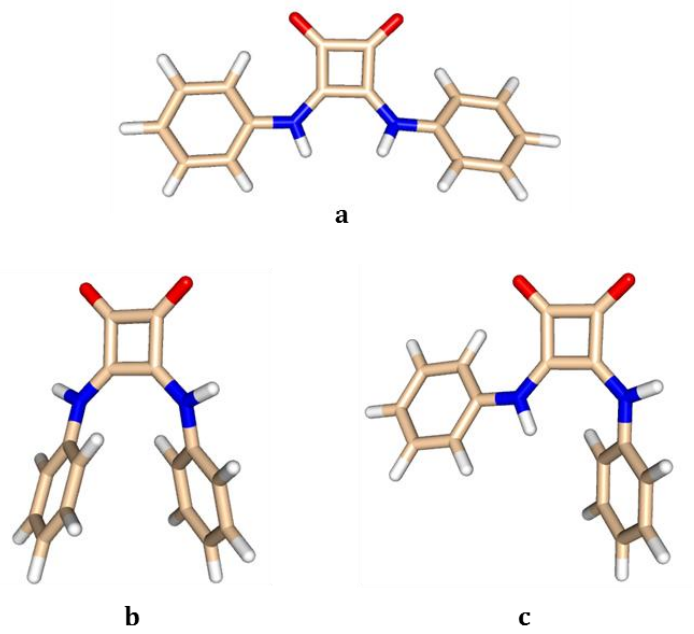

Figure 35 – Molecular mechanics structures a- *anti/anti* (a), *syn/syn* (b) and *syn/anti* (c) conformations of S01.

Moreover, in Table 32 are listed the RMSDs calculated between the *anti/anti* conformations obtained by conformational analyses for S01, S09, S10 , S19 and S20. For all five squaramides, the RMSDs values indicate that the selected conformations are significantly different in order to be used in the multi-RESP charge calculations.

Table 32 – RMSD values calculated between *anti/anti* conformations of S01, S09, S10, S19 and S20.

Conf. numbers	Squaramide				
	S01	**S09**	**S10**	**S19**	**S20**
1/2	1.00	1.32	1.23	1.79	1.54
1/3	1.51	1.29	0.96	1.04	2.08
1/4	-	1.06	1.24	1.47	2.01
2/3	1.00	1.20	1.00	1.27	2.12
2/4	-	1.20	1.06	2.01	1.68
3/4	-	0.73	1.35	1.60	2.44

2.2.2. *Conformational analysis of chloride associations*

Methodology

The conformational analyses on the receptor chloride associations were performed using the quenched dynamics approach described earlier in Section 2.2.1 for free S10. The chloride net charge was assigned as -1 and described with van der Waals parameters developed for the TIP3P water model.(115)

Results and Discussion

The lowest energy structure found in the conformational analysis of each anion squaramide complex displays an *anti/anti* conformation binding the chloride anion by two N-H···Cl$^-$ independent hydrogen bonds, as depicted in Figure 36. The dimensions of these hydrogen bonds, listed in Table 33, are comparable to those found in the crystal structures with CSD Refcodes FAWZAG (**S05⊃Cl$^-$**), FAXBUD (**S01⊃Cl$^-$**), FAXCEO (**S10⊃Cl$^-$)**, MUYYOV (**S02⊃Cl$^-$)** and REPGIE (**S26⊃Cl$^-$**). The crystal structures of the first three complexes were not available when this study, in gas phase, was undertaken. The lowest energy binding arrangements

found for chloride associations were used in the subsequent MD simulations in membrane simulations reported in Chapter 3.

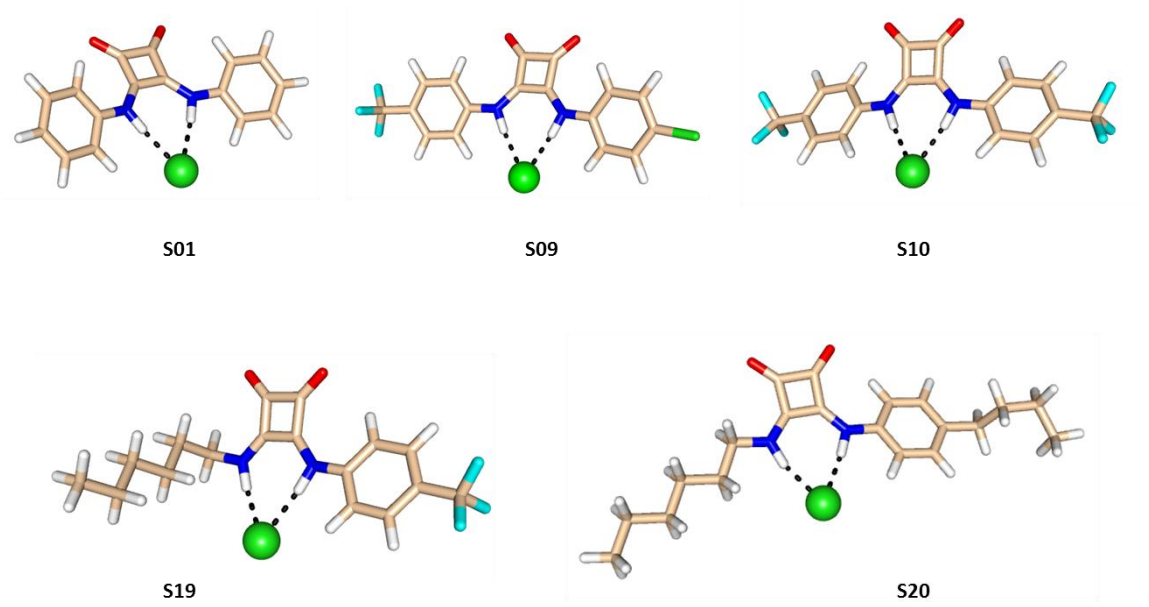

Figure 36 – Lowest energy conformations found in conformational analysis of chloride associations with S01, S09, S10, S19 and S20. Carbon, oxygen, nitrogen, hydrogen, chloride and fluorine atoms are represented in wheat, red, blue, white, green and cyan, respectively. Chloride anion is represented as a green sphere and the hydrogen bonds are represented as black dashed lines.

Table 33 – Number and dimensions of N-H···Cl^- hydrogen bonds found in lowest energy conformations of receptor chloride associations.

Association	Number of hydrogen bonds	Distance N···Cl^- (Å)		Angle N-H···Cl^- (°)	
		Min.	Max.	Min.	Max.
S01⊃Cl^-	2	3.337	3.337	173.5	173.5
S09⊃Cl^-	2	3.317	3.319	173.5	173.8
S10⊃Cl^-	2	3.315	3.315	173.7	173.7
S19⊃Cl^-	2	3.276	3.372	169.1	174.5
S20⊃Cl^-	2	3.217	3.263	166.5	173.4

3. Chloride transport across a phospholipid bilayer with squaramide receptors

In this chapter we report the molecular dynamics study on the chloride transmembrane transport mediated by squaramide receptors S01, S09, S10, S19, S20 (see Figure 36, Chapter 2). The bilayer models used in this study are composed of POPC phospholipids (see Figure 22, Chapter 1) in agreement with the experimental studies described in Chapter 1.(72)

Over the last few years, significant theoretical studies on pure POPC membranes with specific force field parameterization of phospholipids have been reported. Klauda and co-workers simulated pure bilayers of six lipids (DMPC, DOPC, POPE, DPPC, DLPC and POPC) with the CHARMM36 all-atom force field. Each membrane consisted of 72 lipids and approximately 2232 water molecules (81). Another example is the work developed by Poger *et al*. (86), a study on fully hydrated pure membranes of DLPC, DMPC, DOPC and POPC. The G53A6$_L$ force field, used in this study, proved to properly reproduce the structure and hydration of bilayers formed by 128 lipid molecules and 5120 (SPC) water molecules.(86)

A notorious attempt to simulate lipid membranes using GAFF together with AMBER software package was reported by Rosso and co-workers in 2008 (82). They simulated DMPC and DOPC membranes composed of 72 lipids and 2449 to 2935 water molecules. Although they were able to reproduce several structural and dynamic experimental properties of the lipids, often, the area per lipid values were underestimated in comparison to the experimental data. This was associated with the need of a defined surface tension when using GAFF.(82)

In the present work, the experimental reference data were obtained from Kučerka group's results.(116) The results presented in this work will also be compared with findings from Félix and co-workers.(117)

This chapter is organized in sections as follows: in the first part, the simulation performed in a pure membrane model is described and the results are compared with literature. The second part reports and discusses the structural and dynamic results from the simulations with squaramide receptors in membrane models. This second part also analyses how the permeation and interaction of these receptors affect the membrane properties when they are initially positioned within the hydrophobic core of the bilayer or in the aqueous phase of the system.

All the MD simulations were performed with the AMBER12 suite (118) under periodic boundary conditions. The receptors were described using GAFF (108), apart from the squaric rings that were parameterized in Section *2.1*, and atomic RESP charges.(119) The chloride anion and sodium counter-ion (to obtain the charge neutrality of the system) were described with net charges of -1 and +1, respectively, and van der Waals parameters (120) developed for the TIP3P water model.(115) The POPC lipids were described with parameters from the LIPID11 force field. The images were rendered with the *PyMOL* software.(121)

3.1. Pure membranes

In order to evaluate the integrity and structural properties of the membrane models used in the following MD simulations with receptors, simulation of the pure membrane models was performed. Table 34 summarizes the simulation conditions of the pure membranes systems.

Table 34 – Summary of simulation conditions used to simulate pure membrane models.

Membrane Model	**Number of molecules**		**Water/Lipid ratio**	**Surface tension γ (dyn/cm)**	**Temperature (K)**
	POPC	Water			
I	128	6500	50.78 : 1	17	303
II	128	4040	31.56 : 1	17	303

Since membrane model I was already simulated by Félix and co-workers (117), only the pure membrane model II is simulated in this work.

Methodology

Membrane model II

This membrane model was obtained from the CHARMM-GUI library of lipid bilayers. The selected membrane has a pore large enough (~ 16 Å diameter) to accommodate the receptors and was previously equilibrated.(122) The system was simulated at the physiological temperature 303 K. The lipid molecules were described with LIPID11 (84) and the TIP3P water model (115) was used. The simulation was performed with AMBER12 (118) using the following protocol:

Preparation stage

Since the initial structure presented a pore, a preparation step was necessary to close the pore. Therefore, the initial system was submitted to 10000 steps of MM energy minimization with a positional restraint of 500 kcal/mol $Å^2$ on the lipids through 3000 steps using the steepest descent method followed by 7000 steps using conjugate gradient. The same method was applied again, but restraining only the water molecules. After this, the entire system was relaxed for another 10000 steps, with the same approach. Following the three minimization stages, a MD run was performed for 100 ps at 303 K in an NVT ensemble with no restraints. At the end of this stage the membrane pore was closed.

Simulation

The final structure from the previous preparation stage was subjected to a new minimization. A MM minimization ran for 3000 steps in steepest descent and 7000 steps in conjugate gradient. Strong restraints of 500 kcal/mol $Å^2$ were applied to the POPC lipids to keep the membrane structure and integrity during the initial minimization. This process was repeated with restraints applied instead to the water molecules. Afterwards, the system was minimized without restraints. A NVT MD run as then performed for 100 ps at 303K with weak restraints (10 kcal/mol $Å^2$) on the POPC lipids, followed by an equilibration process of 5 ns in an NPγT ensemble using a surface tension of 17 dyn/cm. The system was subjected to 50 ns of production run.

The non-bonded interactions were truncated with an 8 Å cut-off and the long-range electrostatic interactions were described with Particle Mesh Ewald (PME).(123) The temperature of the system was maintained by coupling the system to an external bath temperature of 303 K using Langevin thermostat (124) with a coupling constant of 0.1 ps^{-1}. The pressure was controlled by the Berendsen barostat (125) at 1 atm, using a compressibility of $44.6x10^{-6}$ bar^{-1}. The covalent bonds to hydrogen atoms were constrained using SHAKE algorithm (126), thus allowing the use of 2 fs time step. Frames were saved every 1 ps, resulting in a total of 50000 frames per simulation. The membrane simulations were performed with the CUDA versions of the PMEMD (127-129) executable and their structural parameters assessed and analyzed with the *cpptraj* utility of Ambertools 13.(118)

Results and Discussion

Area per lipid

An important structural parameter to evaluate the equilibration of the lipid bilayer is the area per lipid. The equilibration is achieved when the area (A_L), given by Eq. 13 and stabilizes around a value for a considerable amount of time. In this equation, A_{xy} represents the area of the x-y section of the system and $n_L/2$ is the number of lipids in each monolayer.

$$A_L = \left(\frac{A_{xy}}{n_L/2}\right) \qquad \text{Eq. 13}$$

The area per lipid values 64.3 (116) and 64.9 $Å^2$ (117), obtained at 303 K by Kučerka *et al* and Félix *et al*, respectively, will be used as references in the subsequent results' analysis.

The evolution of the area per lipid in pure membrane model II is depicted in Figure 37. For model II, the graphic shows that the area stabilizes after 30ns of simulation time, around a value of 65.5 $Å^2$, close to both reference values mentioned above.

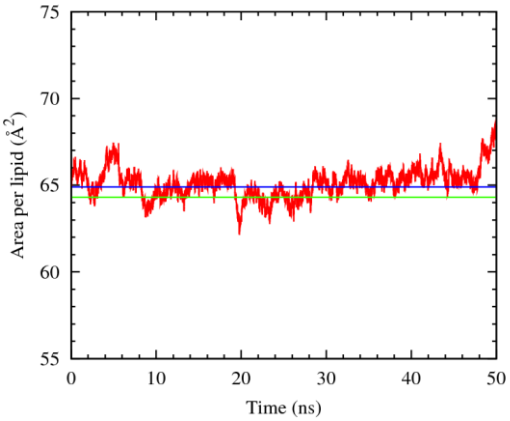

Figure 37 – Evolution of the area per lipid in the MD simulation of membrane model II (red line) in comparison with reference values from Kučerka (116) (green line) and Félix (117) (blue line).

Bilayer thickness

Along with area per lipid, the bilayer thickness is also an important parameter for structural characterization of a phospholipid membrane. During the simulation time, bilayer thickness was measured as the distance between the average *z* coordinate of phosphorus atoms from the lipids head groups of each monolayer. Evolution of the bilayer thickness for membrane model II is illustrated in Figure 38. Reference values 36.5 (116) and 38.1 Å (117), are also represented as green and blue lines.

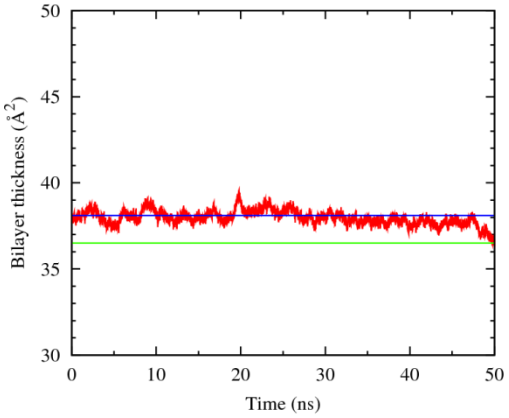

Figure 38 – Evolution of bilayer thickness in the 50ns of MD simulation time (red line) in in comparison with experimental values from Kučerka (116) (green line) and Félix (117) (blue line).

Through the 50 ns of MD simulation, the bilayer thickness of both systems oscillates around the reference values, stabilizing after 30 ns of simulation time with mean values of 37.7 Å. These findings indicate that the structural integrity of the membrane is preserved in both membrane models.

Order parameters (chain order)

The disorder of the acyl chains of membrane lipids is an important structural property of lipid bilayer and can be quantified using the experimental deuterium order parameters ($|S_{CD}|$). This parameter was also assessed in the MD simulations reported, with a *ptraj* modification by Hannes Loeffler (130), using Eq. 14, in in which θ is the angle between the C-H bond of an acyl tail and the bilayer normal.

$$S_{CD} = \frac{1}{2}(3cos^2\theta - 1) \qquad \text{Eq. 14}$$

High $|S_{CD}|$ values indicate that the acyl chains are highly ordered and more rigid, typical of lipid gel phase.(131) For fluid phase bilayers, as ours, lower $|S_{CD}|$ values indicate a high degree of disorder and flexibility of the lipids hydrocarbon tails.

The chain order was assessed during the last 20ns of simulation time of both models, when the membrane was equilibrated, and the computed $|S_{CD}|$ values are depicted in Figure 39. In both cases the $|S_{CD}|$ values calculated for *sn*-1 chain are shown in red and the values for *sn*-2 chain in green. In plot *a* the experimental reference values for *sn*-1 chain are represented in brown (132) and orange (133), while *sn*-2 chain values are represented in magenta (134) and blue (133). The theoretical reference values in plot *b* were obtained for a pure membrane and are presented in blue (117) and orange (84) for *sn*-1 chain, and in magenta (117) and brown (84) for *sn*-2 chain.

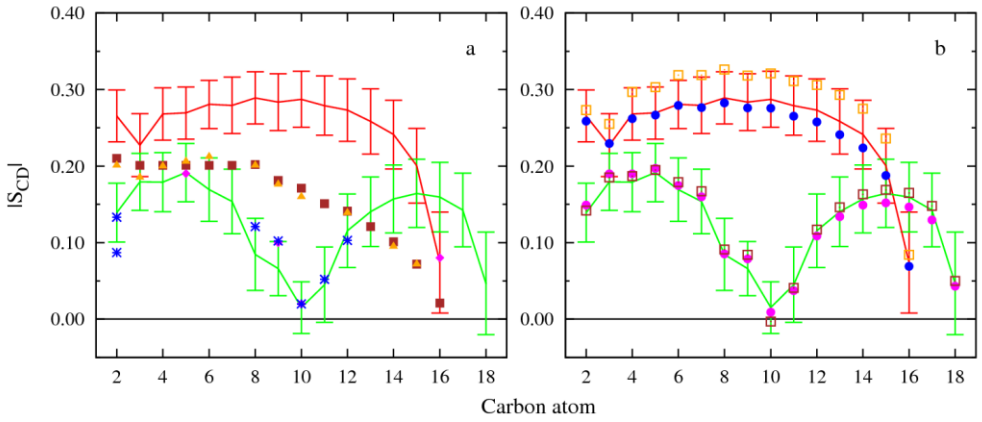

Figure 39 – Computed order parameters, $|S_{CD}|$, for the palmitoyl and oleyl chains for the last 20 ns of imulation time of model II. The $|S_{CD}|$ calculated values are in red and in green for the *sn*-1 and *sn*-2 chains, respectively. The error bars shown correspond to the standard deviation. In plot *a* the experimental values for the *sn*-1 chain were obtained from reference (132) (brown) and (133) (orange), while the values for *sn*-2 chain were taken from reference (134) (magenta) and (133) (blue). In plot *b,* the reference values for $|S_{CD}|$ were obtained from LIPID11 paper (84) (*sn*-1 chain in orange and *sn*-2 chain in brown) and from Félix *et al*. paper (117) (*sn*-1 chain in blue and *sn*-2 chain in magenta).

The computed $|S_{CD}|$ values of the *sn*-1 chains are over-estimated when compared with the experimental data, as expected for a membrane simulated with LIPID11.(84) Still, the inflexion of the $|S_{CD}|$ values for the first two carbons in this chain matches the experimental data. The sets of experimental data available for *sn*-2 chains order parameters have few points defined with, thus complicating the comparison with the calculated values of membrane model II.

A clear tendency to follow reference values from Félix *et al.* (117) and Skjevik *et al.* (84) is shown in plot *b*. The comparison of the *sn*-1 chain values with the results from Félix *et al.* shows that both values are almost superimposable and lower than the $|S_{CD}|$ values from Skjevik *et al*, meaning a good degree of disorder and flexibility. Results for the *sn*-2 chain show even better matches with the theoretical reference values. The computed $|S_{CD}|$ values are higher for carbon atoms close to the water/lipid interface and they become lower towards the bilayer core, as expected.(131)

Electron density profile

The electron density profiles allow the assessment of the distribution of the system components through the *z* axis. For example, the distance between the peaks assigned to the phosphate groups is often used to roughly estimate bilayer thickness.(81) The electron density profiles along the *z* axis were computed by dividing this dimension into 0.1 Å slices and calculating the number of atoms in each slice through their partial electronic charge.(84) The profiles were averaged over the last 20 ns of simulation time.

The electron density profiles for membrane model II are shown in Figure 40. The *z* coordinate axis is perpendicular to the membrane surface and *z*= 0 Å was defined as the core of the bilayer. The black line represents the system profile, the blue line corresponds to the water slabs, and the green line represents the POPC lipids profile, while the dark yellow line represents the phosphorus from the head groups. Shown as a magenta line, in plot *a*, is the experimental electron density profile for a POPC membrane obtained at 303 K with X-ray scattering (116) and, in plot *b*, in red the density profile for the pure membrane simulated by Félix *et al*.(117)

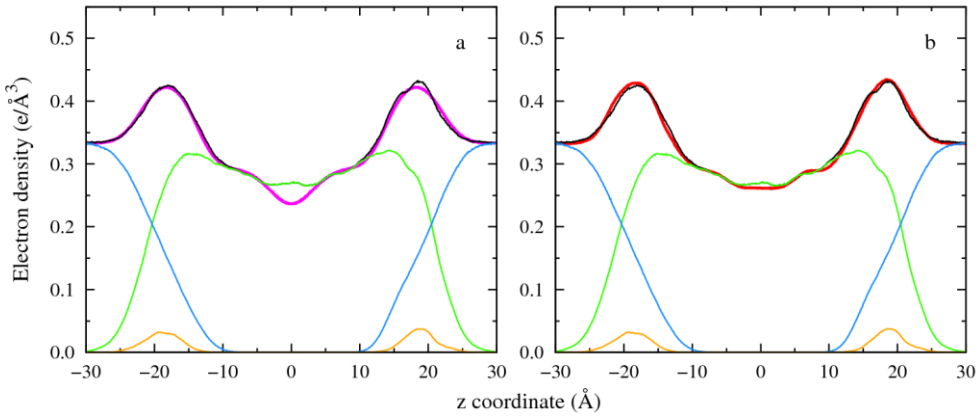

Figure 40 – Electron density profiles of the pure membrane model II for the last 20 ns of MD simulation with full system profile plotted in black, water in blue, phospholipids in green and phosphorus in dark yellow. The z=0 Å corresponds to the core of the POPC bilayer. In plot *a*, the X-ray scattering of the POPC bilayer profile at 303 K is shown as a magenta line (116). In plot *b*, the full system density profile for the pure membrane simulated by Félix *et al* is shown as a red line.(117)

The two profiles are symmetric around z= 0 Å, as expected.(116-117) The alignment of the black line with the magenta (plot *a*) and red (plot *b*) lines indicates a good fitting of the theoretical and reference system profiles for the membrane model. At the edges of the plots, the blue line overlaps the black line, indicating that water is the main contributor to the system's density. Moving to the middle of the system (membrane core), the electronic density of the water slabs decreases, while the electronic density of the POPC lipids increases until z=± 17 Å. The electron densities of the lipids decrease slightly from there to z= 0 Å, where the black line overlaps the green line, since the density of the system corresponds to the density of the lipids. However, at the bilayer core the system's profile does not match the experimental one (magenta line in plot *a*), due to the intercalation between the *sn*-1 tails of each leaflet. This feature is also observed in the density profile results from Skjevik *et al* (84) and Félix *et al* (117) (red line in plot *b*).

The two symmetrical peaks plotted in dark yellow in both plots correspond to the phosphorus atoms from the lipids head groups. The distance between peaks is approximately 38 Å, in good agreement with the previously calculated value for bilayer thickness (37.7 ± 0.33 Å).

In order to summarize the results presented so far, a brief and comparative perspective of the previous MD simulation results from membrane models I and II is presented on Table 35.

Table 35 – Comparison between the structural parameters for the MD simulations of pure membrane model II and of reference data.

Parameter [a]	**Membrane**		
	Model II	Reference	
		Experimental	Model I
Area per lipid (Å^2)	65.5 ± 0.75	64.3[c]	64.9[d]
Bilayer thickness (Å)	37.7 ± 0.33	36.5[c]	38.1[d]
Order parameters	Disorder and flexibility	(84)	(117)
Electron Density Profile	Good fitting to reference profiles	(116)	(117)

[a] Last 20ns of the MD simulations as sampling time

[c] Experimental values from ref. (116)

[d] Simulated values from ref. (117)

Indeed, in spite of the small variations in the area per lipid and the bilayer thickness values, these results are close to the reference values, indicating that this membrane is equilibrated. Also, the electron density profile and the order parameters results show a good fitting of to the experimental and theoretical references.

Membrane model II was found to reproduce quite well the structural parameters evaluated and will be used to support the following MD simulations of membranes with squaramide complexes. Membrane model I will be used in MD simulations with the complex initially positioned on the water slab, while membrane model II will be used in the MD simulations where the complex is placed within the lipid bilayer.

3.2. Membranes and squaramide receptors

To study the receptors' ability to diffuse and permeate the membrane, as well as their impact on its properties, chloride complexes were placed in two different starting positions: in the aqueous phase of the system and within the POPC bilayer. They were then left free of restrains to move and diffuse towards the water/lipid interface. Independent systems were built for each receptor and are listed in Table 36.

Table 36 – Summary of the simulation conditions of the membrane systems with receptors S01, S09, S10, S19 and S20.

System ID	Receptor	Membrane model	Starting position of the receptor	Temperature (K)	Surface tension γ (dyn/cm)	Water model
A	S01	I	In the water slab	303	17	TIP3P
B	S09					
C	S10					
D	S19					
E	S20					
F	S01	II	Within the lipid bilayer			
G	S09					
H	S10					
I	S19					
J	S20					

The main goals of these MD simulations are given below.

For systems A to E:

a. Evaluate the ability of squaramides to complex chloride ions in water;
b. Understand the behaviour of these associations when near a lipid bilayer;
c. Evaluate the squaramide complexes' effect on the membrane properties.

For systems F to J:

d. Evaluate the effect of squaramide complexes on the membrane properties when embedded in the bilayer;
e. Observe the behaviour of chloride complexes when inserted in the membrane core.

3.2.1. *MD Simulations of the receptors starting from the water phase*

Methodology

Molecular dynamics simulations were carried out with receptor·chloride complexes using a POPC vesicle model represented by membrane model I. The receptors were described with the new force field parameters and RESP atomic charges given above (see Section 2.1 and 0), while the lipid were described with LIPID11 force field parameters. The chloride ion, with net charge of -1, was described with van der Waals parameters developed for the TIP3P water model. The simulations were performed under periodic boundary conditions and the charge neutrality of the membrane system was attained by the addition of a sodium counter-ion, with net charge of +1 and van der Waals parameters developed to be used with the TIP3P water model.

Chloride complexes were immersed in the water slab at at least 8 Å away from the membrane interface with *Packmol*.(135) The system was relaxed by MM, using 3000 steps in steepest descent plus 7000 steps of conjugate gradient minimization to remove bad contacts. Large harmonic restraints (500 kcal/mol $Å^2$) were applied to the lipids, chloride complex and sodium in this first stage of MM minimization. A full system MM minimization was performed, followed by an NVT MD run of 100ps at 303 K with weak restraints (10 kcal/mol $Å^2$) on the POPC lipids and chloride complex.

Afterwards, an equilibration run in an NPγT ensemble ensued for 5ns, using a surface tension of 17 dyn/cm and keeping weak positional restraints on the complex. Then the restraints were removed and each system was subject to a 100 ns production run. Two replicates were produced for each system, using random seeds for the initial velocities generation. The remaining simulation conditions were as given for simulations in Section 3.1.

Results and Discussion

Two replicates were performed for each system. In order to facilitate the discussion of the results, only one of the replicates will be depicted below. However, all replicates follow an equivalent behaviour to the one illustrated and the results can be consulted in Appendix 1.

Initial and final snapshots

Figures 45-49 present three snapshots illustrating the diffusion of each squaramide molecule over the 100 ns MD simulation. All receptors migrated from the water slab to the water/lipid interface. None of the receptors was able to bind the chloride ion during the unconstrained MD simulation, releasing it at the beginning of the simulation.

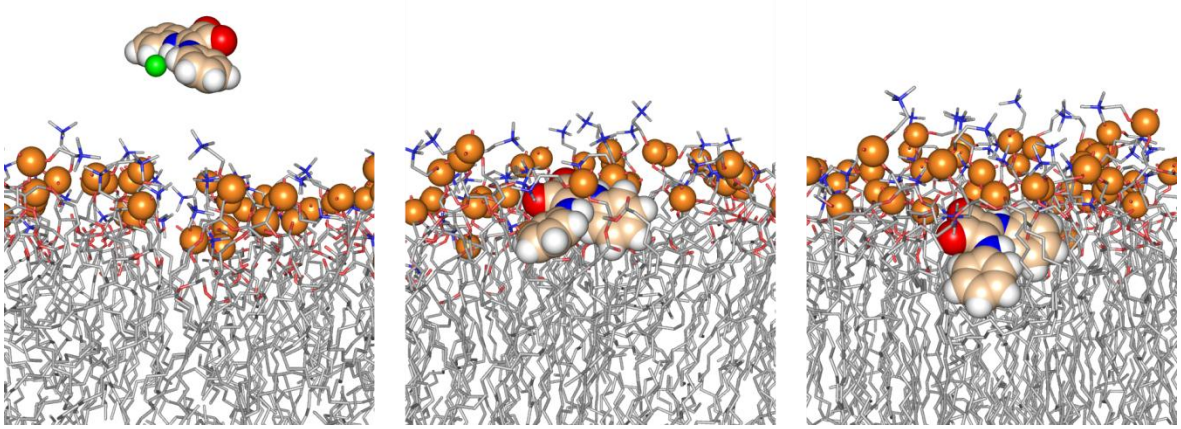

Figure 41 - Snapshots of system A, taken at different simulation times (0, 50 and 100 ns), showing the diffusion of S01. Images show the different positions of the receptor in the membrane. The receptor is drawn in a space filling model with carbon atoms in wheat, oxygen atoms in red, nitrogen atoms in blue and hydrogen atoms in white. The chloride ion and the phosphorus atoms are represented as green and orange spheres, scaled to 0.7 vdW radius, respectively. In POPC lipids, carbon, nitrogen and oxygen atoms are drawn as grey, blue and red lines, respectively, while C-H hydrogen atoms have been omitted for clarity.

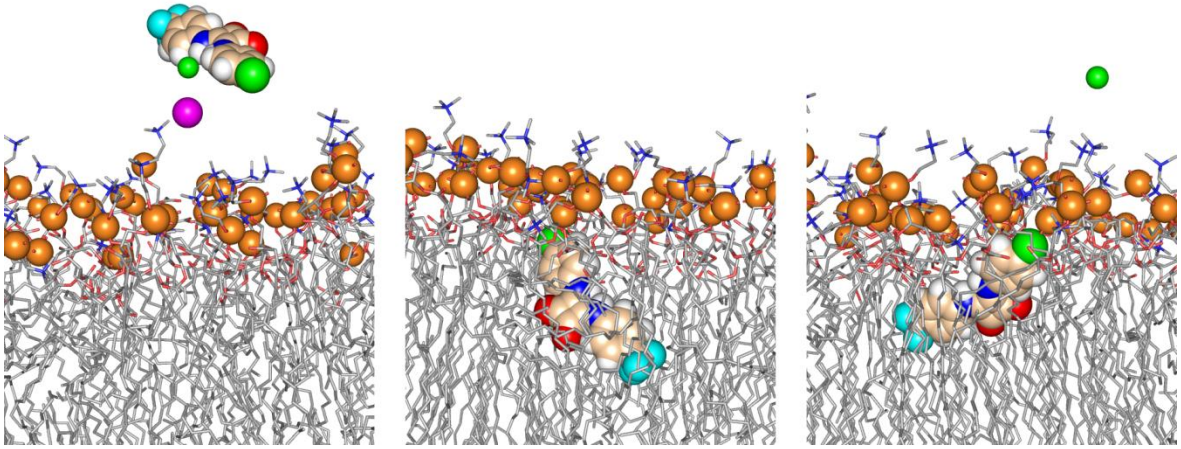

Figure 42 – Snapshots of system B showing S09 diffusion towards the membrane. Fluorine atoms and sodium ion are drawn as cyan and magenta spheres, respectively. Remaining details as given in Figure 41.

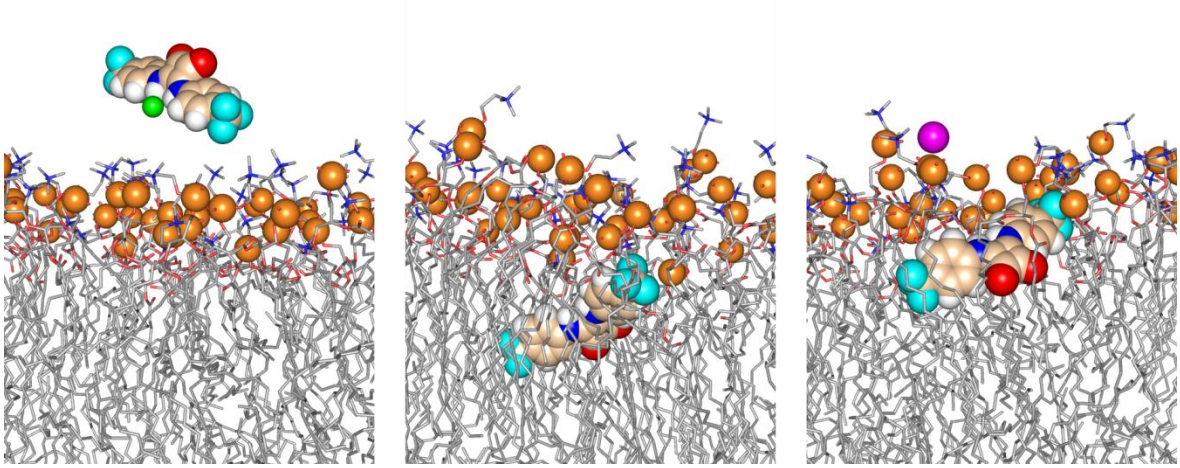

Figure 43 - Snapshots of system C showing S10 diffusion towards the membrane. Fluorine atoms and sodium ion are drawn as cyan and magenta spheres, respectively. Remaining details as given in Figure 41.

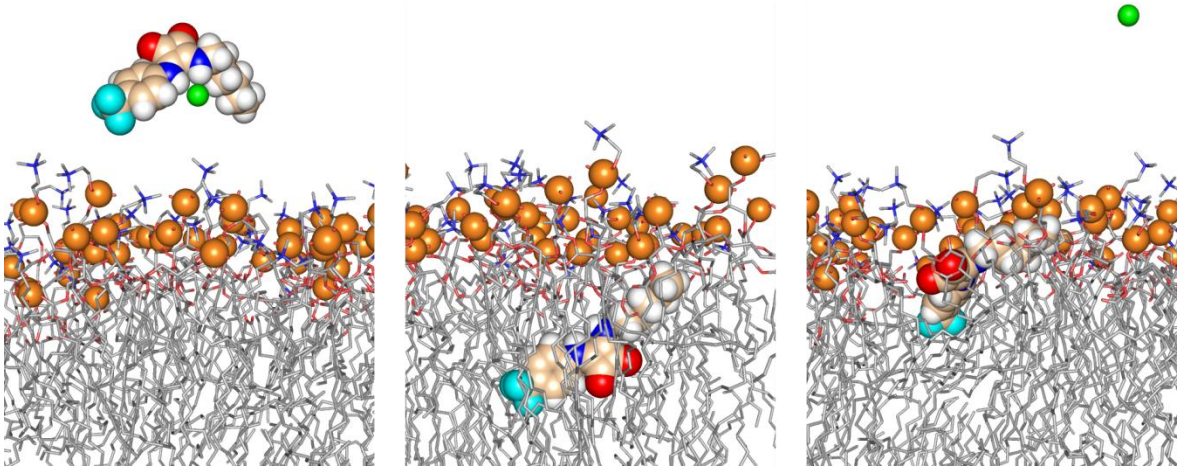

Figure 44 - Snapshots of system D showing S19 diffusion towards the membrane. Fluorine and chloride atoms are drawn as cyan and green spheres, respectively. Remaining details as given in Figure 41.

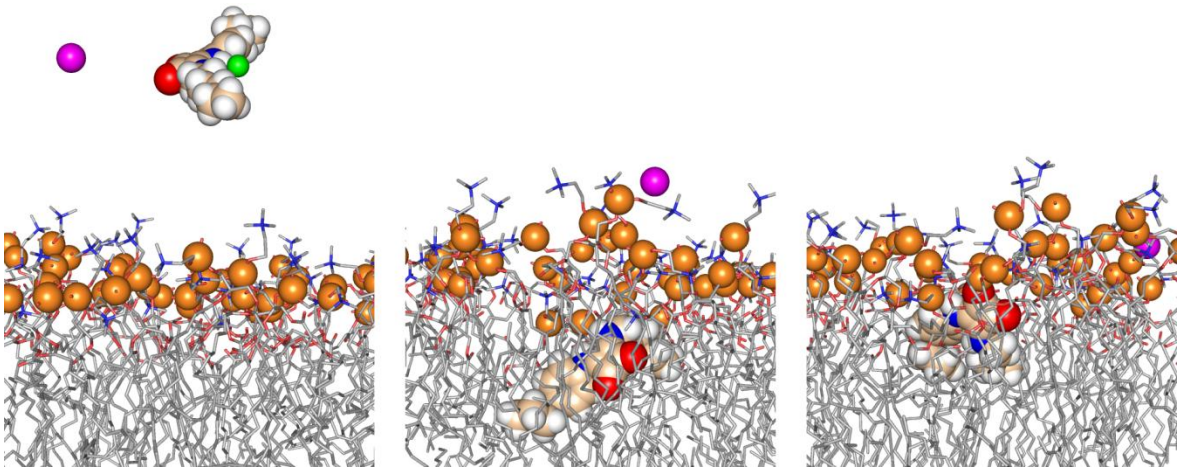

Figure 45 - Snapshots of system E showing S20 diffusion towards the membrane. The sodium ion is drawn as a magenta sphere. Remaining details as given in Figure 41.

In the following section, the evolution of the relative position of each receptor to the water/lipid interface, through the 100ns MD simulation time, will be analysed.

Relative position to interface

The passive diffusion of the squaramide complexes in the membrane system was evaluated by monitoring the relative position between the centre of mass of each receptor and the closest water/lipid interface (average *z* coordinate of the phosphorus atoms on the respective monolayer). The evolution of the relative positions for S01, S09, S10, S19 and S20 is given in plots A to E, in this order, in Figure 46. In agreement with the data in the snapshots above, at the beginning of the MD simulation, the complexes are initially positioned in the water slab, and afterwards each receptor migrates towards the interface, at different simulation times (red line). S01, S10 and S20 (systems A, C and E) crossed the bilayer interface at 15ns of simulation, while S09 (system B) and S19 (system D) crossed earlier, at 5 and 10ns of simulation time, respectively (see Figure 46). Once inside the membrane, the receptors accommodate themselves below the phospholipid head groups, in a semi-stable position, over the last 40ns of simulation time. The average distance between each receptor and the closest interface, for this period of simulation time, is given in Table 37.

In addition, the receptors relative orientation to the membrane interface was assessed through the distances between the interface and the individual substituent groups, represented by the centre of mass of the six carbon atoms of the aromatic rings of S01, S09 and S10, the carbon atoms of the aromatic ring and of the hexyl group of S19 or the carbon atoms of the propyl and hexyl groups of S20 (see Figure 46).

Table 37 – Relative distance (Å) between the receptors and the closest water/lipid interface for systems A-E for the last 40ns of simulation time.

System	Receptor	R1		R2	
		Average	Std. Dev.	Average	Std. Dev.
A	S01	7.8	1.0	7.8	2.0
B	S09	9.2	1.6	8.2	2.5
C	S10	9.0	1.5	4.6	7.3
D	S19	8.5	1.4	9.2	1.4
E	S20	7.2	1.4	10.4	8.4

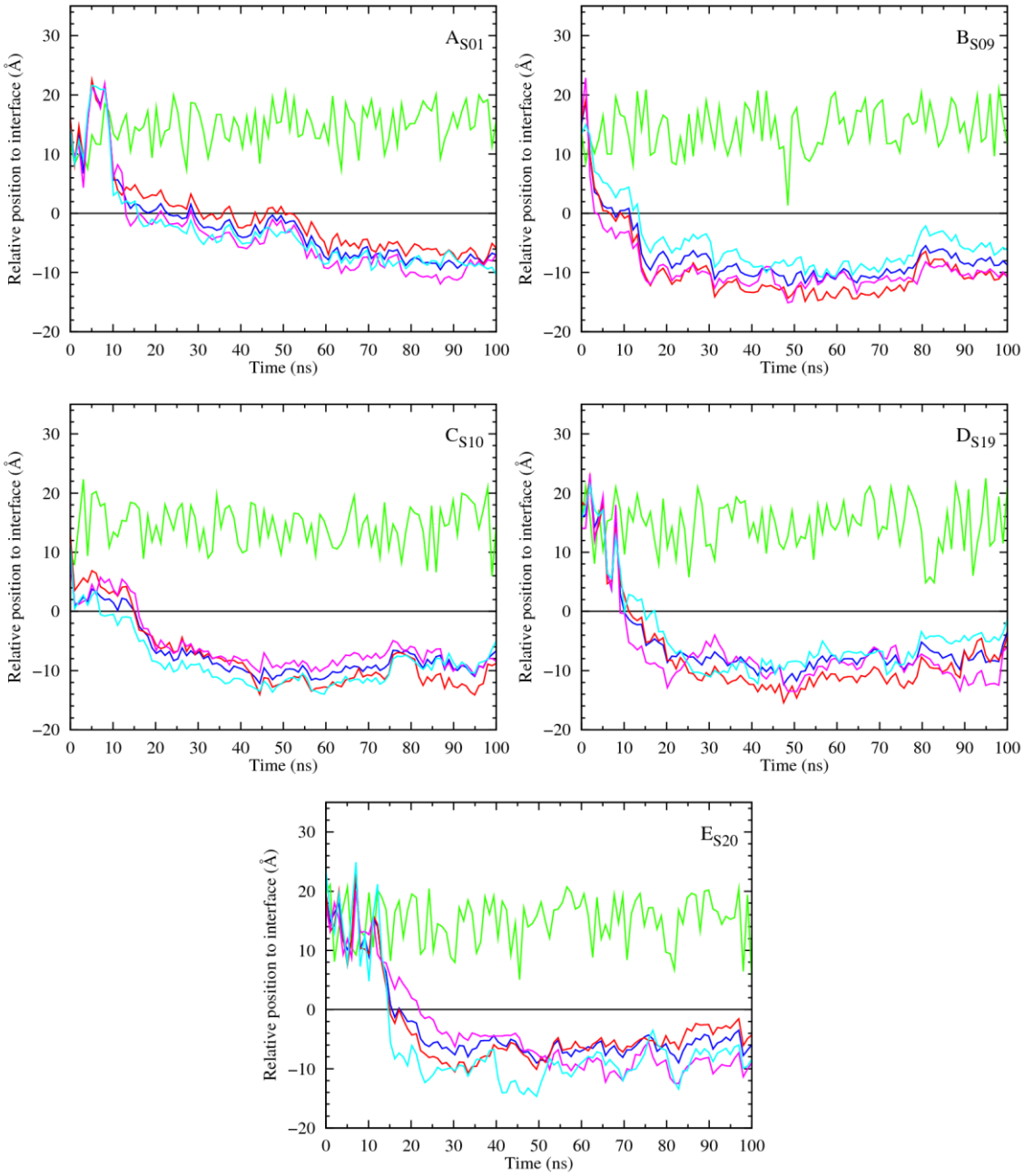

Figure 46 - Evolution of the receptor and chloride relative positions to the water/lipid interface (z=0 Å). In green is represented the chloride ion, in red the centre of mass of the oxygen atoms from the receptor, in blue the centre of mass of the nitrogen atoms, in magenta and cyan are represented the phenyl groups (A, B and C); a phenyl group and an aliphatic chain (D) or an aliphatic chain and a butyl group (E), respectively. Data was smoothed using Bézier curves.

A single phenyl group of S01 begins to permeate the membrane at 15 ns, followed by the second phenyl group. The core of the squaramide (represented by the nitrogen and oxygen atoms) is pulled towards the interface: first the nitrogen atoms and then the oxygen ones. The achieved position is close to the one represented at 100 ns in Figure 41. In the case of S09, a

phenyl group initially interacts with the head groups at 5 ns, and then drives the core and the other phenyl group towards the centre of the membrane, through the interaction of the N-H groups with head groups of the bilayer. Receptor S10 permeates the lipid bilayer first with a phenyl group, *ca.* 8 ns, and 7 ns later the rest of the receptor is pulled towards the interface, first the core and then the other phenyl group. With S19, the phenyl group approaches the head groups and permeates the bilayer, pulling the core and the aliphatic chain. In the case of S20, the first group to reach the interface is the propylbenzyl, followed by the remaining molecule.

Hydration

In the beginning of the simulation, with the receptor in the water slab, a high number of water molecules can be found within a radius of 3.5 Å (the first solvation shell). However, as the receptor starts to move towards the water/lipid interface the number of water molecules in the first solvation shell decreases drastically (see Figure 47). After each receptor crosses the interface, on average, 5 to 8 water molecules can be found within the 3.5 Å radius (see Table 38). For the second replicate of systems C and E, a higher number of water molecules was found within the receptor's first solvation shell, due to the receptors relative position. Indeed, in these simulations, S10 and S20 slightly permeated the membrane and accommodated themselves closer to the water slab.

Table 38 – Summarized information of receptor hydration of systems A-E, in the last 40ns of simulation time.

System	Receptor	R1		R2	
		Average	Std. Dev.	Average	Std. Dev.
A	S01	5.0	2.5	6.2	2.6
B	S09	5.1	2.1	6.0	2.4
C	S10	6.0	2.4	14.7	3.4
D	S19	8.1	2.7	5.9	2.3
E	S20	7.8	2.4	25.7	3.7

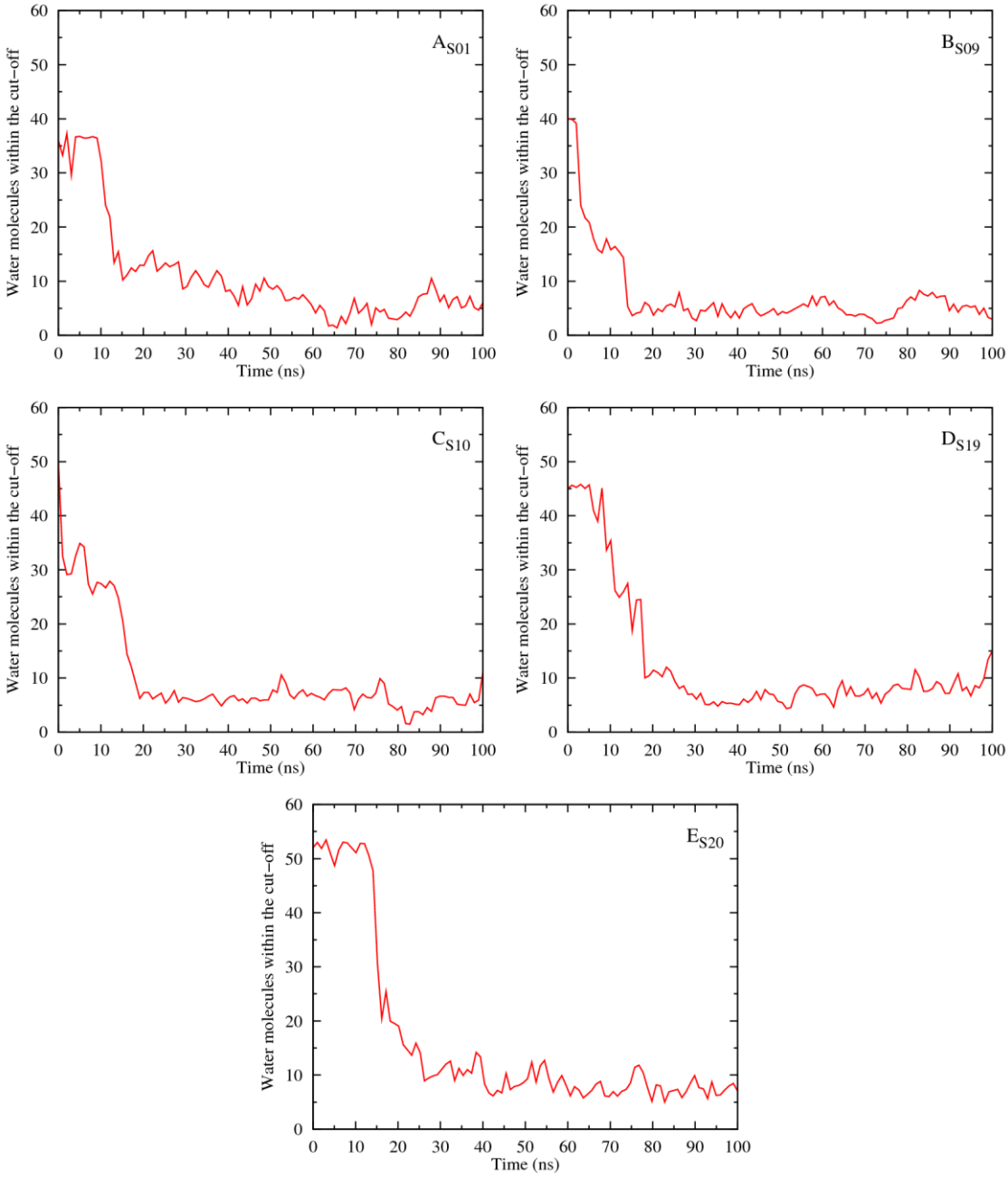

Figure 47 – Variation of the number of water molecules within the solvation shell defined by a cut-off of 3.5Å from receptors S01 (A), S09 (B), S10 (C), S19 (D) and S20 (E). Data was smoothed using Bézier curves.

Hydrogen bonds

The number of hydrogen bonds that each receptor establishes with other species is an important parameter to evaluate its ability to complex and transport chloride, as well as to diffuse in the membrane system. Each squaramide receptor commonly establishes two hydrogen bonds. These hydrogen bonds vary during the diffusion of the receptor along the *z* coordinate, depending on its position and orientation in the system (see Figure 48).

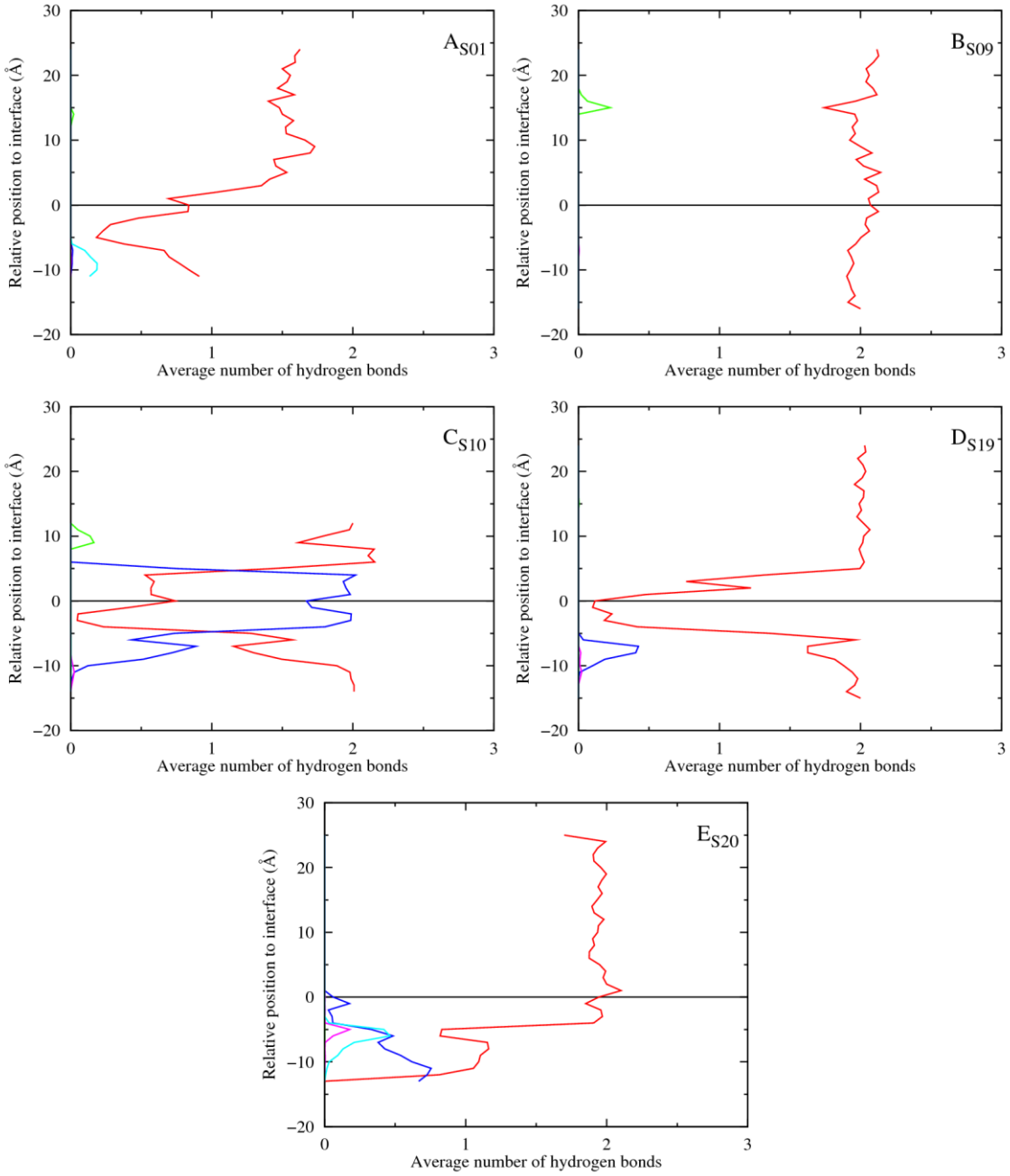

Figure 48 – Average number of hydrogen bonds *vs* the relative position of the centre of mass of each receptor. The following colour scheme was used for the hydrogen bonds established between the receptor and water molecules (red), chloride ion (green), POPC head groups (blue), ester groups from POPC *sn*-1 chains (magenta) and *sn*-2 chains (cyan).

The receptors begin by complexing the chloride ion through hydrogen bonds. In the water phase, the N-H···Cl^- bonds are replaced by hydrogen bonds to water molecules. As the receptors approach the interface, the number of water molecules solvating the receptors decrease and the N-H···OH_2 bonds are replaced by intermolecular hydrogen bonds with the membrane lipid binding sites (phosphate lipid heads and ester groups of *sn*-1 and *sn*-2 lipid chains). In the case of S01, the receptor established hydrogen bonds with the ester group of the *sn*-2 lipid chains (N-H···O=C), while S10 bonded to the phosphate lipid heads (N-H···O_4P) and *sn*-1 lipid chains' ester groups through hydrogen bonds. On the other hand, S19 established N-H···O_4P and N-H···O=C hydrogen bonds with phosphate lipid heads and *sn*-1 lipid chains, while S20 was able to bind to all the membrane lipid binding sites (PO_4, *sn*-1 and *sn*-2 lipid chains' ester groups). S09 was the only receptor that, once the chloride ion was released, established hydrogen bonds with water until the end of the MD simulation. The fact that, even after permeating the water/lipid interface, hydrogen bonding interactions with water are still established (at distances of 10 Å) is in agreement with the hydration data discussed above.

Torsion angles

The conformational changes experienced by each receptor throughout the 100 ns of MD simulation time were evaluated using the C=C-N-C torsion angles (see Figure 49). The conformations experienced by each receptor whilst in the water phase (*pre interaction*) and after reaching the interface (*post interaction*), were assessed by plotting the distribution of C=C-N-C torsion angles in histograms (see Figure 50 and Figure 51). To simplify this analysis, the C=C-N-C torsion angles lower than -120° were shifted by the addition of 360°. In the subsequent analysis, torsion angles within the 120° to 240° range correspond to a *anti/anti* conformation, whereas angles outside this range represent *syn/anti* conformations.

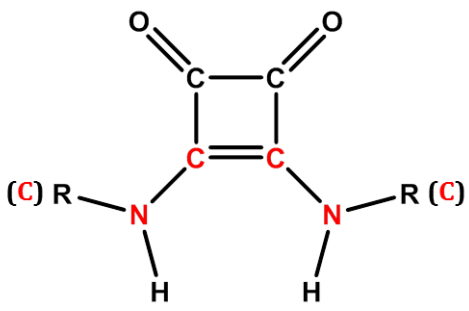

Figure 49 – Schematic representation of the sqauaramide's core. The atoms involved in the dihedral angles analysis are identified in red.

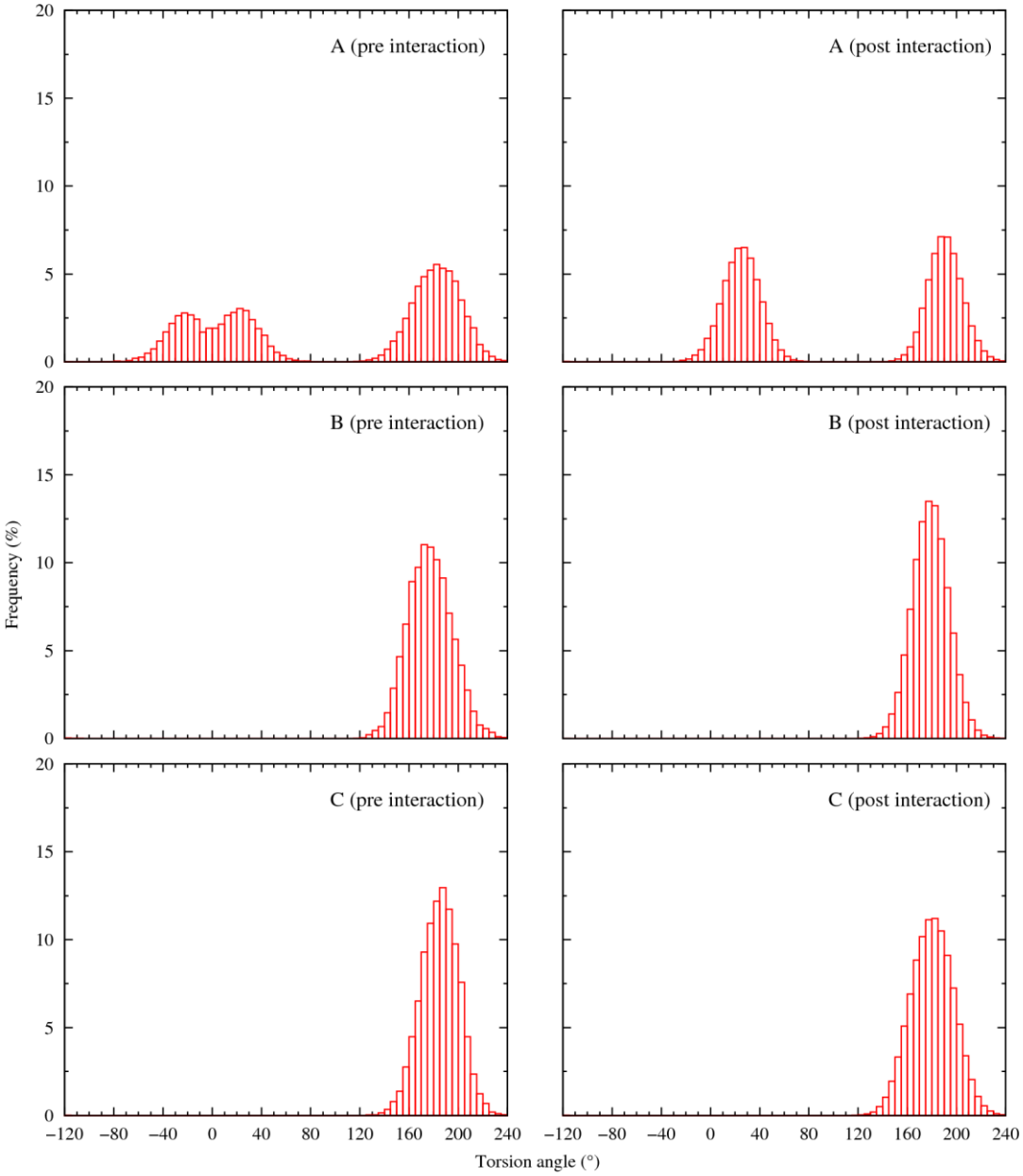

Figure 50 – Frequency histograms showing the distribution of the two C=C-N-C torsion angles values of S01, S09 and S10 in systems A, B and C, before the interaction with the water/lipid interface (*pre interaction*) and after (*post interaction*).

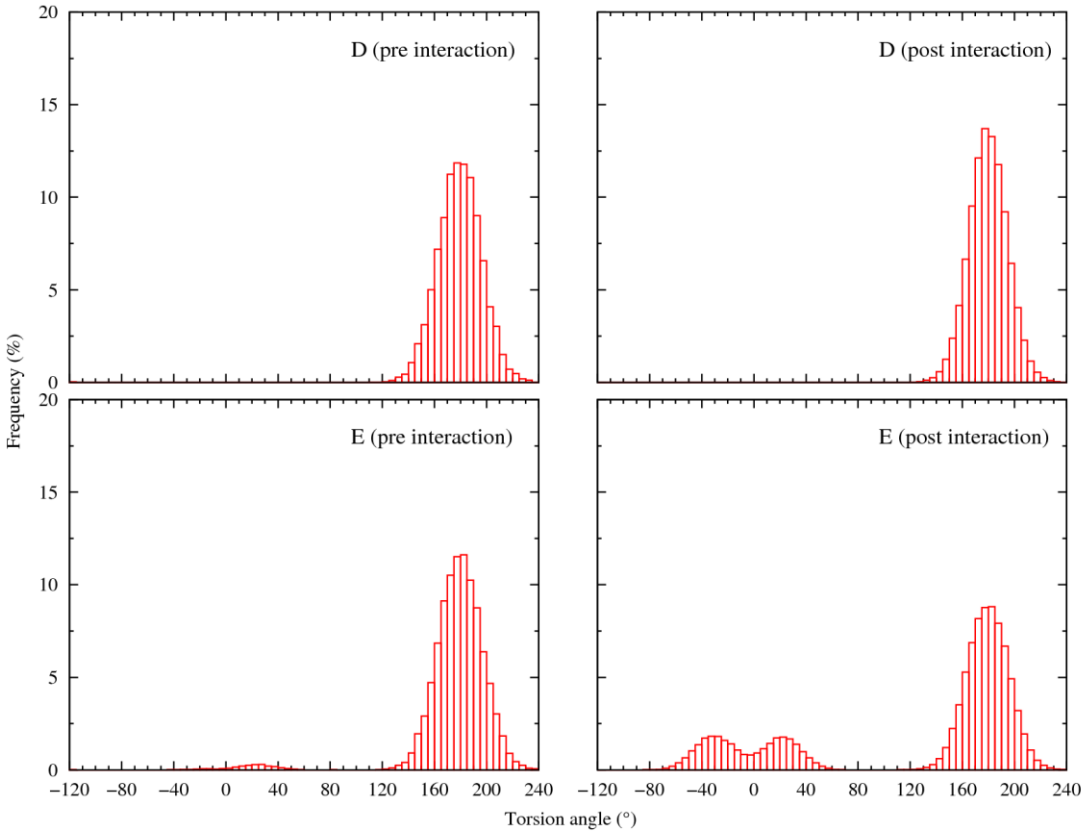

Figure 51 – Frequency histograms showing the distribution of the two C=C-N-C torsion angles values of S19 and S20 in systems D and E, before the interaction with the water/lipid interface (*pre interaction*) and after (*post interaction*).

These histograms reveal that the two C=C-N-C torsion angles experienced mostly values between 120° and 240°. Indeed, in systems B, C and D, the distribution of torsion angles is mainly around 180°, either before or after the interaction with the membrane, consistent with an *anti/anti* conformation. On the other hand, in systems A and E, values outside the 120° to 240° range were observed, therefore, besides an *anti/anti* conformation, receptors S01 and S20 experienced *syn/anti* conformations.

These findings indicate that S09, S10 and S19 are more stable molecules, with more rigid C=C-N-C torsion angles, while S01 and S20 lose the *anti/anti* conformational with the anion release in the water phase, alternating it with a *syn/anti* conformations.

Area per lipid

The evolution of area per lipid in systems A to E through the 100 ns of MD simulation, plotted in Figure 52, indicates that this biophysical parameter is slightly affected by the internalization and presence of squaramide receptors in the bilayer, when compared to the average values of membrane models I. The values for the area per lipid generally decrease when a receptor is present, however when calculating the average area per lipid for each system, the difference to the theoretical value 64.9 $Å^2$ is equal to or less than 4 $Å^2$ (see Table 39). This indicates that, even though receptors affect membrane properties, this effect is negligible and does not compromise the membrane integrity.

Table 39 – Summarized results of area per lipid ($Å^2$) parameter for systems A-E, over 40ns of sampling time.

System	Receptor	R1		R2	
		Average	Std. Dev.	Average	Std. Dev.
A	S01	64.4	0.8	64.2	2.3
B	S09	64.9	0.7	65.4	0.8
C	S10	64.2	1.0	63.1	0.6
D	S19	61.8	0.9	60.6	0.8
E	S20	65.1	0.96	63.4	0.5

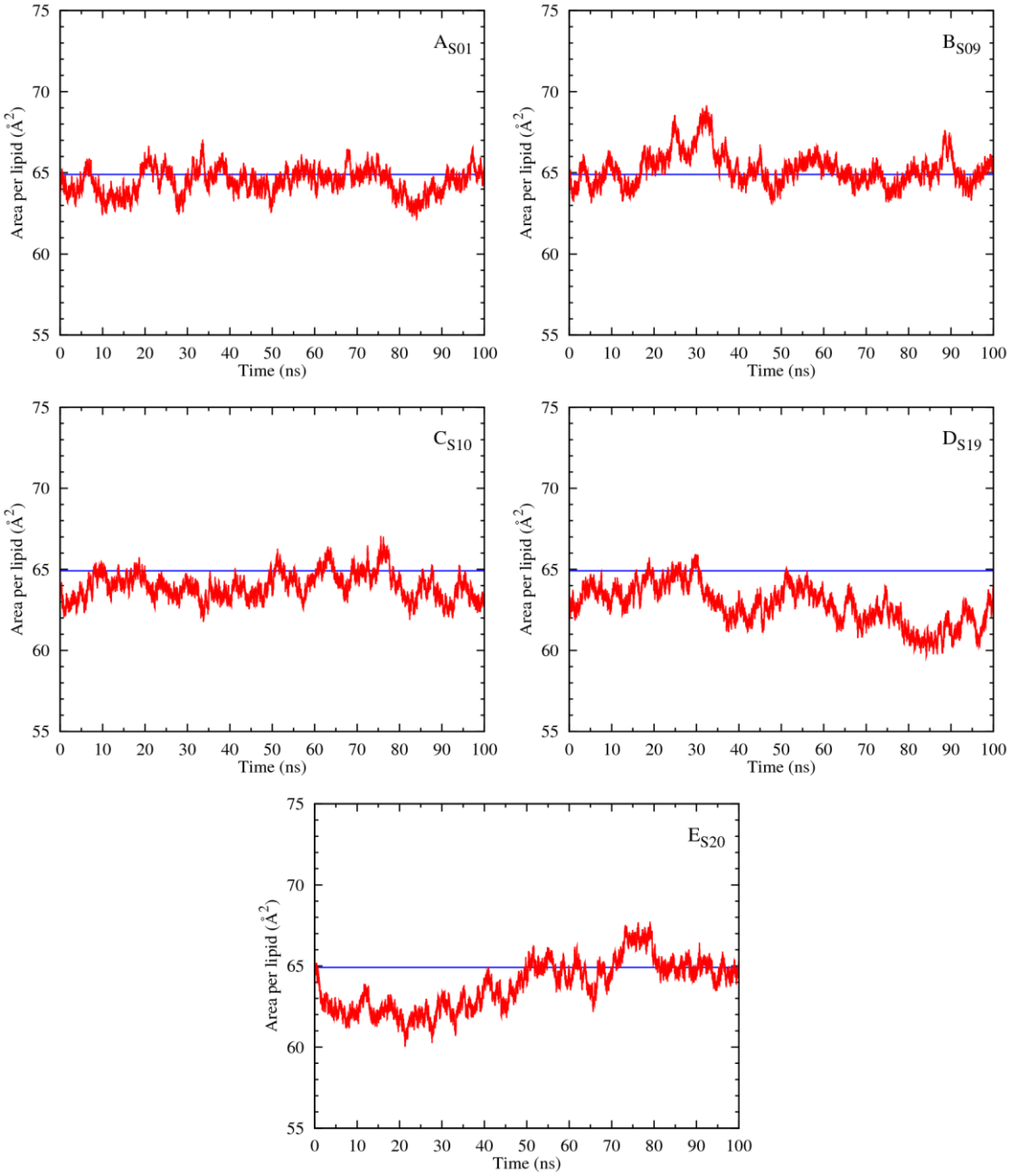

Figure 52 – Evolution of area per lipid through the course of the MD simulation time is represented in red. The reference value from Félix *et al* (117) is plotted as a blue line.

Bilayer thickness

Given that area per lipid and bilayer thickness are two inversely proportional parameters, when the area per lipid increases, the bilayer thickness decreases. Following this concept and the analysis above for area per lipid evolution of systems A-E, the estimated bilayer thickness for these systems is expected to vary accordingly (see Figure 53). Overall there is a slight

increase in the average value for the bilayer thickness increase relatively to the average bilayer thickness reported by Félix *et al*. (38.1 Å). However the difference to the reference value varies between 0.1 Å, for systems A and E, and 2.1 Å, for system D. Therefore, the bilayer thickness of systems A-E seems to undergo little interference from the presence of each receptor (see Table 40).

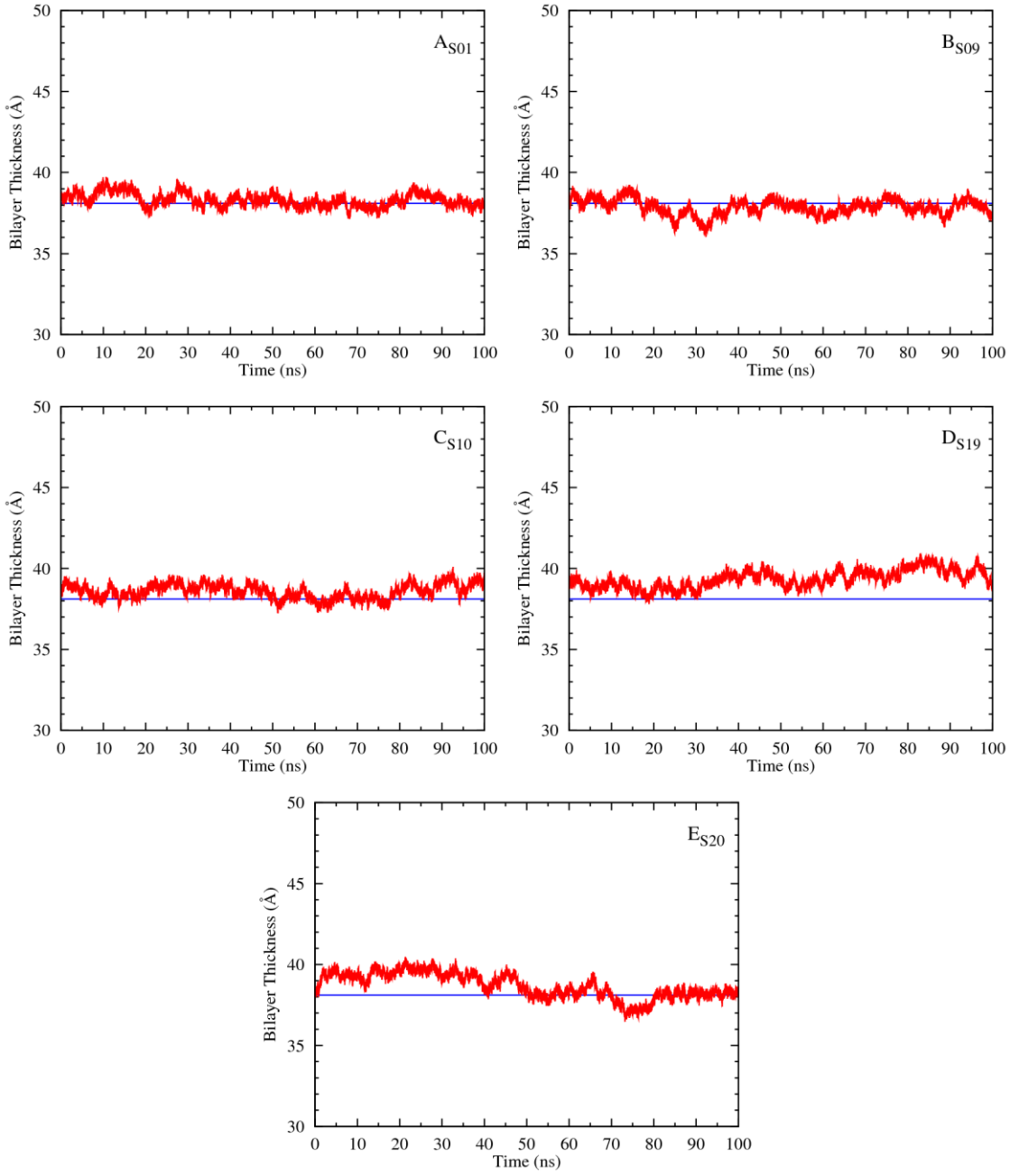

Figure 53 – Evolution of the bilayer thickness (red line) through the MD simulation of systems A-E. Comparison with theoretical values from membrane model I simulation (64.9 Å in blue).

Table 40 – Summarized results of bilayer thickness parameter for systems A-E, over 40ns of sampling time.

System	Receptor	R1		R2	
		Average	Std. Dev.	Average	Std. Dev.
A	S01	38.2	0.5	38.5	1.0
B	S09	37.9	0.4	37.7	0.4
C	S10	38.5	0.5	39.0	0.3
D	S19	39.8	0.4	40.2	0.4
E	S20	38.0	0.5	38.7	0.2

Electron density profile

As stated before, the electron density profiles allow the determination of individual positions occupied by the different components of the system, during a period of the simulation. In this context, it is of special interest to verify the position occupied by S01, S09, S10, S19 and S20 in systems A to E. Each system electron density profiles (water, phospholipids, phosphorus atoms and receptor) are plotted in Figure 54, along with the system profile of reference model I.

The density profiles of systems A-E were calculated for the last 40ns of simulation time. All systems exhibit two peaks separated by 38 to 40Å; these distances are in agreement with the previous calculated bilayer thicknesses (see Table 37). The profiles show a good fitting with the reference profile, although system D shows a small misalignment in the system profile.

Figure 54 reveals that during the sampling time, receptors were constantly near to the phospholipids head groups, always below the water/lipid interface. The density profiles of S01, S09, S10, S19 and S20 present peaks at 7.8, 9.2, 9.0, 8.5 and 7.2Å from the closest interface, respectively. These findings corroborate the results obtained from the analysis of the receptors relative positions to the interface (see Table 37 in Relative position to interface).

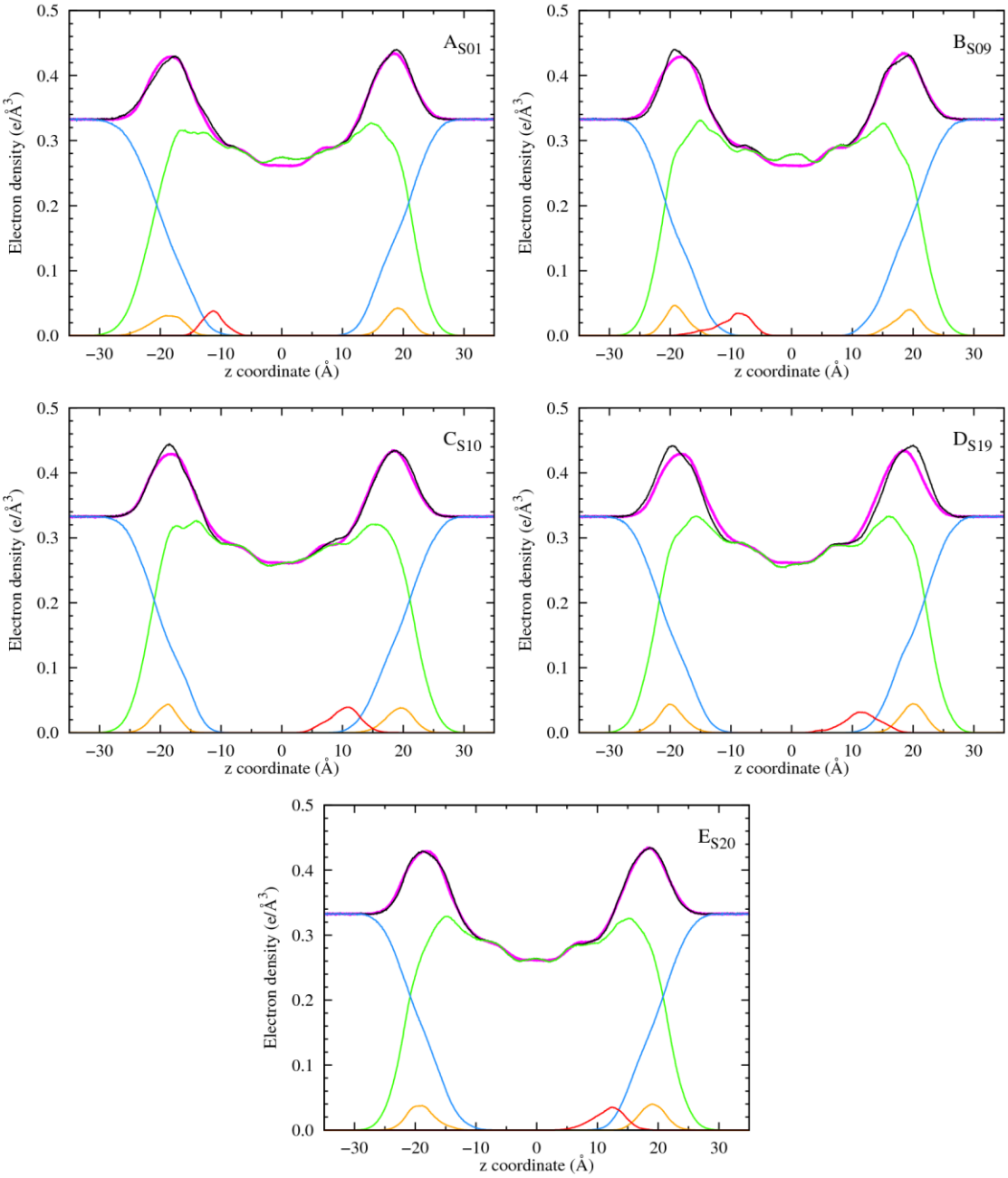

Figure 54 – Electron density profiles of the membrane systems A-E, estimated for the last 40 ns of MD simulation. The receptor is plotted as a red line and scaled 5 times. The full system is plotted in black, the water in blue, the phospholipids in green and the phosphorus in dark yellow. *z*= 0 Å corresponds to the core of the POPC bilayer. Reference profile from membrane model is represented in magenta.

Order parameters (chain order)

The order parameters of these systems shown a slight increase in the $|S_{CD}|$ values when a receptor has permeated the water/lipid interface (see Figure 55). The increase of the $|S_{CD}|$

values for the *sn*-1 and *sn*-2 chains, when compared with the order parameters for reference model I, occurs in systems A, B and D. Although the increase of the $|S_{CD}|$ values for the *sn*-2 chains indicates that these chains are more ordered, it is important to note that the computed *sn*-1 parameters for POPC are systematically overestimated when simulated with the LIPID11 force field.

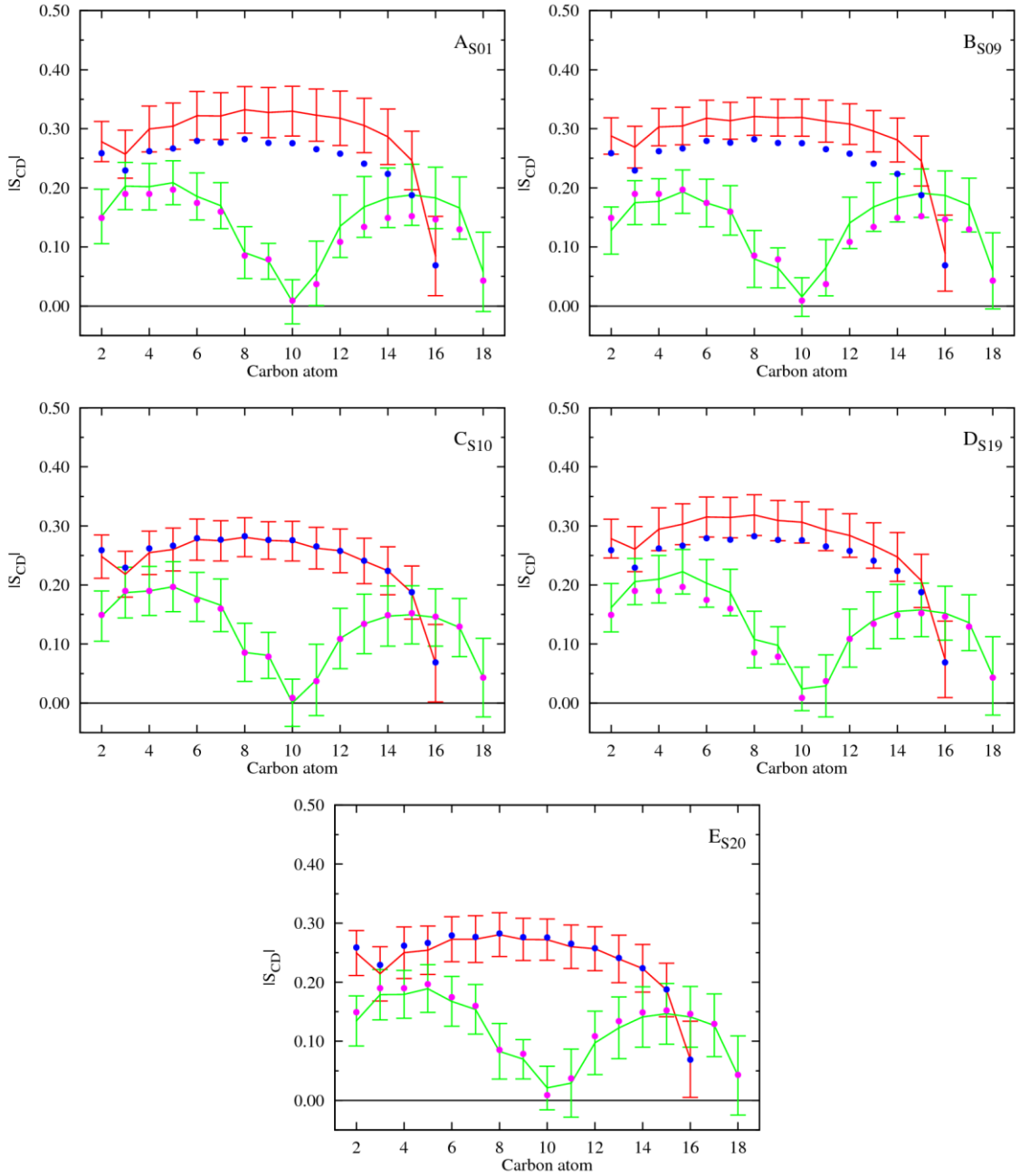

Figure 55 – Computed $|S_{CD}|$ for palmitoyl and oleyl chains for 40 ns of sampling of simulations A, B and D; for the last 15 ns of sampling of system C and for the last 10ns of system E. The $|S_{CD}|$ values calculated for the *sn*-1 chain are shown in red, while the values for the *sn*-2 chain are shown in green. The error bars associated with these results correspond to the standard deviation. The computed $|S_{CD}|$ values from reference model I are presented in blue (*sn*-1 chain), and magenta (*sn*-2 chain).

The results for the parameters evaluated on a representative replicate of systems A-E are summarized in Table 41.

Table 41 –Comparison between the parameters for the MD simulations of systems A to E.

Parameter	**System**					
	A	B	C	D	E	Theoretical (model I)
Arrival to interface (ns)	16	7	15	10	15	-
Receptor hydration	5.0±2.5	5.1±2.1	6.0±2.4	8.1±2.7	7.8±2.4	-
Area per lipid ($Å^2$)	64.4±0.8	64.9±0.7	64.2±1.0	60.6±0.8	65.1±1.0	64.9
Bilayer thickness (Å)	38.2±0.4	37.9±0.4	38.5±0.54	40.2±0.4	38.0±0.5	38.1
Electron density profile	Good fitting with theoretical results	Good fitting with theoretical results	Good fitting with theoretical results	Misalignment with theoretical results	Good fitting with theoretical results	(116-117)
Order parameters	$\|S_{CD}\|$ increased values	$\|S_{CD}\|$ increased values	$\|S_{CD}\|$ increased values	$\|S_{CD}\|$ increased values	$\|S_{CD}\|$ increased values	(116-117)

The data shown in Table 41 indicates that the presence of the receptors has negligible effects on the membrane structural properties with a decrease of 6.6 % maximum in the area per lipid, and an increase of 5.9 % in the bilayer thickness (S19 in system D). This indicates that, even though receptors affect membrane properties, this effect is negligible and does not compromise the membrane integrity. Regarding the bilayer thickness, in spite of the differences, the bilayer thickness of systems A-E seems to undergo little interference from the presence of each receptor. The electron density profiles show a good fitting with the reference profile of model I, although system D shows a small misalignment in the system profile. The impact of the receptors in the membrane properties reflects more significantly in the *sn*-2 order parameters, showing a tendency of these lipid tails to order. The analysis of the chloride binding ability of the squaramides has shown that neither of the receptors were able to capture the anion after the beginning of the simulation. These findings demonstrate that one squaramide molecule is not enough to establish hydrogen bonds in competitive media, such as water.

3.2.2. *MD Simulations of the receptors starting from within the membrane*

Methodology

To simulate the systems F to J, membrane model II was used to place each chloride association within the bilayer pore, using *Packmol*. Topology and coordinate files were created using *tLEaP*. Systems F to J underwent a subsequent preparation stage followed by a final multi-step simulation stage. The methodology used is similar to the one previously described for pure membrane model II (see Section 3.1), with the exception for the applied restraints.

In the preparation stage, restraints were applied to the POPC lipids, chloride complex and sodium ion (500 kcal/mol Å^2), while the water molecules, chloride complex and sodium ion were restrained in the following minimization step (500 kcal/molÅ^2). Restrains were removed and the full system was minimized. During the NVT MD run, at 303 K, weak restraints of 10 kcal/mol Å^2 were applied to the chloride association to maintain the complex relative position. At the end of this stage the pore was closed.

The preparation stage is followed by a multi-stage simulation, in which the system is equally minimized and heated under the same simulation conditions as the systems A-E. This is followed by an equilibration run of 5 ns in an NPγT ensemble, using a surface tension of 17 dyn/cm and weak restraints (5 kcal/mol Å^2) on the chloride association complex. The restraints were then removed and the system was subjected to 100 ns of production run. Two replicates were performed with the CUDA versions of the PMEMD executable.

Results and Discussion

Initial and final snapshots

As for the simulations with the receptors in the water phase, two replictaes were also performed for simulations with the receptors within the bilayer core. All replicates follow an equivalent behaviour to the ones illustrated and the results can be consulted in Appendix 1.

Figures 60-64 present three snapshots illustrating the different positions of each chloride complex over the 100ns of MD simulation. Complexes were placed within the bilayer core. All

the receptors migrated from the bilayer core to the water/lipid interface, releasing the chloride to the water phase

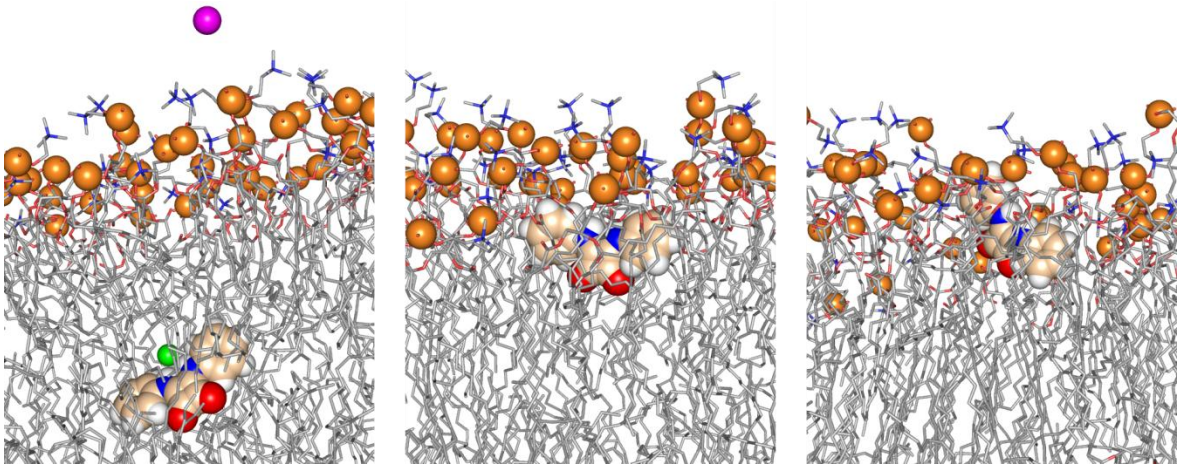

Figure 56 – Snapshots of system F, taken at different simulation times (0, 50 and 100 ns), showing the diffusion of S01. Images show the different positions of the receptor in the membrane. The receptor is drawn in a space filling model with carbon atoms in wheat, oxygen atoms in red, nitrogen atoms in blue and hydrogen atoms in white. The chloride and sodium ions, as well as the phosphorus atoms from the bilayer are represented as green, magenta and orange spheres, scaled to 0.7 vdW radius, respectively. In POPC lipids, carbon, nitrogen and oxygen atoms are drawn as grey, blue and red lines, respectively, while C-H hydrogen atoms have been omitted for clarity.

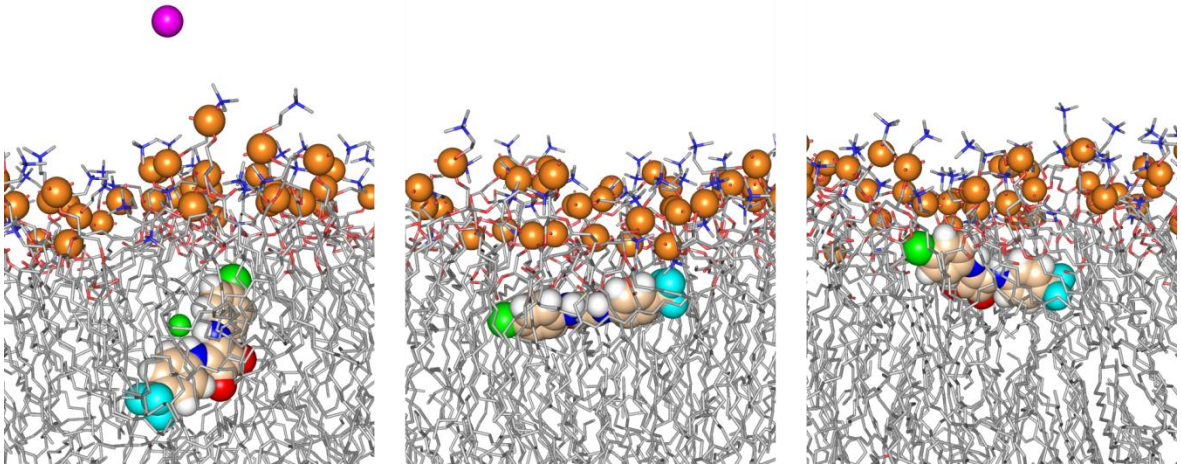

Figure 57 - Snapshots of system G, illustrating the diffusion process of S09. Fluorine atoms are drawn as cyan spheres. Remaining details as given in Figure 56.

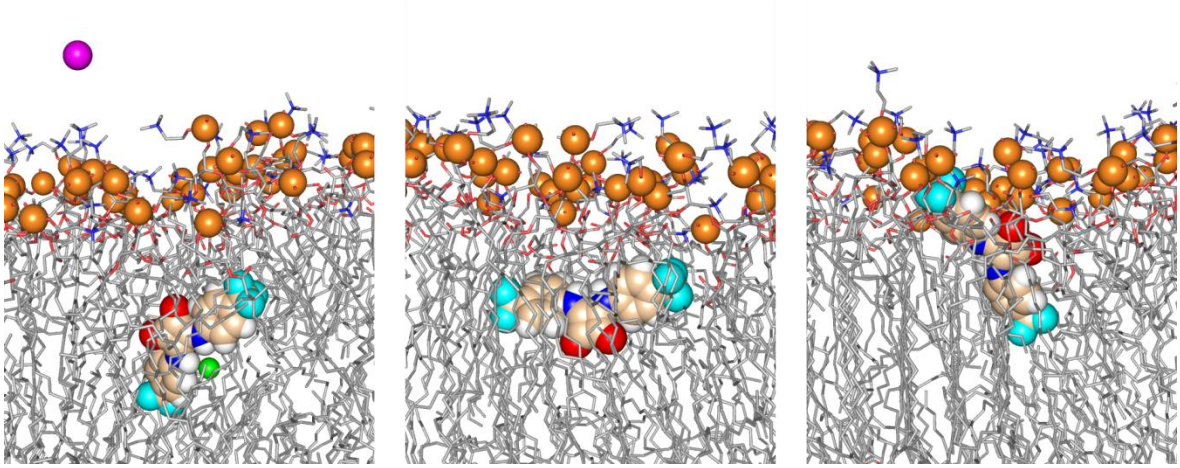

Figure 58 - Snapshots of system H, illustrating the diffusion process of S10. Fluorine atoms are drawn as cyan spheres. Remaining details as given in Figure 56.

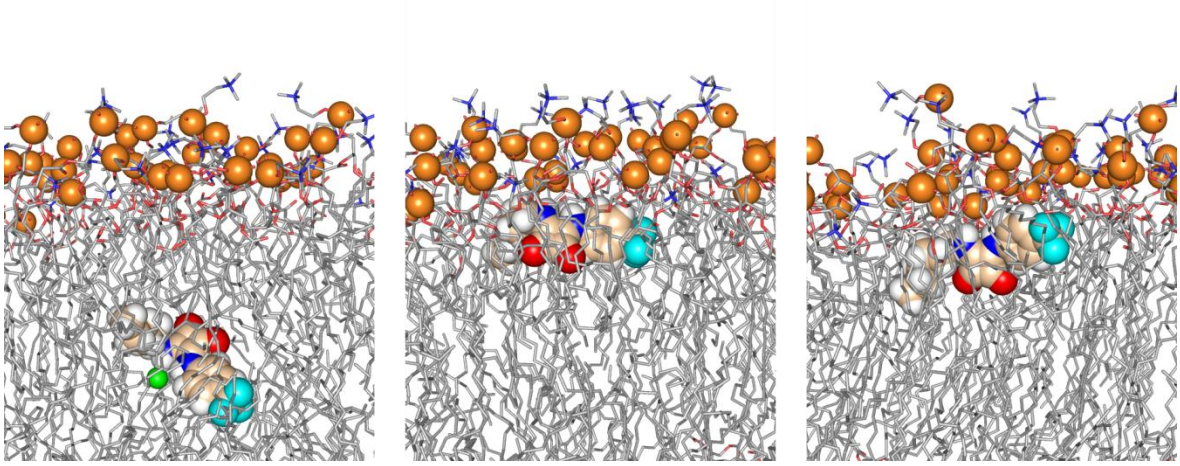

Figure 59 - Snapshots of system I, illustrating the diffusion process of S19. Fluorine atoms are drawn as cyan spheres. Remaining details as given in Figure 56.

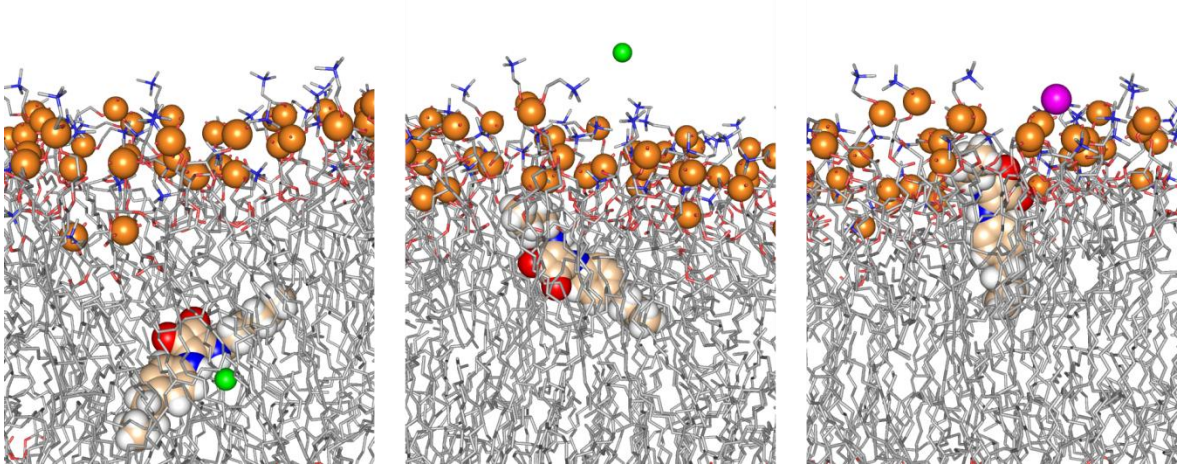

Figure 60 - Snapshots of system J, illustrating the diffusion process of S20. Remaining details as given in Figure 56.

Relative position to interface

Similarly to systems A to E, when the squaramide complexes started within the bilayer the relative positions were also evaluated tracking the distance along the *z* axis between the centre of mass of the receptor and the closest membrane interface. The evolution of these relative positions is shown in Figure 61.

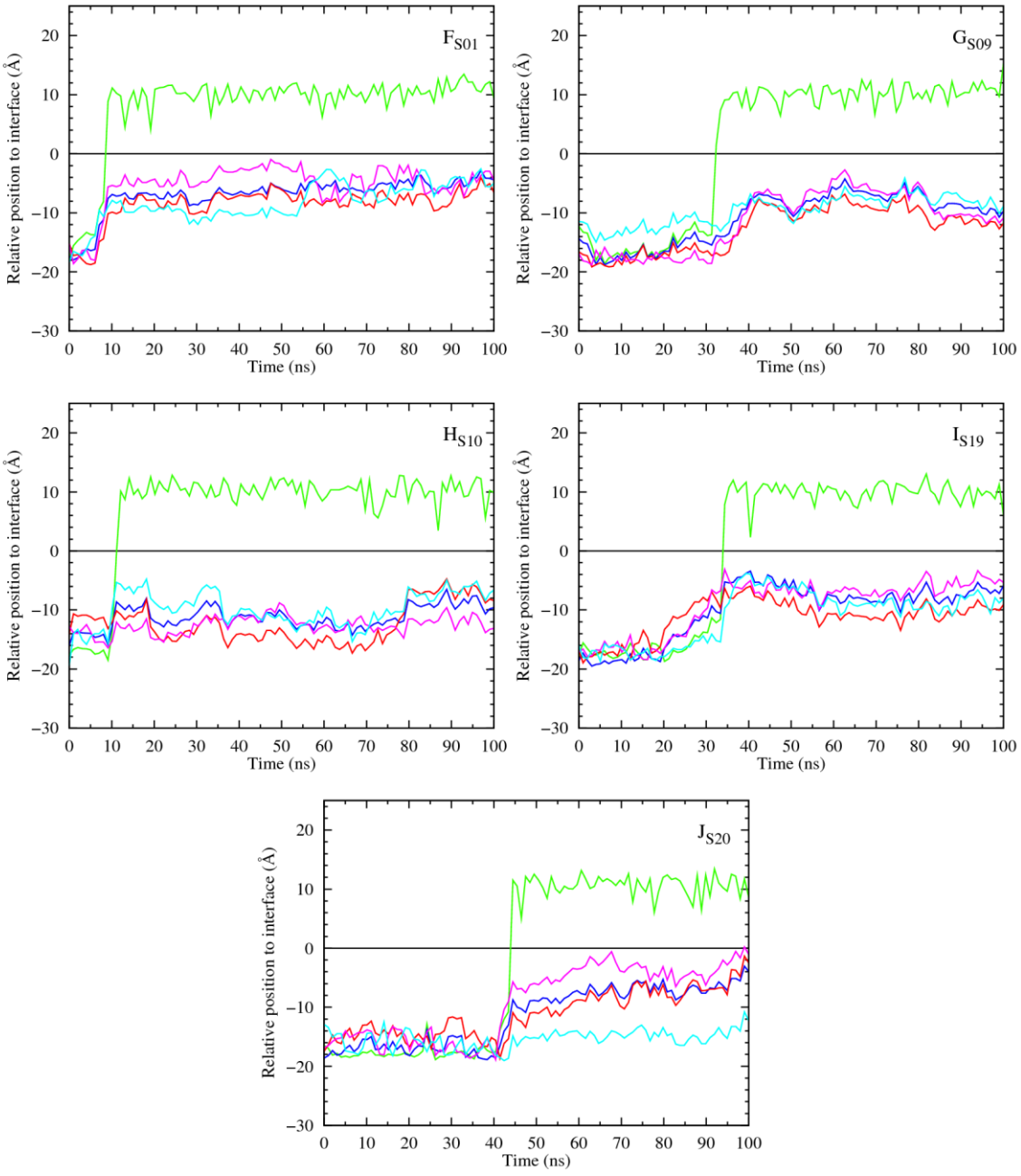

Figure 61 - Evolution of the receptor and chloride relative positions to the water/lipid interface (*z* = 0 Å). In green is represented the chloride ion, in red the centre of mass of the oxygen atoms from the receptor, in blue the centre of mass of the nitrogen atoms, in magenta and cyan are represented the phenyl groups (F, G and H); a phenyl group and an aliphatic chain (I) or an aliphatic chain and a butyl group (J), respectively. Data was smoothed using Bézier curves.

Receptors diffused within the lipid tails during the initial period of simulation and, when they reached approximately 10 Å from the water/lipid interface, the chloride was spontaneously released to the water phase. S01 and S10 released the chloride at 8 ns and 11 ns of simulation time respectively, while S09 and S19 maintained the chloride ion bonded over 32 ns and 34 ns respectively. In system J, S20 released the chloride after 44 ns of simulation time. When the receptors reached the phospholipid head groups, they stabilized at a defined distance from the interface (see Table 42).

As mentioned before, the diffusion of the five receptors is very similar (see Figure 61). As the receptor moves towards the interface, a substituent group begins to breach between the phospholipid head groups. In the case of systems F to I, it is a phenyl group of each receptor, while for S20, in system J, it is the hexyl chain. As further discussed below, hydrogen bonds are then established between the each receptor's core and the phospholipid head groups.

Table 42 – Relative distance (Å) of the receptors to the water/lipid interface for systems F-J, for the last 40ns of simulation time.

System	Receptor	R1		R2	
		Average	Std. Dev.	Average	Std. Dev.
F	S01	5.6	1.2	7.1	1.4
G	S09	8.0	1.9	7.5	0.8
H	S10	12.3	1.0	10.9	2.0
I	S19	7.5	1.0	7.6	1.2
J	S20	8.3	1.3	9.8	1.0

Hydration

The number of water molecules within the first solvation shell (3.5 Å cut-off) is unsurprisingly lower than the observed in the simulations of systems A to E, due to the starting positions of the receptors in the membrane. The evolution of this parameter is shown in Figure 62 for systems F to J

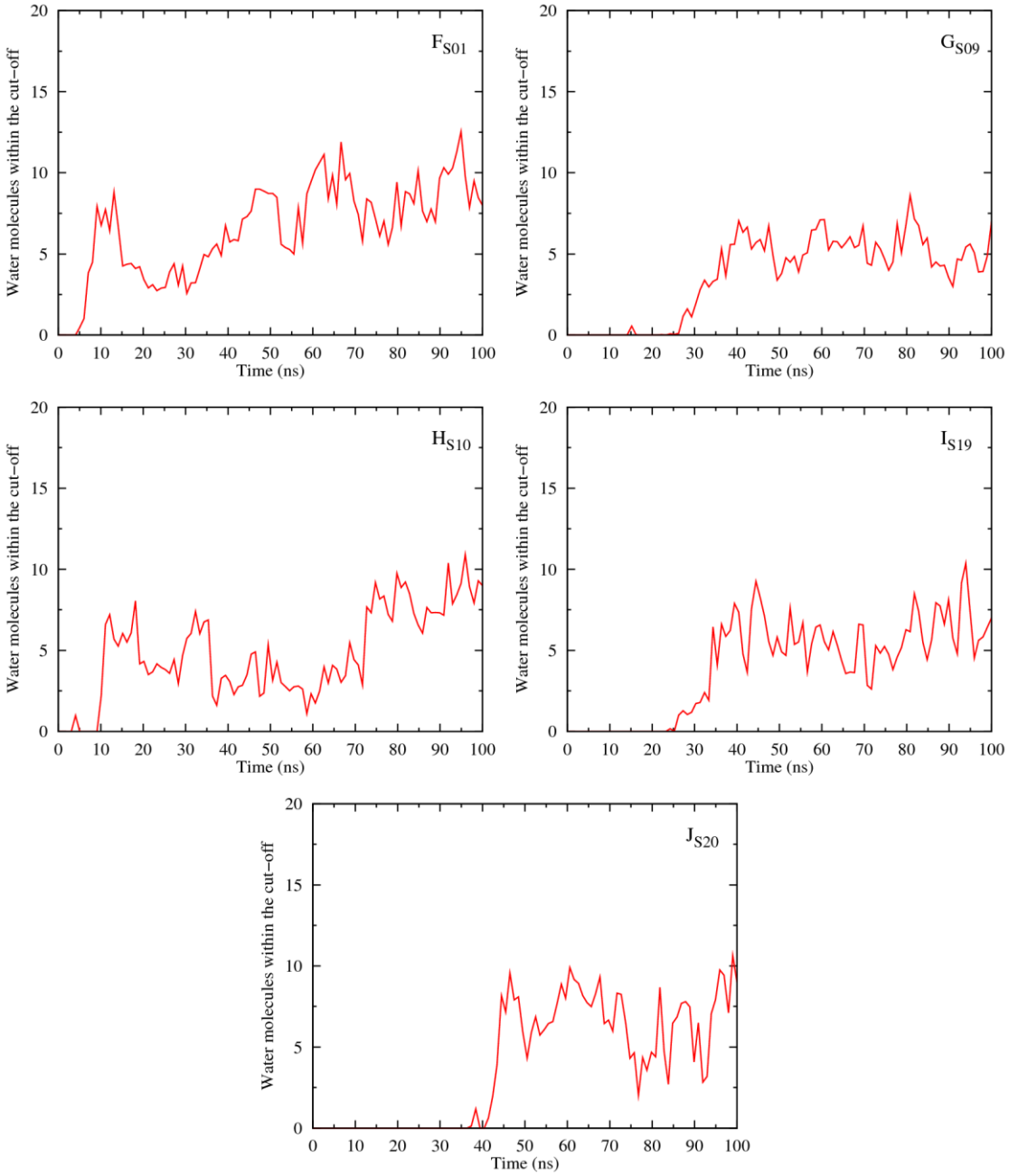

Figure 62 - Variation of the number of water molecules within the solvation shell defined by a cut-off of 3.5Å from receptors S01 (F), S09 (G), S10 (H), S19 (I) and S20 (J). Data was smoothed using Bèzier curves.

In the beginning of the MD simulation the receptors were in the membrane core and the number of waters at 3.5Å is approximately zero. However, as the receptors moved towards the water/lipid interface, the number of water molecules in the first solvation shell increased, although neither of the receptors reached the water phase. On average, 5 to 10 water molecules were present within this solvation shell for each receptor (see Table 43).

Table 43 – Summarized information of receptor's hydration of systems F-J, in the last 40ns of simulation time.

System	Receptor	R1		R2	
		Average	Std. Dev.	Average	Std. Dev.
F	S01	8.8	2.6	8.5	2.6
G	S09	5.3	1.8	6.1	1.8
H	S10	4.9	1.8	6.8	2.9
I	S19	9.1	2.9	5.6	2.3
J	S20	6.7	2.6	9.6	3.0

Hydrogen bonds

Insights of the receptors' interactions within the POPC bilayer were obtained by the analysis of hydrogen bonds established between the N-H binding groups from the receptor and the anion, the lipid head groups or the ester groups present in the *sn-1* and *sn-2* lipid chains. As mentioned before, the hydrogen bonds that each receptor establishes with different system components depend on the relative position of the receptor to the water/lipid interface (see Figure 63).

Since the chloride complexes started within the bilayer core, N-H···Cl^- hydrogen bonds were established until the receptor diffused until approximately 10 Å from the interface. At this point, the number of water molecules in the receptor's first solvation shell increased, promoting the chloride release and the replacement of the N-H···Cl^- interactions for NH···OH_2 hydrogen bonds, mostly in systems G, H and I. N-H···O=C interactions with the *sn*-1 and *sn*-2 lipid chains were also observed in the systems with receptors S10 and S20. On the other hand, S09 could only establish N-H···O=C hydrogen bonds with the ester groups of the *sn*-1 lipid chains. In systems F and I, S01 and S19's N-H···Cl^- hydrogen bonds were replaced by N-H···O_4P and N-H···O=C hydrogen bonds, with the lipid head groups and the ester groups from *sn*-1 lipid chains, respectively.

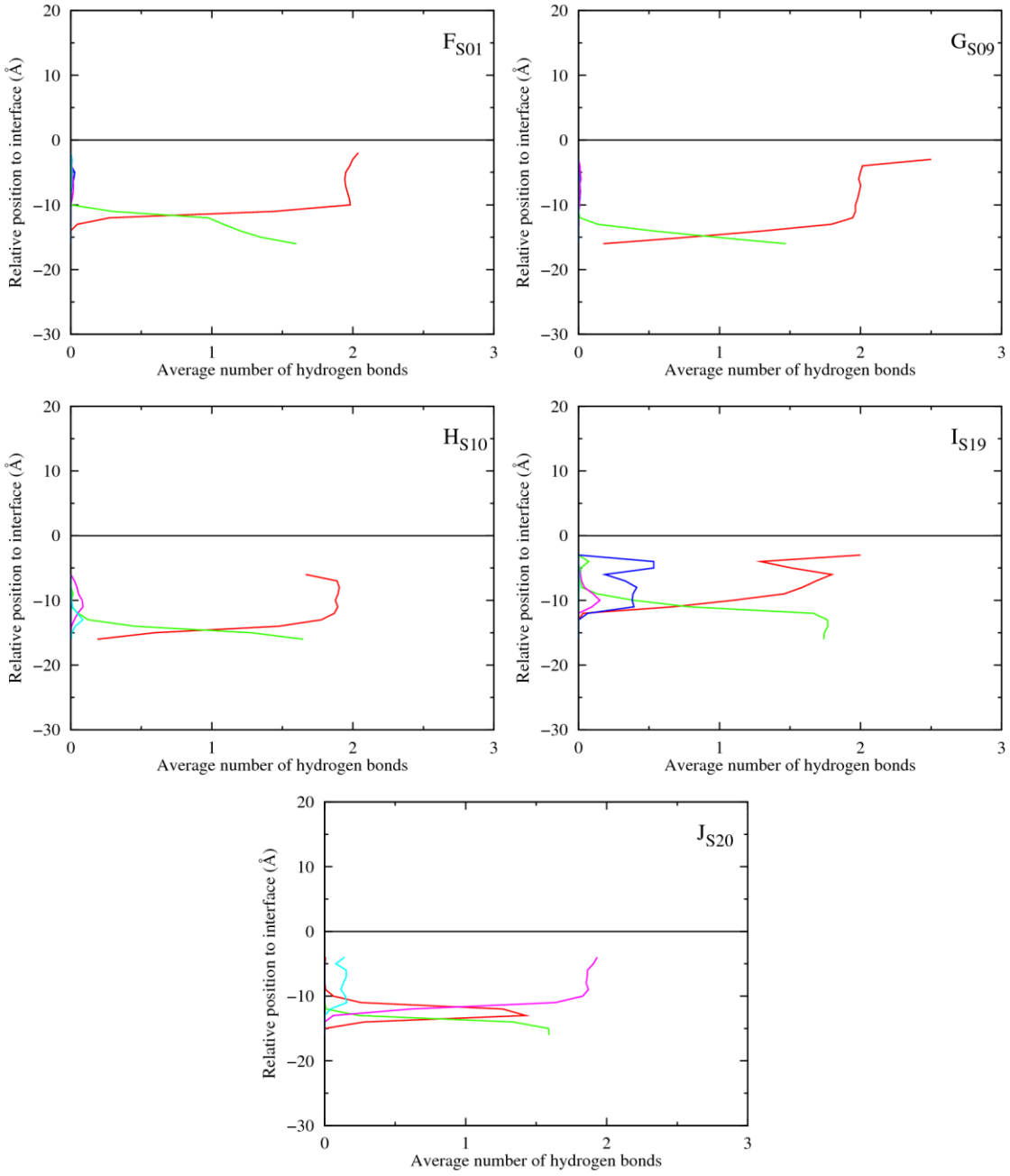

Figure 63 - Average number of hydrogen bonds *vs* the relative position of the centre of mass of each receptor. The following colour scheme was used for the hydrogen bonds established between the receptor and water molecules (red), chloride ion (green), POPC head groups (blue), ester groups from POPC *sn*-1 chains (magenta) and *sn*-2 chains (cyan).

Torsion angles

The conformational changes experienced by each receptor throughout the 100 ns of MD simulation time were evaluated using the C=C-N-C torsion angles (see Figure 49). The conformational changes experienced by each receptor within the bilayer, before or after the chloride release are equivalent. Therefore, the distribution of C=C-N-C torsion angles for the 100 ns simulation is plotted in the histograms of Figure 64. The negative C=C-N-C torsion angles lower than -120° were shifted by the addition of 360°. In the subsequent analysis, torsion angles within the 120° to 240° range correspond to an *anti/anti* conformation consistent with chloride bonding.

As mentioned before, squaramides are naturally rigid molecules and the POPC bilayer is a highly packed medium. Considering both conditions, the conformational freedom of the receptors is limited and the initial *anti/anti* conformation is preserved during the simulation time in all systems.

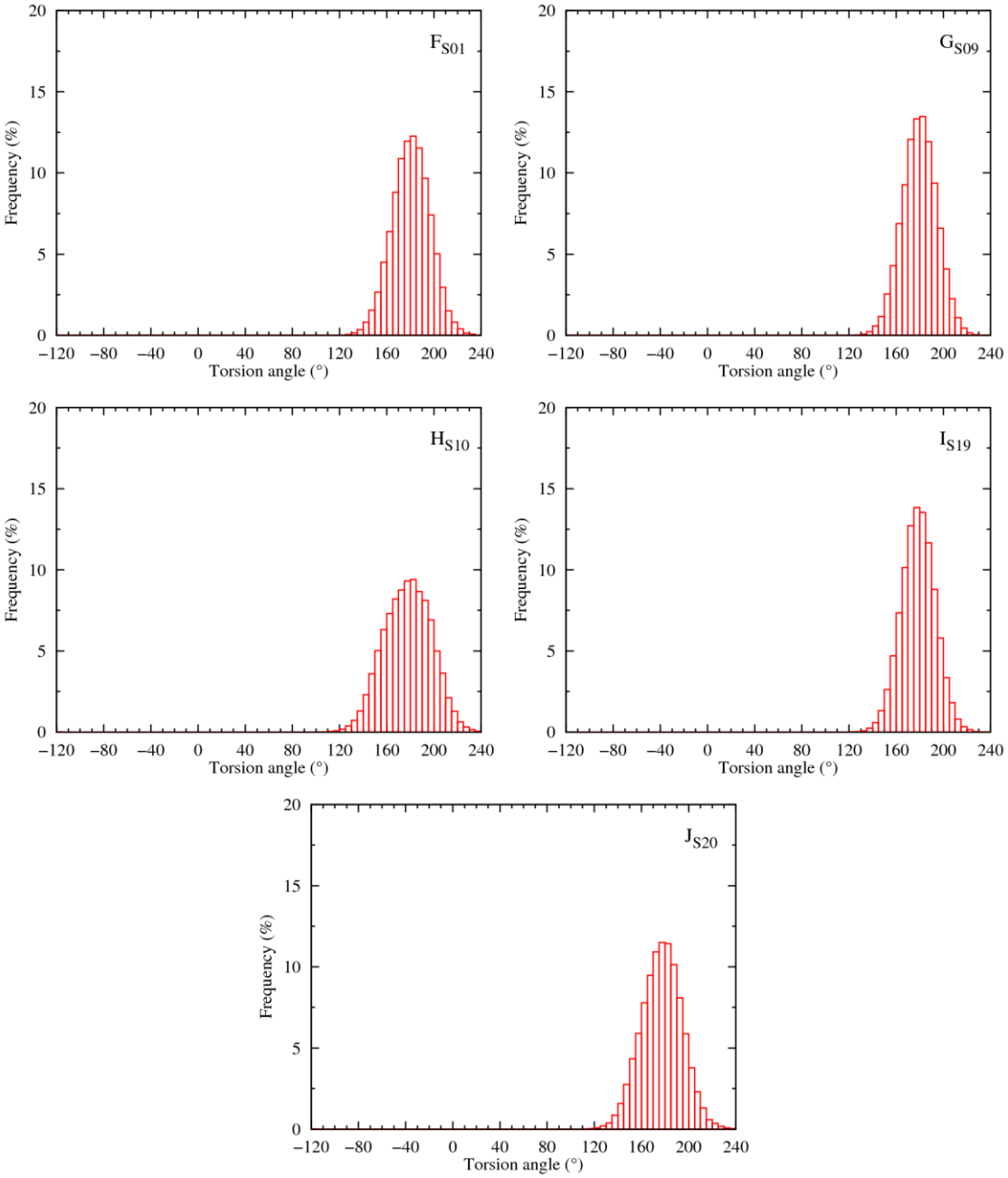

Figure 64 - Frequency histograms showing the distribution of the two C=C-N-C torsion angles values of S01-S20 in simulations F-J, in the last 40ns of simulation time.

Area per Lipid

The impact caused by receptors S01 to S20 in the membrane structure was estimated for systems F to J through the evaluation of the corresponding area per lipid for the last 40 ns of each MD simulation. The average area per lipid values for each system are listed in Table 44 and the evolution of this parameter during the 100 ns of simulation time is presented in Figure 65.

According to Figure 65, receptors S01-S20 have a small impact on the area per lipid parameter. In fact, the highest variations correspond to decreases of approximately 4 $Å^2$ area per lipid relatively to the average value in the free membrane model II simulation (65.5 $Å^2$). The impact of the receptors on this structural parameter was not significant, with an area per lipid variation of less than 6.2 %.

Table 44 – Summarized results of area per lipid ($Å^2$) parameter for systems F-J, over 40ns of sampling time.

System	Receptor	R1		R2	
		Average	Std. Dev.	Average	Std. Dev.
F	S01	62.7	0.9	62.9	0.9
G	S09	63.2	0.67	62.4	0.8
H	S10	63.2	1.3	63.1	0.6
I	S19	64.2	0.9	65.3	1.2
J	S20	62.0	1.0	61.4	1.5

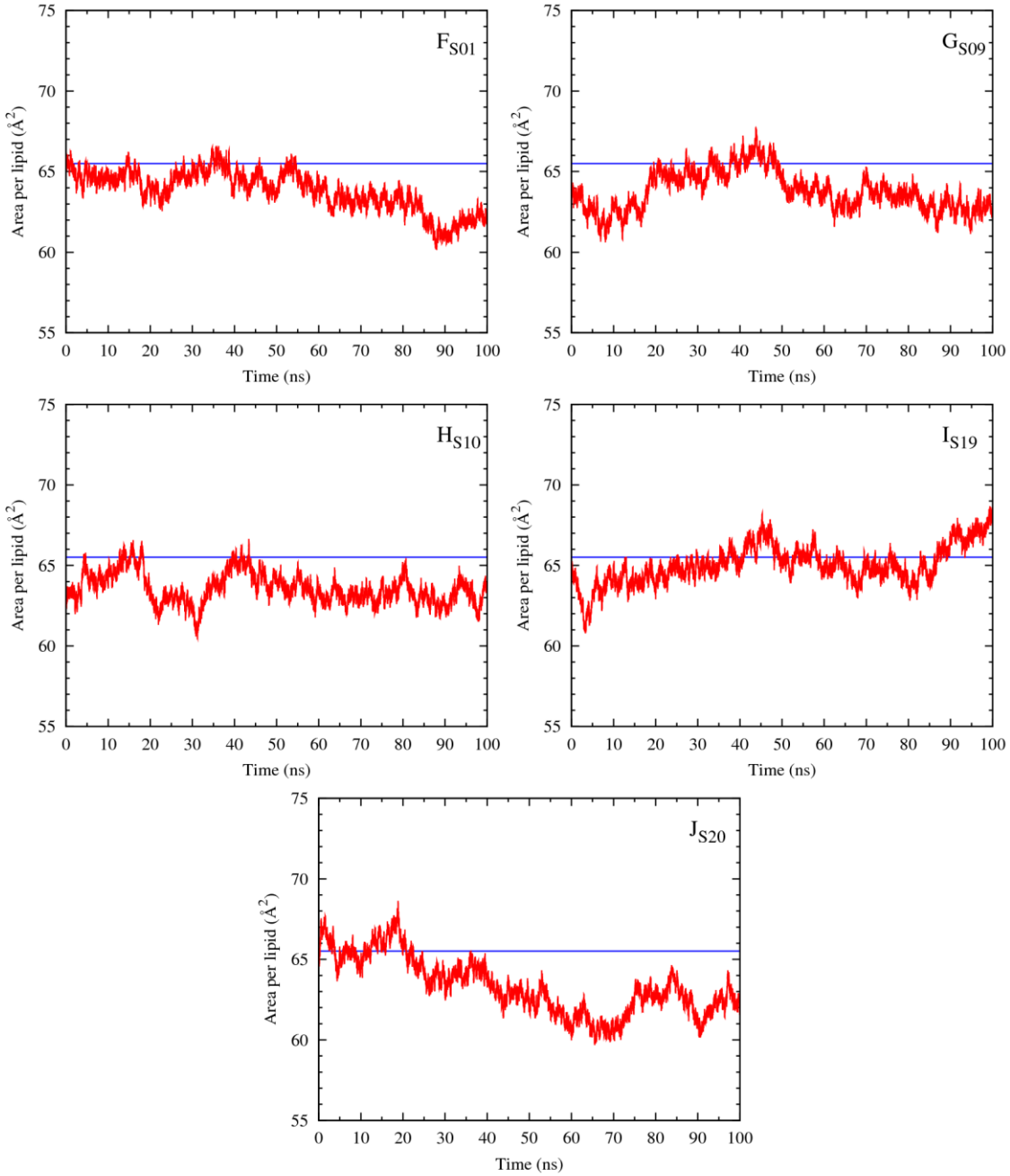

Figure 65 - Evolution of area per lipid through the course of the MD simulation time is represented in red. The reference value from the simulation of membrane model II is plotted as a blue line.

Bilayer thickness

The bilayer thickness was also assessed, to evaluate the impact of each receptor on the membrane properties. As discussed earlier, the area per lipid and the bilayer thickness are inversely proportional parameters so a concomitant slight increase in most systems was expected. The variation of the bilayer thickness of each system during the simulation time is

shown in Figure 66 and the average bilayer thickness values found for each one of them are listed in Table 45.

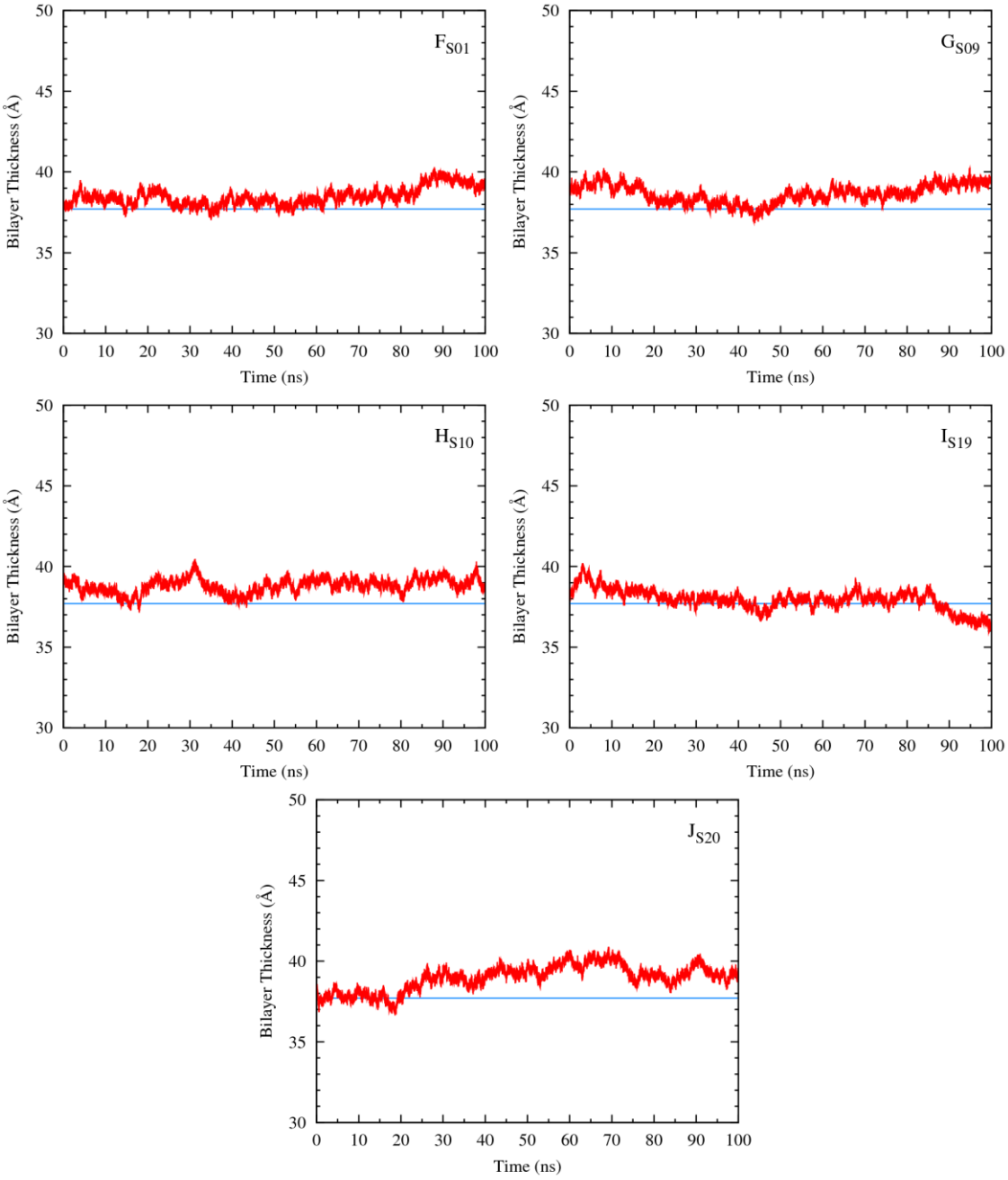

Figure 66 - Evolution of the bilayer thickness (red line) through the MD simulation of systems A-E. The reference value from the simulation of membrane model II is plotted as a blue line.

Table 45 – Summarized results of bilayer thickness parameter for systems A-E, over 40ns of sampling time.

System	Receptor	R1		R2	
		Average	Std. Dev.	Average	Std. Dev.
F	S01	38.9	0.5	39.1	0.5
G	S09	38.9	0.4	39.1	0.4
H	S10	38.6	0.6	39.0	0.3
I	S19	38.3	0.5	37.7	0.7
J	S20	39.4	0.5	39.9	0.7

For system F to J the average value for the bilayer thickness increases relatively to the average value from the free membrane model II simulation (37.7 Å). However the difference to the reference value varies between 0.6 Å, for system I, and 2.2 Å, for system J. In spite of the variations, a fluctuation of 5.7 % in the bilayer thickness does not appear to compromise the membrane integrity.

Electron density profile

The electron density profiles of systems F-J were obtained from the last 40 ns of MD simulation time of each system and are plotted in Figure 67. Individual density profiles for the water slabs (blue line), phospholipid bilayer (green line) and phosphate head groups (dark yellow line) were represented, along with the electron density profile of each receptor (red line).

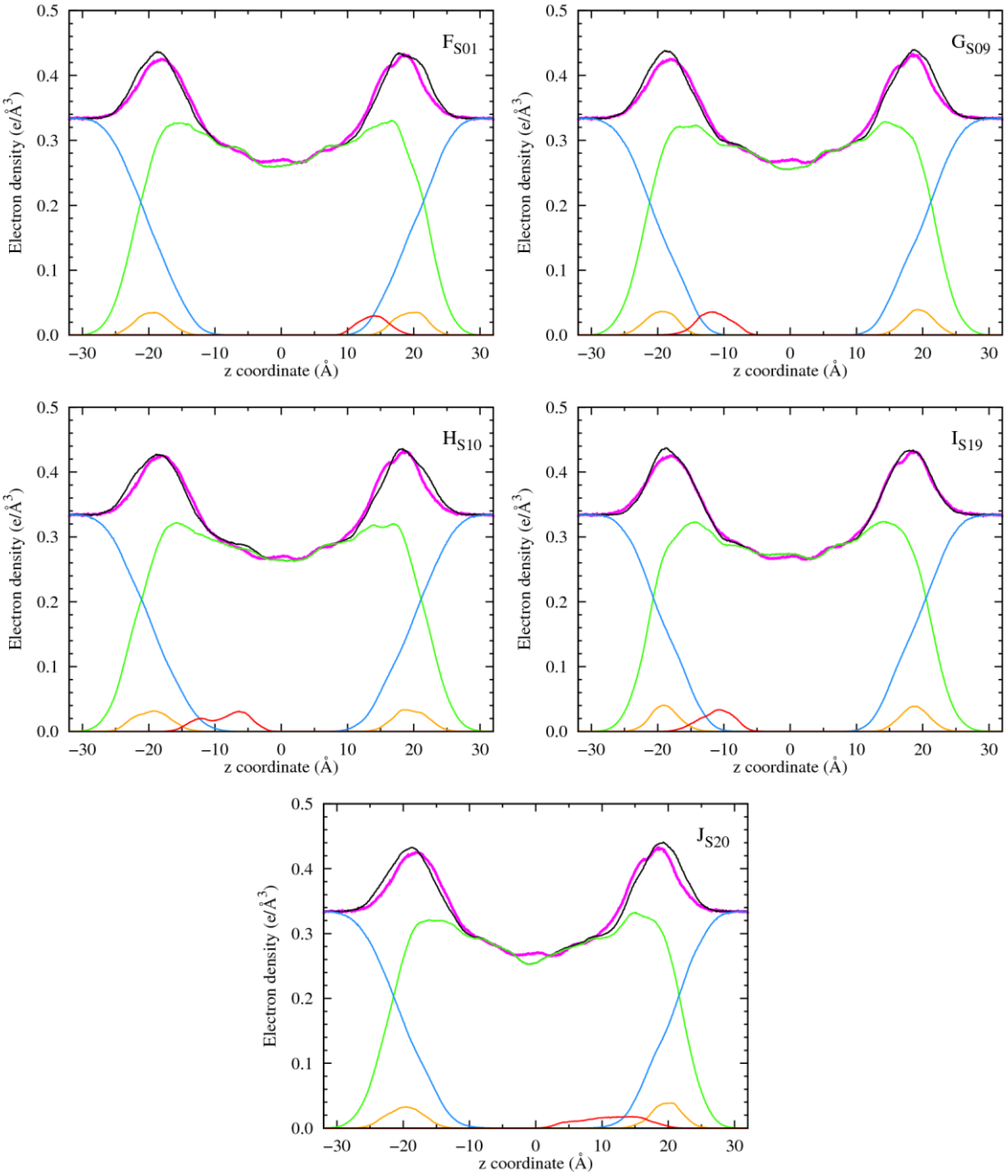

Figure 67 - Electron density profiles of the membrane systems F-J, estimated for the last 40 ns of MD simulation. The receptor is plotted as a red line and scaled 5 times. The full system is plotted in black, the water in blue, the phospholipids in green and the phosphorus in dark yellow. *z* =0 Å corresponds to the core of the POPC bilayer. System profile from membrane model II simulation is represented in magenta.

The electron density profile of each system shows a symmetric shape around the *z* = 0 Å, with two peaks at similar distances from it. The distance between the two phosphorus peaks is consistent with the bilayer thickness previously calculated for each system. The electron densities around *z* = 0 Å indicates a possible intercalation between the phospholipid tails of each leaflet, consistent with membrane model II.

During the sampling time, receptors were close to the lipid head groups. S01 presents a peak at 6 Å from the interface, while S09, S19 and S20 present a peak at approximately 8 Å from the interface. On the other hand, in system H, S10 has a peak *ca.* 11 Å from the interface. These findings supported the results obtained during the analysis of the relative position of the receptors in each system.

Overall there is a good alignment between each individual system profile (black line) and the experimental electronic density profile for the free membrane model II simulation (magenta line), meaning that the bilayer structure is preserved during the simulation. Small discrepancies were detected only in system J with receptor S20.

Order parameters (chain order)

Order parameters were evaluated during the last 40 ns of MD simulation (see Figure 68). Supporting the findings obtained so far, the order parameters approach to the theoretical values from the simulation of the free membrane model II. However, for systems H and I, when the receptor is present, increased |SCD| values for the sn-1 and sn-2 chains are observed. This indicates that the presence of the receptors in the membrane core may influence the lipid organization and the membrane flexibility, without compromising its structure and function.

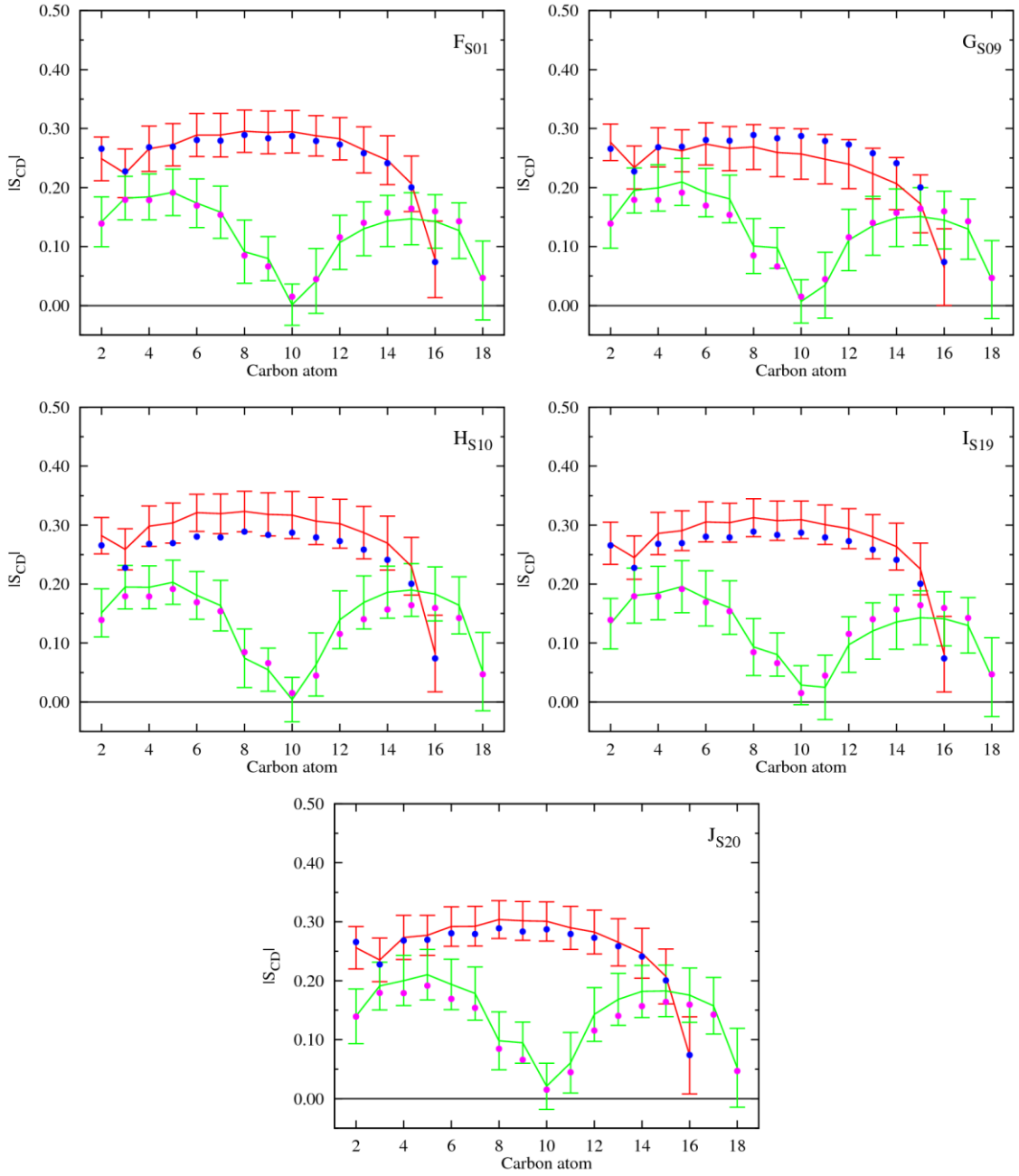

Figure 68 – Computed $|S_{CD}|$ for palmitoyl and oleyl chains for 40 ns of sampling of simulations F-J. The $|S_{CD}|$ values calculated for the *sn*-1 chain are shown in red, while the values for the *sn*-2 chain are shown in green. The error bars associated with these results correspond to the standard deviation. The computed $|S_{CD}|$ values from membrane model II simulation are presented in blue (*sn*-1 chain), and brown (*sn*-2 chain).

The results for the parameters evaluated on a representative replicate of systems F-J are presented in Table 46.

Table 46 - Comparison between biophysical parameters for the phospholipid bilayer systems F-J.

Parameter	**System**					
	F	G	H	I	J	Theoretical (model II)
Arrival to interface (ns)	15	11	32	34	44	-
Receptor hydration	5.3±2.3	5.3±1.8	6.8±2.9	5.6±2.3	6.7±2.6	-
Area per lipid (Å^2)	64.7±0.9	63.2±0.7	63.1±0.6	65.3±1.2	61.4±1.5	65.5
Bilayer thickness (Å)	37.9±0.8	38.9±0.4	39.0±0.3	37.7±0.7	39.9±0.7	37.7
Electron density profile	Good fitting with theoretical results	Good fitting with theoretical results	Good fitting with theoretical results	Good fitting with theoretical results	Misalignment with theoretical results	(116-117)
Order parameters	$\|S_{CD}\|$ increased values	Disorder and flexibility	$\|S_{CD}\|$ increased values	Disorder and flexibility	Disorder and flexibility	(116-117)

Results depicted herein show a marginal effect of the receptors on the membrane structural parameters. Indeed, for the selected replicates, the maximum variation of 6.2 % and 5.7 % in area per lipid and bilayer thickness, respectively, does not seem large enough to alter the membrane structure and integrity. The electron density profiles show a good fitting with the theoretical values from free membrane (model II) simulation, although system J shows a small misalignment in the system individual profile. The order parameters show slight increases in the $|S_{CD}|$ values, however, still compatible with a fluid phase membrane. When inserted in the bilayer core, squaramides were able to hold the chloride anion, which was released only when the complexes reached the 10 Å distance from the interface.

4. Conclusions

As mentioned in the beginning of this work, the anion transport across cellular membranes is an important process, essential for the cell functioning. Therefore the development of synthetic transporters capable of replacing defective membrane transporters is a great challenge and a growing research field in the supramolecular chemistry area. The design of these synthetic molecules requires knowledge and expertise so that a fine balance between anion selectivity and lipophilic character can be achieved, granting transport activity to molecules.

In this context, since June 2012, an *in silico* study was carried out in POPC membrane models to assess the behaviour of squaramide chloride complexes and their interaction with the phospholipid bilayer.

As a first step in this theoretical investigation, specific bond term parameters for the squaramide entity were generated using the crystal data deposited with CSD, which were used together with GAFF default parameters to describe the squaramides. Overall, this combination accurately reproduced the structure of the squaramide unit in the crystal state, which is characterized by the existence of multiple N-H···O hydrogen bonds. Therefore, the new set of parameters is more appropriate to be used in simulation of squaramides in solvents, as water, with donor and acceptor hydrogen ability.

The study was continued with MD simulations of membrane systems. A free POPC membrane model (fully hydrated) was simulated and then used to accommodate the receptors in the bilayer core. This simulation was used as reference to evaluate the impact of the squaramides on the structural parameters of lipid bilayer (area per lipid, bilayer thickness, electron density profile and order parameters). When the receptors were placed in the water phase, an overhydrated membrane previously simulated with LIPID11 was used as reference.

Squaramide chloride complexes were then placed in the water slab and in the membrane core of the system. The structural parameters aforementioned were assessed to evaluate the impact of each squaramide in the membrane properties. The diffusion and interaction of each small molecule with phospholipid bilayer was evaluated through the analysis of the receptor relative position, hydration, hydrogen bonds and C=C-N-C torsion angles (between the squaramide core and C adjacent from the substituent) for 100 ns. Two replicates of each system were simulated to confirm the results. Data showed that all the receptors have the ability to diffuse from the water slab and permeate the phospholipid bilayer, as well as the

ability to move from the bilayer core towards the water/lipid interface, releasing the chloride from the complex. Some biophysical parameters of the membrane were perturbed by the presence of the complexes. However, since squaramides are small molecules with low molecular weight, the differences from the estimated values for pure membrane models were marginal. In the systems where the complexes were placed in the water slab, the structural parameters showed slight perturbations in the area per lipid and bilayer thickness parameters.

Summarizing, these molecules present a high degree of lipophilicity but were still able to diffuse in lipophilic and hydrophilic media with a marginal impact to the membrane structure and properties. In agreement to previous experimental studies squaramides have a great potential as functional binding units to integrate new transmembrane anion transporters much more efficient than their ureas and thioureas analogous.

Moreover, Molecular Dynamics simulation is a very comprehensive and powerful tool to understand, at the molecular level, the diffusion of the chloride associations trough the membrane, the interaction with phospholipid head groups as well as the transport mechanisms, enabling the rational research and development of new drug-like molecules for channel replacement therapies.

5. Future work

Following the same reasoning, more MD studies can be performed to test the transmembrane transport of physiologically relevant anions such as bicarbonate, sulphate, phosphate and nitrate. In addition, this theoretical investigation will be extended to new and more sophisticated squaramide molecules, in collaboration with Prof. Gale´s group.

Another approach can be the molecular design and simulation of squaramide-based transporters with amino acid moieties. Since the squaramide unit is not enough to maintain hydrogen bonds in competitive media, more complex molecules with several "squaric units" suitable for anion transport using ion carrier mechanism, channels or anion π-slides, among others. The molecular dynamics will be an excellent tool to investigate this crucial feature of the anion transmembrane transport.

The theoretical studies will include MD simulations in phospholipid bilayer models complemented by quantum-chemical calculations to evaluate the binding affinity of each squaramide to different anions. These results will also be correlated with receptors experimental transport activity (*e.g.* EC_{50}).

This work will be carried out using a similar approach to the one used so far, however the lipid molecules will be eventually described with new a force field compatible with GAFF, but not requiring the use of surface tension as LIPID11. Other significant step forward in the anion transport area will be the estimative of the free energy barrier required by the anion-squaramide complex to cross the lipid interface by constraint MD simulations with extraction of the corresponding potential of mean force (PMF). The application of other MD approaches that allow an enhanced sampling of biological membrane systems, such as replica-exchange molecular dynamics (REMD), will be also tested. In other words, these type of MD methodologies combined with unconstrained MD simulations will be valuable insights towards the full understanding of the anion transport assisted by artificial receptors. All these *in silico* studies will be a major breakthrough in the field of the anion transport.

6. References

1. Alberts, B., Johnson, A., Lewis, J., Raff, M., Roberts, K. and Walter, P., *Molecular Biology of the Cell*, 4th Ed., Garland Science, 2002.

2. Lodish, H., Berk, A., Matsudaira, P., Kaiser, C. A., Krieger, M., Scott, M. P., Zipursky, L. and Darnell, J., *Molecular Cell Biology*, 4th Ed., W. H. Freeman, 2000.

3. McNally, B. A., Leevy, W. M. and Smith, B. D., *Recent Advances in Synthetic Membrane Transporters*, Supramol Chem, 2007, ***19***, 29-37.

4. Red Blood Cell Laboratory Children's Hospital Oakland Research Institute, 2010, .

5. Rhoades, R. A. and Tanner, G. A., *Medical Physiology*, 2nd Ed., Lippincott Williams & Wilkins, 2003.

6. Davis, J. T., Okunola, O. and Quesada, R., *Recent Advances in the Transmembrane Transport of Anions*, Chem. Soc. Rev., 2010, ***39***, 3843-3862.

7. Boron, W. F. and Boulpaep, E., *Medical Physiology - Updated Edition*, Updated Edition, Saunders, 2004.

8. Cannon, S., *Physiologic Principles Underlying Ion Channelopathies*, Neurotherapeutics, 2007, ***4***, 174-183.

9. Ashcroft, F. M., *Ion Channels and Disease*, 1st Ed., Academic Press, 1999.

10. Gaillard, T. and Case, D. A., *Evaluation of DNA Force Fields in Implicit Solvation*, Journal of Chemical Theory and Computation, 2011, ***7***, 3181-3198.

11. Cook, G. A., Prakash, O., Zhang, K., Shank, L. P., Takeguchi, W. A., Robbins, A., Gong, Y. X., Iwamoto, T., Schultz, B. D. and Tomich, J. M., *Activity and Structural Comparisons of Solution Associating and Monomeric Channel-Forming Peptides Derived from the Glycine Receptor M2 Segment*, Biophys. J., 2004, ***86***, 1424-1435.

12. Valkenier, H. and Davis, A. P., *Making a Match for Valinomycin: Steroidal Scaffolds in the Design of Electroneutral, Electrogenic Anion Carriers*, Acc. Chem. Res., 2013, .

13. George, A. L. J., *Inherited Channelopathies Associated with Epilepsy*, Epilepsy currents / American Epilepsy Society, 2004, ***4***, 65-70.

14. Scotet, V., Dugueperoux, I., Saliou, P., Rault, G., Roussey, M., Audrezet, M.-P. and Ferec, C., *Evidence for Decline in the Incidence of Cystic Fibrosis: A 35-Year Observational Study in Brittany, France*, Orphanet Journal of Rare Diseases, 2012, ***7***, 14.

15. Ionophores, *Available On: <Http://Www.Ncbi.Nlm.Nih.Gov/Mesh/68007476>*, MeSH Database, Accessed on April 4th 2013.

16. De Riccardis, F., Izzo, I., Montesarchio, D. and Tecilla, P., *Ion Transport through Lipid Bilayers by Synthetic Ionophores: Modulation of Activity and Selectivity*, Acc. Chem. Res., 2013, .

17. I-Lev. *Encyclopedia of Science and Technology*, McGraw-Hill, 2007, *9*, 445-447.

18. Seganish, J. L. and Davis, J. T., *Prodigiosin Is a Chloride Carrier That Can Function as an Anion Exchanger*, Chem. Commun., 2005, ***0***, 5781-5783.

19. Davis, A. P., Sheppard, D. N. and Smith, B. D., *Development of Synthetic Membrane Transporters for Anions*, Chem. Soc. Rev., 2007, ***36***, 348-357.

20. McNally, B. A., O'Neil, E. J., Nguyen, A. and Smith, B. D., *Membrane Transporters for Anions That Use a Relay Mechanism*, J. Am. Chem. Soc., 2008, ***130***, 17274-17275.

21. Gale, P. A., Pérez-Tomás, R. and Quesada, R., *Anion Transporters and Biological Systems*, Acc. Chem. Res., 2013, .

22. Davis, J. T., Gale, P. A., Okunola, O. A., Prados, P., Iglesias-Sanchez, J. C., Torroba, T. and Quesada, R., *Using Small Molecules to Facilitate Exchange of Bicarbonate and Chloride Anions across Liposomal Membranes*, Nat Chem, 2009, ***1***, 138-144.

23. Hernandez, P. I., Moreno, D., Javier, A. A., Torroba, T., Perez-Tomas, R. and Quesada, R., *Tambjamine Alkaloids and Related Synthetic Analogs: Efficient Transmembrane Anion Transporters*, Chem. Commun., 2012, ***48***, 1556-1558.

24. Saggiomo, V., Otto, S., Marques, I., Felix, V., Torroba, T. and Quesada, R., *The Role of Lipophilicity in Transmembrane Anion Transport*, Chem. Commun., 2012, ***48***, 5274-5276.

25. Antonisse, M. M. G. and Reinhoudt, D. N., *Neutral Anion Receptors: Design and Application*, Chem. Commun., 1998, 443-448.

26. Sidorov, V., Kotch, F. W., Abdrakhmanova, G., Mizani, R., Fettinger, J. C. and Davis, J. T., *Ion Channel Formation from a Calix[4]Arene Amide That Binds Hcl*, J. Am. Chem. Soc., 2002, ***124***, 2267-2278.

27. Sidorov, V., Kotch, F. W., Kuebler, J. L., Lam, Y. F. and Davis, J. T., *Chloride Transport across Lipid Bilayers and Transmembrane Potential Induction by an Oligophenoxyacetamide*, J. Am. Chem. Soc., 2003, ***125***, 2840-2841.

28. Seganish, J. L., Santacroce, P. V., Salimian, K. J., Fettinger, J. C., Zavalij, P. and Davis, J. T., *Regulating Supramolecular Function in Membranes: Calixarenes That Enable or Inhibit Transmembrane Cl- Transport*, Angew. Chem. Int. Ed. Engl., 2006, ***45***, 3334-3338.

29. Okunola, O. A., Seganish, J. L., Salimian, K. J., Zavalij, P. Y. and Davis, J. T., *Membrane-Active Calixarenes: Toward 'Gating' Transmembrane Anion Transport*, Tetrahedron, 2007, ***63***, 10743-10750.

30. Sessler, J. L., Weghorn, S. J., Morishima, T., Rosingana, M., Lynch, V. and Lee, V., *Rosarin - a New, Easily Prepared Hexapyrrolic Expanded Porphyrin*, J. Am. Chem. Soc., 1992, ***114***, 8306-8307.

31. Sessler, J. L., Andrievsky, A., Gale, P. A. and Lynch, V., *Anion Binding: Self-Assembly of Polypyrrolic Macrocycles*, Angewandte Chemie-International Edition in English, 1996, ***35***, 2782-2785.

32. Sessler, J. L., An, D. Q., Cho, W. S. and Lynch, V., *Calix[N]Bipyrroles: Synthesis, Characterization, and Anion-Binding Studies*, Angew Chem Int Edit, 2003, ***42***, 2278-2281.

33. Sessler, J. L., Eller, L. R., Cho, W. S., Nicolaou, S., Aguilar, A., Lee, J. T., Lynch, V. M. and Magda, D. J., *Synthesis, Anion-Binding Properties, and in Vitro Anticancer Activity of Prodigiosin Analogues*, Angew Chem Int Edit, 2005, ***44***, 5989-5992.

34. Gale, P. A., Light, M. E., McNally, B., Navakhun, K., Sliwinski, K. E. and Smith, B. D., *Co-Transport of H+/Cl- by a Synthetic Prodigiosin Mimic*, Chem. Commun., 2005, ***0***, 3773-3775.

35. Fisher, M. G., Gale, P. A., Hiscock, J. R., Hursthouse, M. B., Light, M. E., Schmidtchen, F. P. and Tong, C. C., *1,2,3-Triazole-Strapped Calix[4]Pyrrole: A New Membrane Transporter for Chloride*, Chem. Commun., 2009, 3017-3019.

36. Haynes, C. J. E., Moore, S. J., Hiscock, J. R., Marques, I., Costa, P. J., Felix, V. and Gale, P. A., *Tunable Transmembrane Chloride Transport by Bis-Indolylureas*, Chem. Sci., 2012, ***3***, 1436-1444.

37. Moore, S. J., Haynes, C. J. E., Gonzalez, J., Sutton, J. L., Brooks, S. J., Light, M. E., Herniman, J., Langley, G. J., Soto-Cerrato, V., Perez-Tomas, R., Marques, I., Costa, P. J., Felix, V. and Gale, P. A., *Chloride, Carboxylate and Carbonate Transport by Ortho-Phenylenediamine-Based Bisureas*, Chem. Sci., 2013, ***4***, 103-117.

38. Madhavan, N., Robert, E. C. and Gin, M. S., *A Highly Active Anion-Selective Aminocyclodextrin Ion Channel*, Angew. Chem. Int. Ed., 2005, ***44***, 7584-7587.

39. Difabio, G., Randazzo, A., D'Onofrio, J., Ausin, C., Pedroso, E., Grandas, A., De Napoli, L. and Montesarchio, D., *Cyclic Phosphate-Linked Oligosaccharides: Synthesis and Conformational Behavior of Novel Cyclic Oligosaccharide Analogues*, J. Org. Chem., 2006, ***71***, 3395-3408.

40. Brotherhood, P. R. and Davis, A. P., *Steroid-Based Anion Receptors and Transporters*, Chem. Soc. Rev., 2010, ***39***, 3633-3647.

41. Davis, A. P. and Joos, J. B., *Steroids as Organising Elements in Anion Receptors*, Coord. Chem. Rev., 2003, ***240***, 143-156.

42. Clare, J. P., Ayling, A. J., Joos, J. B., Sisson, A. L., Magro, G., Perez-Payan, M. N., Lambert, T. N., Shukla, R., Smith, B. D. and Davis, A. P., *Substrate Discrimination by Cholapod Anion Receptors: Geometric Effects and the "Affinity-Selectivity Principle"*, J. Am. Chem. Soc., 2005, ***127***, 10739-10746.

43. Davis, A. P., *Anion Binding and Transport by Steroid-Based Receptors*, Coord. Chem. Rev., 2006, ***250***, 2939-2951.

44. Judd, L. W. and Davis, A. P., *From Cholapod to Cholaphane Transmembrane Anion Carriers: Accelerated Transport through Binding Site Enclosure*, Chem Commun (Camb), 2010, ***46***, 2227-2229.

45. Reddy, G. L., Iwamoto, T., Tomich, J. M. and Montal, M., *Synthetic Peptides and Four-Helix Bundle Proteins as Model Systems for the Pore-Forming Structure of Channel Proteins. Ii. Transmembrane Segment M2 of the Brain Glycine Receptor Is a Plausible Candidate for the Pore-Lining Structure*, J. Biol. Chem., 1993, ***268***, 14608-14615.

46. Schlesinger, P. H., Ferdani, R., Liu, J., Pajewska, J., Pajewski, R., Saito, M., Shabany, H. and Gokel, G. W., *Scmtr: A Chloride-Selective, Membrane-Anchored Peptide Channel That Exhibits Voltage Gating*, J. Am. Chem. Soc., 2002, ***124***, 1848-1849.

47. Schlesinger, P. H., Ferdani, R., Pajewski, R., Pajewska, J. and Gokel, G. W., *A Hydrocarbon Anchored Peptide That Forms a Chloride- Selective Channel in Liposomes*, Chem. Commun., 2002, ***0***, 840-841.

48. You, L., Ferdani, R., Li, R. Q., Kramer, J. P., Winter, R. E. K. and Gokel, G. W., *Carboxylate Anion Diminishes Chloride Transport through a Synthetic, Self-Assembled Transmembrane Pore*, Chem-Eur J, 2008, ***14***, 382-396.

49. Djedovic, N., Ferdani, R., Harder, E., Pajewska, J., Pajewski, R., Weber, M. E., Schlesinger, P. H. and Gokel, G. W., *The C- and N-Terminal Residues of Synthetic Heptapeptide Ion Channels Influence Transport Efficacy through Phospholipid Bilayers*, New J. Chem., 2005, ***29***, 291-305.

50. Sakai, N., Sorde, N., Das, G., Perrottet, P., Gerard, D. and Matile, S., *Synthetic Multifunctional Pores: Deletion and Inversion of Anion/Cation Selectivity Using Pm and Ph*, Org Biomol Chem, 2003, ***1***, 1226-1231.

51. Das, G., Onouchi, H., Yashima, E., Sakai, N. and Matile, S., *Binding of Organic Anions by Synthetic Supramolecular Metallopores with Internal Mg2+–Aspartate Complexes*, ChemBioChem, 2002, ***3***, 1089-1096.

52. Gorteau, V., Julliard, M. D. and Matile, S., *Hydrophilic Anchors for Transmembrane Anion-Pi Slides*, J. Membr. Sci., 2008, ***321***, 37-42.

53. Janout, V. and Regen, S. L., *Bioconjugate-Based Molecular Umbrellas*, Bioconj. Chem., 2009, ***20***, 183-192.

54. Deng, G., Dewa, T. and Regen, S. L., *A Synthetic Ionophore That Recognizes Negatively Charged Phospholipid Membranes*, J. Am. Chem. Soc., 1996, ***118***, 8975-8976.

55. Quiñonero, D., Frontera, A., Ballester, P. and Deyà, P. M., *A Theoretical Study of Aromaticity in Squaramide and Oxocarbons*, Tetrahedron Lett., 2000, ***41***, 2001-2005.

56. Quiñonero, D., Prohens, R., Garau, C., Frontera, A., Ballester, P., Costa, A. and Deyà, P. M., *A Theoretical Study of Aromaticity in Squaramide Complexes with Anions*, Chem. Phys. Lett., 2002, ***351***, 115-120.

57. Rotger, C., Soberats, B., Quinonero, D., Frontera, A., Ballester, P., Benet-Buchholz, J., Deya, P. M. and Costa, A., *Crystallographic and Theoretical Evidence of Anion-Pi and Hydrogen-Bonding Interactions in a Squaramide-Nitrate Salt*, Eur. J. Org. Chem., 2008, 1864-1868.

58. Quinonero, D., Garau, C., Frontera, A., Ballester, P., Costa, A. and Deya, P. M., *Quantification of Aromaticity in Oxocarbons: The Problem of the Fictitious "Nonaromatic" Reference System*, Chemistry, 2002, ***8***, 433-438.

59. Storer, R. I., Aciro, C. and Jones, L. H., *Squaramides: Physical Properties, Synthesis and Applications*, Chem Soc Rev, 2011, ***40***, 2330-2346.

60. Prohens, R., Portell, A., Puigjaner, C., Barbas, R., Alcobe, X., Font-Bardia, M. and Tomas, S., *Cooperative Induction in Double H-Bonding Donor/Acceptor Compounds: Chains Vs. Ribbons*, CrystEngComm, 2012, ***14***, 5745-5748.

61. Kawahara, S.-i., Taira, K. and Uchimaru, T., *Hydrogen Bond Cooperativity Derived from Neighboring Hydrogen Bond Formation: Case Study in Three Iso-Complexes of C8h9n5o2*, Chem. Phys., 2003, ***290***, 79-83.

62. Amendola, V., Bergamaschi, G., Boiocchi, M., Fabbrizzi, L. and Milani, M., *The Squaramide Versus Urea Contest for Anion Recognition*, Chem-Eur J, 2010, ***16***, 4368-4380.

63. Garau, C., Frontera, A., Ballester, P., Quinonero, D., Costa, A. and Deya, P. M., *A Theoretical Ab Initio Study of the Capacity of Several Binding Units for the Molecular Recognition of Anions*, Eur. J. Org. Chem., 2005, ***2005***, 179-183.

64. Quiñonero, D., Frontera, A., Suñer, G. A., Morey, J., Costa, A., Ballester, P. and Deyà, P. M., *Squaramide as a Binding Unit in Molecular Recognition*, Chem. Phys. Lett., 2000, ***326***, 247-254.

65. Amendola, V., Fabbrizzi, L., Mosca, L. and Schmidtchen, F. P., *Urea-, Squaramide-, and Sulfonamide-Based Anion Receptors: A Thermodynamic Study*, Chem-Eur J, 2011, ***17***, 5972-5981.

66. Rostami, A., Colin, A., Li, X. Y., Chudzinski, M. G., Lough, A. J. and Taylor, M. S., *N,N'-Diarylsquaramides: General, High-Yielding Synthesis and Applications in Colorimetric Anion Sensing*, J. Org. Chem., 2010, ***75***, 3983-3992.

67. Rostami, A., Wei, C. J., Guerin, G. and Taylor, M. S., *Anion Detection by a Fluorescent Poly(Squaramide): Self-Assembly of Anion-Binding Sites by Polymer Aggregation*, Angew. Chem. Int. Ed. Engl., 2011, ***50***, 2059-2062.

68. Prohens, R., Tomas, S., Morey, J., Deya, P. M., Ballester, P. and Costa, A., *Squaramido-Based Receptors: Molecular Recognition of Carboxylate Anions in Highly Competitive Media.*, Tetrahedron Lett., 1998, ***39***, 1063-1066.

69. Frontera, A., Orell, M., Garau, C., Quinonero, D., Molins, E., Mata, I. and Morey, J., *Preparation, Solid-State Characterization, and Computational Study of a Crown Ether Attached to a Squaramide*, Org Lett, 2005, ***7***, 1437-1440.

70. Kim, C. U. and Misco, P. F., *A Facile Synthesis of 1-Hydroxy-2- Phosphonocyclobutenedione*, Tetrahedron Lett., 1992, ***33***, 3961-3962.

71. Ramalingam, V., Domaradzki, M. E., Jang, S. and Muthyala, R. S., *Carbonyl Groups as Molecular Valves to Regulate Chloride Binding to Squaramides*, Organic Letters, 2008, ***10***, 3315-3318.

72. Busschaert, N., Kirby, I. L., Young, S., Coles, S. J., Horton, P. N., Light, M. E. and Gale, P. A., *Squaramides as Potent Transmembrane Anion Transporters*, Angew. Chem. Int. Ed. Engl., 2012, ***51***, 4426-4430.

73. Siu, S. W., Vacha, R., Jungwirth, P. and Bockmann, R. A., *Biomolecular Simulations of Membranes: Physical Properties from Different Force Fields*, J. Chem. Phys., 2008, ***128***, 125103.

74. Leach, A. R., *Molecular Modelling: Principles and Applications*, 1st Ed., Longman, 1996.

75. Hinchliffe, A., *Molecular Modelling for Beginners*, 1st Ed., Wiley, 2003.

76. Cramer, C. J., *Essentials of Computational Chemistry: Theories and Models*, 2nd Ed., Wiley, 2004.

77. Arinaminpathy, Y., Sansom, M. S. P. and Biggin, P. C., *Molecular Dynamics Simulations of the Ligand-Binding Domain of the Ionotropic Glutamate Receptor Glur2*, Biophys. J., 2002, ***82***, 676-683.

78. Marrink, S. J., Risselada, H. J., Yefimov, S., Tieleman, D. P. and de Vries, A. H., *The Martini Force Field: Coarse Grained Model for Biomolecular Simulations*, J. Phys. Chem. B, 2007, ***111***, 7812-7824.

79. Alder, B. J. and Wainwright, T. E., *Phase Transition for a Hard Sphere System*, The Journal of Chemical Physics, 1957, ***27***, 1208-1209.

80. Janosi, L. and Gorfe, A. A., *Simulating Popc and Popc/Popg Bilayers: Conserved Packing and Altered Surface Reactivity*, Journal of Chemical Theory and Computation, 2010, ***6***, 3267-3273.

81. Klauda, J. B., Venable, R. M., Freites, J. A., O'Connor, J. W., Tobias, D. J., Mondragon-Ramirez, C., Vorobyov, I., MacKerell, A. D. and Pastor, R. W., *Update of the Charmm All-Atom Additive Force Field for Lipids: Validation on Six Lipid Types*, J. Phys. Chem. B, 2010, ***114***, 7830-7843.

82. Rosso, L. and Gould, I. R., *Structure and Dynamics of Phospholipid Bilayers Using Recently Developed General All-Atom Force Fields*, J. Comput. Chem., 2008, ***29***, 24-37.

83. Jojart, B. and Martinek, T. A., *Performance of the General Amber Force Field in Modeling Aqueous Popc Membrane Bilayers*, J. Comput. Chem., 2007, ***28***, 2051-2058.

84. Skjevik, A. A., Madej, B. D., Walker, R. C. and Teigen, K., *Lipid11: A Modular Framework for Lipid Simulations Using Amber*, J. Phys. Chem. B, 2012, ***116***, 11124-11136.

85. Dickson, C. J., Rosso, L., Betz, R. M., Walker, R. C. and Gould, I. R., *Gafflipid: A General Amber Force Field for the Accurate Molecular Dynamics Simulation of Phospholipid*, Soft Matter, 2012, ***8***, 9617-9627.

86. Poger, D. and Mark, A. E., *On the Validation of Molecular Dynamics Simulations of Saturated and Cis-Monounsaturated Phosphatidylcholine Lipid Bilayers: A Comparison with Experiment*, Journal of Chemical Theory and Computation, 2010, ***6***, 325-336.

87. Chiu, S. W., Pandit, S. A., Scott, H. L. and Jakobsson, E., *An Improved United Atom Force Field for Simulation of Mixed Lipid Bilayers*, J. Phys. Chem. B, 2009, ***113***, 2748-2763.

88. Kirschner, K. N., Yongye, A. B., Tschampel, S. M., Gonzalez-Outeirino, J., Daniels, C. R., Foley, B. L. and Woods, R. J., *Glycam06: A Generalizable Biomolecular Force Field. Carbohydrates*, J. Comput. Chem., 2008, ***29***, 622-655.

89. Quiñonero, D., Tomàs, S., Frontera, A., Garau, C., Ballester, P., Costa, A. and Deyà, P. M., *Opls All-Atom Force Field for Squaramides and Squaric Acid*, Chem. Phys. Lett., 2001, ***350***, 331-338.

90. Allen, F., *The Cambridge Structural Database: A Quarter of a Million Crystal Structures and Rising*, Acta Crystallographica Section B, 2002, ***58***, 380-388.

91. Jin, X. Q., Min, Q. Q., Zheng, Y. F., Wang, P. C., Zhu, J. and Zhou, H. B., *Synthesis and Structural Features of Chiral Cyclic Squaramides and Their Application in Asymmetric Catalytic Reaction*, Arkivoc, 2010, 322-335.

92. Kolev, T., Seidel, R. W., Mayer-Figge, H., Spiteller, M., Sheldrick, W. S. and Koleva, B. B., *Crystal Structures and Spectroscopic Properties of Ester Amide and Diamide of Squaric Acid with Prolinamide*, Spectrochimica Acta Part A: Molecular and Biomolecular Spectroscopy, 2009, ***72***, 502-509.

93. Lunelli, B., Roversi, P., Ortoleva, E. and Destro, R., *Geometry and Molecular Parameters of 3,4-Bis(Dimethylamino)-3-Cyclobutene-1,2-Dione and Its Isomer Bis(Dimethylamino)Squaraine. Combined Study by Ir Spectroscopy, Xrd and Ab Initio Mo Calculations*, J. Chem. Soc., Faraday Trans., 1996, ***92***, 3611-3623.

94. Oh, J.-S., Kim, K. I. and Song, C. E., *Enantioselective Synthesis of [Small Alpha]-Deuterium Labelled Chiral [Small Alpha]-Amino Acids Via Dynamic Kinetic Resolution of Racemic Azlactones*, Org Biomol Chem, 2011, ***9***, 7983-7985.

95. Silva, C. E., Dos Santos, H. l. F., Speziali, N. L., Diniz, R. and de Oliveira, L. F. C., *Role of the Substituent Effect over the Squarate Oxocarbonic Ring: Spectroscopy, Crystal Structure, and Density Functional Theory Calculations of 1,2-Dianilinosquairane*, The Journal of Physical Chemistry A, 2010, ***114***, 10097-10109.

96. Porel, M., Ramalingam, V., Domaradzki, M. E., Young, V. G., Ramamurthy, V. and Muthyala, R. S., *Chloride Sensing Via Suppression of Excited State Intramolecular Proton Transfer in Squaramides*, Chem. Commun., 2013, .

97. Muthyala, R. S., Subramaniam, G. and Todaro, L., *The Use of Squaric Acid as a Scaffold for Cofacial Phenyl Rings*, Org. Lett., 2004, ***6***, 4663-4665.

98. Portell, A., Barbas, R., Braga, D., Polito, M., Puigjaner, C. and Prohens, R., *New Polymorphic Hydrogen Bonding Donor-Acceptor System with Two Temperature Coincident Solid-Solid Transitions*, CrystEngComm, 2009, ***11***, 52-54.

99. Mattes, R., Johann, G. and Pieper, C., *Bisamide Der Quadratsäure*, Monatsh Chem, 1987, ***118***, 105-113.

100. Malerich, J. P., Hagihara, K. and Rawal, V. H., *Chiral Squaramide Derivatives Are Excellent Hydrogen Bond Donor Catalysts*, J. Am. Chem. Soc., 2008, ***130***, 14416-14417.

101. Estarellas, C., Rotger, M. C., Capó, M., Quiñonero, D., Frontera, A., Costa, A. and Deyà, P. M., *Anion–Π Interactions in Four-Membered Rings*, Org. Lett., 2009, ***11***, 1987-1990.

102. Bayly, C. I., Cieplak, P., Cornell, W. and Kollman, P. A., *A Well-Behaved Electrostatic Potential Based Method Using Charge Restraints for Deriving Atomic Charges: The Resp Model*, The Journal of Physical Chemistry, 1993, ***97***, 10269-10280.

103. Jakalian, A., Bush, B. L., Jack, D. B. and Bayly, C. I., *Fast, Efficient Generation of High-Quality Atomic Charges. Am1-Bcc Model: I. Method*, J. Comput. Chem., 2000, ***21***, 132-146.

104. Jakalian, A., Jack, D. B. and Bayly, C. I., *Fast, Efficient Generation of High-Quality Atomic Charges. Am1-Bcc Model: Ii. Parameterization and Validation*, J. Comput. Chem., 2002, ***23***, 1623-1641.

105. Wang, J., Wang, W., Kollman, P. A. and Case, D. A., *Automatic Atom Type and Bond Type Perception in Molecular Mechanical Calculations*, J. Mol. Graphics Model., 2006, ***25***, 247-260.

106. Walker, R. C., Crowley, M. F. and Case, D. A., *The Implementation of a Fast and Accurate Qm/Mm Potential Method in Amber*, J. Comput. Chem., 2008, ***29***, 1019-1031.

107. Frisch, M. J., Trucks, G. W., Schlegel, H. B., Scuseria, G. E., Robb, M. A., Cheeseman, J. R., Scalmani, G., Barone, V., Mennucci, B., Petersson, G. A., Nakatsuji, H., Caricato, M., Li, X., Hratchian, H. P., Izmaylov, A. F., Bloino, J., Zheng, G., Sonnenberg, J. L., Hada, M., Ehara, M., Toyota, K., Fukuda, R., Hasegawa, J., Ishida, M., Nakajima, T., Honda, Y., Kitao, O., Nakai, H., Vreven, T., Montgomery, J. A., Peralta, J. E., Ogliaro, F., Bearpark, M., Heyd, J. J., Brothers, E., Kudin, K. N., Staroverov, V. N., Kobayashi, R., Normand, J., Raghavachari, K., Rendell, A., Burant, J. C., Iyengar, S. S., Tomasi, J., Cossi, M., Rega, N., Millam, J. M., Klene, M., Knox, J. E., Cross, J. B., Bakken, V., Adamo, C., Jaramillo, J., Gomperts, R., Stratmann, R. E., Yazyev, O., Austin, A. J., Cammi, R., Pomelli, C., Ochterski, J. W., Martin, R. L., Morokuma, K., Zakrzewski, V. G., Voth, G. A., Salvador, P., Dannenberg, J. J., Dapprich, S., Daniels, A. D., Farkas, Foresman, J. B., Ortiz, J. V., Cioslowski, J. and Fox, D. J. *Gaussian 09, Revision D.01*, Wallingford CT, 2009, .

108. Wang, J., Wolf, R. M., Caldwell, J. W., Kollman, P. A. and Case, D. A., *Development and Testing of a General Amber Force Field*, J. Comput. Chem., 2004, ***25***, 1157-1174.

109. Wang, J., Wolf, R. M., Caldwell, J. W., Kollman, P. A. and Case, D. A., *Junmei Wang, Romain M. Wolf, James W. Caldwell, Peter A. Kollman, and David A. Case, "Development and Testing of a General Amber Force Field"Journal of Computational Chemistry(2004) 25(9) 1157–1174*, J. Comput. Chem., 2005, ***26***, 114-114.

110. Halgren, T. A., *Merck Molecular Force Field. I. Basis, Form, Scope, Parameterization, and Performance of Mmff94*, J. Comput. Chem., 1996, ***17***, 490-519.

111. Kolossváry, I. and Guida, W. C., *Low Mode Search. An Efficient, Automated Computational Method for Conformational Analysis: Application to Cyclic and Acyclic Alkanes and Cyclic Peptides*, J. Am. Chem. Soc., 1996, ***118***, 5011-5019.

112. Kolossváry, I. and Guida, W. C., *Low-Mode Conformational Search Elucidated: Application to C39h80 and Flexible Docking of 9-Deazaguanine Inhibitors into Pnp*, J. Comput. Chem., 1999, ***20***, 1671-1684.

113. Kolossváry, I. and Keserü, G. M., *Hessian-Free Low-Mode Conformational Search for Large-Scale Protein Loop Optimization: Application to C-Jun N-Terminal Kinase Jnk3*, J. Comput. Chem., 2001, ***22***, 21-30.

114. Keserû, G. M. and Kolossváry, I., *Fully Flexible Low-Mode Docking: Application to Induced Fit in Hiv Integrase*, J. Am. Chem. Soc., 2001, ***123***, 12708-12709.

115. Jorgensen, W. L., Chandrasekhar, J., Madura, J. D., Impey, R. W. and Klein, M. L., *Comparison of Simple Potential Functions for Simulating Liquid Water*, J. Chem. Phys., 1983, ***79***, 926-935.

116. Kucerka, N., Nieh, M. P. and Katsaras, J., *Fluid Phase Lipid Areas and Bilayer Thicknesses of Commonly Used Phosphatidylcholines as a Function of Temperature*, Bba-Biomembranes, 2011, ***1808***, 2761-2771.

117. Marques, I., Colaço, A. R., Costa, P. J., Busschaert, N., Gale, P. A. and Félix, V. *Tris-Thiourea Tripodal-Based Molecules as Chloride Transmembrane Transporters: Insights from Molecular Dynamics Simulations*, 2013, (submitted).

118. Case, D. A., Darden, T. A., Cheatham III, T. E., Simmerling, C. L., Wang, J., Duke, R. E., Luo, R., Walker, R. C., Zhang, W., Merz, K. M., Roberts, B., Hayik, S., Roitberg, A., Seabra, G., Swails, J., Götz, A. W., Kolossváry, I., Wong, K. F., Paesani, F., Vanicek, J., Wolf, R. M., Liu, J., Wu, X., Brozell, S. R., Steinbrecher, T., Gohlke, H., Cai, Q., Ye, X., Wang, J., Antonisse, M. G., Hsieh, M. J., Cui, G., Roe, D. R., Mathews, D. H., Seetin, M. G., Salomon-Ferrer, R., Sagui, C., Babin, V., Luchko, T., Gusarov, S., Kovalenko, A. and P.A., K. *Amber12*, University of California, San Francisco, 2012, .

119. Bayly, C. I., Cieplak, P., Cornell, W. D. and Kollman, P. A., *A Well-Behaved Electrostatic Potential Based Method Using Charge Restraints for Deriving Atomic Charges - the Resp Model*, J. Phys. Chem., 1993, ***97***, 10269-10280.

120. Joung, I. S. and Cheatham, T. E., 3rd, *Determination of Alkali and Halide Monovalent Ion Parameters for Use in Explicitly Solvated Biomolecular Simulations*, The journal of physical chemistry. B, 2008, ***112***, 9020-9041.

121. Schrodinger, LLC *The Pymol Molecular Graphics System, Version 1.3r1*, 2010, .

122. Jo, S., Kim, T. and Im, W., *Automated Builder and Database of Protein/Membrane Complexes for Molecular Dynamics Simulations*, PloS one, 2007, ***2***, e880.

123. Darden, T., York, D. and Pedersen, L., *Particle Mesh Ewald - an N.Log(N) Method for Ewald Sums in Large Systems*, J. Chem. Phys., 1993, ***98***, 10089-10092.

124. Loncharich, R. J., Brooks, B. R. and Pastor, R. W., *Langevin Dynamics of Peptides - the Frictional Dependence of Isomerization Rates of N-Acetylalanyl-N'-Methylamide*, Biopolymers, 1992, ***32***, 523-535.

125. Berendsen, H. J. C., Postma, J. P. M., van Gunsteren, W. F., DiNola, A. and Haak, J. R., *Molecular Dynamics with Coupling to an External Bath*, The Journal of Chemical Physics, 1984, ***81***, 3684-3690.

126. Ryckaert, J. P., Ciccotti, G. and Berendsen, H. J. C., *Numerical-Integration of Cartesian Equations of Motion of a System with Constraints - Molecular-Dynamics of N-Alkanes*, Journal of Computational Physics, 1977, ***23***, 327-341.

127. Salomon-Ferrer, R., Götz, A. W., Poole, D., Le Grand, S. and Walker, R. C. *Routine Microsecond Molecular Dynamics Simulations with Amber on Gpus. 2. Explicit Solvent Particle Mesh Ewald*, American Chemical Society, 2013, *9*, 3878-3888.

128. Götz, A. W., Williamson, M. J., Xu, D., Poole, D., Le Grand, S. and Walker, R. C. *Routine Microsecond Molecular Dynamics Simulations with Amber on Gpus. 1. Generalized Born*, American Chemical Society, 2012, *8*, 1542-1555.

129. Le Grand, S., Götz, A. W. and Walker, R. C. *Spfp: Speed without Compromise—a Mixed Precision Model for Gpu Accelerated Molecular Dynamics Simulations*, 2013, *184*, 374-380.

130. Loeffler, H. *Handy Routines for Ptraj/Cpptraj*, 2010, .

131. Siwko, M. E., Marrink, S. J., de Vries, A. H., Kozubek, A., Uiterkamp, A. J. M. S. and Mark, A. E., *Does Isoprene Protect Plant Membranes from Thermal Shock? A Molecular Dynamics Study*, Bba-Biomembranes, 2007, ***1768***, 198-206.

132. Huber, T., Rajamoorthi, K., Kurze, V. F., Beyer, K. and Brown, M. F., *Structure of Docosahexaenoic Acid-Containing Phospholipid Bilayers as Studied by H-2 Nmr and Molecular Dynamics Simulations*, J. Am. Chem. Soc., 2002, ***124***, 298-309.

133. Seelig, J. and Waespesarcevic, N., *Molecular Order in Cis and Trans Unsaturated Phospholipid Bilayers*, Biochemistry (Mosc). 1978, ***17***, 3310-3315.

134. Perly, B., Smith, I. C. P. and Jarrell, H. C., *Effects of the Replacement of a Double-Bond by a Cyclopropane Ring in Phosphatidylethanolamines - a H-2 Nmr-Study of Phase-Transitions and Molecular-Organization*, Biochemistry (Mosc). 1985, ***24***, 1055-1063.

135. Martinez, L., Andrade, R., Birgin, E. G. and Martinez, J. M., *Packmol: A Package for Building Initial Configurations for Molecular Dynamics Simulations*, J. Comput. Chem., 2009, ***30***, 2157-2164.

7. Appendix 1

MD simulations of the receptors starting from the water phase

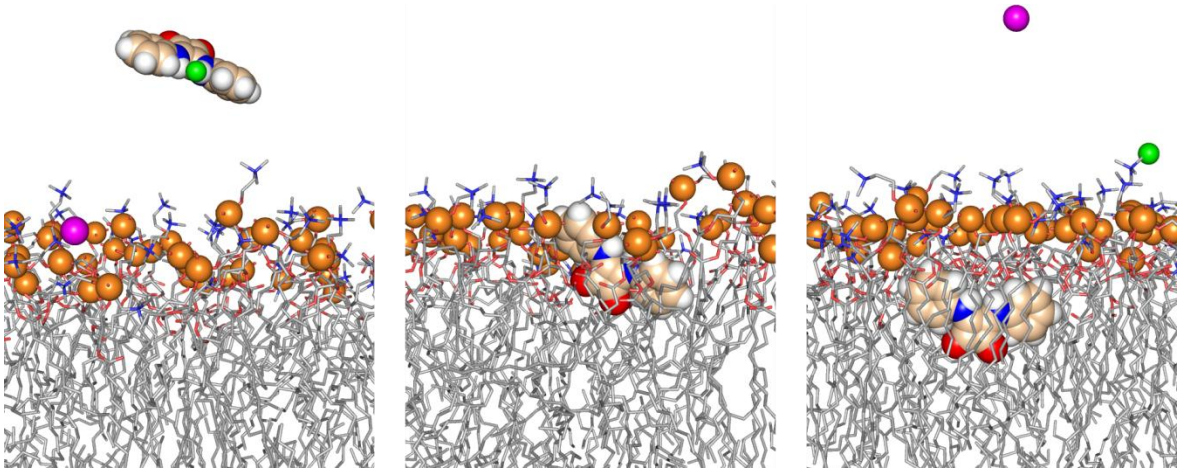

Figure 69 – Snapshots of system A, taken at different simulation times (0ns, 50ns and 100ns), showing the diffusion of S01. Images show the initial and final positions of the receptor in the membrane. The receptor is drawn as a space filing model with carbon atoms in wheat, oxygen atoms in red, nitrogen atoms in blue and hydrogen atoms in white. The chloride and sodium ions, as well as the phosphorus atoms from the bilayer are represented as green, magenta and orange spheres, respectively, and scaled to 0.7 vdW radius. In POPC lipids, carbon atoms are drawn as grey lines and C-H hydrogen atoms have been omitted.

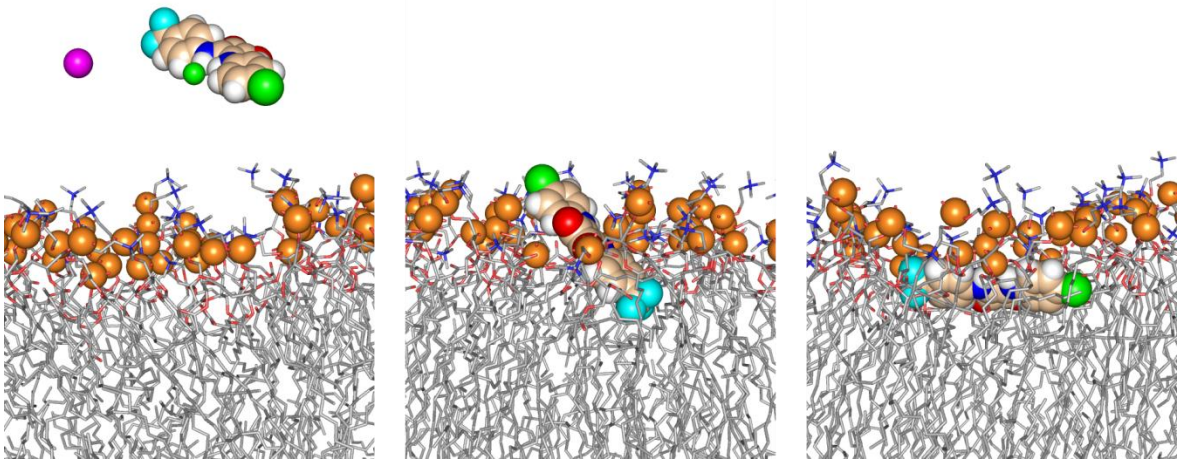

Figure 70 – Snapshots of system B showing S09 diffusion towards the membrane. Fluorine atoms are drawn as cyan spheres. Remaining details as given in Figure 69.

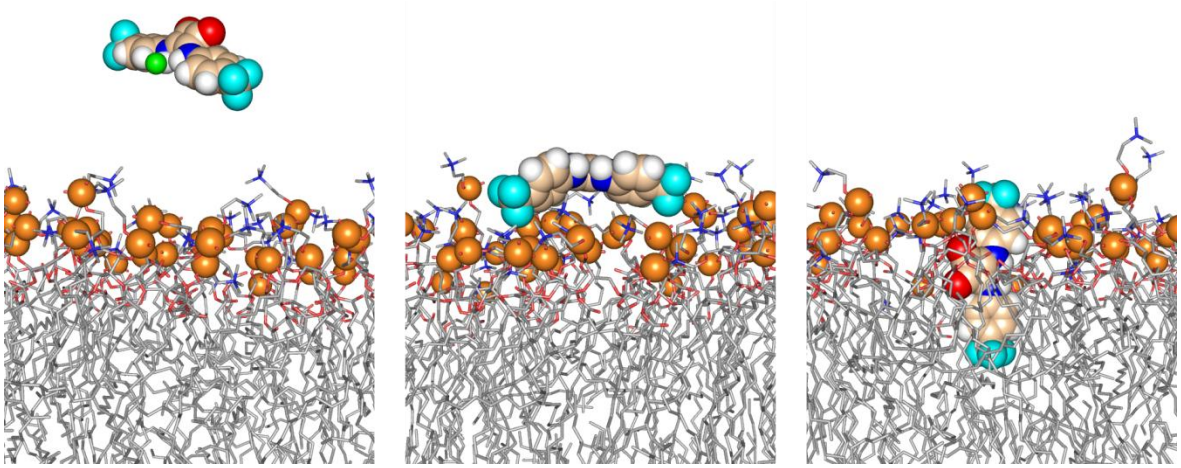

Figure 71 – Snapshots of system C showing S10 diffusion towards the membrane. Fluorine atoms are drawn as cyan spheres. Remaining details as given in Figure 69.

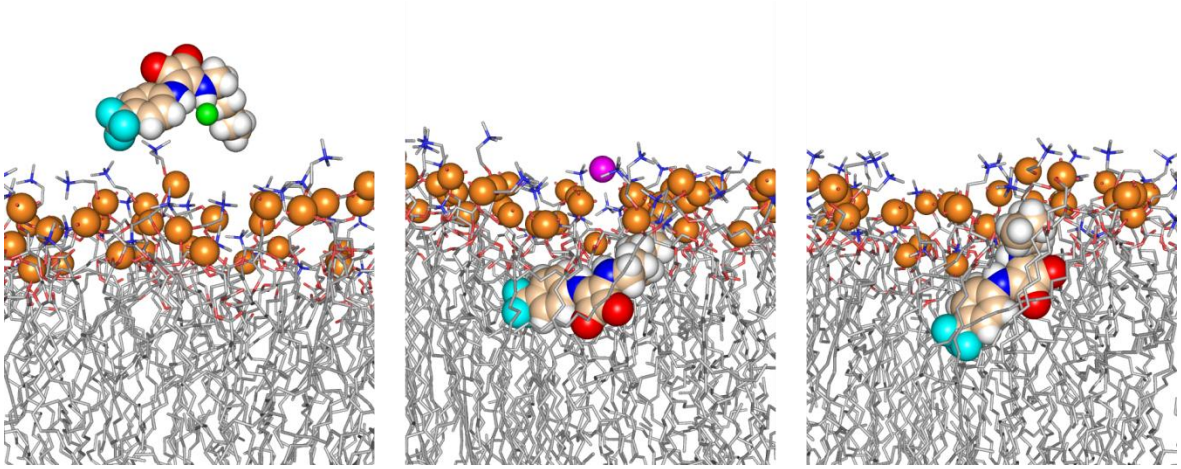

Figure 72 – Snapshots of system D showing S19 diffusion towards the membrane. Fluorine atoms are drawn as cyan spheres. Remaining details as given in Figure 69.

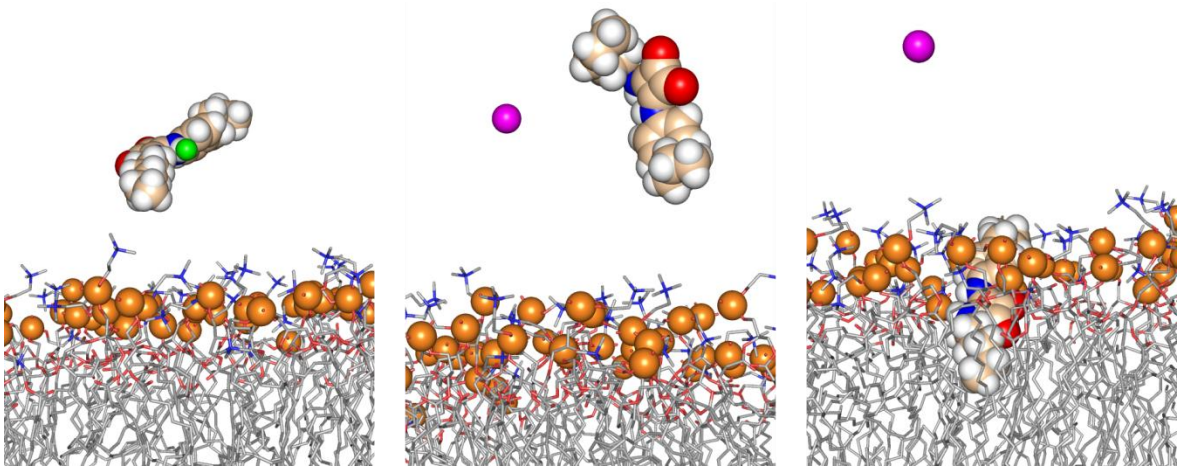

Figure 73 – Snapshots of system E showing S20 diffusion towards the membrane. Remaining details as given in Figure 69.

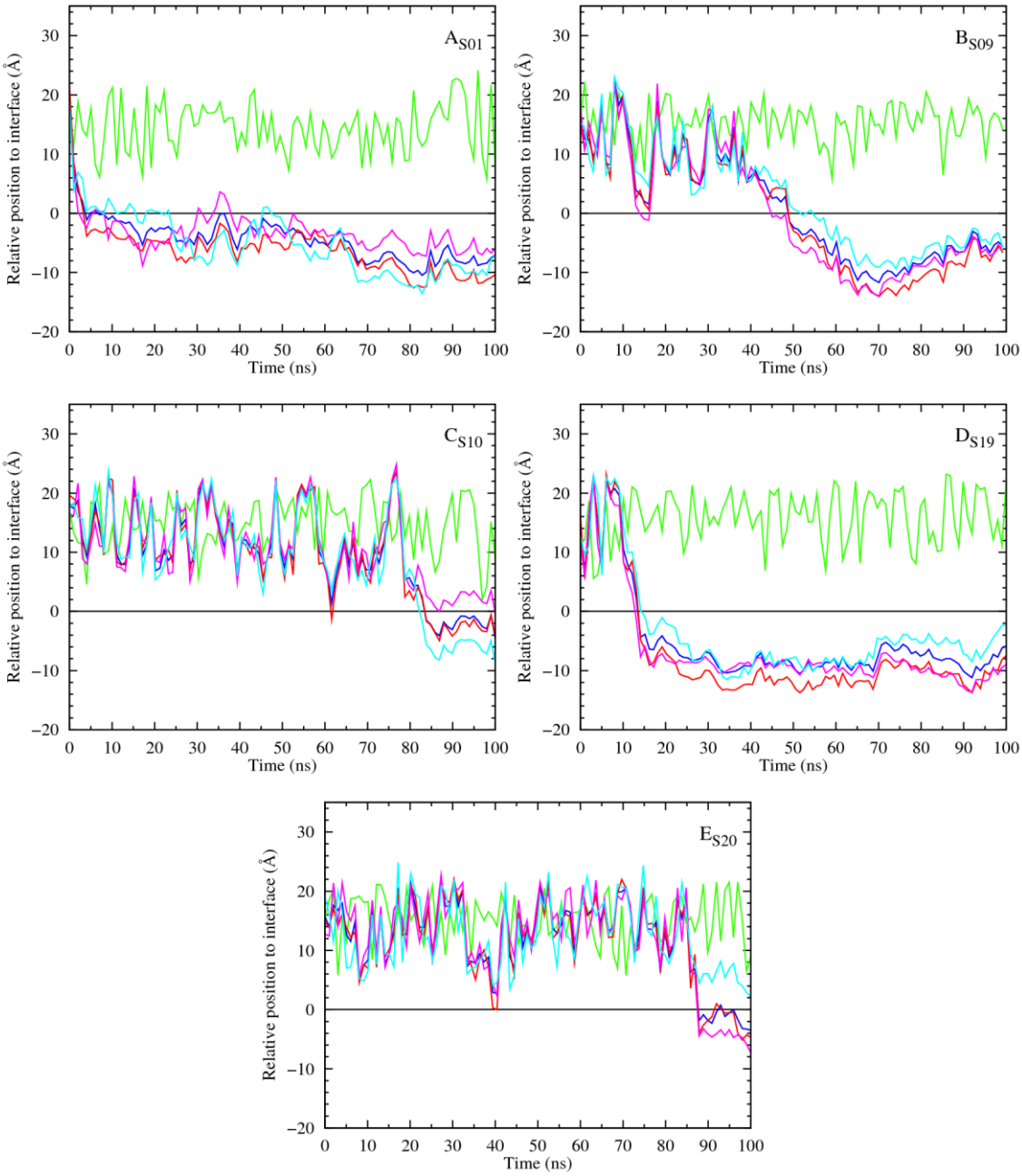

Figure 74 – Evolution of the receptor and chloride relative positions to the water/lipid interface (z = 0 Å). In green is represented the chloride ion, in red the centre of mass of the oxygen atoms from the receptor, in blue the centre of mass of the nitrogen atoms, in magenta and cyan are represented the phenyl groups (A, B and C); a phenyl group and an aliphatic chain (D) or an aliphatic chain and a butyl group (E), respectively. Data was smoothed using Bézier curves.

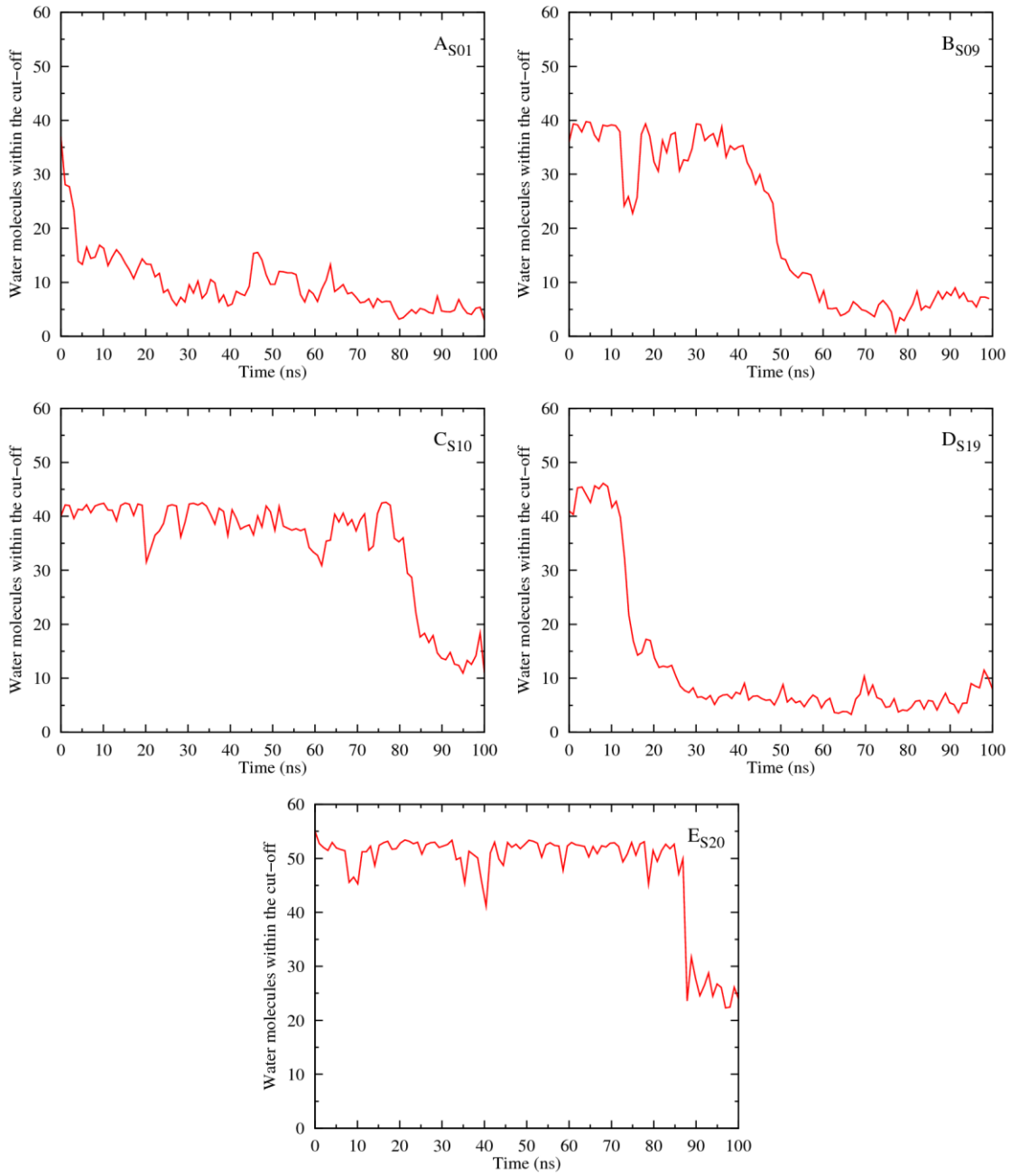

Figure 75 – Variation of the number of water molecules within the solvation shell defined by a cut-off of 3.5 Å from receptors S01 (A), S09 (B), S10 (C), S19 (D) and S20 (E). Data was smoothed using Bèzier curves.

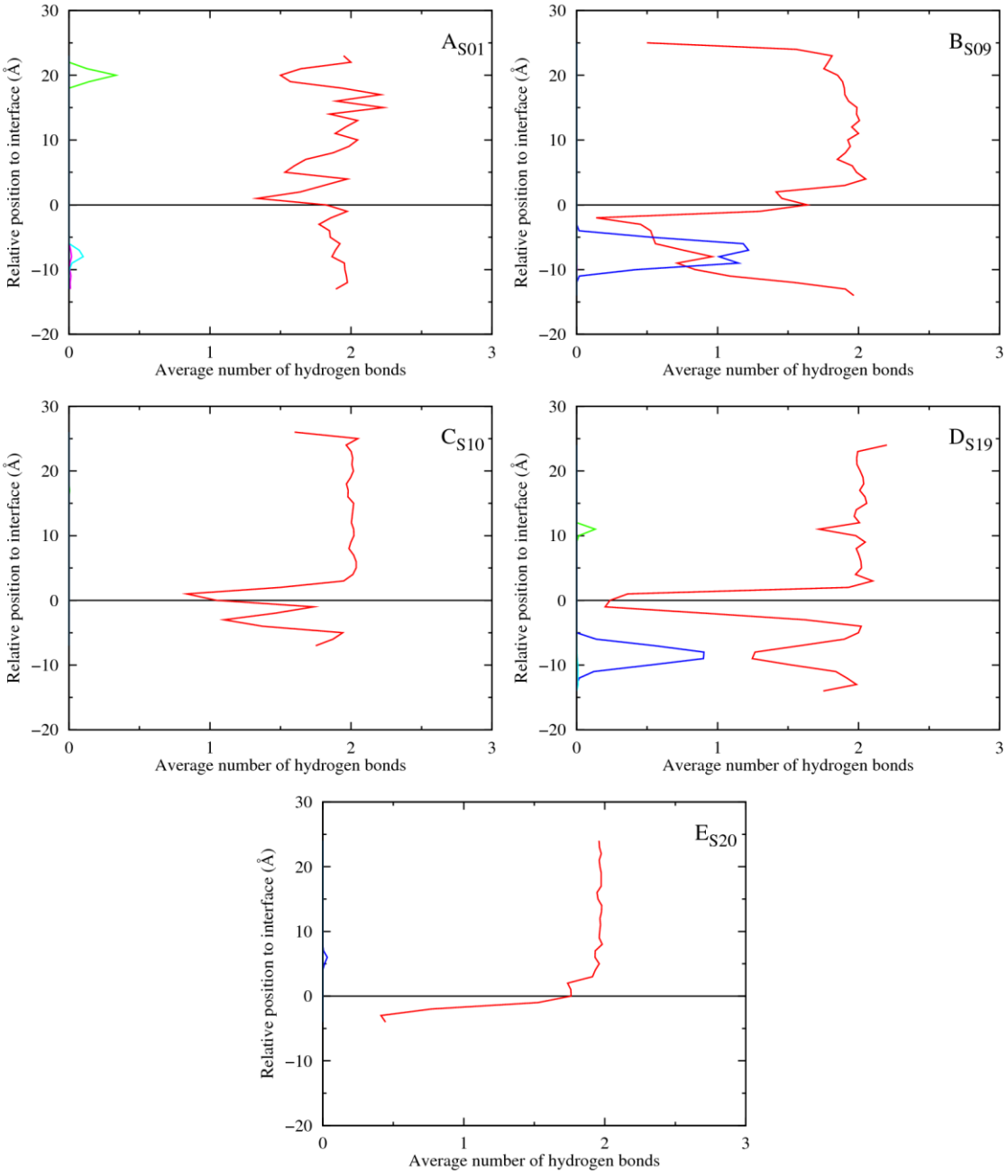

Figure 76 – Average number of hydrogen bonds *vs* the relative position of the centre of mass of each receptor. The following colour scheme was used for the hydrogen bonds established between the receptor and water molecules (red), chloride ion (green), POPC head groups (blue), ester groups from POPC *sn*-1 chains (magenta) and *sn*-2 chains (cyan).

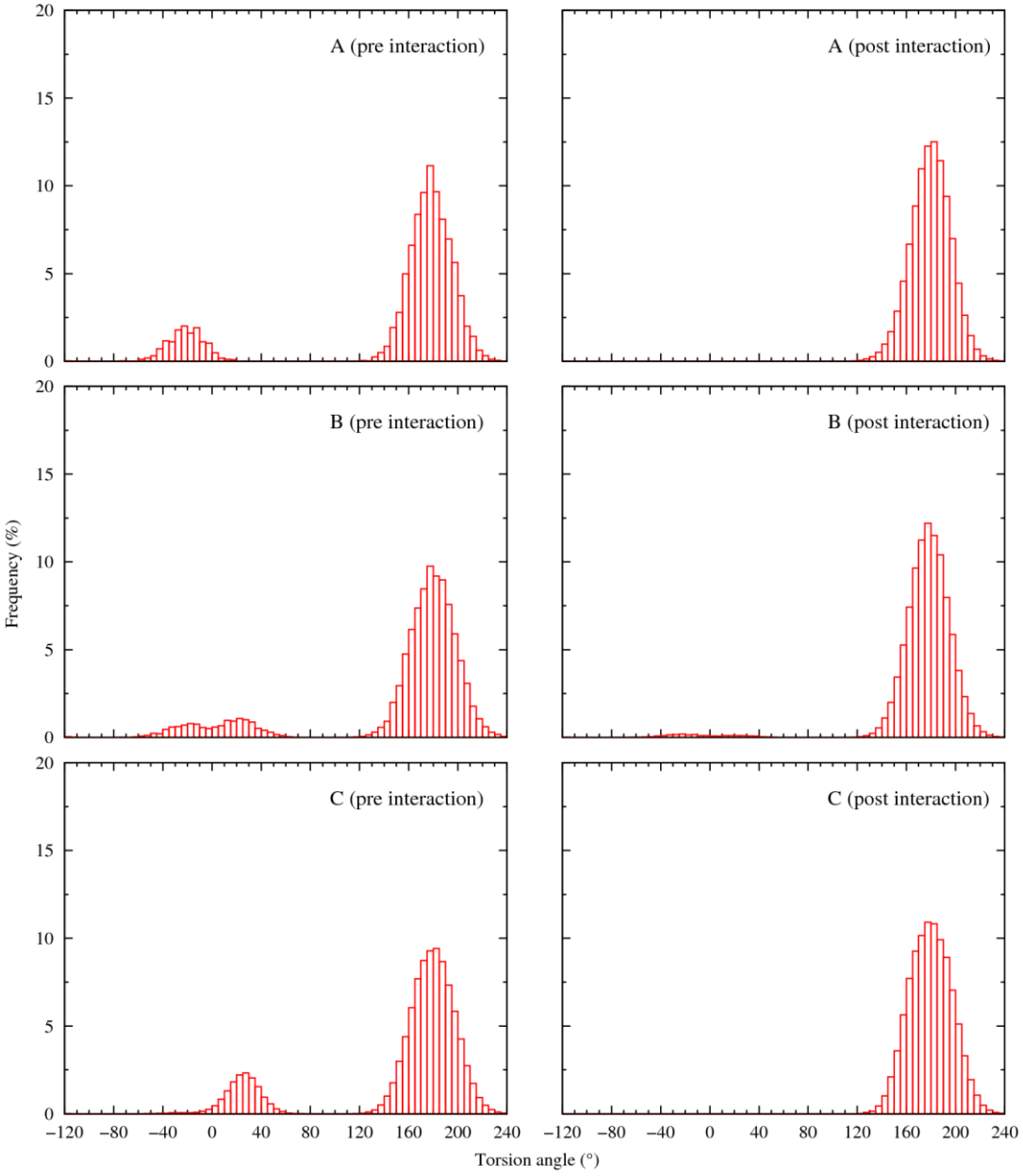

Figure 77 – Frequency histograms showing the distribution of the two C=C-N-C torsion angles values of S01, S09 and S10 in systems A, B and C, before the interaction with the water/lipid interface (*pre interaction*) and after (*post interaction*).

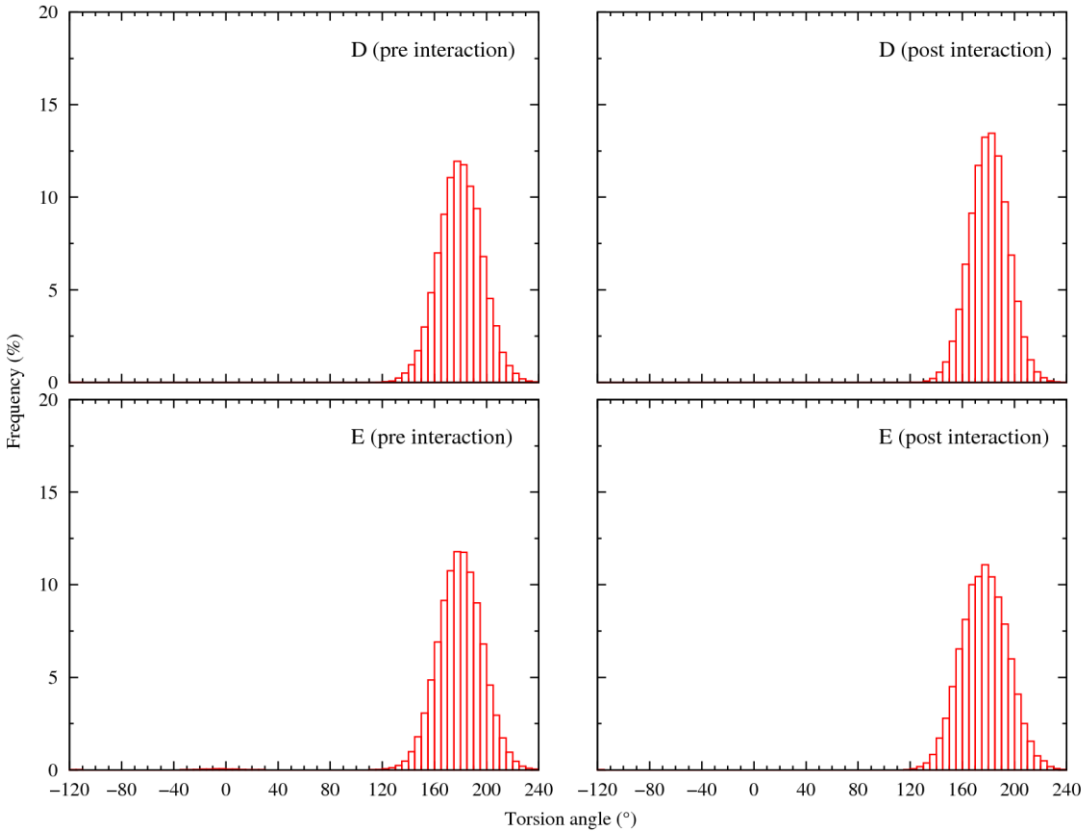

Figure 78 – Frequency histograms showing the distribution of the two C=C-N-C torsion angles values of S19 and S20 in systems D and E, before the interaction with the water/lipid interface (*pre interaction*) and after (*post interaction*).

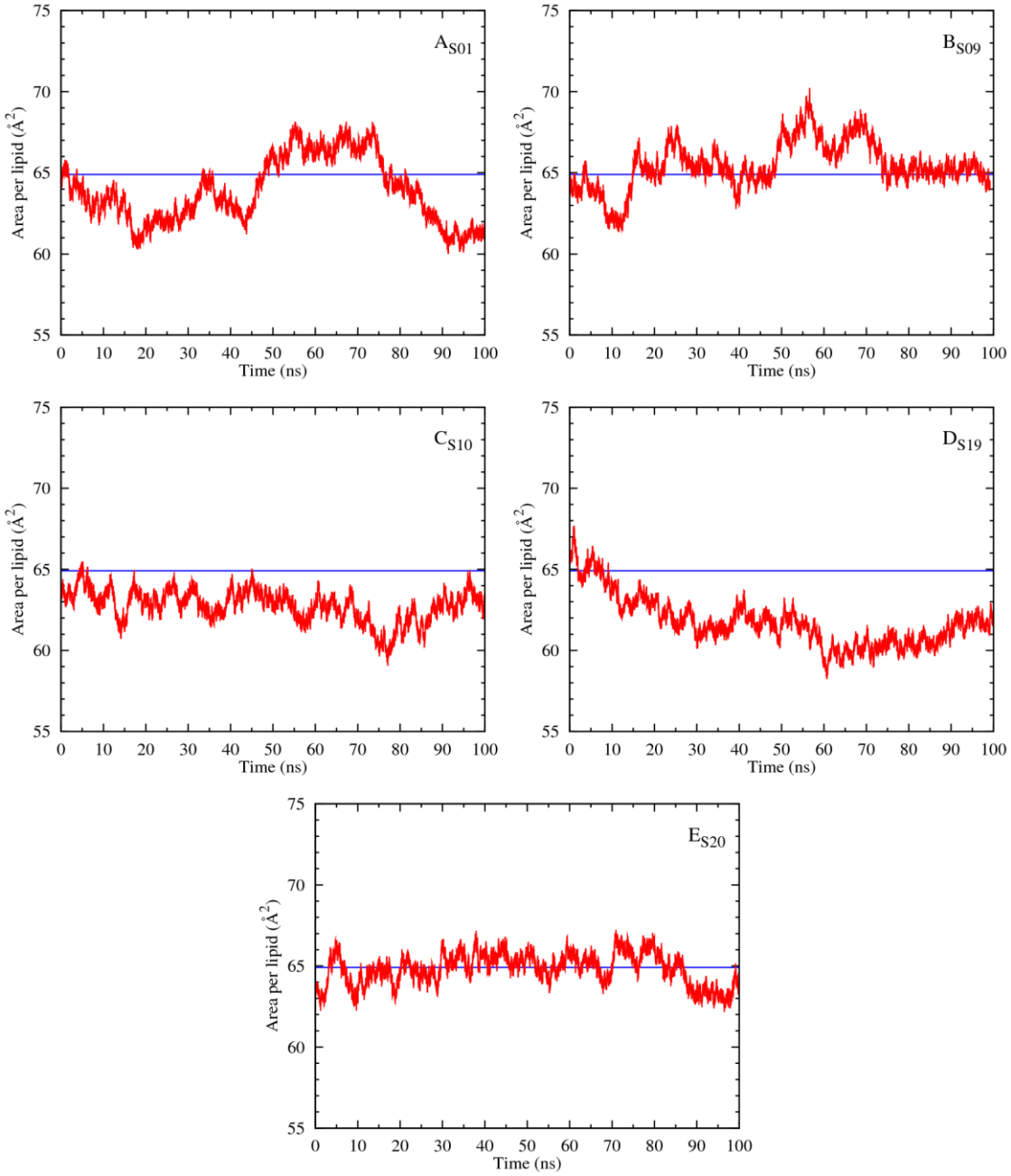

Figure 79 – Evolution of area per lipid through the course of the MD simulation time is represented in red. The reference value from Félix *et al* (117) is plotted as a blue line.

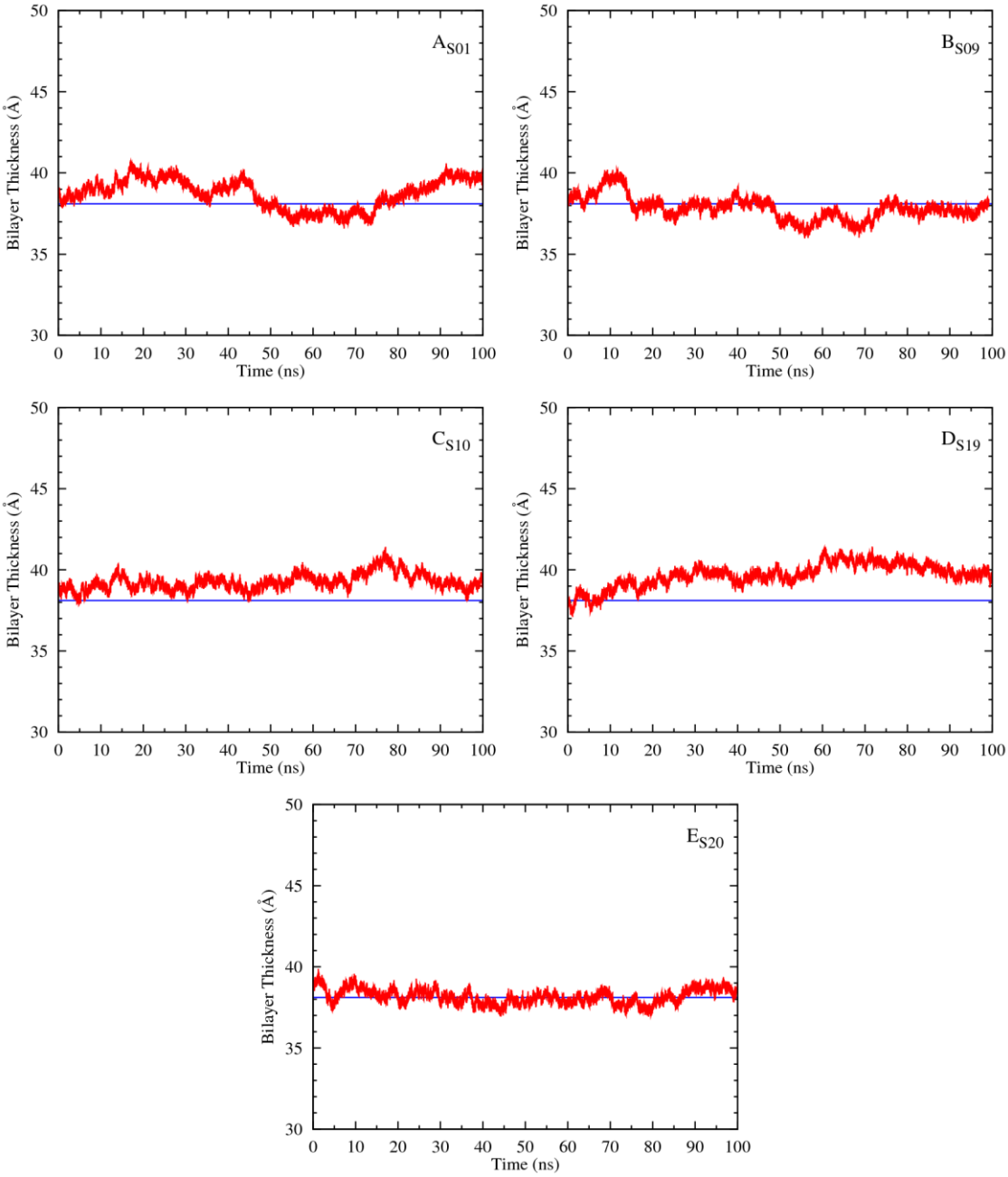

Figure 80 – Evolution of the bilayer thickness (red line) through the MD simulation of systems A-E. Comparison with theoretical values from membrane model I simulation (64.9 Å in blue).

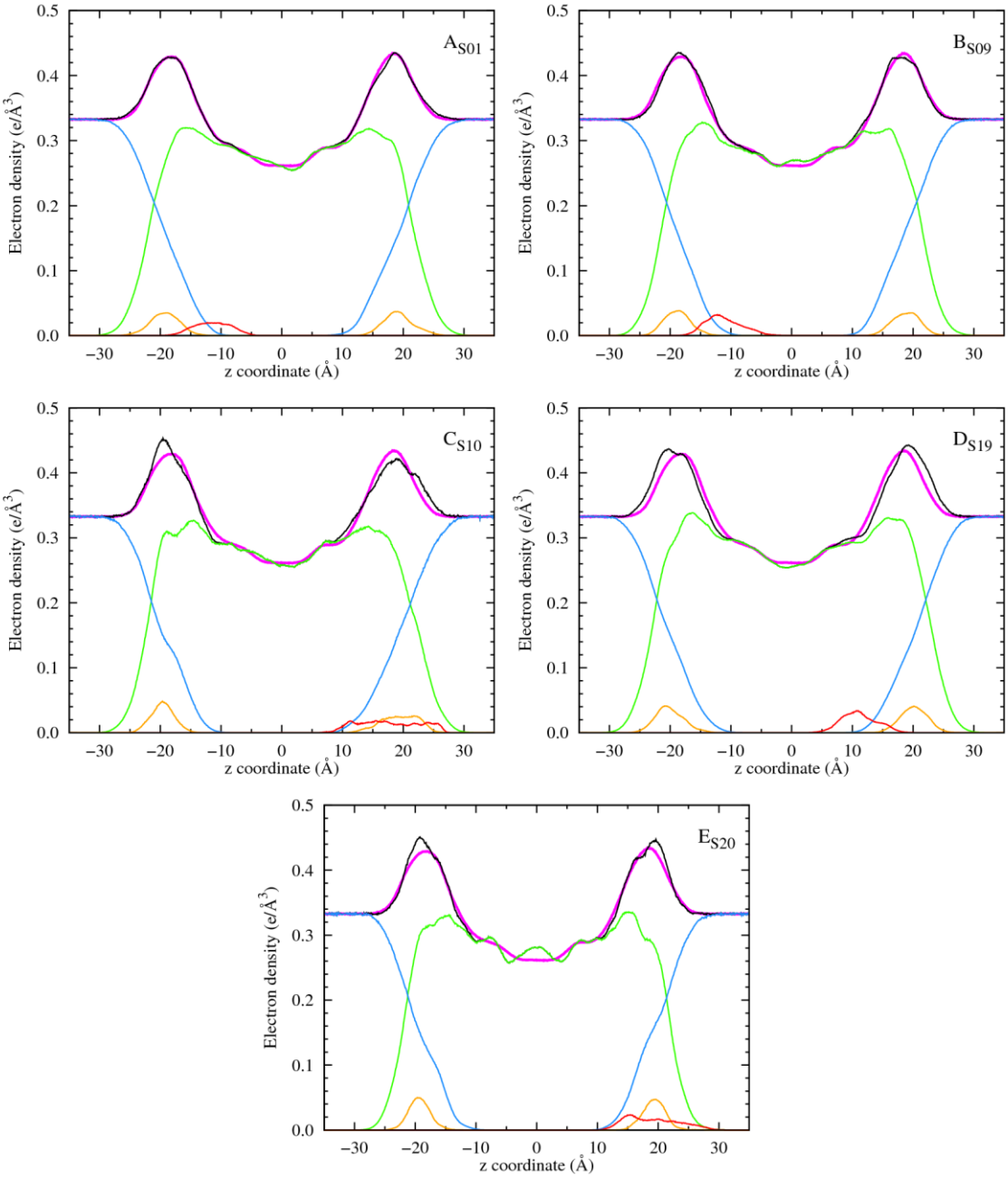

Figure 81 – Electron density profiles of the membrane systems A-E, estimated for the last 40 ns of simulations A, B and D; for the last 15 ns of sampling of system C and for the last 10ns of system E. The receptor is plotted as a red line and scaled 5 times. The full system is plotted in black, the water in blue, the phospholipids in green and the phosphorus in dark yellow. *z*= 0 Å corresponds to the core of the POPC bilayer. Reference profile from membrane model is represented in magenta.

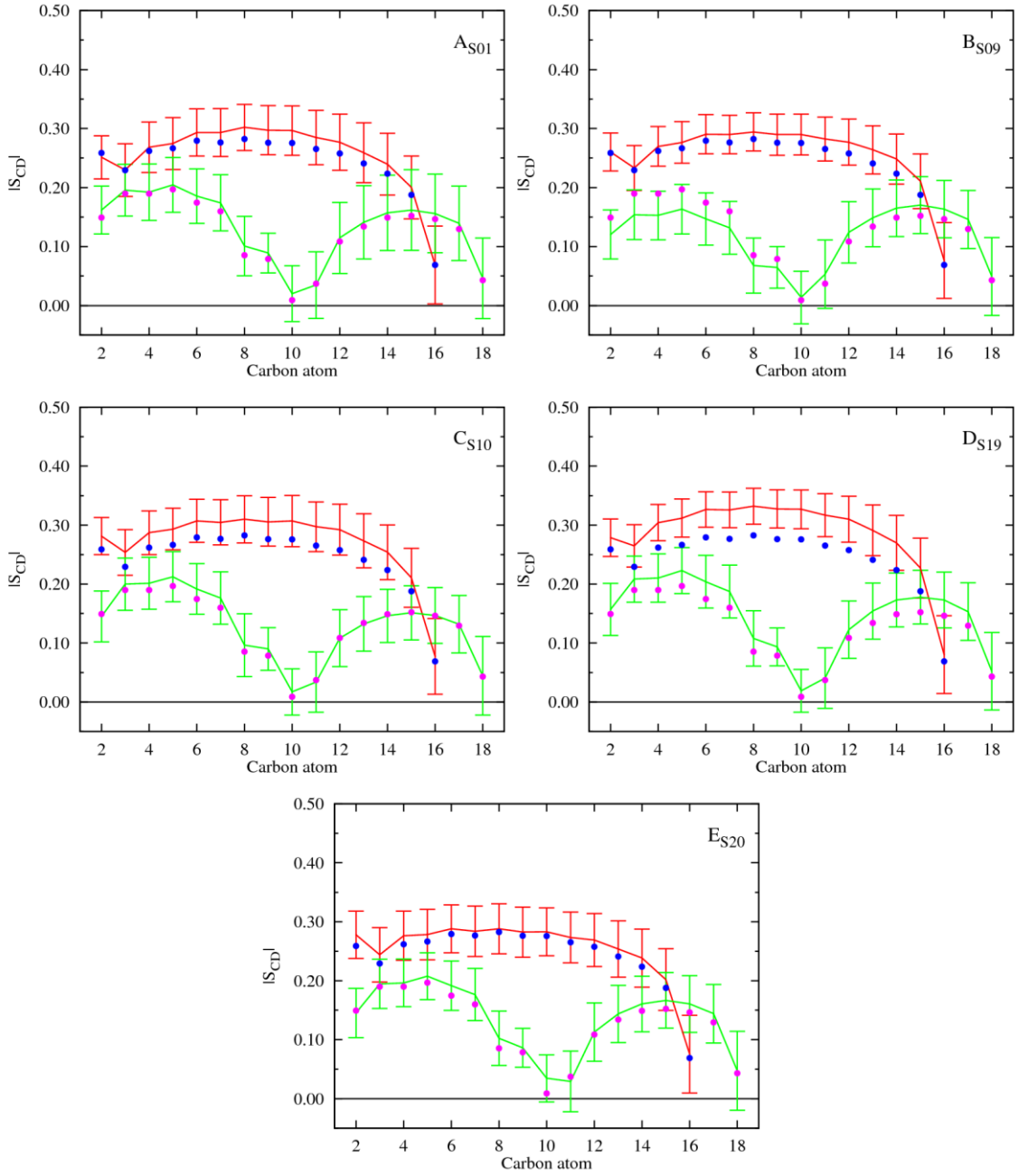

Figure 82 – Computed |S_{CD}| for palmitoyl and oleyl chains for 40 ns of sampling of simulations A, B and D; for 15 ns of sampling of system C and for 10ns of system E. The |S_{CD}| values calculated for the *sn*-1 chain are shown in red, while the values for the *sn*-2 chain are shown in green. The error bars associated with these results correspond to the standard deviation. The computed |S_{CD}| values from reference model I are presented in blue (*sn*-1 chain), and magenta (*sn*-2 chain).

MD simulations of the receptors starting from within the membrane

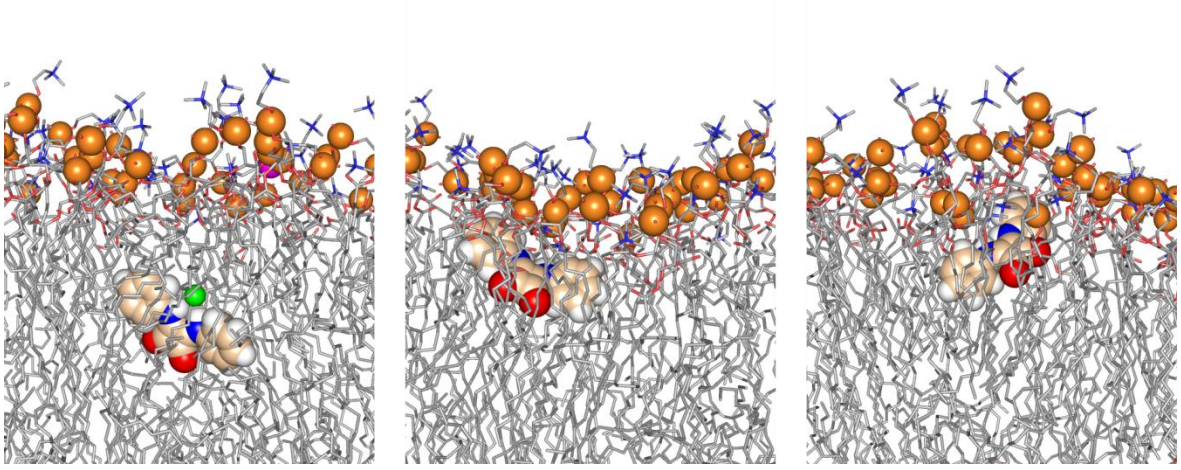

Figure 83 – Snapshots of system F, taken at different simulation times (0, 50 and 100 ns), showing the diffusion of S01. Images show the different positions of the receptor in the membrane. The receptor is drawn in a space filling model with carbon atoms in wheat, oxygen atoms in red, nitrogen atoms in blue and hydrogen atoms in white. The chloride and sodium ions, as well as the phosphorus atoms from the bilayer are represented as green, magenta and orange spheres, scaled to 0.7 vdW radius, respectively. In POPC lipids, carbon, nitrogen and oxygen atoms are drawn as grey, blue and red lines, respectively, while C-H hydrogen atoms have been omitted for clarity.

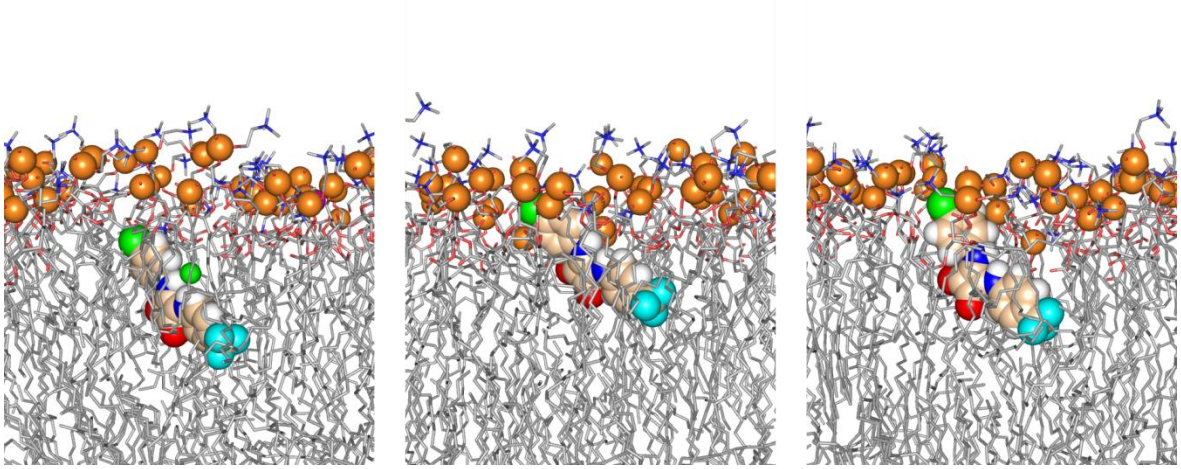

Figure 84 – Snapshots of system G, illustrating the diffusion process of S09. Fluorine atoms are drawn as cyan spheres. Remaining details as given in Figure 83.

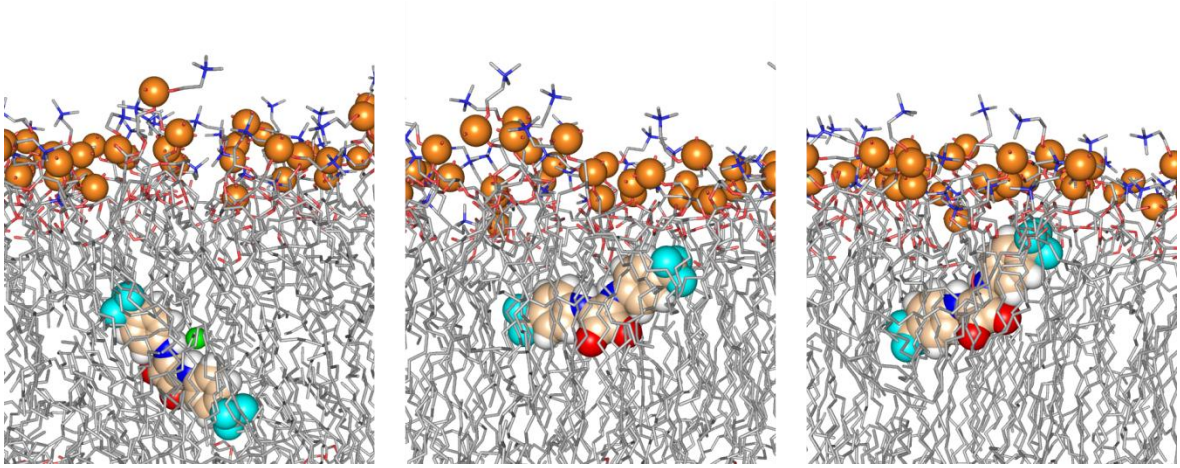

Figure 85 – Snapshots of system H, illustrating the diffusion process of S10. Fluorine atoms are drawn as cyan spheres. Remaining details as given in Figure 83.

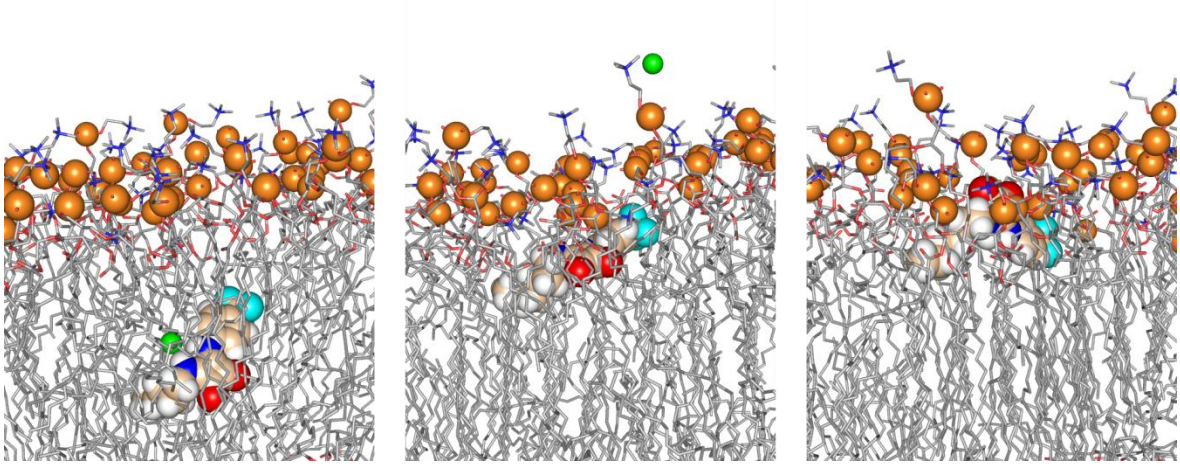

Figure 86 – Snapshots of system I, illustrating the diffusion process of S19. Fluorine and chloride atoms are drawn as cyan and green spheres. Remaining details as given in Figure 83.

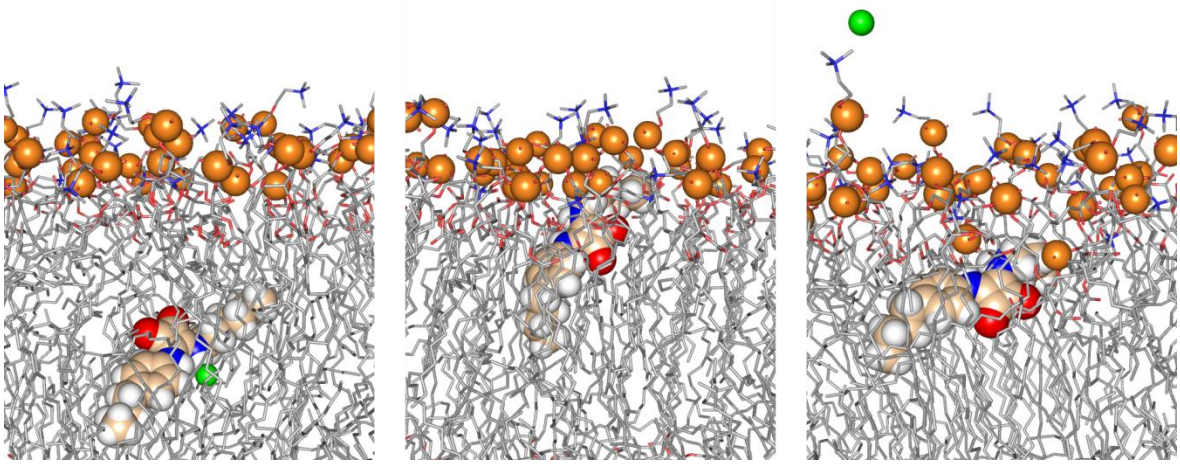

Figure 87 – Snapshots of system J, illustrating the diffusion process of S20. Remaining details as given in Figure 83.

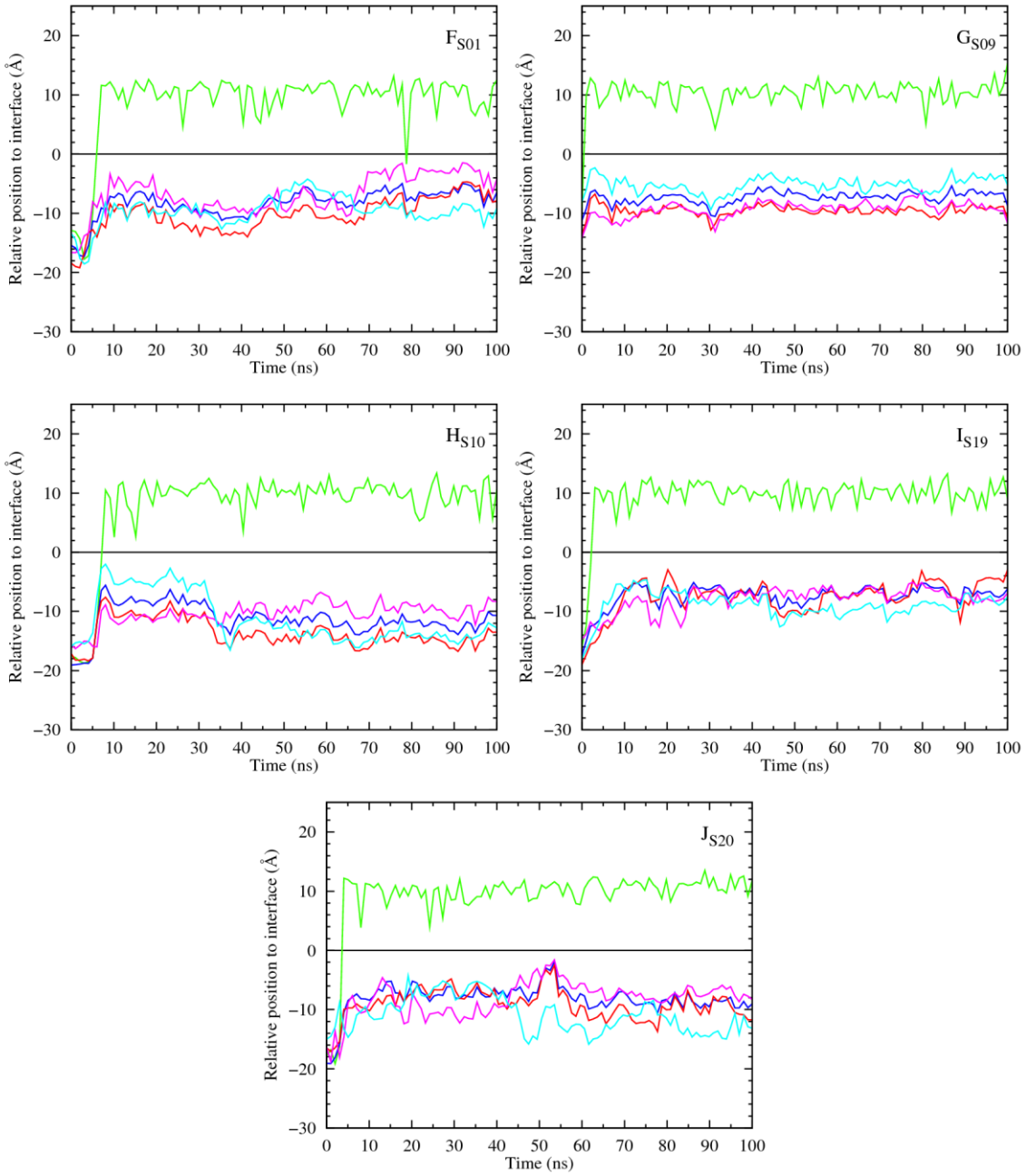

Figure 88 – Evolution of the receptor and chloride relative positions to the water/lipid interface (z = 0 Å). In green is represented the chloride ion, in red the centre of mass of the oxygen atoms from the receptor, in blue the centre of mass of the nitrogen atoms, in magenta and cyan are represented the phenyl groups (F, G and H); a phenyl group and an aliphatic chain (I) or an aliphatic chain and a butyl group (J), respectively. Data was smoothed using Bézier curves.

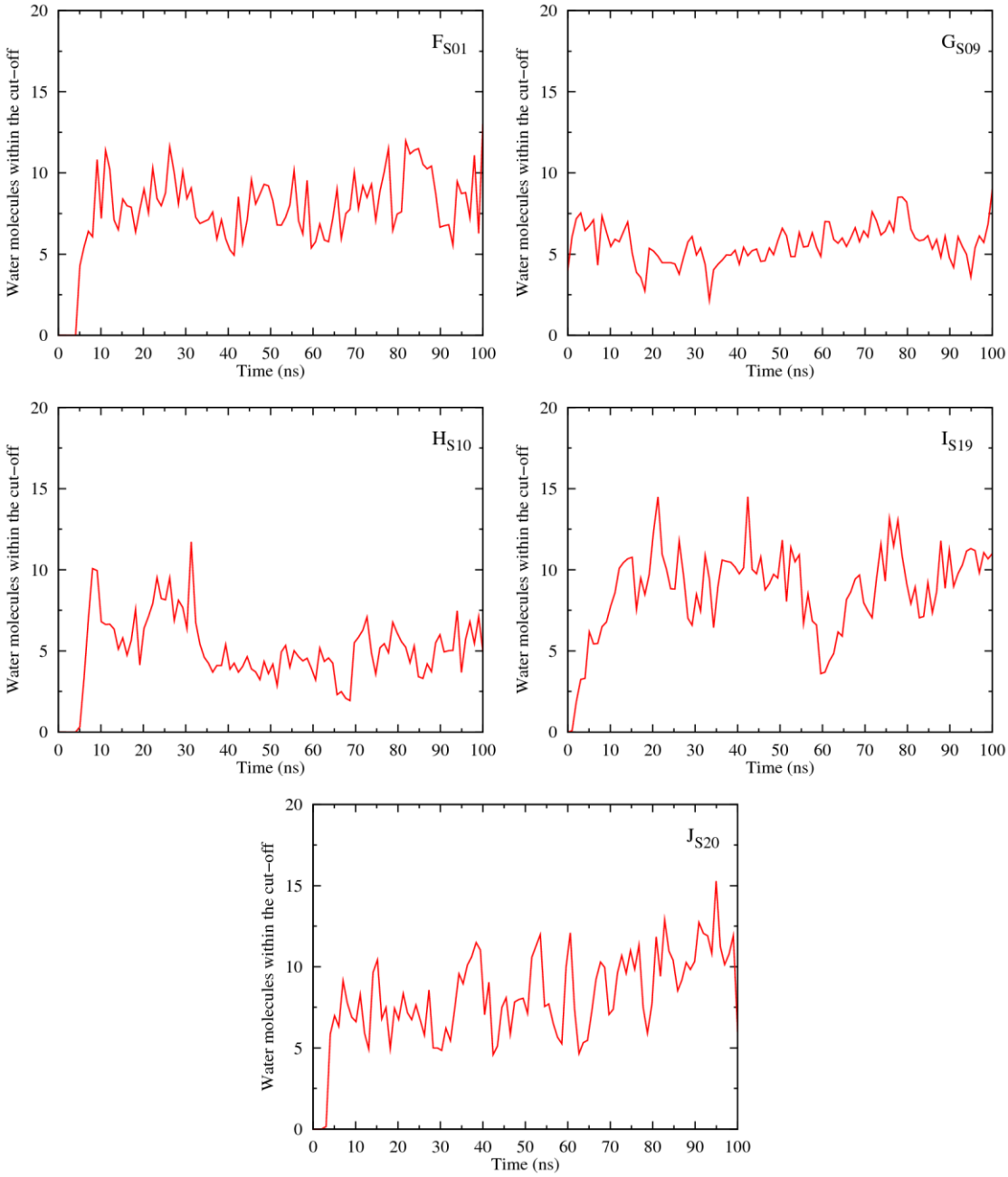

Figure 89 – Variation of the number of water molecules within the solvation shell defined by a cut-off of 3.5Å from receptors S01 (F), S09 (G), S10 (H), S19 (I) and S20 (J). Data was smoothed using Bèzier curves.

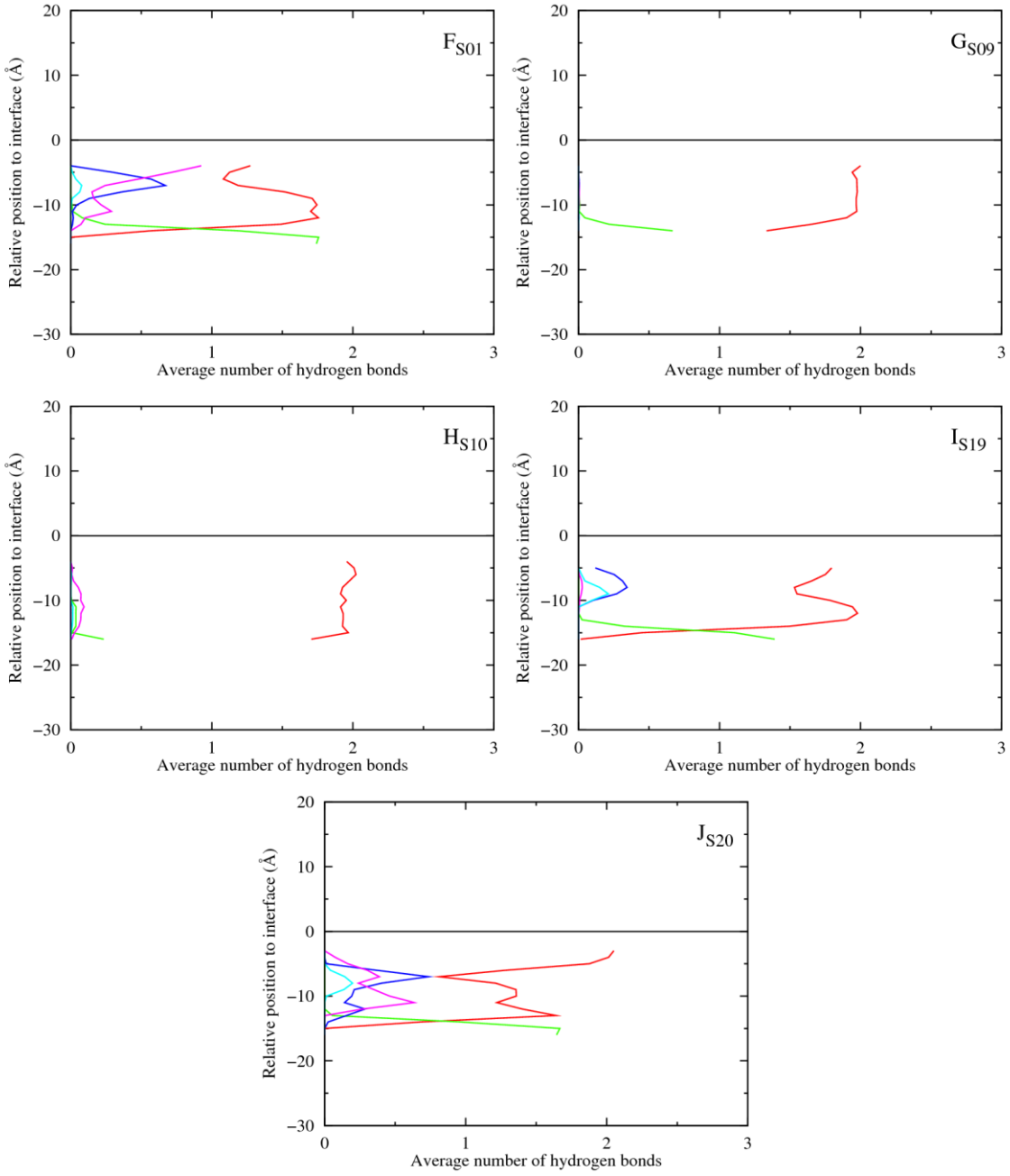

Figure 90 – Average number of hydrogen bonds *vs* the relative position of the centre of mass of each receptor. The following colour scheme was used for the hydrogen bonds established between the receptor and water molecules (red), chloride ion (green), POPC head groups (blue), ester groups from POPC *sn*-1 chains (magenta) and *sn*-2 chains (cyan).

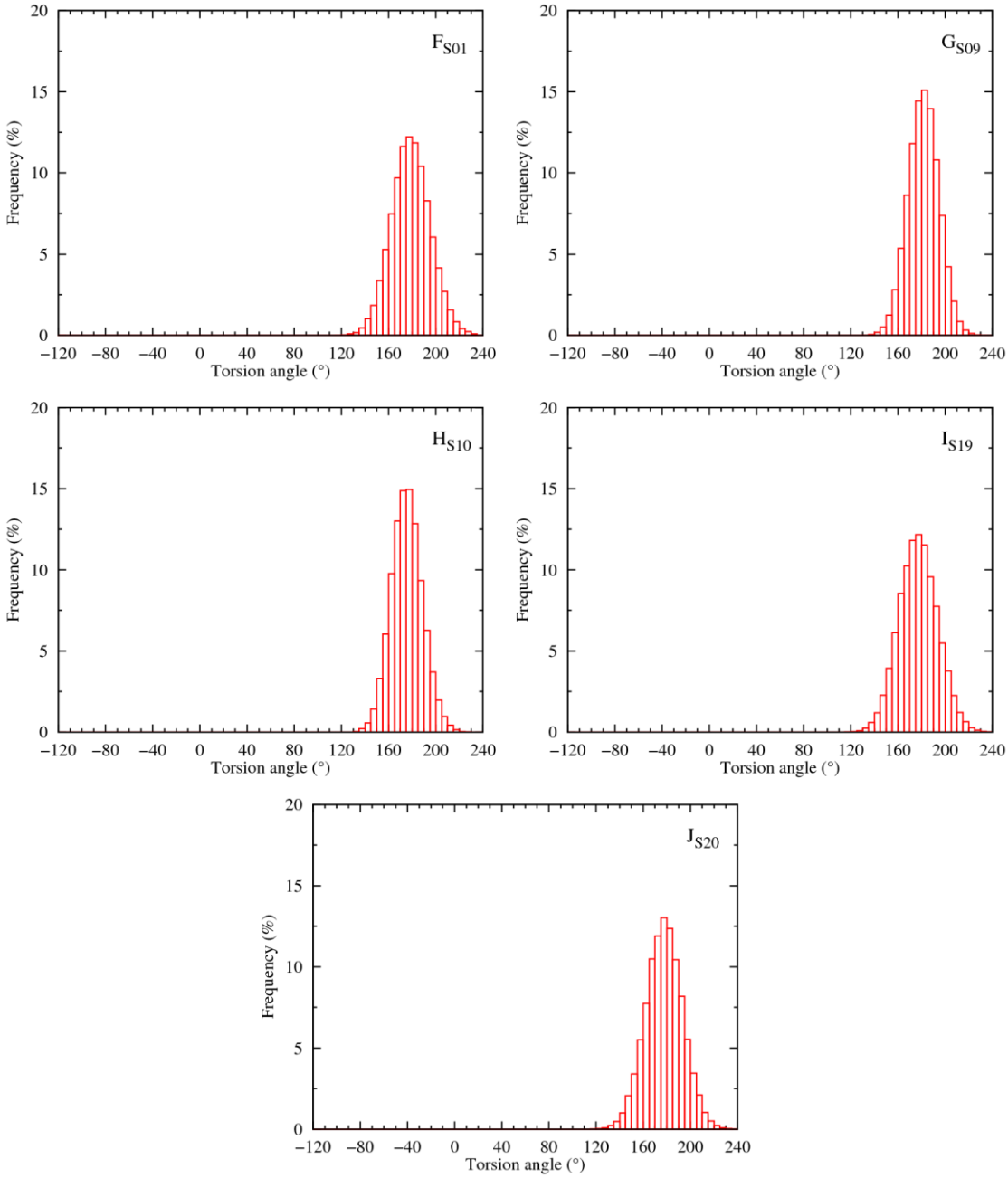

Figure 91 – Frequency histograms showing the distribution of the two C=C-N-C torsion angles values of S01-S20 in simulations F-J, in the last 40ns of simulation time.

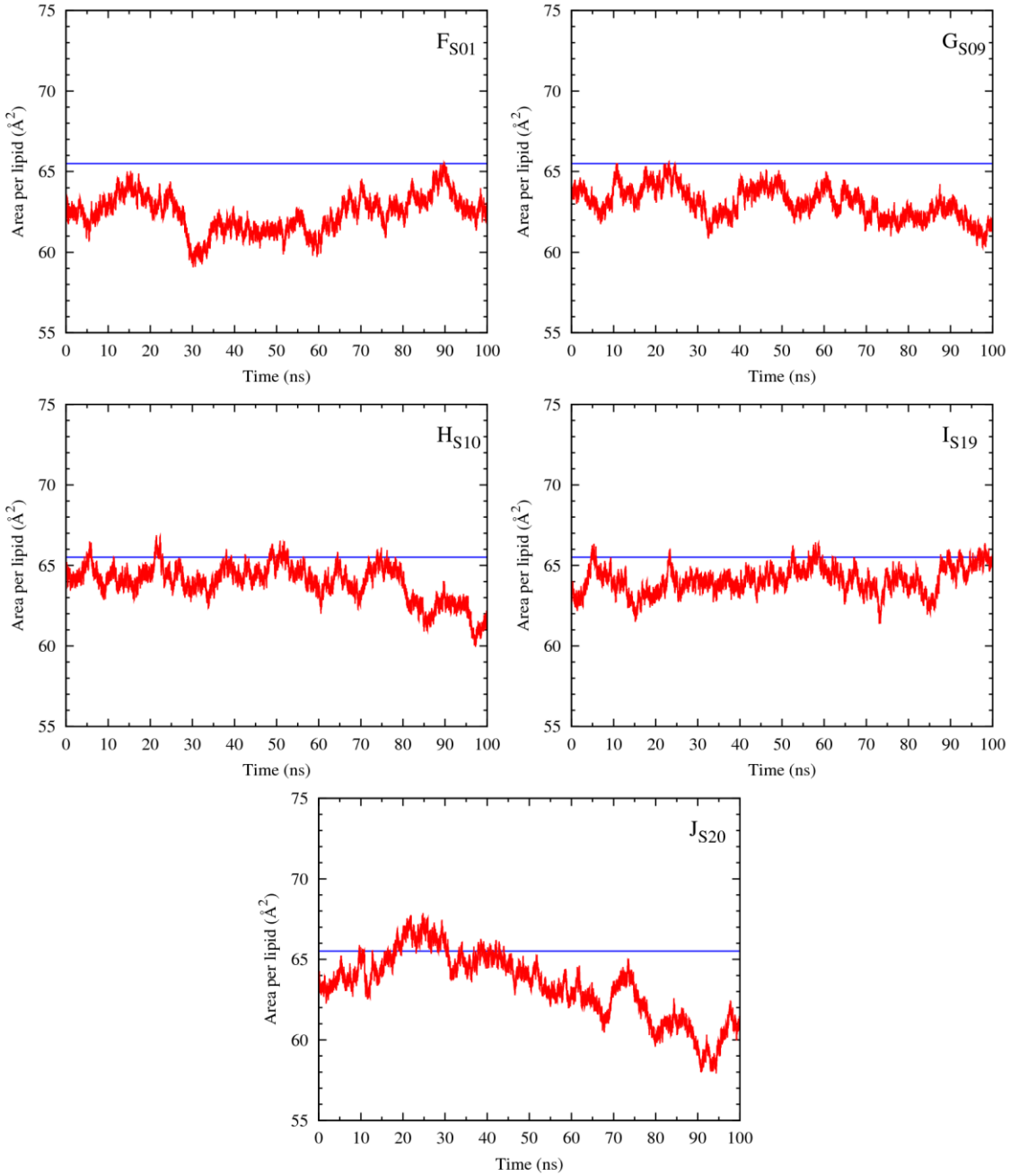

Figure 92 – Evolution of area per lipid through the course of the MD simulation time is represented in red. The reference value from the simulation of membrane model II is plotted as a blue line.

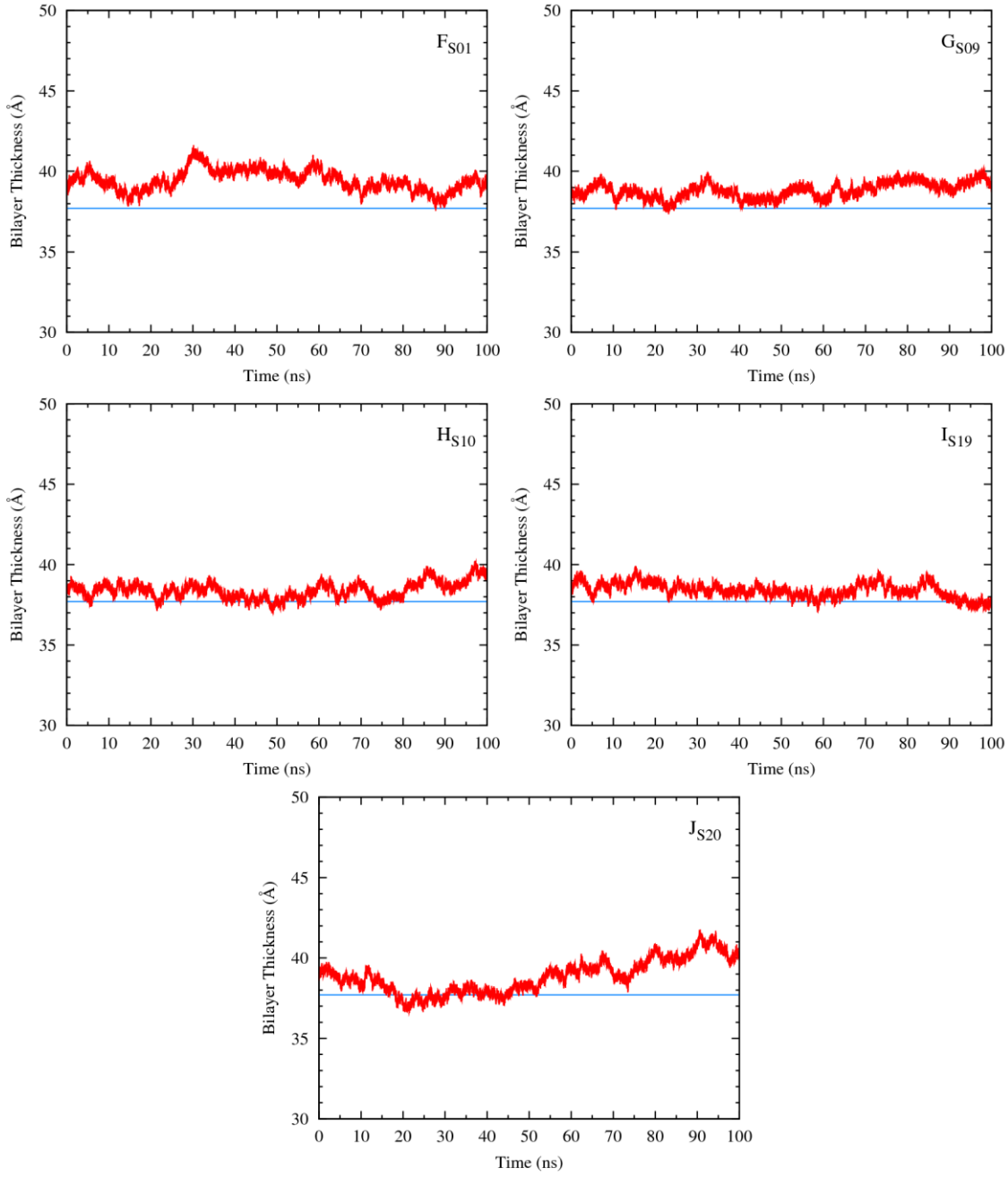

Figure 93 – Evolution of the bilayer thickness (red line) through the MD simulation of systems A-E. The reference value from the simulation of membrane model II is plotted as a blue line.

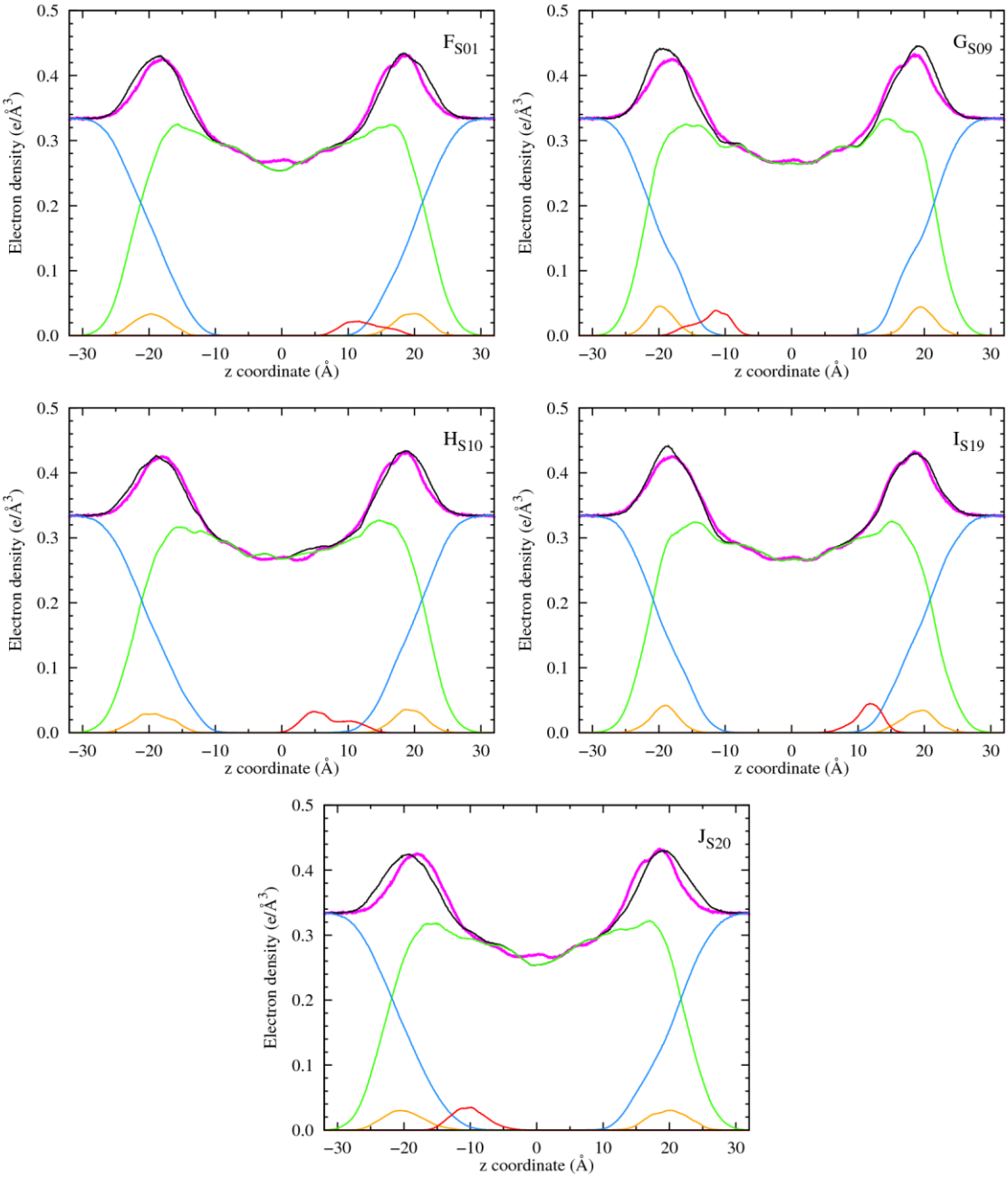

Figure 94 – Electron density profiles of the membrane systems F-J, estimated for the last 40 ns of MD simulation. The receptor is plotted as a red line and scaled 5 times. The full system is plotted in black, the water in blue, the phospholipids in green and the phosphorus in dark yellow. *z* =0 Å corresponds to the core of the POPC bilayer. System profile from membrane model II simulation is represented in magenta.

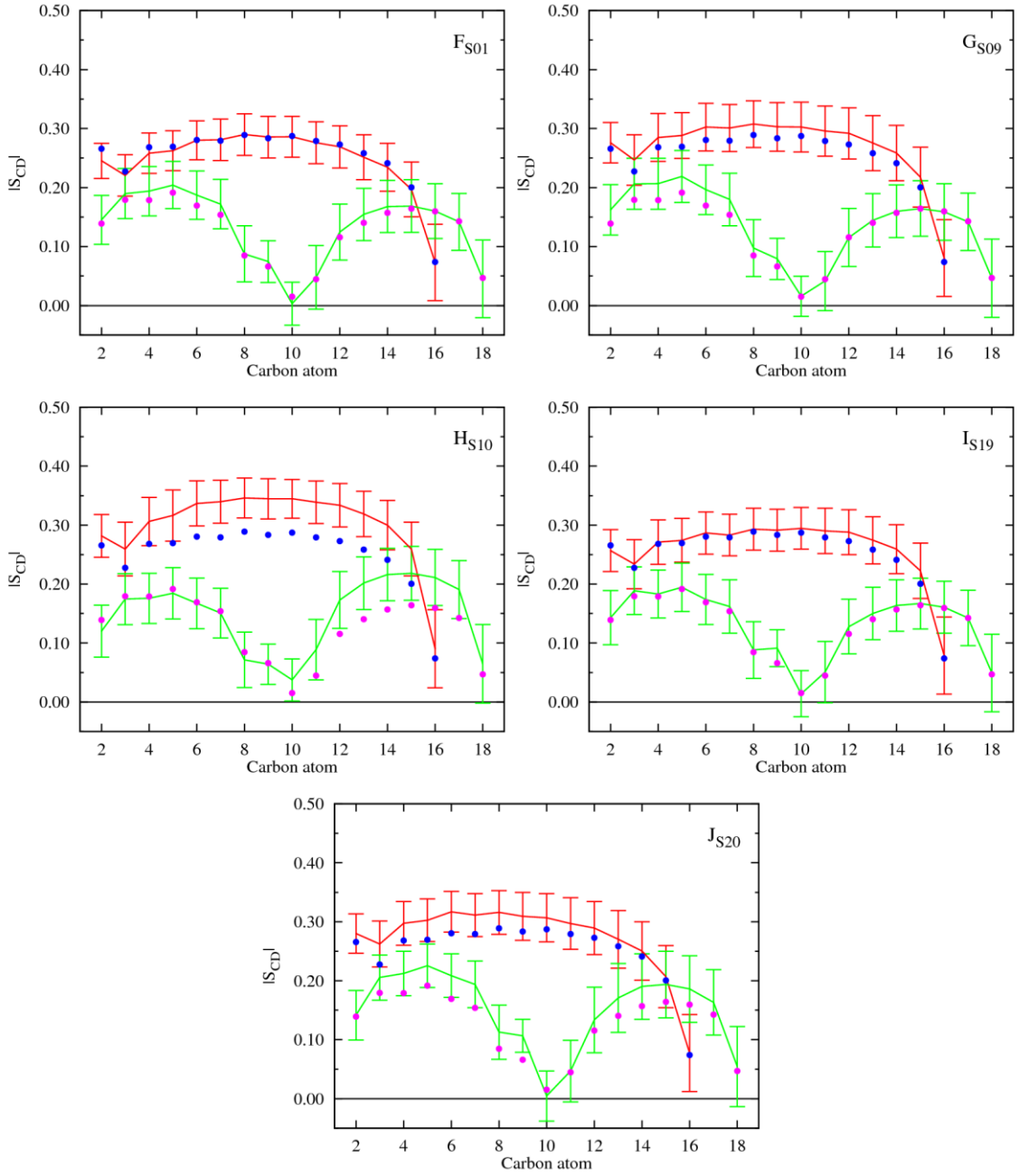

Figure 95 – Computed $|S_{CD}|$ for palmitoyl and oleyl chains for 40 ns of sampling of simulations F-J. The $|S_{CD}|$ values calculated for the *sn*-1 chain are shown in red, while the values for the *sn*-2 chain are shown in green. The error bars associated with these results correspond to the standard deviation. The computed $|S_{CD}|$ values from membrane model II simulation are presented in blue (*sn*-1 chain), and brown (*sn*-2 chain).